TESIS DOCTORAL

2017

Resolution of neutronic challenges for the development of ITER and DEMO-EU magnetic fusion reactors

Raquel García Martín

Ingeniera Química

PROGRAMA DE DOCTORADO EN TECNOLOGÍAS INDUSTRIALES

DIRECTOR ***Javier Sanz Gozalo***

CODIRECTOR ***Juan Pablo Catalán Pérez***

TESIS DOCTORAL

2017

Resolution of neutronic challenges for the development of ITER and DEMO-EU magnetic fusion reactors

Raquel García Martín

Ingeniera Química

PROGRAMA DE DOCTORADO EN TECNOLOGÍAS INDUSTRIALES

DIRECTOR Javier Sanz Gozalo

CODIRECTOR Juan Pablo Catalán Pérez

Acknowledgments

First of all, I would like to express my gratitude to my two supervisors, who have been fundamental for the development of this thesis. To Javier, for giving me the opportunity to start from scratch in a new field that seemed alien to my training, and especially for trusting I could carry it out. To Juan, for the day to day, for his continuous guidance and patience to explain me much of what I have learned along this period. Without either of them this thesis would not have been possible.

I would also like to thank the support of everyone at the TECF3IR research group, and especially Mauricio, with whom I have worked closely over the last years and who has always been willing to help me.

Special thanks to my coffee colleagues and great friends at UNED: Lucía and Miryam, with whom I have shared the best moments and laughs of this time (and, with Lucia, the best brownie I have ever tasted). Thanks to Estibalitz, who has had to deal with me asking the whole issue of paperwork for the PhD a thousand times, and who has made everything easier. And thanks to you three, above everything, for your encouragements.

Thanks to Pablo, for putting up with me in my worst moments, and continuously cheer me up. No one like you to get it since, as I told you once... you are able to make me smile whatever the circumstance is and, with that smile, everything seems different. You know that without you, I would not have gotten this far.

To my family. To my mother, the greatest influence in my life, who has always been up to date with how I was dealing with the thesis; to my father for hurrying me to finish, among other good advices; and to my two brothers, simply for being there and make me disconnect from time to time with some silly laughs. And to my in-laws, for the interest and affection they have always shown in all my training stages.

It is not possible to thank all those who have helped and encouraged me in this work since the list would be too large, but I would not want to miss the opportunity to say thanks to my lifelong friend Olga; to Marcos, who is part of my life since more than 10 years ago; and Rafa, who, despite the time and distance has always made a way to see us. With you three I have been able to relieve myself in the some of the more stressed moments, so a big thank you to all of you.

Finally, I would like to mention that this work has been performed mostly under support of Grant FPI UNED 2013. It has been also partially supported, as part of the TECF3IR contributions, by the Spanish MINECO (Ministerio de Economía y Competitividad) under Programa Estatal I+D+I-Retos, Proyecto ENE2015-70733-R; the Programa de Actividades I+D de la Comunidad de Madrid under TECHNOFUSION-CM (S2009/ENE-1679) and TECHNOFUSION(II)-CM, (S2013/MAE-2745) Projects for the development of the "Area of Computational Simulation"; and by the EUROfusion Consortium (Programme 2014-2018), under the Work Package Safety and Environment (WPSAE). The views and opinions expressed herein do not necessarily reflect those of the European Commission.

Index

List of tables

List of figures

Abbreviations and acronyms

BB	Breeding Blanket
BP	BackPlate
BSM	Blanket Shield Module
BSS	Back Supporting Structure
CAD	Computer-Aided Design
CADIS	Consistent Adjoint Driven Importance Sampling
CATIA	Computer Aided Three-dimensional Interactive application
CCFE	Culham Centre for Fusion Energy
CDR	Contact Dose Rate
Cu	Copper
CRM	Complex Recycle Material
CSG	Constructive Solid Geometry
CY	Calendar Year
D	Deuterium
DCLL	Dual-Coolant Lithium-Lead
DEMO	DEMOnstration
EAF	European Activation File
EFDA	European Fusion Development Agreement
ENDF	US Evaluated Nuclear data Library
EXFOR	Experimental Nuclear Reaction Data Library
F4E	Fusion For Energy
FCI	Flow Channel Inserts
FENDL	Fusion Evaluated Nuclear Data Library
FPP	Fusion Power Plant
FW	First Wall
FW-CADIS	Forward Weighted CADIS
FWS	First Wall Samples

GVR	Global Variance Reduction
H	Hydrogen
HCF	Hot Cell Facility
HCLL	Helium-Cooled Lithium-Lead
HCPB	Helium Cooled Pebble Bed
He	Helium
HLW	High Level Waste
IAEA	International Atomic Energy Agency
ICF	Inertial Confinement Fusion
IFMIF	International Fusion Materials Irradiation Facility
IO	ITER Organization
ITER	International Thermonuclear Experimental Reactor
JANIS	Java-based Nuclear Data Information System
JEFF	Joint Evaluated Fission and Fusion File
JET	Joint European Torus
KIT	Karlsruhe Institute of Technology
LILW	Low and Intermediate Level Waste
LILW-LL	Low and Intermediate Level Waste-Short Lived
LILW-SL	Low and Intermediate Level Waste-Long Lived
LiPb	Lithium-Lead
LOCA	Loss Of Coolant Accidents
MAGIC	Method of Automatic Generation of Importances by Calculation
MCAM	Monte Carlo Automatic Modeling system
MCF	Magnetic Confinement Fusion
MCNP	Monte Carlo N-Particle
MHD	Magneto-HydroDynamic
NAS	Neutron Activation System
NAW	Non Active Waste
NIF	National Ignition Facility
PC	Port Cell

PI	Port Interspace
PPPT	Power Plant Physics and Technology
PWD	Permanent Disposal Waste
QA	Quality Assurance
QS	Quality Score
R&D	Research And Development
R2S	Rigorous 2-Step
RAMI	Reliability/Maintainability/Availability/Inspectability
RFP	Reversed Field Pinch
SDDR	ShutDown Dose Rate
SRM	Simple Recycle Material
SuperMC	Super Monte Carlo
T	Tritium
TBS	Tritium Breeding System
3D	Three-Dimensional
TECF3IR	TECnología de Fisión, Fusión y Fuentes de Irradiación
TENDL	TALYS-based Evaluated Nuclear Data Library
TFCs	Tororidal Field Coils
VLLW	Very Low Level Waste
VR	Variance Reduction
VV	Vacuum Vessel
W	Tungsten
WCLL	Water-Cooled Lithium-Lead

Resumen

El objetivo de esta tesis doctoral es contribuir en el desarrollo de la fusión por confinamiento magnético, abordando cuestiones de interés en el marco de ITER y DEMO.

El Reactor Termonuclear Experimental Internacional, ITER, es un experimento científico a gran escala que tiene como objetivo resolver problemas, tanto técnicos como científicos, para poder avanzar en el campo de la fusión nuclear. Con él se pretende demostrar la viabilidad de la fusión como fuente de energía y recoger los datos necesarios para el diseño y posterior operación de la primera planta comercial de producción de electricidad a partir de la energía de fusión. Actualmente se encuentra en construcción en el sur de Francia, aunque algunos componentes y sistemas se encuentran todavía en fase de diseño. ITER Organization (IO) es la entidad jurídica responsable de la construcción, funcionamiento, explotación y desactivación de las instalaciones de ITER. En el proyecto participan la Unión Europea, India, Japón, China, Rusia, Corea del Sur y Estados Unidos.

El reactor DEMOstración DEMO es el siguiente paso en el camino para hacer realidad la energía de fusión. Su objetivo es desarrollar y probar tecnologías de ensayo, los regímenes de la física y las rutinas de control para el funcionamiento de un reactor de fusión no como un experimento científico, sino como una planta comercial de potencia.

Uno de los problemas actuales que se identifican en ITER es conseguir valores de dosis residual por debajo de ciertos límites en las áreas de Port Cell y Port Interspace para poder llevar a cabo tareas de mantenimiento manual. Para evaluar la calidad de los resultados que se obtienen, es fundamental conocer cómo son las herramientas que nos permiten llegar a ellos. En este sentido, la aportación que se presenta se basa en el estudio de la calidad que las secciones eficaces de la librería EAF-2007, que es con la que habitualmente se llevan a cabo estos cálculos de dosis residual de mantenimiento en ITER, de manera que se pueda conocer el grado de fiabilidad que tienen estas secciones eficaces. Además, se evalúan las posibles mejoras y/o actualizaciones tanto en la versión más reciente de EAF (2010) como en la librería TENDL (versiones 2013-2015).

Como principales conclusiones obtenidas de esta primera parte de la tesis, se ha visto que, hasta la fecha, la dosis calculada (producida por la activación de cada uno de los materiales) es fiable (es decir, más del 90% de la producción de los radionucleidos principales se debe a reacciones cuyas secciones eficaces en la librería EAF están validadas) para los siguientes materiales: SS316LN-IG, SS304L, Eurofer, LiPb, W, hormigón convencional de B-lite y hormigón

L2N. Por el contrario, la predicción de la dosis para el hormigón baritado (potencial candidato para usarse en ITER) y el cobre no resulta fiable.

Por otra parte, ITER contará con una serie de sistemas de diagnósticos para proporcionar las medidas necesarias para controlar, evaluar y optimizar el rendimiento del plasma y para fomentar también la comprensión de la física del mismo. Los sistemas de diagnóstico estarán localizados en distintos componentes del reactor: en la envoltura, cámara de vacío, criostato, puertos (superiores y ecuatoriales), divertor, etc. Al introducir estos diagnósticos en el reactor, se producen dos efectos. Por un lado, se elimina material de blindaje y, por otro, se generan caminos por los que puede haber fugas de radiación. Como consecuencia, algunos componentes tales como las bobinas de campo toroidal (TFCs) o la vasija de vacío (VV) pueden verse afectados por el cambio producido en el campo de radiación al que están sometidos. El hecho de que cambie el campo de radiación puede tener consecuencias en el funcionamiento de estos componentes, lo que podría desembocar en la pérdida del estado superconductor de dichas bobinas y, en última instancia, del confinamiento del plasma.

Precisamente por este motivo, dentro de ITER IO, existe cierta preocupación por las cargas de radiación a las que están sometidos estos componentes, dado que estudios previos demostraban que los valores de estas cargas se encontraban muy cerca del límite y, en algunos casos, por encima. Por esta razón, un capítulo de la tesis aborda el estudio del efecto que tiene incluir cuatro sistemas de diagnósticos in-vessel (reflectometría, Neutron Activation System, First Wall Samples y bolómetros) sobre la VV y las TFCs. En este sentido, los resultados muestran que la contribución de los sistemas de diagnóstico estudiados, a las cargas de radiación que reciben estos componentes, no resulta crítica para el correcto funcionamiento de los mismos.

La parte dedicada a DEMO, se centra en la envoltura DCLL (Dual-Coolant Lithium-Lead) y consiste en, partiendo del modelo CAD del reactor (tanto el correspondiente al año 2014 como al 2015), realizar cálculos de transporte (MCNP) y activación (ACAB) de los materiales que componen la envoltura y, finalmente, dar resultados en cuanto a activación y calor residual. Estos resultados son el punto de partida para posteriores análisis relacionados con seguridad y gestión de residuos radioactivos. Además, se calcula la producción de residuos y se analiza la viabilidad de almacenarlos en la instalación de El Cabril, incluyendo la determinación de la reducción de impurezas necesaria para ello. Los resultados reflejan que únicamente es necesario reducir una impureza (el Nb) para conseguir almacenar los residuos procedentes de esta envoltura en las instalaciones de almacenamiento superficial de El Cabril.

Abstract

The objective of this thesis is contributing to the development of the magnetic confinement fusion, addressing issues of interest within the framework of ITER and DEMO.

The International Thermonuclear Experimental Reactor, ITER, is a large-scale scientific experiment which aims to solve technical and scientific problems to advance in the nuclear fusion field. Its goal is to demonstrate the feasibility of fusion as an energy source and collect the necessary data for the design and subsequent operation of the first plant producing electricity from fusion energy. It is currently under construction in the south of France, although some components and systems are still in the design phase. ITER Organization (IO) is the legal entity responsible for building, operating, exploiting and deactivating ITER. The European Union, India, Japan, China, Russia, South Korea and the United States are the countries participating in the project.

Beyond ITER, the DEMOnstration power plant DEMO aims to develop and test technologies for the operation of a fusion reactor not as a scientific experiment, but as a power plant, applying the know-how gained with the ITER project.

One of the current identified problems in ITER is to achieve shutdown dose rates (SDDR) values below certain limits in the Port Cell (PC) and Port Interspace (PI) areas, in order to carry out manual maintenance activities. In this context, the quality of the EAF-2007 activation cross sections, which are usually used for these SDDR calculations in ITER, is assessed in order to set their reliability. In addition, possible improvements/updates in both the latest version of EAF (2010) and the TENDL library (2013 to 2015 versions) is evaluated.

As a conclusion from this first part of the thesis, it has been seen that, to date, calculated doses (produced by the activation of each of the materials) are trustworthy (i.e. more than 90% of the production of major radionuclides is due to reactions with EAF validated cross sections) for the following materials: SS316LN-IG, SS304L, Eurofer, LiPb, W, conventional concrete from B-lite, and L2N concrete. On the contrary, the SDDR prediction for Cu and barite concrete (potential candidate material) is not reliable.

On the other hand, ITER will have several diagnostic systems to provide the necessary measures to control, evaluate and optimize plasma performance and also to promote understanding of plasma physics. These diagnostic systems will be located at different components of the reactor: blanket, vacuum chamber, cryostat, ports (upper and equatorial), divertor, etc. By introducing these diagnostics into the reactor, two effects are produced. On

the one hand, shielding material is removed and, on the other hand, streaming paths are generated. As a consequence, some components such as the toroidal coils (TFCs) or the vacuum vessel (VV) might be affected by the change in the radiation field. The fact that the radiation field changes may affect their appropriate functioning, endangering the superconducting state of the TFCs and, as a result, the plasma confinement.

It is precisely for this reason that, within ITER IO, there is some concern about the radiation loads to which these components are subjected, since previous studies showed that the radiation load values were very close to the limit and, in some cases, above. For this reason, a chapter of the thesis addresses the impact of the inclusion of four in-vessel diagnostics (reflectometry, NAS-neutron activation system, FW-first wall samples and bolometers) on the radiation loads (nuclear heating and neutron induced damage) on the VV and the TFCs of the ITER reactor. In this sense, results show that the contribution of the analyzed diagnostic systems to the radiation loads on both the VV and the TFC is not critical for the appropriate functioning of these components.

Regarding DEMO, the focus is on the DCLL (Dual-Coolant Lithium-Lead) blanket concept. The work consists of performing transport (MCNP) and activation (ACAB) calculations of the blanket materials on the basis of 2014 and 2015 DEMO models and, finally, providing results in terms of activation and residual heat. These results are the starting point for further assessments on safety and/or waste management. Furthermore, the radioactive waste production is assessed and the possibility of waste disposal in El Cabril facility is analyzed, including the determination of the impurities limits needed to achieve this goal. Results show that it is only necessary to reduce one impurity content (Nb) in order to dispose the waste coming from this blanket at the El Cabril near-surface facility.

Chapter 1
Introduction

The research subject of this thesis is included within the field of nuclear fusion technology. This work addresses fundamental problems within international projects such as ITER and DEMO. This chapter is devoted to provide an introduction to the nuclear analysis in fusion devices, a summary regarding the motivation and the different contributions of this thesis, and a description about the organization of this document.

1. The need of nuclear analysis in fusion devices

In Deuterium-Tritium (D-T) fusion reaction, one neutron is released for each 17.6 MeV of fusion energy with a kinetic energy of 14.1 MeV. This is a significant difference compared to fission, where one neutron is released per 80 MeV of fission energy, and with 2 MeV as an average energy. This implies that a fusion D-T reactor is a greater neutron source in both quantity and energy terms [1].

In particular, the future magnetic confinement fusion (MCF) plants based on the D-T fuel cycle entail high levels of radiation. The International Thermonuclear Experimental Reactor (ITER) will operate at 500 MW of power ($\sim 10^{20}$ n/s) with a total of about 10^{27} neutrons [2]. On the other hand, the DEMOnstration (commonly called DEMO) concepts reactors that are being developed in Europe will reach about 5 times more power and around 50 times more neutrons during their operation.

These nuclear fusion facilities will have radiation fields both during the operation and during its shutdown. During the operation phase, the radiation field will come from neutrons released from the plasma which interact with the different materials of the reactor, producing prompt neutrons and gammas which will also contribute to the radiation field. Additionally, neutrons will activate the materials of the reactor being the cause of the radiation field during the shutdown period [3]. From the different kinds of decay radiation, only gammas will be considered as a relevant field for most of the studies, since they are widespread around all the facility whereas alpha and beta particles only have local effects, as they are charged. For a complete characterization of the facility, the isotopic inventory, which implicitly contains the source terms of this charged radiation, also has to be estimated.

In this context, it is necessary to evaluate the effects that these radiation fields might cause on people (workers and public) and the machinery involved in the reactor operation and its shutdown, as well as the mentioned radioisotope inventory produced by neutron induced material activation, which is an essential input for the design of components, maintenance planning, safety analysis and waste management asessments.

The nuclear analysis is in charge of the assessment of all these nuclear aspects and its goal is ensuring a safe operation of the facility taking into account the correct functioning of the components and the adequate design of shielding, in order to minimize the radiation exposure of both components and people. Thus, nuclear analysis is indispensable for the design, optimization, engineering, safety and waste management of the projects involved in the progress and development of fusion energy (e.g. ITER and the next-step, DEMO), and also for proving that the commitments of the Licensing Authorities in this sense are met [2]-[4].

For the nuclear analysis, computational tools for simulating the physics of radiation transport and neutron activation in fusion conditions are required. Currently, the type of calculations to be performed are very challenging due to the high level of detail involved and the huge impact that these calculations can have on fusion facilities already under construction, like ITER. These calculations imply the combined use of Computer-Aided Design (CAD), radiation transport, and activation tools, as well as coupling schemes between them. In this situation, the expertise of the user and software resources arise as key points to reach the level of accuracy and confidence required in fusion devices.

Within the aims of the nuclear analysis is to check, not only the capability of the nuclear codes codes and data to predict nuclear responses, but predicting with high accuracy in a real three-dimensional (3D) reactor configuration [5]. Therefore, for meaningful and satisfactory nuclear analyses, quality assurance (QA) and continuous improvement of the computational tools and nuclear data are essential [4]. Within the QA, it is essential to have: i) well-established, verified and validated guidelines and instructions to perfectly approach the nuclear analysis; ii) references and standards of materials, models, etc. iii) validated nuclear data methods and tools [6].

As it will be seen in the following Section 2, the work developed in this doctoral thesis is framed within the field of nuclear analysis.

2. Contributions and scope of the work

This thesis has sought to make different contributions in the nuclear analysis framework in order to progress in the MFC development, replying to some current identified problems and

needs. Hence, it addresses a number of issues related to both ITER and DEMO. Specifically, three contributions are made, focused on: i) activation nuclear data for ShutDown Dose Rate (SDDR) calculation in ITER, ii) radiation loads on the ITER Toroidal Field Coils (TFCs) and Vacuum Vessel (VV), and iii) DEMO DCLL (Dual-Coolant Lithium-Lead) characterization for safety and environment purposes. The following subsections are devoted to provide the motivation and description for each of the contributions.

2.1. Activation nuclear data for SDDR calculation in ITER

It is well known that the validity of the nuclear results greatly depends on the accuracy degree of the nuclear data (given as cross sections which are grouped into libraries) used in the calculation. This is extremely important taking into account that some tasks, designs etc. depend on the compliance of certain limits for several magnitudes. If the calculations are not reliable, how can the results be guidance for the implementation of these mentioned activities, shielding designs, etc.? Therefore, the accuracy of the nuclear data is fundamental for the accuracy of the result. In other words, as long as there is not certain about the reliability of the involved nuclear data, the validity of the results can not be corroborated.

In particular, for the reliability of nuclear inventory and the subsequent SDDR the accuracy of activation nuclear data is fundamental. The SDDR prediction is a critical aspect in the design of ITER[1] since it is essential to evaluate the effect that the nuclear radiation might have on workers, public and machines [7]. As an example, maintenance activities to repair and replace complex and heavy components in a nuclear environment are extremely challenging and the feasibility of maintenance operations is based on the compliance of some imposed SDDR limits to be applied in each working area.

It is worth noting that the fulfillment of imposed limit values for the SDDR is an ongoing challenge, especially in high exposed areas where hands-on maintenance is scheduled, such as the Port Cell (PC) and Port Interspace (PI). Furthermore, an accurate SDDR prediction is important, beyond maintenance can be carried out or not, in order to establish time limits from when people or machines access to certain areas could be allowed. In addition, it should not be forgotten that having to modify maintenance access times (as a consequence of non-compliance with the imposed limits) would have a high cost repercussion. For these reasons, it is crucial to trust the libraries used in order to accurate estimate SDDR.

[1] Actually in the design of all this kind of facilities.

Available cross section libraries for fusion applications such as EAF (European Activation File), ENDF (US Evaluated Nuclear data Library), FENDL (Fusion Evaluated Nuclear Data Library), JEFF (Joint Evaluated Fission and Fusion File) and TENDL (TALYS-based Evaluated Nuclear Data Library), among others, have been developed considering expected materials to be placed in fusion facilities. However, despite having been created considering fusion applications, they have not been developed taking into account the specific neutron spectra in the different components of an advanced 3D-geometric model for ITER. At present, the geometric model and specific materials in the different areas of ITER are currently clearly established and thus, the neutron spectra for the major components responsible of the SDDR can be accurately obtained.

In this context, large part of this thesis is dedicated, now that the materials and spectra in ITER are defined, to explore the status of available activation cross section data for accurate SDDR prediction in the PC and PI areas of ITER, where different maintenance activities are foreseen. For this purpose, EAF-2007, which is typically used for the determination of the SDDR in ITER, as well as the last EAF version (EAF-2010) and the most recent versions of TENDL (2013, 2014 and 2015) are selected. The final goal is to know if these SDDR calculations are overall trustworthy.

The results of this assessment have been well received by the scientific community, since the need of evaluating the cross section data for this application was already being raised in different scientific forums and meetings. Specifically, within the frame of Fusion For Energy (F4E)[2], there was an expert task (*F4E-2014_EXP-156*) performed by J. Sanz (director of this thesis) related to this matter, which was the basis for this work. Furthermore, a JCR paper has been published collecting the achieved results [9], and an extension of this work has been also presented in the International Conference on Nuclear Data for Science and Technology (ND2016), hold in Bruges (Belgium) during from 11th to 16th September 2016 and included in the corresponding proceeding [10].

2.2. Radiation loads on the ITER TFCs and VV

As it has been previously mentioned in Section 1, it is essential to evaluate the radiation field and its consequences during the operation of the fusion reactor, which is especially important for some components. In particular, for MCF reactors based on superconducting coils, one of the most relevant aspects of this radiation field during the operation phase is the effect that the high radiation loads have on this component, since their superconducting state can be

[2] F4E is the organization responsible for providing Europe's contribution to ITER [8].

endangered and, consequently, the plasma confinement too. Thus, the determination of the radiation loads on the coils is fundamental in the design of this kind of reactors [1], [4].

In ITER, there is some concern about the nuclear responses in the Toroidal Field Coils (TFCs), since the analyses carried out some years ago reflected values very close to the design limits, or even above. In particular, fast neutron flux on the electrical insulator and integral heat deposition were found to be very critical [4]. Furthermore, it was detected that the TFC inboard leg was the major contributor to the total nuclear heating and, also, that it is specially affected by the gap width among the blanket modules. As a consequence, a change in the design has been performed, in order to reduce these mentioned gaps in the blanket, and consequently, increasing its shielding capability [11]-[13].

Given the importance of the blanket gaps on the radiation loads on the TFCs, and the fact of being so close to the limits, it seems essential to study the effect that any modification of these blankets could have too. This is the case of the in-vessel diagnostics systems that introduce some cutouts in the blanket modules shielding (BSMs), decreasing their shielding capability. The current thesis studies the significance that these modifications in the BSMs would have, in terms of increase of the radiation loads on the TFCs. Specifically, in this work the analyzed in-vessel diagnostics are: reflectometry, Neutron Activation System (NAS), First Wall Samples (FWS) and bolometers. In addition to the radiation loads on the TFCs, the ones on the VV were also analyzed as also present limits due to thermal stresses.

This work has supported the ITER Diagnostic Division in the analysis of the diagnostics design within the project *'Neutronics Analysis of ITER Diagnostics Components' contract number 4300000919*. In addition, the achieved results were collected in several reports [14]-[17] and there is an already prepared paper that is currently under ITER review [18].

2.3. DEMO DCLL characterization for safety and environment purposes

In the DEMO framework, a roadmap of fusion energy was defined by the EFDA (European Fusion Development Agreement) at the end of 2012. The aims were the achievement of the necessary know-how to begin the construction of a DEMO by 2030, in order to allow the start of operation in the early 2040s and so, reaching the goal of fusion electricity in the grid by 2050. In this context, eight strategic missions were established. For the Horizon 2020, a series of activities within each of the missions are defined within the Eurofusion Consortium program. In particular, related to mission 5 (*Implementation of the intrinsic safety features of fusion*) comes out the Safety And Environment Work Package (WPSAE) [19]-[20].

The challenges in the frame of WPSAE are based on the experience in the ITER licensing process, and are related to the management of activated materials and, especially T, since DEMO has higher neutron fluence. Therefore, the WPSAE deals with the establishment of fundamental safety strategies, definition of safety criteria, safety evaluation of the impact of fundamental design choices (materials, coolant, etc.), review of licensing regulatory requirements, selection of adequate disposal routes, establishment of material composition limits to minimize the radiological impact of activation, as well as development of strategies for minimization the quantity of waste, and studies about the feasibility of waste recycling, among other issues.

The performed DEMO work in this thesis is included in the framework of this mentioned WPSAE and, more specifically, in the *SAE-2.17.1-T01-D04* task. This task was planned for the 2015-2018 period and this thesis contains the work done during 2015 [21] and the updates corresponding to 2016. The main objective is to estimate the decay heat and nuclide inventory for the DCLL blanket concept in order to provide the essential input for further safety and/or waste management assessments.

Similar tasks for the other three blanket models are being carried out in parallel, by well-known European institutions, so, in addition, some comparison about the differences in the achieved results is done among the four blanket concepts. This comparison has been presented at the 29th edition of the Symposium on Fusion Technology (SOFT 2016) hold in Prague (Czech Republic), from 5th to 9th September 2016, and there is a sent paper for considering its publication in Fusion Engineering and Design journal [22].

Moreover, considering that one of the presuppositions of fusion energy is that only low and medium radioactive waste are generated, a preliminary assessment of the radioactive waste coming from this DCLL model is carried out. This assessment has reference to the IAEA/SEAFP-2 standards and to the specific regulations of El Cabril near-surface facility. In addition, considering the important role that impurities play in the activation of the different materials, the possible need of impurities mitigation, in wastes, is also performed. This work on radioactive waste assessment has also been presented at the SOFT 2016, and there is also a submitted paper for considering its publication in Fusion Engineering and Design journal [23]. In addition, and also within the Eurofusion framework, a report with the obtained results is currently being prepared.

3. Document organization

This last section of the chapter is dedicated to describing the structure followed in this thesis and the chapter's fragmentation.

First of all, Chapter 2 is devoted to introduce the fusion energy and to give the context for describing ITER and DEMO, which are the main MCF devices in which this thesis is focused on.

Chapter 3 is dedicated to the description of the methodology used along this work. As it has been said, the nuclear calculations are very challenging. Thus, the aim of this chapter is to describe these challenges and to provide information about different available nuclear data and computational tools to carry out the nuclear analysis, as well as to justify the selection of some of them for the development of this thesis.

The following chapters collect the different contributions to ITER (Chapter 4 and Chapter 5) and DEMO advancement (Chapter 6).

Chapter 4 describes the assessment of the status of relevant cross sections involved in the prediction of the SDDR for manual maintenance in the ITER PC and PI areas. Meanwhile, Chapter 5 is connected with operation aspects and deals with the nuclear analyses performed to assess the impact of four different in-vessel diagnostic systems, namely reflectometry, NAS, FWS and bolometers, on the radiation loads on the VV and the TFCs.

Chapter 6 deals with the DCLL characterization for further safety and/or waste management studies. In addition, this chapter also includes the results comparison among the different DEMO blanket concept. Last but not least, a radioactive waste analysis with reference to the IAEA and SEAFP-2 standards and to the specific regulations of El Cabril, as well as the possible need of impurities mitigation is also contained in this chapter.

Finally, Chapter 7 is devoted to review the achieved conclusions and describe the ongoing and future work.

4. References

[1] F. Wasastjerna. *Using MCNP for fusion neutronics*. Thesis dissertation. Helsinki University of Technology (**2008**). ISBN 978-951-38-7129-1.

[2] R. Pampin, A. Davis, J. Izquierdo, D. Leichtle, M.J. Loughlin, J. Sanz, A. Turner, R. Villari, P.P.H. Wilson. *Developments and needs in nuclear analysis of fusion technology*. Fusion Engineering and design, Vol. 88, pp. 454 – 460 (**2013**). Doi: http://dx.doi.org/10.1016/j.fusengdes.2013.03.049

[3] M. Loughlin, M. Angelone, P. Batistoni, L. Bertalot, J. Eskhult, C. Konno, R. Pampin, A. Polevoi, E. Polunovskiy. *Status and verification strategy for ITER neutronics*. Fusion Engineering and design, Vol. 89, pp. 1865 – 1869 (**2014**). Doi: http://dx.doi.org/10.1016/j.fusengdes.2014.03.070

[4] H. Iida, V. Khripunov, L. Petrizzi, G. Federici. *Nuclear Analysis Report*. ITER IDM location: https://user.iter.org/?uid=22F2ST (**2004**).

[5] U. Fischer, P. Batistoni, A. Klix, I. Kodeli, R.L. Perel. *Neutronics R&D Efforts in Support of the European Breeder Blanket Development Programme*. Nuclear Fusion, Vol. 49, nº 6 (**2009**). Doi: http://dx.doi.org/10.1088/0029-5515/49/6/065009

[6] D. Leichtle. *Quality of Nuclear Analysis (QNA)*. Nuclear Integration Unit (NIU) Progress Report. ITER IDM location: https://user.iter.org/?uid=T8JRTQ (**2016**).

[7] R.A. Pitts. *ITER status and challengues*. ITER IDM location: https://user.iter.org/?uid=S3W8V7 (**2015**).

[8] *Objectives. About F4E*. Available: http://fusionforenergy.europa.eu/aboutfusion/ [Accessed: 28 November 2016].

[9] R. García. M. García, R. Pampin, J. Sanz. *Status of reliability in determining SDDR for manual maintenance activities in ITER: Quality assessment of relevant activation cross sections involved*. Fusion Engineering and Design, Vol. 112, pp. 177 – 191 (**2016**). Doi: http://dx.doi.org/10.1016/j.fusengdes.2016.08.016

[10] R. García, M. García, F. Ogando, R. Pampin, J. Sanz. *Reliability of activation cross sections for estimation of shutdown dose rate in the ITER port cell and port interspace*. Proceeding of ND 2016 International Conference on Nuclear Data for Science and Technology. EPJ Web of Conferences (**submitted**).

[11] H. Iida. *The Contributions of the Vertical and Horizontal Gaps among the Blanket Modules to the Inboard TF Coil Leg Nuclear Heating (NAR)*. Design Integration Unit Analysis Report. ITER IDM location: https://user.iter.org/?uid=22A4H8 (**2003**).

[12] H. Iida. *The Nuclear Heat Local Peaking at the first Turn of the Winding Pack of Inboard TF Coil Legs due to Gaps among Blanket Modules (NAR)*. Design Integration Unit Analysis Report. ITER IDM location: https://user.iter.org/?uid=2267AX (**2003**).

[13] H. Iida. *Fast Neutron Flux and Nuclear Heat in the TF Coil Inboard Legs vs. Gap Width among Blanket Modules (NAR)*. Design Integration Unit Analysis Report. ITER IDM location https://user.iter.org/?uid=226DRK (**2003**).

[14] J.P. Catalán, R. García, A. Suárez. *Impact of reflectometry diagnostic on the radiation loads of the Vacuum Vessel and Toroidal Field Coils*. ITER Neutronics Report. ITER IDM location: https://user.iter.org/?uid=QEJYFF (**2015**).

[15] J.P. Catalán, R. García, A. Suárez. *Impact of Neutron Activation System (NAS) diagnostic on the radiation loads of the Vacuum Vessel and Toroidal Field Coils.* ITER Neutronics Report. ITER IDM location: https://user.iter.org/?uid=QEKTWA (**2014**).

[16] J.P. Catalán, R. García, A. Suárez. *Neutronics for the First Wall Diagnostics and impact on toroidal field coils (TFC) and vacuum vessel (VV) heating*. ITER Neutronics Report. ITER IDM location: https://user.iter.org/?uid=QN66Q7 (**2015**).

[17] J.P. Catalán, R. García, A. Suárez. *Impact of blanket cutouts for bolometers on the radiation loads of the Vacuum Vessel and Toroidal Coils*. ITER Neutronics Report. ITER IDM location: https://user.iter.org/?uid=QEYKCW (**2015**).

[18] J.P. Catalán, R. García, A. Suarez, L. Bertalot, J. Sanz, G. Vayakis, V. Krasilnikov, P. Shigin, R. Reichle, V. Udintsev, M. Walsh. *Impact of ITER in-vessel diagnostics on the radiation loads of the Vacuum Vessel and Toroidal Field Coils* (**under ITER review**).

[19] EFDA. *Fusion electricity. A roadmap to the realisation of fusion energy*. EUROFusion IDM location: https://idm.euro-fusion.org/?uid=2M8JBG (**2012**).

[20] N. Taylor. *Safety and Environment Project*. Project Management Plan (PMP). EUROFusion IDM location: https://idm.euro-fusion.org/?uid=2L9WGS (**2016**).

[21] J. **Sanz**, R. García, M. García, F. Ogando. *Decay heat and activity calculations for the DCLL DEMO neutronic model.* SAE-2.17.1-T01-D04. EUROFusion IDM location: https://idm.euro-fusion.org//?uid=2CZ6L5 (**2015**).

[22] T. Eade, M. Garcia, R. Garcia, F. Ogando, P. Pereslavtsev, J. Sanz, G. Stankunas, A. Travleev. *Activation and decay heat analysis of the European DEMO blanket concepts*. Fusion Engineering and Design (**submitted**).

[23] I. Palermo, R. García, M. García, J. Sanz. Radiological impact mitigation of waste coming from the European Fusion Reactor DCLL DEMO. Fusion Engineering and Design (**submitted**).

Chapter 2

Nuclear fusion and magnetic fusion devices

This chapter is dedicated to describing both the interest of the nuclear fusion energy as well as its main principles, and the two magnetic confinement fusion devices which this thesis deals with: ITER and the foreseen DEMO.

1. Energy consumption and demand trends

Several studies suggest that energy consumption will increase in the coming years at a global scale. Since more than 80% of the energy consumption is currently derived from fossil fuels, it is essential to find alternative options to satisfy the expected energy demand, especially considering that fossil fuel reserves tend to run out and would not to meet the demand forecast for the future. It is therefore necessary to seek new forms of energy with abundant resources, covering the increasing demand at a reasonable cost and with limited environmental effects [1].

Nowadays, nuclear power, based on nuclear fission, provides about 4% of the total energy consumed on the Earth, as shown in Figure 2.1. This energy has the advantages of large stocks of fissile material and non-production of greenhouse gases. However, fission energy is a problem from the standpoint of wastes, which are characterized by a high activity, having to be controlled for long periods of time.

The nuclear fusion energy is one of the proposals currently under investigation due to the great potential it entails to quench this increasing energy demand. It is a clean energy (CO_2 emission free during the plant operation), safer than fission as there would be no risk of a runaway fusion reaction as this is intrinsically impossible. Furthermore, raw materials (light nuclei) are more plentiful than fissile nuclei.

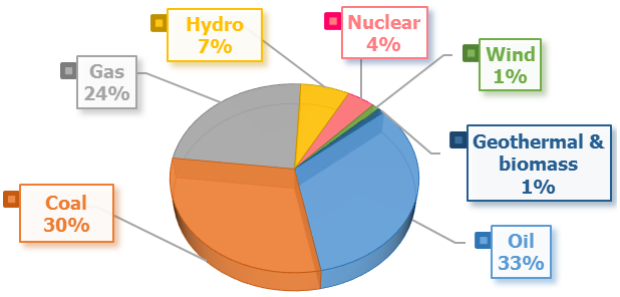

Figure 2.1. Distribution of global energy consumption Source: BP2014.

Regarding the possible radioactive wastes, although nuclear fusion does not generate long-lived radioactive products to create a burden on future generations and the unburned gases can be treated on site, low and medium radioactive waste are generated due to the activation of the structural materials. The currently limitation to fusion energy is that more technological development is needed before obtaining energy on a commercial scale [2]-[3].

2. Nuclear fusion

For a nuclear fusion reaction, two light nuclei need to be closer enough to overcome the electrostatic repulsion between them and merge, obtaining a heavier nuclide with a slightly smaller mass than the sum of the masses of its constituent nucleons; the mass difference is released as energy.

As a general remark, it can be said that the fusion of two nuclei with lower mass than iron releases energy, while fusion of heavier nuclei, absorbs it (and the other way round for fission) [4]. In addition to this, the electrostatic repulsion is proportional to the product of the nuclear charges, and therefore it increases as the atomic numbers of the involved nuclei do. Hence, the Hydrogen (H) and Helium (He) isotopes seem to be the more suitable nuclei for a fusion power plant.

Within all possibilities, it has been concluded that the best fusion process is that involving the two heavier isotopes of H (D and T), since this reaction is the producing more energy and with the highest cross section at achievable energies, as shown in Figure 2.2 [5].

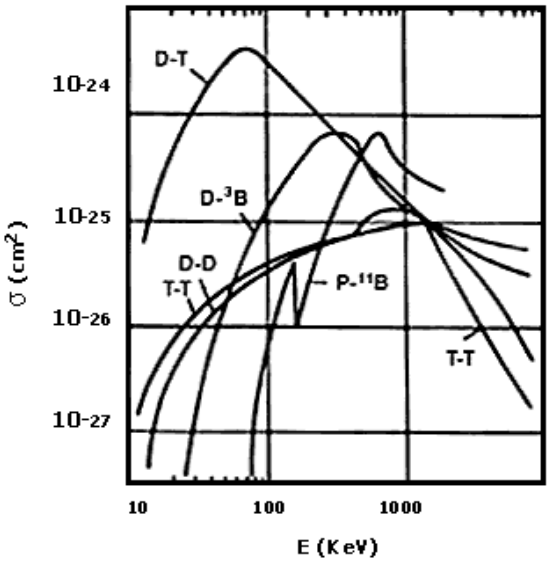

Figure 2.2. Experimental cross sections for different fusion reactions as a function of energy [6].

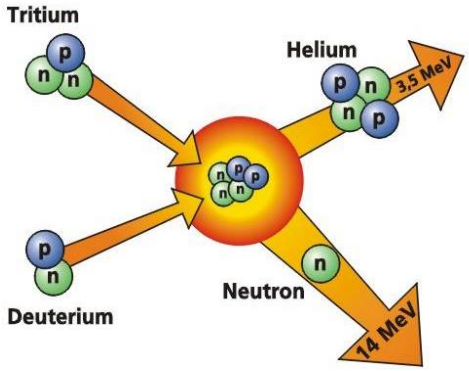

Figure 2.3. D-T fusion reaction scheme [7].

Figure 2.3 shows a typical D-T fusion reaction scheme where each reaction releases 17.6 MeV of energy distributed between a He nucleus/alpha particle (3.5 MeV) and a free neutron (14.1 MeV of kinetic energy) [7].

It is that energy of the neutron which is used for energy production but, on the other hand, the release neutron is responsible for the damage to reactor materials. In addition to this, neutrons not only cause structural damage to the materials, but also the transmutation into radioactive materials (radioactive waste after the shutdown). Furthermore, the presence of T, which is radioactive, suggests that this fusion reaction is not the optimal from an environmental point of view. Nevertheless the D-D reaction produces less energy (3-4 MeV) and is less likely, as it has been said before so all efforts are focused on the D-T reaction [8].

In order to ensure that the fusion reaction occurs, repulsion between nuclei need to be avoid overcoming the Coulomb barrier, guarantying that these nuclei are able to get close enough so they can merge almost simultaneously. This goal is reached by maintaining the gas composed by the required nuclei (fuel) confined under the necessary high conditions of temperature and pressure (to increase the energy of the nuclei in the fuel) to produce fusion, for a long time.

Under these extreme conditions (over 100 million °C) the electrons are no longer trapped in their orbits and the plasma state is obtained. The plasma confinement is also necessary to prevent both the structural materials from damage and the particles from coming into contact with the walls as their heat would dissipate slowing them down. Meanwhile, the released alpha particle in the D-T reaction remains in the plasma and delivers its energy to it, which is essential for the plasma heating and helps to compensate the energy losses. To achieve this confinement, two main approaches are being studied: magnetic confinement fusion (MCF) and inertial confinement fusion (ICF) [2], [9].

The basis for the first method (MCF) is that since the plasma consists of charged particles it can be controlled by a magnetic field. The toroidal configuration is the most effective configuration, doughnut-shaped, in which the magnetic field is curved around to form a closed loop. For a proper and best confinement, a perpendicular field (poloidal field) is also needed. There are several types of systems based on MCF, highlighting the tokamaks, stellarators and Reversed Field Pinch (RFP) devices. The International Thermonuclear Experimental Reactor (ITER) and the Joint European Torus (JET) are representative facilities of this approach.

The ICF consists of compressing and heating a small pellet containing fusion fuel to extremely high densities using lasers or particle beams pulses reaching the plasma state, when the fusion reaction is produced. The National Ignition Facility (NIF), at the Lawrence Livermore Laboratory, built in 2009 is the most important ICF facility [4], [8], [9].

Regarding the availability of the necessary nuclei for the fusion reaction, D, which is present in natural hydrogen (in a 1:6000 ratio), can be easily extracted from water (30 g/m^3) which makes it very abundant compared to other energy resources. However, T is not a stable isotope and has a half-life of around 12 years; hence, it must be obtained from Lithium (Li) by a nuclear reaction. Li is found in large quantities (30 parts per million) in the Earth's crust and, in lower concentrations, in the sea. The neutron released in the D-T reaction can be used for this purpose, through the following reactions (equations 2.1 and 2.2) which take place in the Breeding Blanket[3] (BB) surrounding the reactor's VV and also produces He [4], [8], [10].

$$^{6}Li + n \rightarrow T + {}^{4}He \tag{2.1}$$

$$^{7}Li + n \rightarrow T + {}^{4}He + n \tag{2.2}$$

A Fusion Power Plant (FPP) will consist of a series of structures contained one inside other as shown in Figure 2.4. The burning plasma forms the core of the reactor, covered by the first wall. The BB is behind, surrounding the core and followed by a neutron shield, the VV, the magnetic coils of toroidal and poloidal field, and another shield (the biological shield or bioshield) which role is to reduce radiation at the required levels to ensure the safety of personnel working nearby. The divertor, which duty is to evacuate hot gases (unburned He, D and T) extracting them from the plasma, is located inside the VV and below the plasma.

[3] In most of the breeding module designs, Li appears as a Li based ceramic (Li_2O, Li_4SiO_4, Li_2TiO_3, Li_2ZrO_3) next to a neutron multiplier (Be, BeTi, LiPb). In the LiPb case, it acts as a T generator and a neutron multiplier at the same time.

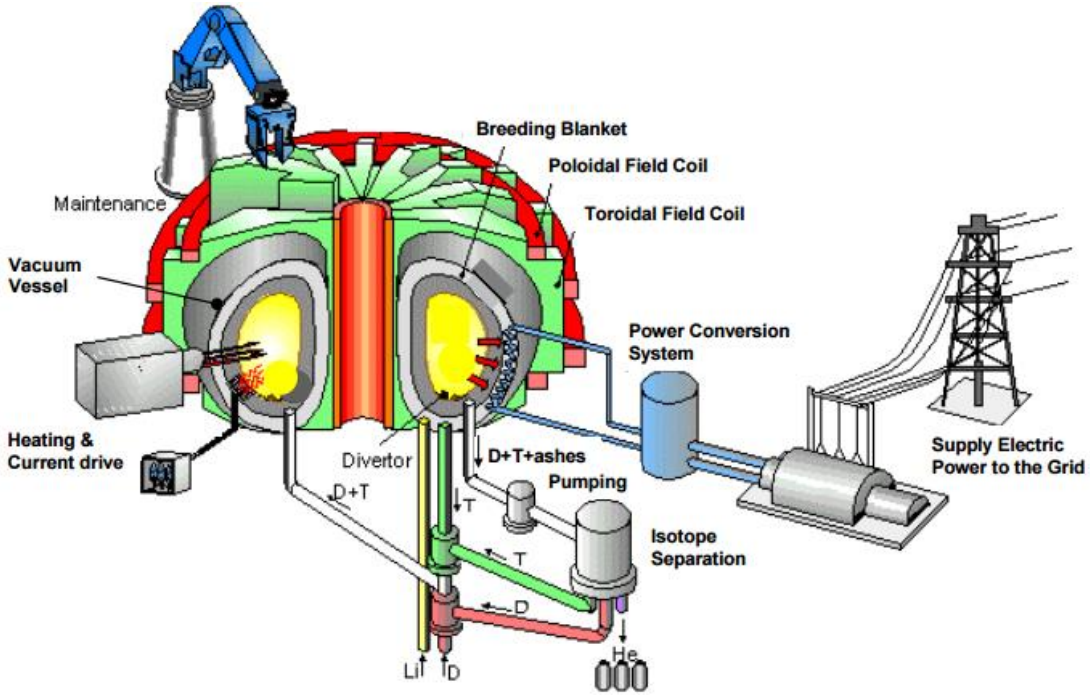

Figure 2.4. Fusion Power Plant scheme [11].

Thus, the generated neutrons in the D-T fusion reaction will be absorbed in the blanket, which contains Li. The Li is then transformed into T (which is used to fuel the reactor) and He, as it has been described before. It is important to note that the blanket must be thick enough (about 1 m) to slow down the high-energy (14 MeV) neutrons. The kinetic energy of the neutrons is absorbed by the blanket, leading it to heat up. Afterwards, the heat energy is collected by the coolant (water, He or LiPb eutectic) flowing through the blanket, transferred to heat exchangers and finally, by means of steam, is used to produce electricity conventionally [7], [8].

Three key steps are required to reach a commercial fusion plant based on the tokamak concept. The first step is to demonstrate that fusion is feasible from a scientific point of view. This first step has been achieved with three large tokamaks: JET (Europe), TFTR (United States) and JT-60 (Japan), built in the 1970s. JET succeeded in generating 70% of input power, the current record for energy release [12].

The second step is to prove that fusion is technically feasible. Thus, a larger machine, such as ITER, where many of the necessary techniques for a power plant will be tested, is required. The aim of the third and last step (DEMO) is to prove that fusion is commercially viable and is the previous point for a commercial FPP.

Figure 2.5 shows a comparison between JET, ITER and DEMO in terms of power output and size. Furthermore, defining Q as the ratio of fusion power produced in a nuclear fusion

reactor to the power required to maintain the plasma in steady state, this value is/pretended to be ~1 for JET, 10 for ITER and 25 for DEMO. A roadmap to fusion energy is described in Figure 2.6 where it is plain to see that ITER is the key facility in it. From then, the plan is to start the construction of a DEMO by 2030, in order to allow the start of operation in the early 2040s and reaching the goal of fusion electricity in the grid by 2050 [13].

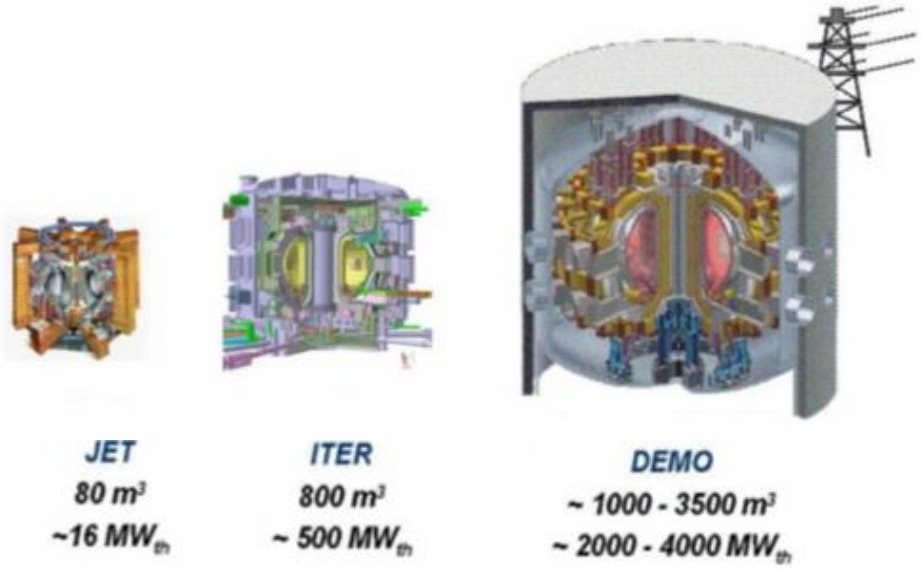

Figure 2.5. Cutaways of JET, ITER, and DEMO reactors for comparison [14].

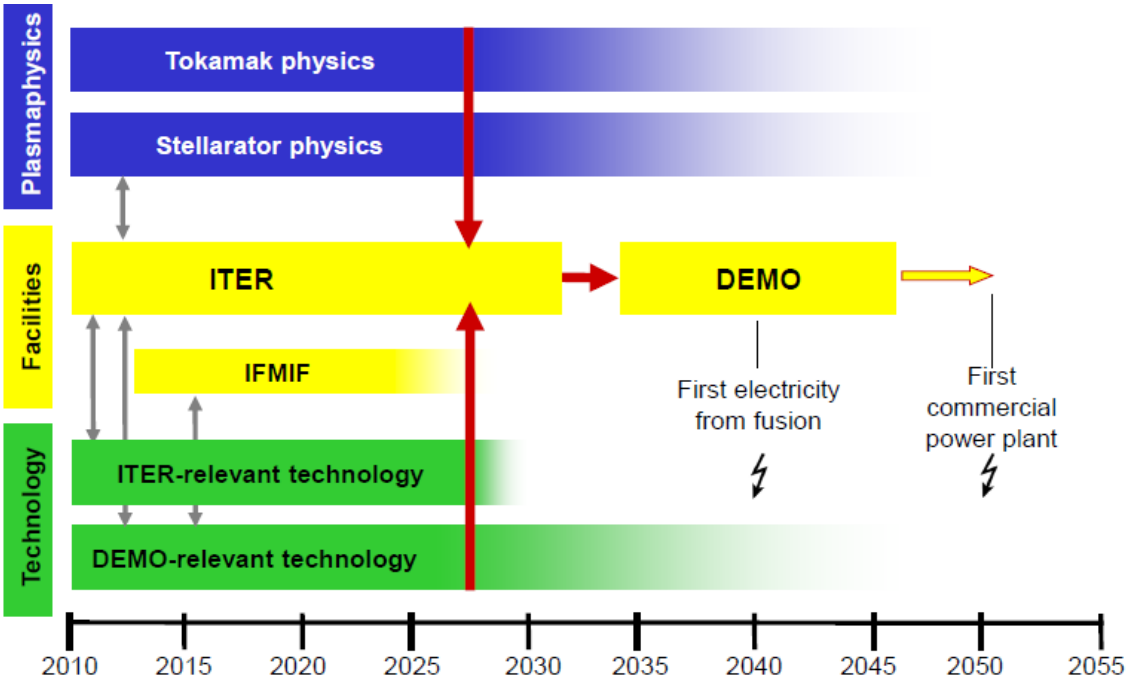

Figure 2.6. Roadmap to fusion energy [12].

3. ITER

The ITER, is a large-scale scientific experiment that aims to prove the feasibility of nuclear fusion as an energy source (i.e. producing more power than it consumes), as well as to provide the necessary knowledge for the design and subsequent operation of the first electricity-producing fusion power plant.

It is actually the world's largest and most advanced fusion experiment and is currently under construction in Cadarache (south of France), although some components and systems are still being designed [7], [15]. ITER Organization (IO) is the legal entity responsible for building, operating, exploiting and deactivating ITER.

A simplified 3D CAD sketch of ITER with the most important components can be seen in Figure 2.7. Aside from the named components, ITER is provided of multiple types of measuring instruments that constitute the diagnostics systems (about 60). The aim of these systems is to provide accurate measurements of the plasma behavior and its confinement. These measurements are necessary both for the protection and the basic operation of the device, and for the advanced plasma control and physics studies. The diagnostic systems will be placed in the VV, cryostat, ports (upper and equatorial), divertor cassettes, etc. [16].

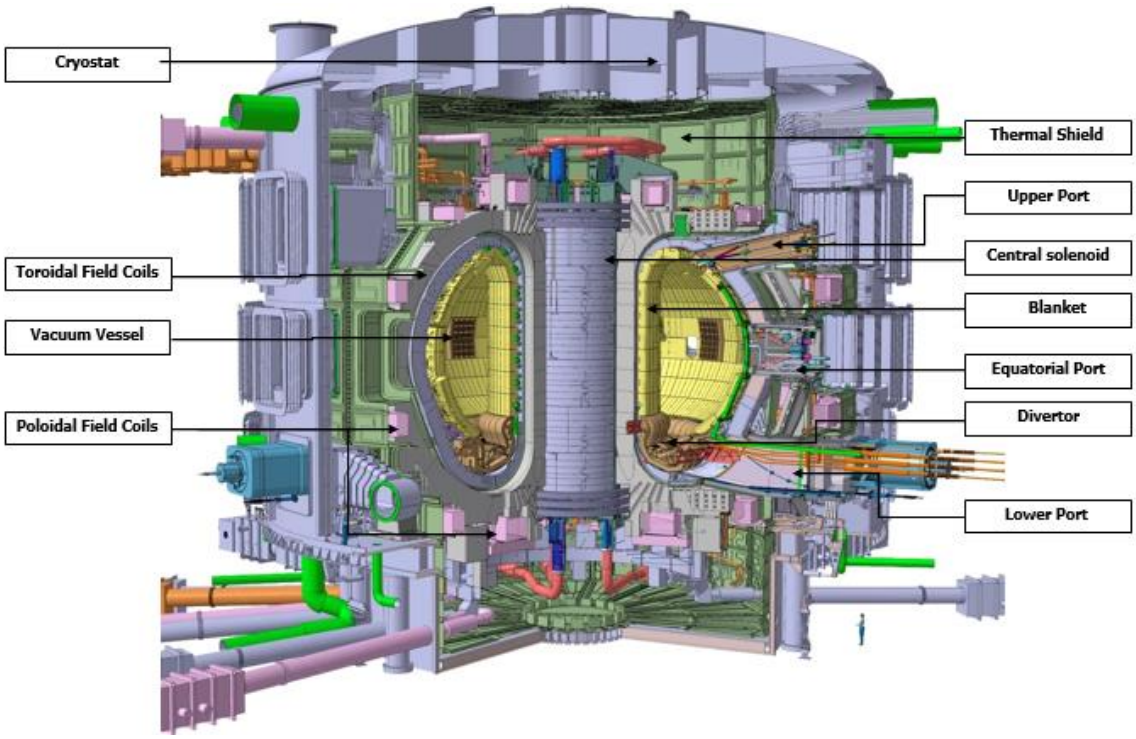

Figure 2.7. ITER components.

Since the achievement of fusion energy fully depends on ITER's success, the vast majority of resources from Horizon 2020 are dedicated to its construction. ITER is developed in the framework of an international cooperation between the European Union (EU), China, India, Japan, Korea, Russia and the United States (US) [17]-[18].

The main goal of ITER is to reach a factor greater than or equal to 10 between the power needed for the reactor and the produced power. Specifically, ITER will produce 500 MW of fusion power from 50 MW input power (which means a fusion gain Q=10.) and $\sim 10^{27}$ neutrons. These values are higher than those of JET (100 and 10^6 times, respectively) but also lower than in a fusion power plant (10 and 100 times, respectively) [18]-[19]. Besides this, other ITER challenges are [18],[20]:

- Demonstrate the integrated operation of technologies for a FPP, since ITER is the key step between today's smaller-scale experimental fusion devices and the demonstration FPP of the future.
- Achieve a D-T plasma in which the reaction is sustained through internal heating. The idea is that the ITER plasma produces a lot of fusion energy but also remains stable for longer periods of time.
- Demonstrate the feasibility of producing T within the vacuum vessel, since the world supply would be not enough to cover the needs of the future FPP.
- Demonstrate the safety characteristics of a fusion device with the control of the plasma and the fusion reactions with negligible consequences to the environment.

Moreover, ITER is supposed to demonstrate the feasibility of T production within the vacuum vessel since the world supply is not enough to cover the needs of future FPP [21]. For this purpose, different DEMO BB, called Test Blanket Modules (TBMs), will be included and tested within the ITER reactor in three equatorial ports that directly faced the plasma [22].

It is supposed that on 2025 the first plasma will be achieved. It will also be the first opportunity to verify the correct functioning of the machine's magnetic fields and systems (electrical supply, cryostat, cooling water, cryogenics, etc.). The first production of fusion power is expected for the middle of the following decade [23].

4. DEMO

After ITER, a Fusion Energy DEMOnstration Reactor, commonly called DEMO, will be built. DEMO will resemble as much as possible to a commercial FPP. Thus, developed and tested technologies for ITER will be also relevant for DEMO, so the development of DEMO needs to

start following a parallel process to ITER, to make the transition between the two stages as smooth as possible. DEMO is intended to demonstrate the large scale production of electrical power and it is designed to produce at least four times the ITER fusion power continuously (2000 to hopefully 4000 MW of thermal output).

Although DEMO is being studied in different regions around the world (E.U., Japan, Korea, India, Russia and other countries) and its objectives vary slightly from on geographical area to another, there is a consensus about the DEMO must demonstrate the commercial practicality of fusion power. There is also agreement about the top level goals, which are the following [21]:

- Demonstrate T self-sufficiency and a closed T fuel cycle.
- Demonstrate attractive safety and environmental impact:
  - ✓ No evacuation plan required.
  - ✓ Only Low and Intermediate Level radioactive Waste (LLW and LILW, respectively).
  - ✓ No disturbance of the public's day-to-day activities.
  - ✓ No worker risk or exposure higher than other power plants.
- Demonstrate simultaneous power extraction at high temperature and efficient T extraction and control.
- Demonstrate acceptable Reliability/Maintainability/Availability/Inspectability (RAMI):
  - ✓ Remote maintenance of fusion core with acceptable repair/replacement time.
  - ✓ Routine operation with minimum number of unscheduled shutdowns per year.
  - ✓ Achieve an availability >50% and extrapolate to commercially practical levels.
- Demonstrate potential for economic competitiveness.

Within the Power Plant Physics and Technology (PPPT) Eurofusion Programme, four breeder blanket (BB) concepts for DEMO (Figure 2.8) are being considered, namely HCLL (Helium-Cooled Lithium-Lead), HCPB (Helium Cooled Pebble Bed), WCLL (Water-Cooled Lithium-Lead), and DCLL [21], [24].

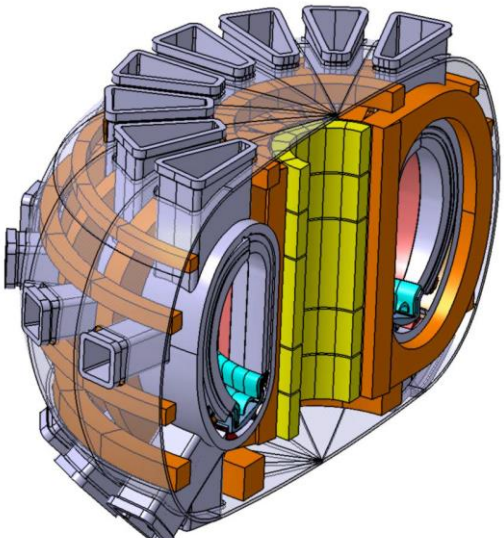

Figure 2.8. 3D view of PPPT DEMO [24].

- HCLL. In this concept, He is used as coolant (300-500°C at 8 MPa), LiPb as breeder material. The T extraction from LiPb is located outside the reactor. Figure 2.9 shows a scheme for this concept.

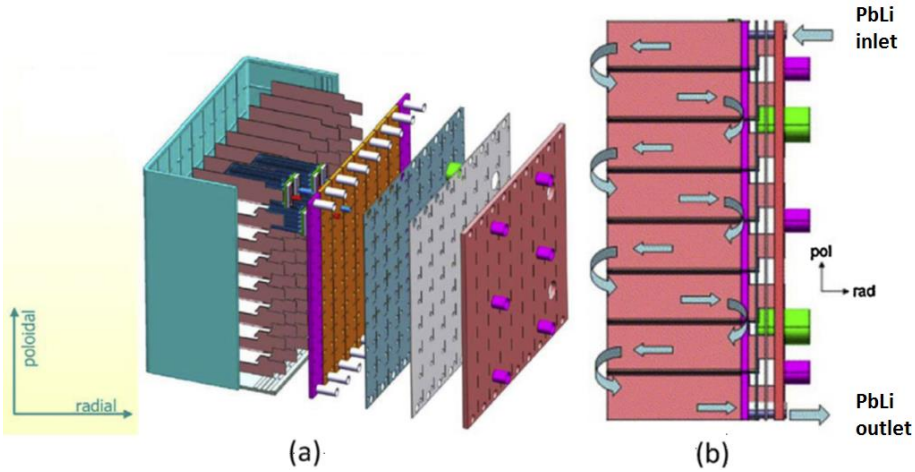

Figure 2.9. Sketch of the HCLL blanket design: (a), general view; (b), LiPb flow path) [25].

- HCPB. This concept is characterized by using He gas as coolant (300-500°C at 8 MPa), Li_4SiO_4 or Li_2TiO_3 as breeder, and beryllium (Be) as a neutron multiplier in order to ensure sufficient T breeding to meet the T self-sufficiency. Both Li_4SiO_4 or Li_2TiO_3 and Be are in form of a pebble bed. The T extraction is carried out in blanket with purge gas. A detailed sketch can be seen in Figure 2.10.

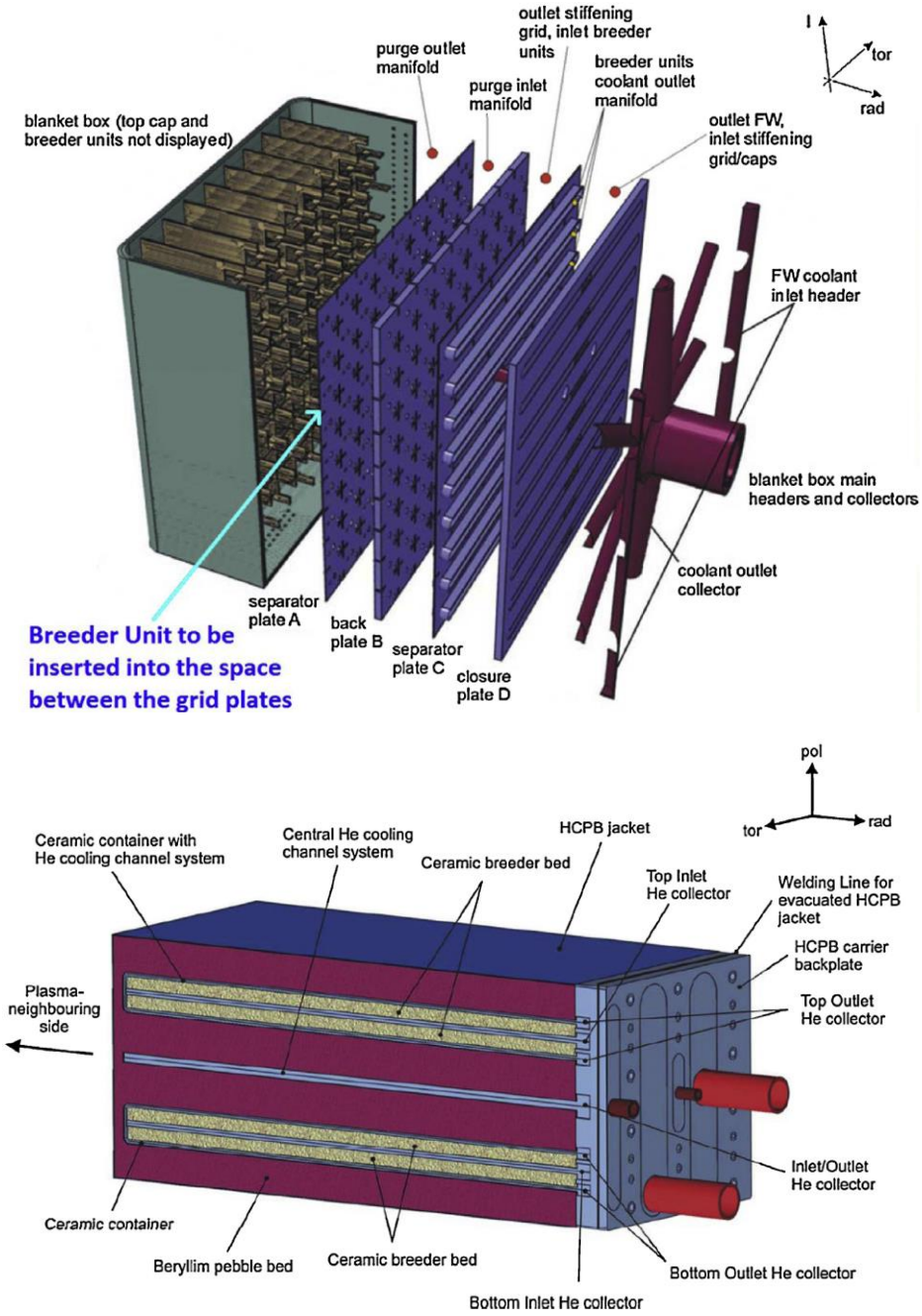

Figure 2.10. Sketch of the HCPB blanket design [25].

- WCLL. In this case the liquid alloy LiPb is used as breeder and neutron multiplier while water is needed as coolant (PWR condition: 285-325°C at 15 MPa). The T extraction from LiPb takes place outside the reactor. Figure 2.11 represents a sketch of this blanket design.

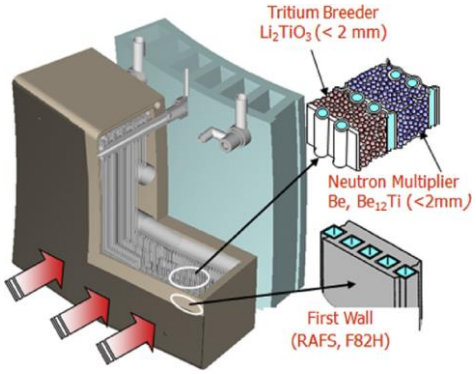

Figure 2.11. Sketch of the WCLL blanket design [25].

- DCLL. In this concept, both He and LiPb are used as coolant. The high-temperature LiPb alloy flows slowly (~10 cm/s) in large poloidal ducts to remove the heat and produce T, while the He (~300-400°C at 8 MPa) is used to remove the surface heat flux and to cool blanket structures including the first wall to temperatures under 550 ºC. Furthermore, the Flow Channel Inserts (FCI) are used for electrical and thermal insulation, due to the magneto-hydrodynamic (MHD) and thermal-hydraulic effects. The T extraction system is outside the reactor. Figure 2.12 shows a sketch of the DCLL blanket design.

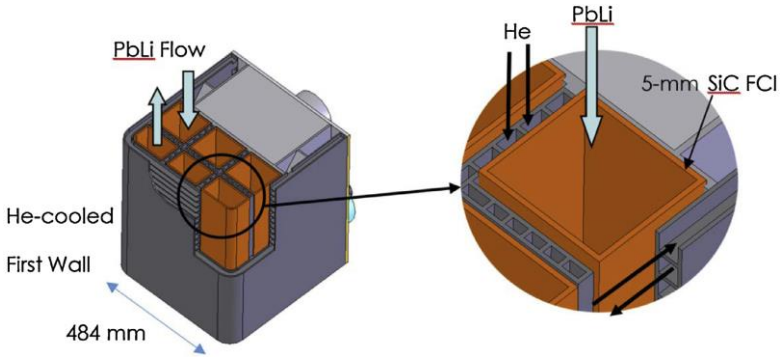

Figure 2.12. Sketch of the DCLL blanket design [25].

Finally, Figure 2.13 presents a diagram regarding the temperature and pressure conditions above-described for each of the blanket concepts.

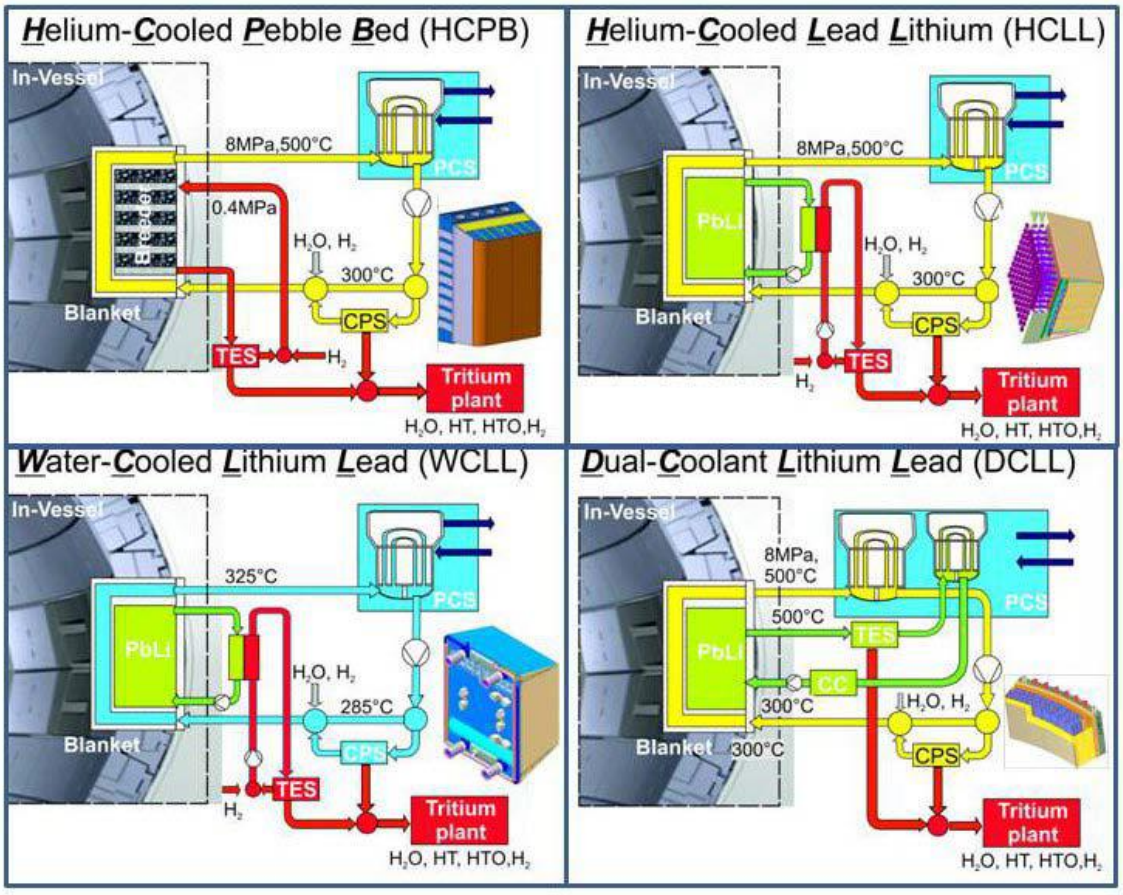

Figure 2.13. Temperature and pressure conditions of the four different blanket concepts for DEMO [24].

5. References

[1] J.H. Brown, W.R. Burnside, A.D. Davidson, J.R. Delong, W.C. Dunn, M.J. Hamilton, N. Mercado-Silva, J.C. Nekola, J.G. Okie, W.H. Woodruff, W. Zuo. *Energetic limits to economic growth*. BioScience, Vol. 61, nº 1, pp. 19 – 26 (**2011**). Doi: http://www.jstor.org/stable/10.1525/bio.2011.61.1.7

[2] Fusion for Energy. *Understanding fusion. The merits of fusion*. Available: http://fusionforenergy.europa.eu/understandingfusion/merits.aspx [Accessed: 11 July 2016].

[3] ITER Organization. *ITER. Advantages of fusion*. Available: https://www.iter.org/sci/Fusion [Accessed: 14 July 2016].

[4] T. Murphy. *Do the math. Nuclear fusion* (**2012**). Available: http://physics.ucsd.edu/do-the-math/2012/01/nuclear-fusion/ [Accessed: 12 July 2016].

[5] S. Glasstone, R. Lovberg. *Controlled Thermonuclear Reactions. An Introduction to Theory and Experiment*. Huntington, New York: Robert E. Publishing Company (**1960**).

[6] Biblioteca digital del Instituto Latinoamericano de la Comunicación Educativa (ILCE). *Qué es la fusión nuclear*. Available:

http://bibliotecadigital.ilce.edu.mx/sites/ciencia/volumen2/ciencia3/106/htm/sec_4.htm [Accessed: 20 July 2016].

[7] Institute of Energy and Climate Research. Plasma Physics IEK-4. *Plasma-Wall Interaction - A Key Issue in Progress Towards Fusion Power Plants*. Available: http://www.fz-juelich.de/iek/iek-4/EN/Research/01_Plasma-Wall_Interaction/artikel_2014.html?nn=1500486 [Accessed: 11 July 2016].

[8] World Nuclear Association. *Nuclear Fusion Power* (**2016**). Available: http://www.world-nuclear.org/information-library/current-and-future-generation/nuclear-fusion-power.aspx [Accessed: 12 July 2016].

[9] The European Fusion Education Network (Fusenet). *What is Plasma?.* Available: http://www.fusenet.eu/node/35 [Accessed: 14 July 2016].

[10] A.M. Bradshaw, T. Hamacher, U. Fischer. *Is nuclear fusion a sustainable energy form?* Fusion Engineering and Design, Vol. 86, pp. 2770 – 2773 (**2011**). Doi: http://dx.doi.org/10.1016/j.fusengdes.2010.11.040

[11] D. Maisonnier, I. Cook, P. Sardain, R. Andreani, L. Di Pace, R. Forrest, L. Giancarli, S. Hermsmeyer, P. Norajitra, N. Taylor, D. Ward. *A conceptual study of commercial fusion power plants. Final report of the European Fusion Power Plant Conceptual Study (PPCS)*, EFDA-RP-RE-5.0 (**2005**).

[12] H. Zohm. *From ITER to DEMO* (**2014**). Available: http://www.dpg-physik.de/dpg/pbh/aktuelles/pdf/Zohm6.pdf [Accessed: 8 August 2016].

[13] EFDA. *Fusion electricity. A roadmap to the realisation of fusion energy*. EUROFusion IDM location: https://idm.euro-fusion.org/?uid=2M8JBG (**2012**).

[14] *Next Big Future* (**2016**). Available: http://www.nextbigfuture.com/2016/05/compact-spherical-tokamak-would-be-100.html [Accessed: 11 December 2016].

[15] V. Barabash. *Role and contribution of ITER in research of materials and reactor*. Journal of Nuclear Materials, Vols. 2329 – 333, Part A, pp. 156 – 160 (**2004**). Doi: http://dx.doi.org/10.1016/j.jnucmat.2004.04.015

[16] ITER Organization. *ITER. Diagnostics*. Available: https://www.iter.org/mach/diagnostics [Accessed 5 October 2016].

[17] EFDA. *Fusion Electricity. A roadmap to the realisation of fusion energy* (**2012**).

[18] ITER Organization. *ITER. What is ITER?*. Available: https://www.iter.org/proj/inafewlines [Accessed: 8 August 2016].

[19] R. Pampin, A. Davis, J. Izquierdo, D. Leichtle, M.J. Loughlin, J. Sanz, A. Turner, R. Villari, P.P.H. Wilson. *Developments and needs in nuclear analysis of fusion technology*. Fusion Engineering and design, Vol. 88, pp. 454 – 460 (**2013**). Doi: http://dx.doi.org/10.1016/j.fusengdes.2013.03.049

[20] ITER Organization. *ITER. 60 years of progress*. Available: https://www.iter.org/sci/BeyondITER [Accessed: 8 August 2016].

[21] J. How, R. Reichle. *Plant Description (PD)*. ITER IDM location: https://user.iter.org/?uid=2X6K67 (**2009**).

[22] L.M. Giancarli, V. Barabash, D.J. Campbell, S. Chiocchio, J.J. Cordier, A. Dammann, G. Dell'Orco, J. Elbez-Uzan, J.M. Fourneron, J.P. Friconneau, M. Gasparotto, M. Iseli, C.Y. Jung, B.Y. Kim, D. Lazarov, B. Levesy, M. Loughlin, M. Merola, J.C. Nevière, R. Pascal, W. Ring, I. Schneiderova, S. Willms, A. Siarras, W. Shu, J.A. Snipes, J.G. van der Laan. *Progress and challenges of the ITER TBM Program from the IO perspective*. Fusion Engineering and Design, Vol. 109 – 111, pp. 1491 – 1497 (**2016**). Doi: http://dx.doi.org/10.1016/j.fusengdes.2015.11.046

[23] ITER Organization. News and Media. *First Plasma: 2025*. Available: http://www.iter.org/mag/9/65 [Accessed: 17 November 2016].

[24] L.V. Boccaccini. *EU blanket design and R&D for DEMO*. University of California, Los Angeles (UCLA): Second EU–US DCLL Workshop (**2014**).

[25] M. Abdou, N. B. Morley, S. Smolentsev, A. Ying, S. Malang, A. Rowcliffe, M. Ulrickson. *Blanket/first wall challenges and required R&D on the pathway to DEMO*. Fusion Engineering and Design, Vol. 100, pp. 2 – 43 (**2015**). Doi: http://dx.doi.org/10.1016/j.fusengdes.2015.07.021

Chapter 3
Methodology

This chapter describes the methodology for the nuclear analysis, naming the available codes and tools but emphasizing those codes and methods that are used along this document.

1. Introduction

The methodology followed in the nuclear analysis can be divided into four major steps: geometry, radiation field characterization, activation simulation, and residual radiation field characterization. Although the geometry step might be considered part of the transport, a separated category has been given in this chapter, given its complexity, which will be detailed in Section 2. Depending on the response function to be predicted it is necessary to go through some or even all the steps. For example, for operation quantities the last step is not carried out while, for instance, it is needed for SDDR calculations.

Figure 3.1 depicted a scheme of this methodology, pointing out these four major steps as well as the main inputs and outputs of each of them. The following bullets shortly describe each of the steps.

- The first step (geometry) consists of obtaining a suitable model for the neutronic simulation.
- The second step is the radiation field characterization. For this purpose, the neutronic model obtained in the first step is used. This radiation field characterization means carrying out the radiation transport simulation for the neutron and gamma fluxes calculation (as well as associated nuclear responses such as damage or deposited energy) during the operation phase of the reactor.
- The third step is the determination of the evolution of the isotopic inventory (as well as associated nuclear responses such as decay heat) for the materials that have been subjected to the neutron radiation. For this purpose, and activation simulation is performed using the neutron fluxes previously obtained in the step 2.
- The last step is the residual radiation field characterization due to the decay of the activated materials and, once again, the associated magnitudes such as doses. In order to perform this last step, the decay gamma source coming from step 3 is needed.

Nuclear data, which describe the way in which radiation interacts with matter, are the fundamental input data for both transport and activation simulations, i.e. for steps 2 – 4.

The following sections describe with more detail these steps as well as the different codes and programs that can be used, specifying the ones chosen for the development of this thesis. The structure is: geometry (Section 2), nuclear data (Section 3) radiation transport (Section 4) and activation ones (Section 5). Finally, Section 6 deals with the coupling of both transport and activation codes.

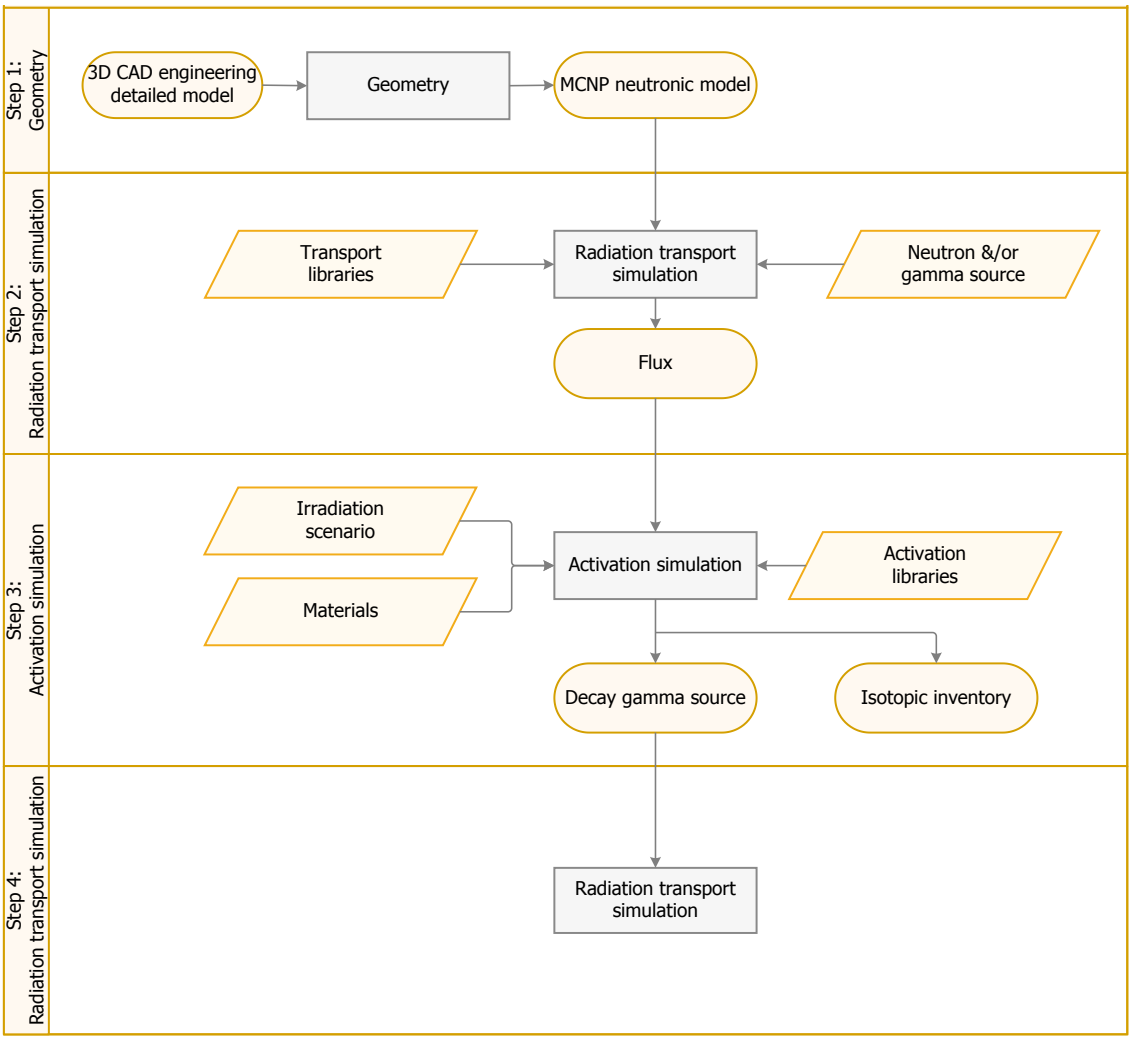

Figure 3.1. Scheme of the methodology followed in nuclear analysis.

2. Geometry

The first part of this section is devoted to describe the geometry process as well as the different necessary codes and tools to carry it out (Section 2.1). The second subsection (Section 2.2) is dedicated to the standard reference models used along the thesis.

2.1. The geometry process

The geometry process represented in Figure 3.2[4] starts with the detailed engineering 3D geometry model in CAD and continues until getting a valid 3D neutronic model for nuclear analysis. As it will be seen, this includes both changes that allow the model to be appropriate for nuclear analysis, and to convert these CAD models so that it can be readable by the chosen transport code. Moreover, sometimes, the model for a component (hereinafter called local model) is later integrated into the model for another component or larger system, or even in one corresponding to the whole reactor.

The geometry process consumes most of the time of the nuclear analysis because, as it will be seen, depending on the complexity of the model, and considering that the process is far from being fully automatic, an iterative process as well as manual corrections are sometimes required until a satisfactory neutronic model is achieved. Thus, the user's experience is fundamental for carrying this process out.

As shown in Figure 3.2, this geometry process, in turn, is divided into five steps: simplification, CAD-MCNP (Monte Carlo N-Particle) conversion, local model verification, set of the materials, and integration and final verification. All these steps as well as the different programs and tools to be used are described in the following subsections. Taking into account that some of the steps might be performed using different tools, the different options are explained in detail as well as the advantages and disadvantages of doing them in one or the other.

[4] The programs and tools used along this thesis to perform the geometry process are indicated with brackets.

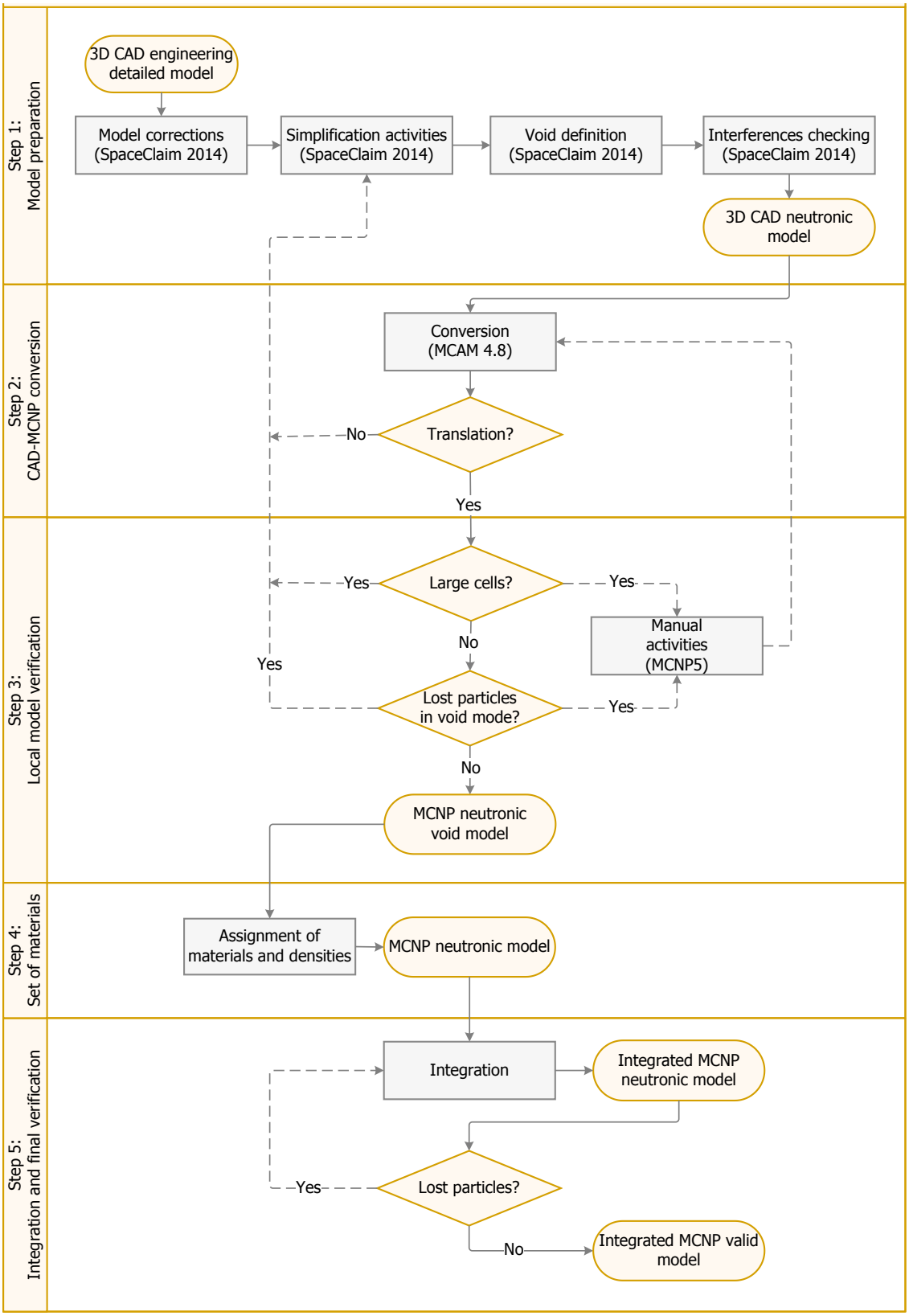

Figure 3.2. Flowchart for the geometry process (⬭ ; starts and ends of processes; ▭, process/actions; ▱, data; ◇, decision/question).

2.1.1. Model preparation

This first step aims at adapting the engineering 3D model, usually designed using the CATIA (Computer Aided Three-dimensional Interactive application) software [1], for being translated into a readable and valid format in MCNP. For this purpose, four are the sub-steps to be followed: correction of the model (Section 2.1.1.1), simplification (Section 2.1.1.2), voids definition (Section 2.1.1.3), and interferences checking (Section 2.1.1.4).

The different required actions in each of the hereunder described sub-steps, can be performed with different CAD programs, including CATIA or SpaceClaim 3D CAD-modeling software [2], among others. For the geometry processes performed in this work, 2014 version of SpaceClaim was selected since it is a fairly intuitive, easy to use and user-friendly program.

2.1.1.1. Model corrections

First of all, it is necessary to underline that this step is not really considered as part of the process for the model preparation, since the need of these corrections depends on the state of the original engineering model.

Taking into account that some problems are often detected when receiving these engineering models, it is considered convenient to explain them. These problems are two: i) the presence of bodies which are not correctly defined, and ii) interferences. In the following lines, these two problems are described with more detail.

- Not well defined bodies. As an example, when any of the components in CAD is not defined as a volume but as a set of surfaces, it is necessary to transform this set into a solid (Figure 3.3). Otherwise, there will be problems on step 2 (Section 2.1.2 CAD-MCNP conversion[5]).

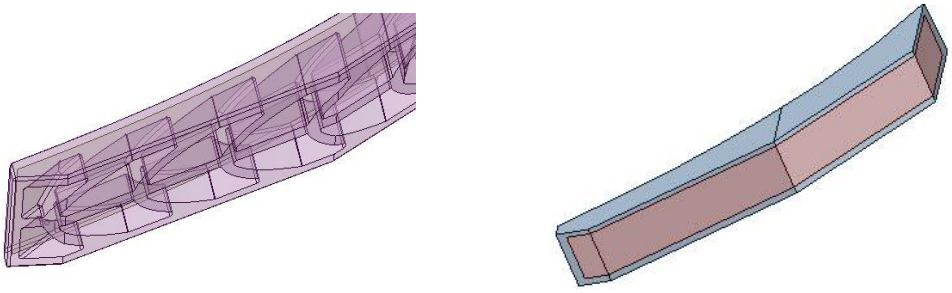

Figure 3.3. Example of a change of surfaces by volumes.

[5] When converting the model from CAD format to MCNP (step 2), the translation software will ignore this component.

- Interferences. In reality, two bodies can not coincide in the same space. However, when working with CAD tools, they can and, although it is not correct, it is not pointed out as an error. For this reason, it is advisable to check these interferences since the MCNP transport code [3] will identify these mistakes (whose result will be reflected in lost particles, as it will be seen later).

  For this purpose, SpaceClaim has an *Interference* tool to point out where this occurs. However, when trying to automatically correct the interferences, SpaceClaim sometimes presents problems that appear to be random. In any case, since the automatic way of fixing the interferences does not always coincide with what is needed, it is advisable to arrange such problems manually. Aside from SpaceClaim, SuperMC/MCAM [4] (which will be the tool used later for translating the model to a MCNP format) also includes this *Interference* tool. Nonetheless, the results do not always match those of SpaceClaim.

2.1.1.2. Simplification actions

Once the original engineering 3D model is correct, the next step to get a neutronic model is to carry out some simplification actions. These simplification activities can be broken down into the following categories:

- Removal of irrelevant details for radiation transport. This is aimed at reducing the complexity of the model since these models usually contain a high level of detail, which is unnecessary for transport calculations. Thus, this group of simplification activities is done in order to allow a fast nuclear analysis.

- Removal of surfaces not supported by MCNP. This kind of simplifications are often needed due to the restrictions that the transport code MCNP has to the geometry definition, which make it impossible to carry out the nuclear analysis. MCNP, as many Monte Carlo (MC) codes, is based on Constructive Solid Geometry (CSG). This means the use of Boolean operations; that is, intersections, unions and complements. In addition, geometric regions (called cells) are constructed using supported surfaces (those up to second order equations: planes, cylinders, etc.) [5].

  Therefore, these simplification actions are devoted to avoid complex curves such as splines[6] and general tori[7], since MCNP can not support them. For illustration, a spline simplification is seen in Figure 3.4 where the spline is replaced by several planes.

[6] Function that is piecewise-defined by polynomial functions of *n* degree [6].

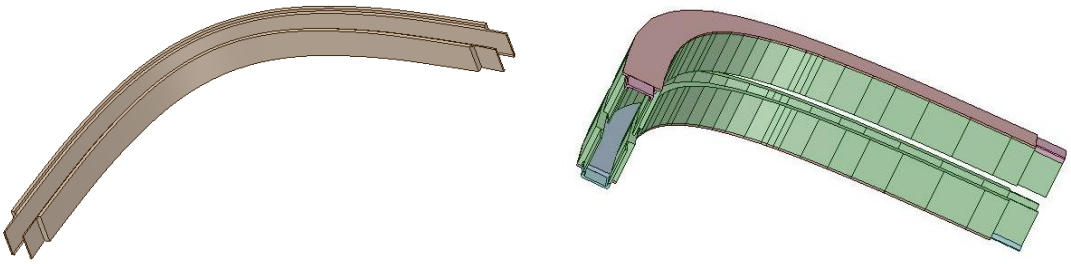

Figure 3.4. Example of replacement of splines by planes.

- Simplification of complex bodies. This simplification is needed due to two different reasons:

  - ✓ The cell definition is too large, i.e. contains a high number of surfaces which results in a slowdown of the nuclear calculations, even if none of these surfaces is really complex. Therefore, some bodies might be split into simpler ones in order to obtain cells with a low number of surfaces for their definition. Figure 3.5 shows an example of this kind of simplification: modification of soft corners to achieve components with a lower number of surfaces.

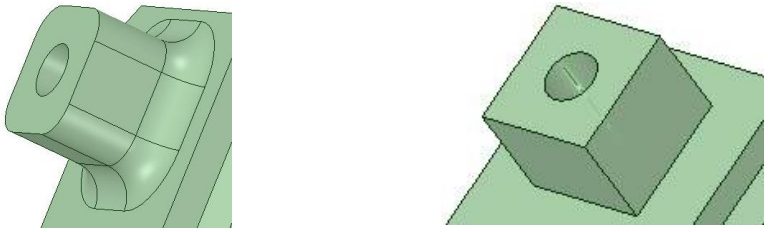

(a) (b)

Figure 3.5. Example of simplification for corners: (a), origibnal model; (b), simplified model.

  - ✓ Some complex cells can not been translated by the conversion code. Thus, they must be split into several cells. Note that, although the action is the same (splitting cells) the reason is different since this problem is not related to the length of the cell description, but to the translation capability of the conversion code.

Lastly, it is worth noting that these simplifications should be done taking into account that the physical information relevant for the nuclear analysis should be preserved in the simplified geometry. This procedure requires both experience and judgement. Furthermore, these modifications must be done trying to keep the volume of the components, in order to avoid

[7] Tori which axis coincides with one of the x, y or z axes can be translated, but no any other tori.

having to adjust the densities of the materials later (step 4). Specifically, these changes must not represent more than 2% of difference in the volume of the component and, if possible, less than 0.1% [7], in order to preserve the optical thickness.

2.1.1.3. Void definition

The void definition is also a key point of the geometry process, since the engineering 3D models usually take into account only those bodies filled with a material. The problem with not representing the voids appears when working with transport codes such as MCNP, in which is mandatory to define all the space, including this void one. Otherwise, the code fails when tracking the particles along the simulation.

The void definition, can be defined either in CAD, by creating new solids, or later in the conversion program, since translation tools had been forced to develop void filling methods in order to improve their capabilities and respond to this need.

- Defining voids in CAD seems more awkward and requires user's experience, although the necessary experience is the same as the one required for performing other geometry actions such as the simplification tasks. The main advantage is that, with this option, the user has a greater control over the model and, therefore, an experienced user will be able to generate a much optimized model from a transport calculation point of view. On the contrary, the main disadvantage is that this option requires more user time.

- For defining voids in SuperMC/MCAM, the implemented basic void filling method consists of a description of the voids by means of complementary descriptions of the parts that intersect the void region. One can see that the main disadvantage of this method is that each void definition contains many other geometry descriptions. As a consequence, void definition are complex, leading to a final model which is not optimized for transport simultions [4]. On the other hand, the main advantage is that for some geometry models this can be a fast way to generate a neutronic model requiring lower spent time by the user and resulting in a lower lost particle rate.

The choice of one method or another depends on the case. For the geometry processes performed throughout this thesis, voids were defined using the abovementioned SpaceClaim software (as shown in Figure 3.2).

2.1.1.4. Interference checking

As it has been previously commented, besides having to define all the space, it is also required to avoid two components coinciding in the same space. In this sense, it should be checked up that the performed simplifications do not lead to any interference. For this purpose, the same tools as in Section 2.1.1.1 are used.

2.1.2. CAD-MCNP conversion

Once the model is appropriately prepared, i.e. all the needed activities from the step 1 (Section 2.1.1 Model preparation) are finished, the next action is to convert the CAD model into a suitable model in MCNP, in order to continue simulating the particle transport.

This step requires specific programs. Among them, the MCAM version 4.8[8] geometry conversion tool [4] developed by the FDS team is selected in this work. Besides it, there are other programs than can be used for this purpose, such as McCAD [8] or Geomit [9]. However, at present, SuperMC/MCAM is the only software able for dealing with very large models as those from ITER, and it is the main reason for choosing it for the translations needed along this thesis [5]. It supports 6 types of surfaces in the CAD model, namely plane, sphere, cylindrical surface, cone surface, torus and ellipse torus. However, SuperMC/MCAM is not able to translate splines[9].

It is worth mentioning that a very useful option of SuperMC/MCAM is that for entering comments for each of the selected cells. This is important because it allows the user to have additional information from each of the cells (such as, for instance, to which component belongs each of the cells), even once translated, and it is especially useful when the model is composed by a high number of cells.

When converting the CAD model into an MCNP one, it can happen that the translation fails (for instance because splines are included in the model or complex cells). In such cases it will be necessary to return to the step 1 and, specifically, to the simplification actions. Nonetheless, the program does not detect errors like left space without definition or interferences (unless it is specifically requested). In the same way, as it has been anticipated, when surfaces are required to be translated, MCAM ignores them, converting the rest of the model but avoiding those bodies defined as surfaces.

[8] During the last times of the thesis, SuperMC version 5.2 was used.

[9] FDS team is trying to get a version with deals with splines but, at present, it can not work with them [10].

2.1.3. Local model verification

Once the CAD-MCNP conversion has been done, it is necessary to verify the generated local neutronic model. Even if the conversion is apparently properly done, it is advisable to verify that the generated cells are simpler enough, since the size of the cells converted is a relevant aspect in terms of demanding time in the further calculations, as seen in Section 2.1.1.

Furthermore, for a successfully geometry conversion, the imposed criteria for this thesis is that when running in void mode the neutronic model in MCNP, with 10^9 histories and a well spread source (guarantying that the neutron source is such that all the born particles enter the geometry), there should be no lost particles in the output[10]. It is worth underlining that the chosen origin points for the particles should never match with boundary surfaces of the model because this produces artificial losses not due to geometry errors.

In case the model loses particles, the display of the point where it does, by using the MCNP plotter, allows the identification of what needs to be corrected (Figure 3.6). The coordinates where particles are lost can be identified in the MCNP output. In addition, SuperMC/MCAM also has the capability to identify and show the coordinates where particles are lost (in fact, it shows their whole track). There are two possible reasons for the loss of particles, either it is because there is undefined space, or there are overlapping cells.

Either in the cases where cells are found to be larger than desired and/or particles are lost, it will be necessary to return to the initial step of simplification or otherwise, repair the problems "by hand" in MCNP (the feasibility of this option depends on the corrections to be done).

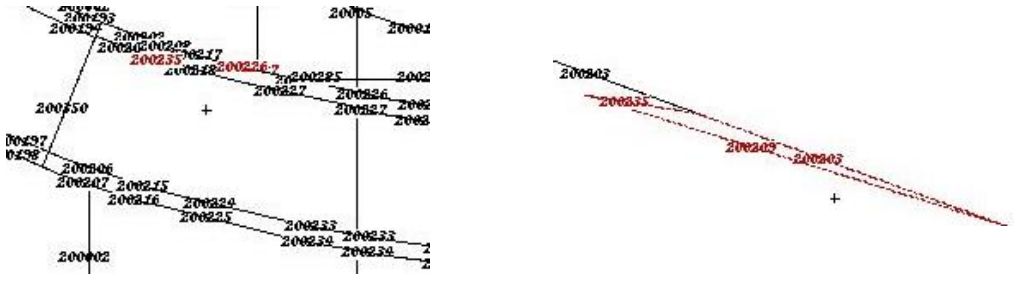

Figure 3.6. Example of a geometry error (red).

[10] Generally, it is commonly accepted a lost particle rate in void less than 10^{-7} [7].

2.1.4. Set of materials

Upon achieving a suitable simplified model, materials and densities for the different cells, the composition definition for such pure or homogenized materials, and the nuclear data to be used (according to the given specifications for each case), are included.

The definition of the composition for the materials can be either done in MCNP or using SuperMC/MCAM. In this thesis, the chosen options was defining the materials directly in MCNP but taking advantage of the mentioned option of SuperMC/MCAM for entering comments. Thus, before converting (step 2, Section 2.1.2) comments regarding the name of the corresponding material can be included, saving time in the present step.

It is worth noting that, depending on the simplifications made, the density value for some cells might need to be corrected since, as it has been said in Section 2.1.1, the optical thickness must be preserved. It is recommended to avoid homogenization of materials having different neutronic properties. When homogenization is necessary, it must be done by following the procedure described in [11].

Once the materials are included, the neutronic model in MCNP format may be run again without the void mode for checking. As in step 3 (Section 2.1.3), the imposed criterion is that when running in void mode with 10^9 histories and a well spread source, there should be no lost particles in the output.

2.1.5. Integration and final verification

As a last step, the achieved local neutronic model for a given system/component might be integrated into another larger model (such as the current standard reference neutronic model for ITER, C-lite), if needed.

After the integration, the new model should be displayed in the MCNP plotter and cut by several planes in order to check, at a first glance, that the introduced model does not intersect at all. If any interference is detected, it should be corrected "by hand" in MCNP.

Then, the achieved integrated MCNP neutronic model must be run again in order to corroborate the achievement of a successfully integrated model. The criterion for validating the model is similar as that of the step 3 (local model verification): when running with 10^9 histories and a well spread source, there should be no additional lost particles in the output. This means that the lost particles in the integrated model can not be due to the generated local model, and only those that were already lost in the reference model (in which the local is integrated) can be lost.

It is worth mentioning that the integration step can be performed either before or after step 4 (set of materials), i.e. one might define the materials previously to the integration, or after it. Moreover, materials could even be defined after the first verification checking, i.e. before the simulation for checking lost particles.

2.2. Reference models

Having reliable models where the reality is faithfully written on, becomes a need in order to make the results believable and realistic. Furthermore, since different teams and research groups are working jointly in the different fusion projects, it facilitates the creation of a common framework so the different assessments and analysis are all referred to the same model, and therefore, comparable. Moreover, the fact of having reference models to work with also maximizes the efficiency of nuclear analysis and helps in the maintenance of traceability. Reference models include geometry, material definition (in terms of both composition and nuclear data) and plasma sources [12]-[13].

In ITER this policy was developed from 2007. ITER IO develops and maintains the «lite» series of models. The «lite» series are based on a 40º sector of the tokamak representing all components up to the bioshield, centered on an equatorial port and with periodic boundary conditions toroidally applied. It has one complete and two half ports at the upper and equatorial levels and either one complete or two half lower ports. It contains materials specifications for transport and activation calculations. The idea behind the «lite» series is to provide the basis for the nuclear analysis of ITER and to allow the rapid development of detailed models for specific systems as the port plugs [7], [12]-[13].

The A-lite model [14] was the first model of the «lite» series, released in 2008. It was an MCNP model with more than 4800 cells, 3000 surfaces and 31 materials [12]. This model was followed by B-lite which, in addition to MCNP, was also in CAD format [15]. The current ITER standard reference neutronic model, C-lite [16] was the one with was worked with.

Regarding reference models for DEMO, under the Eurofusion Programme, the generation of computational models for nuclear analysis of each of the blanket concepts is being performed. As a first step, within the Breeder Blanket Work Package (WPBB) of the PPPT Programme, the KIT (Karlsruhe Institute of Technology) developed a generic reference neutronic model of DEMO "*EU DEMO1 model 2014*" [17] to be used as the basis for the integration of the different blankets [18]. In 2015, a new generic neutronic DEMO model was developed by P. Pereslavtsev (from KIT) [19]. Logically, within this thesis the used models were those corresponding to the DCLL, specifically the models developed during 2014 [20] and 2015 [21], based on the named generic neutronic DEMO models.

3. Nuclear data

Nuclear data are required as input data for both transport and activation simulations. It is worth mentioning that the validity of the results (either related to transport or activation) greatly depends on the accuracy degree of the nuclear data used in the calculation. Transport nuclear data are relevant for the appropriate estimation of the fluxes and associated magnitudes while activation nuclear data are essential for the reliability of nuclear inventory and the decay source.

These data provide the information needed to simulate the physical processes of interaction between radiation and matter. These data are given as cross sections which are grouped into libraries containing the nuclides used and a wide range of energies, including those relevant for the contributions collected in this document. There are different libraries that are being continuously updated due to either new experiments or to a better assessment.

In this thesis the libraries used for neutron transport are Fusion Evaluated Nuclear Data Library (FENDL 2.1 and FENDL 3.0) [22] and Joint Evaluated Fusion File (JEFF-3.1.1) [23] while for photon transport are: MCNPLIB04P[11] [3] and MCNPLIB84. These libraries are recommended for ITER and, also, in the Eurofusion framework [24]-[25].

For activation purposes, cross sections libraries and decay constants libraries used are grouped in EAF-2007 0-0. EAF-2007 libraries are also the reference activation libraries within both Eurofusion Programme and ITER [24]-[25].

An important question that arose in this thesis, was the status of these activation cross sections. In that sense, it is important to mention that one chapter of the thesis (Chapter 4) has been devoted to look into the status of part of them. In particular, those that are determinant for the calculation of the SDDR in ITER.

4. Radiation transport

The radiation transport simulation is needed for the neutron and gamma fluxes calculation (as well as associated nuclear responses) during the operation phase of the reactor, as well as for the residual radiation field characterization.

[11] At present, it is now known that this library gives rise to some errors in the MCNP calculations MCNP due to its format. This fact was unknown at the time of the transport simulations carried out in this thesis. Nevertheless, it is believed that the results are not significantly affected.

These radiation transport simulations often demand a high detailed spatial distribution of neutron and gamma fluxes or some derived quantity. This implies long computer time and, hence, parallel computations and acceleration algorithms are often required.

Different codes are used to simulate the radiation transport problem based either on deterministic or on stochastic methods.

Deterministic methods use different techniques to break the physical system into several subregions wherein a coupled system of linear equations is generated and solved, leading to detailed results and being computationally efficient [28]. The major disadvantage of these methods is their difficulty handling complex geometries. Thus, their results include uncertainties associated with the discretization of the independent variables (e.g. space, energy and angle) of the transport equation. Also, they allow solutions that might not be valid such as negative fluxes [29]. ATTILA [30] is one of the codes based on deterministic method most widely used for fusion applications.

On the other hand, the stochastic MC method is more accurate, especially when dealing with complex geometries. It has the capability to deal with complex variation in spatial and energy variables. Furthermore, since it is a statistical method, results are given accompanied by the associated relative errors. The number of source histories should be increased in order to minimize these relative errors, which lead to larger computing times. Nevertheless, variance reduction (VR) techniques are developed to avoid this enormous increase of computing time for obtaining good statistics. In other words, they improve the computational efficiency of a certain simulation by increasing the number of successful particle contributions to a given tally. Some transport codes using this method are MCNP [23], Serpent[12] [31], PHITS[13] [32] and TRIPOLI[14] [33].

Other relevant issue when delaing with radiation transport problems is the acceleration techniques needed for most of the calculations which, as has been abovementioned, in the case of MC are known as VR techniques. These techniques can be classified into local or global

[12] SERPENT a three-dimensional continuous-energy MC reactor physics burnup calculation code, developed at VTT Technical Research Centre of Finland since 2004.

[13] PHITS (Particle and Heavy Ion Transport code System) is a general purpose MC particle transport simulation code developed between JAEA, RIST, KEK and several other institutes.

[14] It is the generic name of a MC radiation transport codes family dedicated to shielding, reactor physics with depletion, criticality safety and nuclear instrumentation. It was developed by the Service d'Etudes des Réacteurs et de Mathématiques Appliquées (SERMA) at CEA Saclay [34].

(GVR) ones, depending on the extension of the region of interest. In addition, they can also be categorized according to the way for obtaining the input needed:

- From a deterministic code. These methods are also known as hybrid methods [29]. Examples of these hybrid methods are the Consistent Adjoint Driven Importance Sampling (CADIS) [35], which is a local one, and Forward Weighted CADIS (FW-CADIS) [36], which is a global one. Both methods have been implemented in the ADVANTAG code [37].

- From MC. The method to be used for MC codes is known was proposed by n Cooper and Larsen [38] and has different implementations, such as the Method of Automatic Generation of Importances by Calculation (MAGIC) [39], developed by A. Davis and A. Turner from CCFE (Culham Centre for Fusion Energy) and GVRUNED [40].

The MCNP5 code is the chosen code for the simulation of the radiation transport along this thesis, as it has been anticipated in the previous section by saying that the suitable neutronic model for calculation is obtained in MCNP format. It is selected since it is the reference code for ITER calculations [24].

The radiation transport simulations carried out in this work implied transporting neutrons and photons (neutral particles), without fission processes and time dependence, with high energy dependence, multiple materials and 3D complex geometric models. No VR techniques were required. However, these calculations could not be approached in an analytical way and, therefore, it was necessary to use computational tools. The calculated response functions and nuclear responses were fluxes, nuclear heating, and absorbed doses.

5. Activation

Activation calculations determine the temporal evolution of the isotopic inventory and the associated responses functions. These calculations are very important as an input for safety and radioprotection issues or when analyzing radioactive waste as it has been said in Chapter 1.

The necessary data for the activation codes to calculate the time evolution of materials under irradiation and through radioactive decay are:

- The flux of particles that induce activation (neutrons for cases addressed herein) with sufficient energy resolution.

- The composition of the activated material.

- Activation cross sections and decay data.

- The irradiation scenario under which the material is exposed.

Activation calculations of this thesis have been performed using the ACAB code [41], which was developed by J. Sanz[15] and subjected to a validation study under the IAEA supervision [42], which concluded that ACAB and FISPACT [43], being the last the reference in Europe, were the only codes suitable and satisfactory for fusion calculations.

In addition to this, ACAB has been and is being used in international fusion facilities such as NIF, ITER and EFDA/Eurofusion since it was specially conceived for fusion applications. The numeric algorithm that ACAB uses to solve the Bateman equations is the same as the ORIGEN code [44], on which it is based.

In this thesis the calculated radiological responses were activity, decay heat, contact dose rate and waste management ratings.

6. Coupling of transport and activation codes

Coupling transport and activation calculations is a great challenge in fusion neutronics. It implies obtaining the neutron flux with a detailed spatial and energy distribution so activation calculations can be carried out afterwards, getting the decay gamma source that, sometimes, is again transported for the final estimation of the doses.

The fact that there is no code to carry out both transport and activation simulations lead to a need of finding ways for coupling the different codes, avoiding errors and time involved when carrying out this coupling manually [12].

For the analysis performed in this thesis, a domestic computed system was used. These scripts had been developed by F. Ogando, one of the researchers belonging to TECF3IR. Generally speaking, these scripts consist in that, having generated a generic input of ACAB, different inputs are created (as many as activated cells) and each of them is automatically filled using information provided by the user and the data obtained in the previous transport simulation. Afterwards, all these inputs are run. The necessary files, with their given name and a brief description are presented in the following points. For the sake of clarity, Figure 3.7 shows a flowchart regarding the process and where each of the files takes part.

[15] Principal Investigator of the TECF3IR research group from UNED.

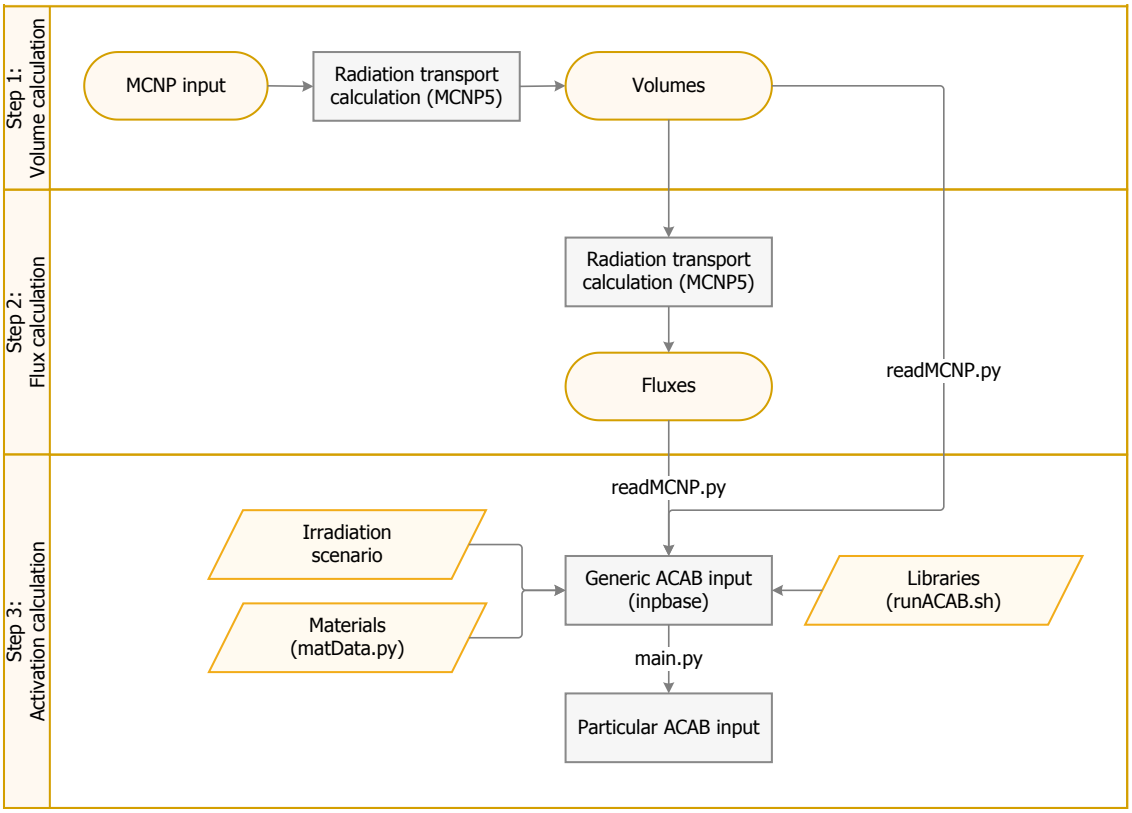

Figure 3.7. Process to be followed for massive transport-activation calculations and where the scripts used are involved.

- *inpbase*. It is a generic ACAB input, which is common to all the activation cases that are going to be run. Therefore, it has the shared information among all the cases, i.e. information regarding the irradiation scenario, response functions required, etc. In addition, some gaps are left blank to be filled by *main.py* using the specific information for each of the particular case, regarding the activated volume, flux and composition of the activated material.

- *main.py*. It is the main program. In short, the function of this program is to create different folders (as many as activation cases) and, in each of them, to copy the generic input *inpbase*, filling it with its particular data. In order to fill the left gaps in each of the inputs for the different cases, this main program calls *readMCNP.py* and *matData.py*.

  For this purpose, it is necessary to indicate the route where the output of MCNP, from which the volumes will be read[16], is located (i.e. where *readMCNP.py* is going to be

[16] Since, in this thesis, calculation of the volumes for the materials and voids is performed using the stochastic volume determination method in MCNP. Another option would have been reading them from MCAM.

run), as well as the one corresponding to the fluxes. Likewise, it is required to select which cells will be activated, as well as the source factor and the activation volume percentage (which is particularly useful when dealing with homogenized cells with several materials, and it is desired to activate each one separately).

- *readMCNP.py*. This program read the MCNP outp/s, in order to find the needed data regarding volumes and fluxes which are used to complete each of the ACAB inputs.

- *matData.py*. This program contains the information about the different materials used for activation along all the calculations. The user must introduce the involved material numbers (as numbered in MCNP transport calculations) and, for each of them, density and composition in percentage by weight (the element is indicated by the value of Z). In addition, the program is designed to normalize the compositions in the case that these do not add up to 100%. Note that, in case the isotopic composition is not the natural one, no change is included here, but the decay library should be modified accordingly.

- *runAcab.sh*. This program runs each ACAB input in each of the folders. It also contains links to all the required activation libraries (user should remove or include a particular library depending on the response function desired).

The calculations dealing with the DCLL model and collected in this thesis have helped to the development of these scripts and their verification.

For completeness, it is worth underlining that the general coupling scheme ends when the decay gamma source obtained in the activation calculation is transported to obtain the residual radiation field. This methodology is known as R2S (Rigorous 2-Step) but no more attention will be dedicated to it since was not used in this thesis.

7. Conclusions

This chapter describes the methodology proposed and applied throughout the thesis for MCF analyzed reactors (ITER and DEMO), both during the operation and the cooling period. This methodology is based on three steps: geometry, radiation field characterization and activation simulation. Along the chapter, special emphasis has been paid to those aspects from the geometry, transport and activation calculations that are considered most relevant for the comprehension of this document.

Taking into account the high degree of detail that the CAD geometry models have, the geometry step is arduous and consumes most of the time of the nuclear analysis since it is not

automatic, often involving iterative processes and manual corrections. This process is challenging and requires a significant degree of insight and expertise by the user. Despite these disadvantages, thanks to the CAD tools, very complex models can now be analyzed, something that would have been impossible without them. Given the importance of this process, the complete followed procedure has been detailed, pointing the critical steps out.

For a complete nuclear characterization of a MCF device, the use of both tools that simulate the transport of radiation and the activation and its corresponding coupling is needed. The radiation transport simulations carried out in this work implied neutron and photon transport, with high energy dependence, multiple materials and 3D complex geometric models. These calculations can not be approached in an analytical way and, therefore, it is necessary to turn to computational tools. Fluxes, nuclear heating, and absorbed doses were calculated in this work. For activation simulations, the calculated radiological responses were activity, decay heat, contact dose rate and waste management ratings. In addition, some domestic computed system is used for coupling transport and activation calculations.

To sum up, in this thesis SpaceClaim and MCAM were the required software for carrying the geometry process out, MCNP5 was chosen as transport code while ACAB was selected for activation calculations. Regarding the reference models, C-lite was the one used when dealing with ITER, while DEMO1-EU DCLL models from 2014 and 2015 were those for the DCLL analysis. Finally, the chosen libraries for neutron transport simulations are FENDL (2.1 and 3.0) and JEFF-3.1.1, whereas MCNPLIB04P and MCNPLIB84P are selected for photon transport. For activation purposes, cross sections libraries and decay constants libraries used are grouped in EAF-2007.

8. References

[1] *CATIA*. *Shape the world we live in.* Available: http://www.3ds.com/products-services/catia/ [Accessed 8 November 2016].

[2] *SpaceClaim*. Available: http://www.spaceclaim.com/ [Accessed 8 November 2016].

[3] X-5 Monte Carlo Team. *MCNP – A General Monte Carlo N-Particle Transport Code Version 5*. LA-CP-03-0245, Los Alamos National Laboratory (**2005**).

[4] Y. Wu. *CAD-based interface programs for fusion neutron transport simulation FDS Team*. Fusion Engineering and Design, Vol. 84, pp. 1987 – 1992 (**2009**). Doi: http://dx.doi.org/10.1016/j.fusengdes.2008.12.041

[5] Y. Shengpeng, C. Mengyun, S. Jing, L. Pengcheng, H. Liqin. *Convex-based void filling method for CAD-based Monte Carlo geometry modeling*. Annals of Nuclear Energy, Vol. 85, pp. 380 – 385 (**2015**). Doi: http://dx.doi.org/10.1016/j.anucene.2015.04.029

[6] S. Wold. *Spline functions in data analysis*. Technometrics, Vol. 16, nº 1, pp. 1 – 11 (**1974**).

[7] R. Pampin. *Quality document. Note on F4E provisions for nuclear analysis management*. F4E_D_26NR86 v2.1 (**2015**).

[8] L. Lu, U. Fischer, P. Pereslavtsev. *Improved algorithms and advanced features of the CAD to MC conversion tool McCad*. Fusion Engineering and Design, Vol. 89, pp- 1885 – 1888 (**2014**). Doi: http://dx.doi.org/10.1016/j.fusengdes.2014.05.015

[9] H. Nasif, F. Msuda, H. Morota. H. Iida, S. Sato, C. Konno. *Development of CAD-MCNP interface program GEOMIT and its applicability for ITER neutronics design calculations*. Nuclear Technology, Vol. 180, nº 1, pp. 89 – 102 (**2012**).

[10] FDS team. MCAM. Frequently Asked Questions. Available: http://fds.org.cn/english/mcam/mcam_faq.html#4 [Accessed 21 April 2016].

[11] A. Kyrieleis. *Development of MCNP Models of In-vessel Components in Blanket Rows 1-6 and the Divertor*. F4E_D_24XRLK v1.1 (**2016**).

[12] R. Pampin, A. Davis, J. Izquierdo, D. Leichtle, M.J. Loughlin, J. Sanz, A. Turner, R. Villari, P.P.H. Wilson. *Developments and needs in nuclear analysis of fusion technology*. Fusion Engineering and design, Vol. 88, pp. 454 – 460 (**2013**). Doi: http://dx.doi.org/10.1016/j.fusengdes.2013.03.049

[13] M. Loughlin. *C-model Terms of Use.* ITER Memorandum/Note. ITER IDM location: https://user.iter.org/?uid=TR7YME (**2016**).

[14] M. Loughlin, E. Polunovskiy. *ITER neutronic model: A-lite* (**2009**). ITER IDM location: https://user.iter.org/?uid=2NEZZS

[15] E. Polunovskiy, A. Serikov, A. Suarez. *ITER neutronic model: B-lite v.3 R121217* (**2012**). ITER IDM location: https://user.iter.org/?uid=9KKVQR

[16] E. Polunovskiy. *ITER neutronic model: C-lite v.1, R.131031* (**2013**). ITER IDM location: https://user.iter.org/?uid=M2TKBE

[17] C. Bachmann. *DEMO Generic MCNP model 11.25° degree* (**2013**). EUROFusion IDM location: https://idm.euro-fusion.org//?uid=2MK5CV

[18] J.C. Jaboulay, F. Damian, G. Aiello, D. Taylor, S. Zheng, B. Bienkowska, K. Drozdowicz, G. Tracz, U. Fischer, C. Bachmann. *Monte Carlo tools evaluation for nuclear analyses of the European DEMO*. Fusion Engineering and Design, Vols. 98 – 99, pp. 1800 – 1803 (**2015**). Doi: http://dx.doi.org/10.1016/j.fusengdes.2015.06.083

[19] P. Pereslavtsev. *2015 Generic DEMO Model for MCNP neutronic simulations* 2L6HJ7 (**2015**). EUROFusion IDM location: https://idm.euro-fusion.org/?uid=2AQ6EF

[20] I. Palermo, D. Rapisarda, I. Fernández. *DEMO2014_DCLL_MCNP_model* 2KZTEM (**2014**). EUROFusion IDM location: https://idm.euro-fusion.org/?uid=2AQ6EF

[21] I. Palermo, D. Rapisarda, I. Fernández. *DEMO2015_DCLL_MCNP_model* 2LNT7C (**2016**). EUROFusion IDM location: https://idm.euro-fusion.org/?uid=2AQ6EF

[22] D. López Aldama, A. Trkov. *FENDL-2.1 Update of an evaluated nuclear data library for fusion applications*. INDC(NDS)-467 Distr. FE. IAEA (**2004**).

[23] A. Santamarina, D. Bernard, Y. Rugama. *The JEFF-3.1.1 Nuclear Data Library.* JEFF Report 22, ISBN 978-92-64-99074-6 (**2009**).

[24] M. Loughlin. *Guidelines for Nuclear Analyses*. ITER IDM location: https://user.iter.org/?uid=R7XRXB (**2015**).

[25] U. Fischer. *Guidelines for Neutronic Analyses* v1.5 (**2016)**. EUROFusion IDM location: https://idm.euro-fusion.org/?uid=2L8TR9

[26] R.A. Forrest, J. Kopecky, J.-Ch. Sublet. *The European Activation File: EAF-2007 neutron-induced cross section libraries*. UKAEA FUS 535 report (**2007**).

[27] R.A. Forrest. *EAF-2007 decay data library*. UKAEA FUS 537 report (**2007**).

[28] S.T. Keller. *Modeling the Oregon State University TRIGA Reactor Using the Attila Three-Dimensional Deterministic Transport Code*. Thesis. Oregon State University (**2007**).

[29] J.C. Wagner, D.E. Peplow, S.W. Mosher, T.M. Evans. *Review of Hybrid (Deterministic/Monte Carlo) Radiation Transport Methods, Codes, and Applications at Oak Ridge National Laboratory*. Progress in Nuclear Science and Technology, Vol. 2, pp. 808 – 814 (**2011**).

[30] The Attila Software Suite. Productive enhancing solutions for radiation transport simulations (**2014**). Available:https://www.varian.com/sites/default/files/resource_attachments/AttilaBriefFinal_0.pdf [Accessed 23 September 2016].

[31] *Serpent. A Continuous-energy Monte Carlo reactor physics burnup calculation code*. http://montecarlo.vtt.fi/index.htm [Accessed 10 August 2016].

[32] *PHITS. Particle and Heavy Ion Transport code System*. http://phits.jaea.go.jp/index.html [Accessed 10 August 2016].

[33] TRIPOLI-4 Project Team. *TRIPOLI-4 version 8.1, 3D general purpose continuous energy Monte Carlo Transport code*. Available: http://www.oecd-nea.org/tools/abstract/detail/nea-1716/ [Accessed 8 August 2016].

[34] E. Brun, F. Damian, C.M. Diop, E. Dumonteil, F.X. Hugot, C. Jouanne, Y.K. Lee, F. Malvagi, A. Mazzolo, O. Petit, J.C. Trama, T. Visonneau, A. Zoia. *TRIPOLI-4®, CEA, EDF and AREVA reference Monte Carlo code*. Annals of Nuclear Energy, Vol. 82, pp. 151 – 160 (**2015**). Doi: http://dx.doi.org/10.1016/j.anucene.2014.07.053

[35] J.C. Wagner, A. Haghighat. *Automated variance reduction of Monte Carlo shielding calculations using the discrete ordinates adjoint function*. Nuclear Science and Engineering, nº 128, pp. 186 – 208 (**1998**).

[36] J.C. Wagner, E.D. Blakeman, D.E. Peplow. *Forward-Weighted CADIS method for global variance reduction*. Transactions of the American Nuclear Society, nº 97, pp. 630 – 633 (**2007**).

[37] S.W. Mosher, et al. *ADVANTG, An Automated Variance Reduction Parameter Generator*. ORNL/TM 2013/416 Rev. 1. Oak Ridge National Laboratory (**2015**).

[38] M.A. Cooper, E.W. Larsen. *Automated Weight Windows for Global Monte Carlo Particle Transport Calculations*. Nuclear Science and Engineer, nº 137 (**2001**). Doi: http://dx.doi.org/10.13182/NSE00-34

[39] A. Davis, A. Turner. *Applications of novel global variance reduction methods to fusion radiation transport problems*. International Conference on Mathematics and Computational Methods Applied to Nuclear Science and Engineering (M&C), Rio de Janeiro. ISBN 978-85-63688-00-2 (**2011**).

[40] L. Pérez. *Optimization of stochastic global variance reduction techniques for Monte Carlo neutron transport with applications to the ITER geometry*. Thesis dissertation. Universidad Nacional de Educación a Distancia (UNED) (**2016**).

[41] J. Sanz, O. Cabellos, N. García-Herranz. *ACAB. Inventory code for nuclear applications. User's manual* (**2008**).

[42] E.T. Cheng, R.A. Forrest, A.B. Pashchenko. *Report on the second international activation calculation benchmark comparison study*. International Nuclear Data Committee-INDC (NDS)-300, TSIR-21 (**1994**).

[43] R. A. Forrest. *FISPACT 2007 user manual*. UKAEA FUS 534 report (**2007**).

[44] A.G. Croff. *A User's Manual for the ORIGEN2 computer code.* ONRL /TM-7175 (**1980**).

Chapter 4

Reliability of activation cross sections for estimation of shutdown dose rate in the ITER port cell and port interspace

This chapter provides relevant information about the quality of available activation cross section data for accurate SDDR prediction in the PC and PI areas, where different maintenance activities are foreseen; since the reliability of the SDDR calculation strongly depends on the quality of the activation cross section data used.

1. Introduction

During the shutdown periods in ITER, some manual maintenance activities are expected to be carried out. These activities are scheduled both in the PC and PI areas (Figure 4.1), where dose limits for worker access are 10 μSv/h 1 day after shutdown in the PC and 100 μSv/h at 10^6 seconds (~12 days) for the PI [1]-[2].

The feasibility of these manual maintenance operations is based on the compliance of some imposed SDDR limits to be applied in each working area. The fulfillment of these target values is an ongoing challenge. Therefore, it is crucial to trust the SDDR calculations and, for that reason, validation of the activation cross section used is essential.

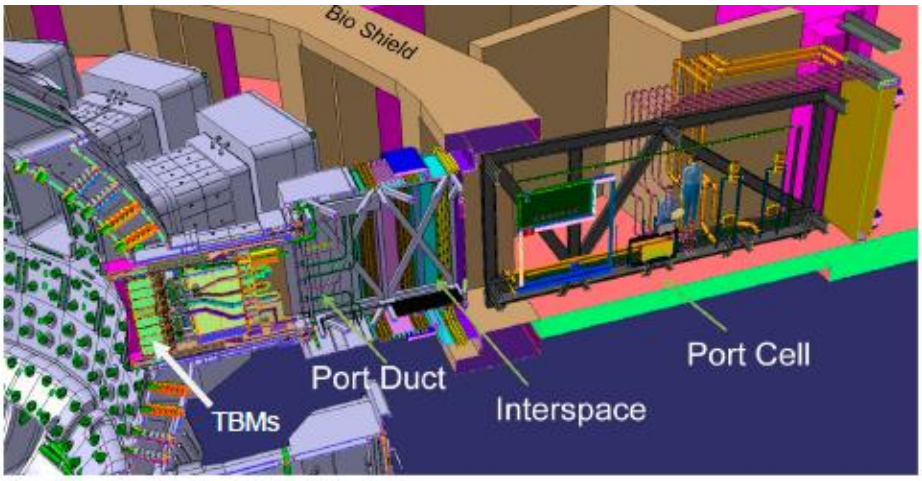

Figure 4.1. ITER PC and PI areas [3].

The activation cross section data contained in the different libraries are assembled from many data sources. Thus, for some reactions the cross section is well measured, while for others, there might be no experimental data and therefore, the cross section data are produced only by model code calculations.

Significant efforts have been carried out in order to obtain reliable neutron activation cross sections data for fusion applications (ITER, JET, IFMIF, DEMO). As a consequence, nowadays there are different available libraries to be used for activation purposes, including EAF (European Activation File), ENDF (US Evaluated Nuclear data Library), FENDL (Fusion Evaluated Nuclear Data Library), JEFF (Joint Evaluated Fission and Fusion File) and TENDL (TALYS-based Evaluated Nuclear Data Library), among others.

These libraries have been developed considering all the expected materials (several kinds of steels, alloys, etc.) to be placed in fusion facilities. Furthermore, validation activities have been undertaken using both D-T and D-D fusion spectra in order to provide an experimental data base for validation purposes [4]-[7].

However, despite having been created considering fusion applications, these libraries have not been developed taking into account the specific neutron spectra in the different components of an advanced 3D-geometric model for ITER.

In this chapter, the quality of the cross sections for some libraries typically used in fusion is evaluated for its specific use in the ITER SDDR prediction, since geometric model and specific materials in the different areas are currently clearly established and, therefore, the neutron spectra for the major components responsible of the SDDR can be obtained. Additionally, some other materials (such as barite and L2N concretes) that are being studied as candidates to be placed in ITER were also considered [8]. This information about activation and SDDR in ITER PC and PI is currently available in different papers and reports carried out within the framework of ITER [8]-[16].

EAF activation libraries were selected to evaluate the reliability of the relevant activation cross sections contributing to the SDDR in the PC and PI. This selection was based on the fact that the EAF libraries have more than 20 years of history and is the reference and recommended activation libraries within EUROFusion Programme and ITER [17]. Specifically, EAF-2007, which is typically used for the determination of the SDDR in ITER [8]-[16], as well as the last EAF version (EAF-2010) were assessed.

Aside from EAF, TENDL library was evaluated especially in those cases where EAF does not provide a reliable cross section. The reason for TENDL consideration is due to European Union

is focused on its development and it is yearly updated since 2008. The latest versions: TENDL-2013, TENDL-2014 and the very recent release from 2015 were used for the current study.

It is worth mentioning that much of the work developed in this chapter of the thesis has been published [18] and, another part, is pending acceptance for publication [19].

Methodology followed to address this work is shown in Section 2. Section 3 is devoted to collect major radionuclides contributing to SDDR and their pathways from both literature and own calculations. The quality classification of the identified relevant activation cross sections is presented in Section 4. Finally, Section 5 shows conclusions highlighting those activation cross sections that should be improved and, also, recommendations on the selection of the cross section activation library to be used in the prediction of the SDDR in ITER are provided.

2. Methodology

The methodology followed in this work is described by a flowchart in Figure 4.2. As it can be seen, the first step starts with the selection of the components and materials to be studied. In this work, Tritium Breeding System (TBS), divertor, vacuum vessel, cryostat and bioshield plug, among others, were selected. Analyzed materials were, therefore, several functional materials that are part of these components and which will contribute significantly to the SDDR at the PC and PI areas of ITER: SS316LN-IG, SS304, Eurofer, Inconel718, A660, XM-19, CuCrZr-IG, copper (Cu), tungsten (W), LiPb and conventional concrete (used in B-lite ITER model). In addition to this, other concretes candidates to be part of the bioshield pulg (L2N and barite) were studied. For the activation calculations compositions of the different materials with impurities were considered, as provided by official documents.

For each of these materials, major radionuclides responsible of SDDR were identified according to the following criteria:

- Criterion #1: Radionuclides which contribute more than 1% to the SDDR produced by the activation of each particular material.

  A value of 1% is fixed since it ensures that the sum of the different radionuclide contributions to the SDDR in any material or component is higher enough: at worst more than 93% and in most of the cases above 98%. Also, it was verified that in case of taking into account radionuclides contributing less than 1%, new pathways appear, but their contribution to the SDDR is not significant enough.

- Criterion #2: Total SDDR produced by the sum of the radionuclide contributions is higher than 20% of the applicable limit. The reason for considering a SDDR value quite

lower than the applicable limit is based on the fact that this total value might have been calculated using unreliable activation cross sections for pathways; therefore, the subsequent improvement of these cross sections can cause the total SDDR to be higher than the limit.

Once dominant radionuclides were identified according to the foregoing criteria, pathways contributing more than 1% to the production of each radionuclide were collected.

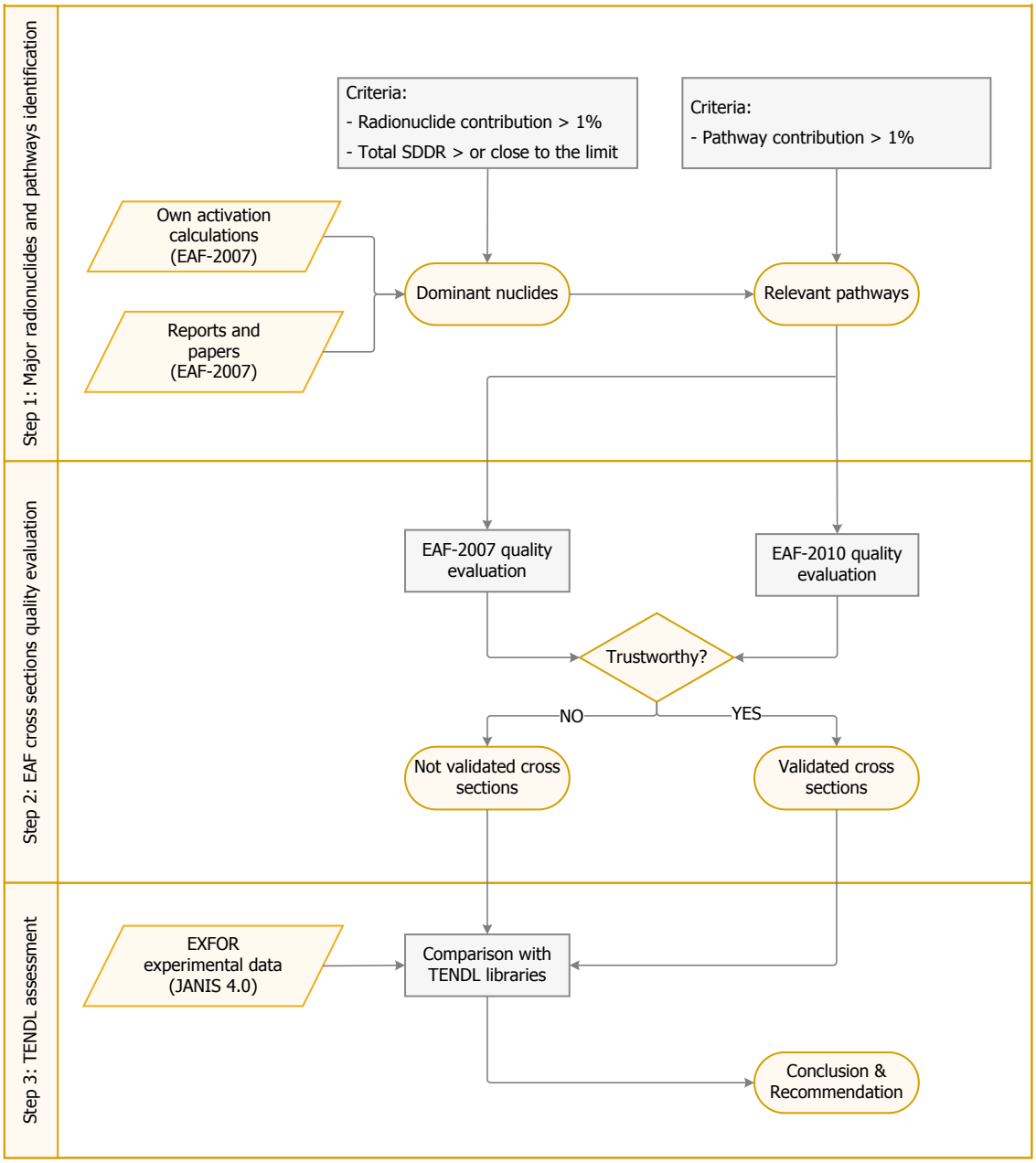

Figure 4.2. Flowchart description of the methodology (⬭; starts and ends of processes; ▭, process/actions; ▽, criteria; ▱, data; ◇, question/decision).

This information concerning both dominant radionuclides and pathways is taken from two complementary sources:

- The assessment and analysis section of recent available reports/papers devoted to calculate SDDR due to the activation of relevant materials at different ITER locations [8]-[16].
- Own activation calculations carried out in order to complete the information of those materials partially or not analyzed in those reports. For this computational analysis ACAB code [20] was used.

The merger of the data from both approaches ensures information enough to determine the main cross sections involved in the SDDR calculation at the PC and PI of ITER in a reliable way.

Next, in a second step, the quality of the cross section for each reaction was analyzed following the EAF procedure used for validating and testing the successive EAF versions since 2001 [21]-[23]. This procedure consists of comparing different integral results for experiments carried out for relevant materials in nuclear facilities with different neutron spectra (including a characteristic D-T fusion spectrum, up to 14 MeV), as well as differential experiments (cross sections at particular energies rather than averaged over a neutron spectrum), with the EAF data. Validation requires that both integral and differential data are consistent with the EAF data. Specifically, reference [24] is focused on the quality of the EAF-2007 cross sections and it was used as the main reference to check the status of the identified relevant cross sections. Furthermore, EAF-2010 was used to check updating in the cross section qualities compared to EAF-2007 version.

In a last step (step 3), data from TENDL library (2013, 2014 and 2015 versions) were used both to:

- Compare to experimental data taken from EXFOR (Experimental Nuclear Reaction Data Library) in order to obtain an estimation of the quality of cross sections for reactions of interest from this library.
- Assess possible improvements in TENDL when compared to EAF libraries, especially in those cross sections reactions with a poor or not provided quality in the above-mentioned reference [24].

This comparison was done using the JANIS (Java-based Nuclear Data Information System) display software (version 4.0) [25].

3. Dominant radionuclides to SDDR and pathways

This section deals with the identification of major radionuclides for SDDR in the PC and PI of ITER as well as the associated production pathways. This information was taken from two complementary sources: literature (Section 3.1) and own activation calculations (Section 3.2). Finally, Section 3.3 is devoted to set the list of the relevant activation cross section reactions to be evaluated, considering all the information from Sections 3.1 and 3.2.

3.1. Review of the literature for determination of main radionuclides and pathways contributing to SDDR

Several reports and papers related to the assessment of SDDR at different locations (PC and PI included) in ITER can be found in the literature. However, only some of them performed an analysis on major radionuclides and, very few, on their production pathways.

This section focuses on those reports in which major radionuclides for SDDR at relevant cooling times were analyzed [8]-[16]. All these works (excluding [14]) use 3D neutronic models of ITER (A-lite [26], B-lite [27] and C-lite [28]) with the standard SA2 irradiation scenario [29] and the EAF-2007 activation library.

In each of the reports, all the materials whose activation induces a relevant SDDR were considered. The composition of these materials was defined in the own references [8]-[16]. Then, dominant radionuclides and the production pathways for these radionuclides (when reported) were collected. Taking into account that the contribution of each radionuclide to SDDR is not specified in all of the reports, the following criterion was applied: in cases in which these contributions were given, only those radionuclides with a contribution to the SDDR above 1% are selected; and for the remaining, the complete list was included. The same reasoning applies for the pathways, also considering a minimum contribution of 1%. All this information is collected in Table 4.1 and Table 4.2.

Table 4.1 shows major radionuclides for SDDR produced by neutron activation for each of the considered materials. It is worth noting that in some cases such as [8], Contact Dose Rate (CDR) for a semi-infinite slab was evaluated instead of SDDR. The shown cooling times are those of interest for maintenance activities in the PC and PI areas. Furthermore, another maintenance activity defined for ITER was also taken into account, namely the transfer of components (blanket first wall modules, TBMs, divertor cassette, diagnostic port plug) in the transfer cask to be carried to the Hot Cell Facility (HCF). This maintenance task requires a maximal dose rate on contact with the transfer cask of 430 Sv/h at 21 days cooling [11].

One can see that results regarding the cask transfer to be carried to the HCF do not include new nuclides compared to the results for the same materials in other reports related to PC and PI.

Table 4.1. Major radionuclides for SDDR from the literature.

Reference	Responsible material	Dominant radionuclides	Cooling time (days)	Reported pathways
[8]	Conventional concrete (B-lite)	^{24}Na	1	No
	Barite concrete	^{24}Na, ^{59}Fe, ^{131}Ba,^{133}Ba		
	L2N concrete	^{24}Na, ^{60}Co, ^{152}Eu		
[9]	Concrete	^{24}Na	1	No
		^{54}Mn, ^{59}Fe	12	
	Eurofer	^{51}Cr, ^{54}Mn, ^{60}Co, ^{124}Sb, ^{182}Ta,	1	
		^{51}Cr, ^{54}Mn, ^{59}Fe, ^{60}Co, ^{124}Sb,	12	
	SS316LN-IG	^{51}Cr, ^{54}Mn, ^{59}Fe, ^{58}Co,	1	
		^{51}Cr, ^{54}Mn, ^{59}Fe, ^{58}Co, ^{182}Ta	12	
	LiPb	^{106m}Ag, ^{110m}Ag, ^{203}Pb, ^{187}W	1	
		^{65}Zn, ^{106m}Ag, ^{110m}Ag, ^{125}Sb,	12	
[10]	SS316LN-IG	^{51}Cr, ^{54}Mn, ^{59}Fe, ^{58}Co, ^{60}Co,	12	Yes
[11]	CuCrZr	^{60}Co, ^{182}Ta	21	Yes
	SS316LN-IG	^{54}Mn, ^{58}Co, ^{60}Co, ^{182}Ta		
	SS316L	^{54}Mn, ^{58}Co, ^{60}Co, ^{182}Ta		
	XM-19	^{54}Mn, ^{58}Co, ^{60}Co, ^{182}Ta		
	A660	^{58}Co, ^{60}Co, ^{182}Ta		
	Inconel 718	^{58}Co, ^{60}Co, ^{182}Ta		
	Eurofer97	^{54}Mn, ^{182}Ta		
	W	^{182}Ta		
[12]	SS316LN-IG, SS316LN-cryogenic steel, SS304/304L	^{60}Co, ^{182}Ta	12	Yes
[13]	SS316LN-IG	^{51}Cr, ^{54}Mn, ^{59}Fe, ^{58}Co, ^{60}Co,	12	No
[14]	Barite concrete	^{42}K, ^{24}Na, ^{131}Ba,^{133}Ba, ^{135m}Ba	1	Yes[17]
		^{131}Ba,^{133}Ba	12	
	L2N concrete	^{24}Na, ^{54}Mn, ^{59}Fe, ^{60}Co, ^{134}Cs, ^{152}Eu, ^{154}Eu, ^{160}Tb, ^{182}Ta	1	
		^{54}Mn, ^{59}Fe, ^{60}Co, ^{134}Cs, ^{152}Eu, ^{154}Eu, ^{160}Tb, ^{182}Ta	12	
[15]	SS304L, Inconel-718, SS316LN-IG	^{54}Mn, ^{59}Fe, ^{58}Co, ^{60}Co, ^{182}Ta	12	No
[16]	SS316L(N)-IG+H_2O, CuCrZr-IG	^{51}Cr, ^{54}Mn, ^{59}Fe, ^{58}Co, ^{60}Co	12	No

[17] Only for the most contributing radionuclides.

On the other hand, Table 4.1 shows slight differences in terms of major radionuclides for SDDR for the same materials, depending on the considered reference. These differences are due to differences in the composition and spectrum, considered cooling times and the fact of considering CDR or SDDR in either case. Table 4.1 also reflects that pathways for the production of major radionuclides are not defined in references [8], [9], [13], [15] and [16].

Table 4.2 collects the pathways, when given. A pathway means the chain of reaction and decays from the parent nuclide to the daughter. Although there were not provided pathways in reference [15], it is based on [30], which reported those pathways. As it can be seen, for each radionuclide, provided reactions from the different authors are practically the same.

Table 4.2. Relevant pathways for SDDR from the literature.

Reference	Dominant nuclide	Pathways
[10]	^{54}Mn	^{55}Mn(n,2n)^{54}Mn
		^{54}Fe(n,p)^{54}Mn
	^{51}Cr	^{50}Cr(n,g)^{51}Cr
		^{52}Cr(n,2n)^{51}Cr
	^{59}Fe	^{58}Fe(n,g)^{59}Fe
		^{59}Co(n,p)^{59}Fe
	^{58}Co	^{59}Co(n,2n)^{58}Co
		^{58}Ni(n,p)^{58}Co
	^{60}Co	^{59}Co(n,g)^{60}Co
		^{60}Ni(n,p)^{60}Co
		^{63}Cu(n,a)^{60}Co
	^{182}Ta	^{181}Ta(n,g)^{182}Ta
[11]	^{54}Mn	^{54}Fe(n,p)^{54}Mn
		^{55}Mn(n,2n)^{54}Mn
	^{58}Co	^{59}Co(n,2n)^{58}Co
		^{58}Ni(n,p)^{58}Co
	^{60}Co	^{59}Co(n,g)^{60}Co
		^{60}Ni(n,p)^{60}Co
		^{63}Cu(n,a)^{60}Co

Reference	Dominant nuclide	Pathways
[11]	^{182}Ta	^{181}Ta(n,g)^{182}Ta
		^{182}W(n,p)^{182}Ta
[12]	^{60}Co	^{59}Co(n,g)^{60}Co
	^{182}Ta	^{181}Ta(n,g)^{182}Ta
[14]	^{24}Na	^{23}Na(n,g)^{24}Na
		^{24}Mg(n,p)^{24}Na
		^{27}Al(n,a)^{24}Na
	^{42}K	^{41}K(n,g)^{42}K
	^{60}Co	^{59}Co(n,g)^{60}Co
	^{131}Ba	^{130}Ba(n,g)^{131}Ba
	^{133}Ba	^{132}Ba(n,g)^{133}Ba
[30]	^{54}Mn	^{54}Fe (n,p)^{54}Mn
	^{58}Co	^{58}Ni(n,p)^{58}Co
	^{60}Co	^{59}Co(n,g)^{60}Co
		^{60}Ni(n,p)^{60}Co
	^{182}Ta	^{181}Ta(n,g)^{182}Ta
		^{182}W(n,p)^{182}Ta

3.2. Activation calculations for determination of main radionuclides and pathways contributing to SDDR

This section is devoted to identify major radionuclides and pathways for SDDR in the PC and PI areas, built from own activation simulations. These calculations were performed in order to complete the information obtained in the previous section regarding not identified pathways. In addition to the considered materials of the previous section, Cu was included since it is expected to be present in the ITER PC and PI areas.

The simulations were performed using the ACAB activation code [20] with the EAF-2007 activation library. It is worth noting that ACAB provides the CDR for a semi-infinite slab that is composed of the radionuclide inventory produced by the neutron activation at each cooling time. This is in contrast with most of the cases of Section 3.1 where SDDR was given; that is, dose rate at any location but considering the transport of the residual photon source. However, despite not carrying out a residual photon transport calculation, the ACAB approach allows the perfect identification of major radionuclides and pathways.

As it has been previously said, the activated materials were those whose presence is assumed in ITER and will contribute to the SDDR at the PC and PI areas, namely: LiPb (with impurities, as defined in [31]-[32]), SS304L (0.2% weight Co, 0.05% weight Ta), SS316LN-IG (0.05% weight Co, 0.01% weight Ta), Eurofer (as defined in [9]), Cu (with impurities, following [33]). Furthermore, some concrete candidates for ITER bioshield plug (conventional used in B-lite model, L2N and barite concretes, all with impurities, as defined in [8]) were also studied.

Aside from that, irradiation scheme SA2 [29] was used and 1 day and 12 days cooling times were selected, according to times of interest for maintenance operations in the PC and PI, respectively.

The neutron spectra used for activation were computed with MCNP5 [34] in specific locations of interest for each material: i) for the LiPb, spectrum used is that from the TBM [31]-[32] with a total neutron flux of $1.04 \cdot 10^{14}$ n/cm^2·s, and ii) for the remaining materials results for 1 day cooling were obtained using spectrum from PC (in the last 5 cm of the bioshield plug frame) with a total neutron flux of $1.65 \cdot 10^{6}$ n/cm^2·s while results for 12 days cooling were obtained using spectrum from PI (in the closure plate of the port plug) with a total neutron flux: $6.06 \cdot 10^{8}$ n/cm^2·s (Figure 4.3).

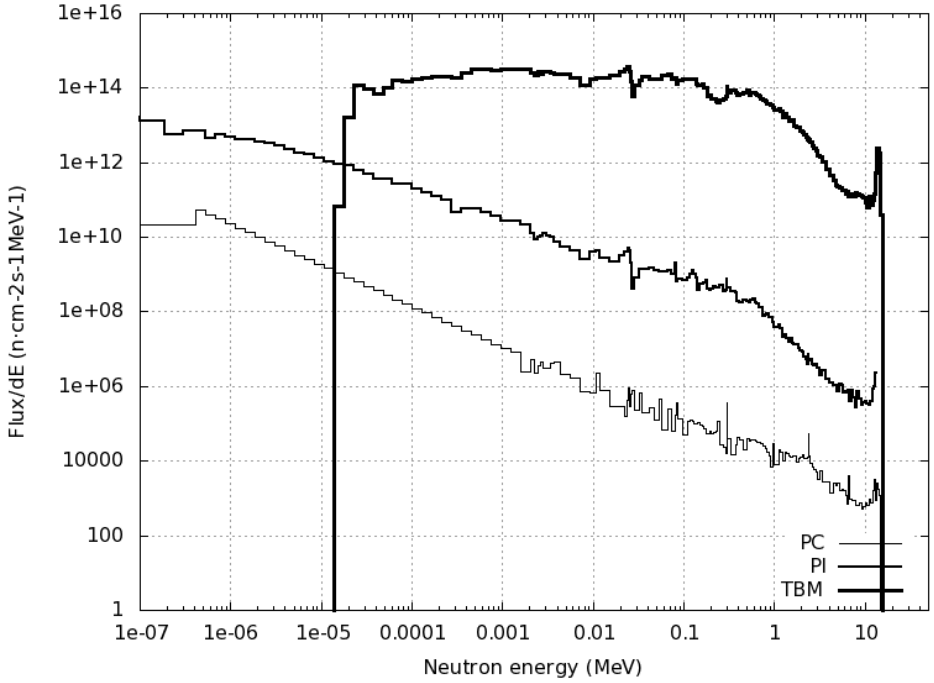

Figure 4.3. Neutron flux per energy interval used for activation calculations [18].

Table 4.3. Major radionuclides and contribution (%) to CDR from ACAB+EAF-2007 activation simulations.

Responsible material	Major radionuclides (%)	
	1 day cooling	12 days cooling
SS316LN-IG	^{60}Co (70.6), ^{59}Fe (8.8), ^{51}Cr (8.6), ^{56}Mn (4.0), ^{182}Ta (3.9), ^{58}Co (1.8), ^{64}Cu (1.3)	^{60}Co (44.5), ^{58}Co (24.3), ^{182}Ta (15.4), ^{54}Mn (10.8), ^{59}Fe (2.9), ^{51}Cr (1.0)
SS304L	^{60}Co (85.3), ^{182}Ta (5.9), ^{51}Cr (2.8), ^{59}Fe (2.8), ^{56}Mn (1.3), ^{64}Cu (1.3)	^{60}Co (60.2), ^{182}Ta (27.6), ^{58}Co (6.5), ^{54}Mn (4.1), ^{59}Fe (1.1)
Eurofer	^{182}Ta (46.0), ^{187}W (24.8), ^{60}Co (11.9), ^{59}Fe (10.2), ^{51}Cr (3.9), ^{56}Mn (1.1)	^{182}Ta (88.2), ^{54}Mn (4.6), ^{60}Co (3.4), ^{124}Sb (1.8), ^{59}Fe (1.6)
W	^{187}W (100)	^{187}W (93.3), ^{182}Ta (3.7), ^{181}W (2.8)
Cu	^{64}Cu (99.8)	^{60}Co (96.6), ^{110m}Ag (2.6)
LiPb	^{203}Pb (62.0), ^{24}Na (14.7), ^{58}Co (7.9), ^{54}Mn (6.4), ^{187}W (2.0), ^{60}Co (1.9)	^{58}Co (35.6), ^{54}Mn (31.2), ^{203}Pb (10.4), ^{60}Co (9.3), ^{110m}Ag (3.3), ^{65}Zn (3.2), ^{92m}Nb (1.9), ^{106m}Ag (1.9)
Conventional concrete (B-lite)	^{24}Na (98.7)	^{22}Na (55.3), ^{54}Mn (28.4), ^{59}Fe (11.1), ^{47}Ca (3.0), ^{40}K (1.1)
L2N concrete	^{60}Co (69.3), ^{24}Na (12.7), ^{152}Eu (7.9), ^{59}Fe (3.3)	^{60}Co (81.6), ^{54}Mn (5.9), ^{182}Ta (2.7), ^{59}Fe (2.2), ^{152}Eu (1.9), ^{160}Tb (1.8), ^{134}Cs (1.6), ^{154}Eu (1.2)
Barite concrete	^{131}Ba (69.0), ^{59}Fe (15.0), ^{133}Ba (8.9), ^{24}Na (3.0), ^{54}Mn (1.7), ^{135m}Ba (1.1)	^{131}Ba (60.4), ^{59}Fe (21.0), ^{133}Ba (14.7), ^{54}Mn (2.7)

As a result of these calculations, Table 4.3 summarizes dominant radionuclides in each of the materials and their contribution to the CDR computed in the present section, both at 1 and 12 days of cooling time. Major radionuclides appearing in Table 4.3 which come from the activation of L2N concrete at 1 day cooling were not taken into account in the following since the total SDDR was much lower than the applicable limit to the PC. The same reasoning was applied in the cases of conventional (B-lite) and barite concrete at 12-days cooling period, when the total computed SDDR was about a factor of 50 lower than the required limit.

Table 4.4 - Table 4.11 list pathways for the production of major radionuclides shown in Table 4.3, for each particular material. For each material major nuclides are sorted by atomic number and, for each of the major radionuclides, cooling times are listed from a single time to more than one, and from lowest to highest. Finally, for a given time important pathways are displayed. Furthermore, these relevant pathways are sorted from highest to lowest contribution to the total production of the radionuclide in each material.

Table 4.4. Pathways for radionuclides of interest from ACAB+EAF-2007 activation simulation for SS316LN-IG.

Major radionuclide	Half-life	Cooling time (days)	Relevant pathways and contribution (%)
^{51}Cr	27.7 d	1	^{50}Cr(n,g) (99.9)
		12	^{50}Cr(n,g) (75.7) ^{52}Cr(n,2n) (22.1) ^{54}Fe(n,a) (2.2)
^{54}Mn	312.1 d	12	^{54}Fe(n,p) (67.5) ^{55}Mn(n,2n) (32.5)
^{56}Mn	2.6 h	1	^{55}Mn(n,g) (99.9)
^{59}Fe	44.5 d	1	^{58}Fe(n,g) (100)
		12	^{58}Fe(n,g) (98.1) ^{62}Ni(n,a) (1.5)
^{58}Co	70.9 d	1	^{58}Ni(n,p) (99.8)
		12	^{58}Ni(n,p) (99.6)
^{60}Co	5.3 y	1	^{59}Co(n,g) (99.8)
		12	^{59}Co(n,g) (93.6) ^{60}Ni(n,p) (6.3)
^{64}Cu	12.7 h	1	^{63}Cu(n,g) (100)
^{182}Ta	114.7 d	1	^{181}Ta(n,g) (99.9)
		12	^{181}Ta(n,g) (99.9)

Table 4.5. Pathways for radionuclides of interest from ACAB+EAF-2007 activation simulation for LiPb.

Major radionuclide	Half-life	Cooling time (days)	Relevant pathways and contribution (%)
^{24}Na	14.9 h	1	^{27}Al(n,a) (100)
^{54}Mn	312.1 d	1	^{55}Mn(n,2n) (94.8) ^{54}Fe(n,p) (5.2)
		12	^{55}Mn(n,2n) (94.8) ^{54}Fe(n,p) (5.2)
^{58}Co	70.9 d	1	^{58}Ni(n,p) (82.9) ^{59}Co(n,2n) (17.1)
	70.9 d	12	^{58}Ni(n,p) (82.9) ^{59}Co(n,2n) (17.1)
^{60}Co	5.3 y	1	^{59}Co(n,g) (78.1) ^{60}Ni(n,p) (21.8)
		12	^{59}Co(n,g) (78.1) ^{60}Ni(n,p) (21.8)
^{65}Zn	243.8 d	12	^{64}Zn(n,g) (72.5) ^{66}Zn(n,2n) (27.5)
^{92m}Nb	10.2 d	12	^{93}Nb(n,2n) (84.3) ^{92}Mo(n,p) (14.9)
^{106m}Ag	8.3 d	1	^{107}Ag(n,2n) (100)
		12	^{107}Ag(n,2n) (100)
^{110m}Ag	249.8 d	1	^{109}Ag(n,g) (99.9)
		12	^{109}Ag(n,g) (99.9)
^{187}W	23.8 h	1	^{186}W(n,g) (100)
^{203}Pb	51.9 h	1	^{204}Pb(n,2n) (100)
		12	^{204}Pb(n,2n) (99.5)

Table 4.6. Pathways for radionuclides of interest from ACAB+EAF-2007 activation simulation for Cu.

Major radionuclide	Half-life	Cooling time (days)	Relevant pathways and contribution (%)
^{60}Co	5.3 y	12	^{63}Cu(n,a) (100)
^{64}Cu	12.7 h	1	^{63}Cu(n,g) (100)
^{110m}Ag	249.8 d	12	^{109}Ag(n,g) (100)

Table 4.7. Pathways for radionuclides of interest from ACAB+EAF-2007 activation simulation for conventional concrete.

Major radionuclide	Half-life	Cooling time (days)	Relevant pathways and contribution (%)
^{24}Na	14.9 h	1	^{23}Na(n,g) (99.6)

Table 4.8. Pathways for radionuclides of interest from ACAB+EAF-2007 activation simulation for barite concrete.

Major radionuclide	Half-life	Cooling time (days)	Relevant pathways and contribution (%)
^{24}Na	14.9 h	1	^{24}Mg(n,p) (33.6) ^{27}Al(n,a) (66.3)
^{54}Mn	312.1 d	1	^{54}Fe(n,p) (100)
^{59}Fe	44.5 d	1	^{58}Fe(n,g) (100)
^{131}Ba	11.5 d	1	^{130}Ba(n,g) (99.9)
^{133}Ba	10.6 y	1	^{132}Ba(n,g) (97.1) ^{134}Ba(n,2n) (2.7)
^{135m}Ba	22.7 h	1	^{134}Ba(n,g) (58.6) ^{135}Ba(n,n') (32.5) ^{136}Ba(n,2n) (8.9)

Table 4.9. Pathways for radionuclides of interest from ACAB+EAF-2007 activation simulation for Eurofer.

Major radionuclide	Half-life	Cooling time (days)	Relevant pathways and contribution (%)
^{51}Cr	27.7 d	1	^{50}Cr(n,g) (99.9)
^{54}Mn	312.1 d	12	^{54}Fe(n,p) (89.5) ^{55}Mn (n,2n) (10.4)
^{56}Mn	2.6 h	1	^{55}Mn(n,g) (100)
^{59}Fe	44.5 d	1	^{58}Fe(n,g) (100)
		12	^{58}Fe(n,g) (99.9)
^{60}Co	5.3 y	1	^{59}Co(n,g) (100)
		12	^{59}Co(n,g) (99.9)
^{124}Sb	60.2 d	12	^{123}Sb(n,g) (100)
^{187}W	23.8 h	1	^{186}W(n,g) (100)
^{182}Ta	114.7 d	1	^{181}Ta(n,g) (100)
		12	^{181}Ta(n,g) (100)

Table 4.10. Pathways for radionuclides of interest from ACAB+EAF-2007 activation simulation for L2N concrete.

Major radionuclide	Half-life	Cooling time (days)	Relevant pathways and contribution (%)
^{54}Mn	312.1 d	12	^{54}Fe (n,p) (94.3) ^{55}Mn (n,2n) (5.7)
^{59}Fe	44.5 d	12	^{58}Fe(n,g) (98.8) ^{59}Co(n,p) (1.2)
^{60}Co	5.3 y	12	^{59}Co(n,g) (100)
^{134}Cs	2.1 y	12	^{133}Cs(n,g) (100)
^{152}Eu	13.5 y	12	^{151}Eu(n,g) (100)
^{154}Eu	8.6 y	12	^{153}Eu(n,g) (100)
^{160}Tb	72.3 d	12	^{159}Tb(n,g) (100)
^{182}Ta	114.7 d	12	^{181}Ta(n,g) (100)

Table 4.11. Pathways for radionuclides of interest from ACAB+EAF-2007 activation simulation for W.

Major radionuclide	Half-life	Cooling time (days)	Relevant pathways and contribution (%)
^{182}Ta	114.7 d	12	^{182}W(n,p) (98.3) ^{183}W(n,D) (1.2)
^{181}W	121.2 d	12	^{180}W(n,g) (50.6) ^{182}W(n,2n) (49.4)
^{187}W	23.8 h	1	^{186}W(n,g) (100)
		12	^{186}W(n,g) (100)

One can see that no new pathways appeared for radionuclides listed in Section 3.1 (Table 4.1 and Table 4.2). On the other hand, it is worth mentioning that the current design of ITER (C-lite) uses a slightly different composition of concrete in terms of percentage contributions, as the constituent isotopes are the same. Therefore, activation calculations performed for this C-lite concrete has given very similar results to B-lite ones.

3.3. Summary of considered reactions for cross section quality analysis

This section is devoted to list and justify the relevant pathways whose cross section quality will be assessed in Section 4.

This list of relevant pathways was built taking into account data provided by both Sections 3.1 and 3.2 are taken into account. Despite having detected some differences between both sections in terms of dominant radionuclides, these differences are always found in those

radionuclides that are less important (those with a lower contribution). These discrepancies are may due to these facts: i) different spectrum used for different positions for the same material, ii) differences in composition for the same material, iii) cooling times compared are not the same, iv) considering CDR in Section 3.2 while in Section 3.1 calculation of SDDR is done or v) percentage selected for considering major radionuclide in Section 3.2 (1%) compared to Section 3.1, where the contribution percentage of the major radionuclides in some cases was not known.

In any case, taking into account that differences are not very significant and preserving a conservative approach, all the information from both sections was taken into account. Therefore, considering both sources of data, 27 relevant radionuclides are identified: ^{24}Na, ^{42}K, ^{51}Cr, ^{54}Mn, ^{56}Mn, ^{59}Fe, ^{58}Co, ^{60}Co, ^{57}Ni, ^{64}Cu, ^{65}Zn, ^{92m}Nb, ^{106m}Ag, ^{110m}Ag, ^{124}Sb, ^{125}Sb, ^{134}Cs, ^{131}Ba, ^{133}Ba, ^{135m}Ba, ^{152}Eu, ^{154}Eu, ^{160}Tb, ^{182}Ta, ^{181}W, ^{187}W, and ^{203}Pb.

- 19 of them are relevant for the SDDR analysis at the ITER PC, namely: ^{24}Na, ^{42}K, ^{51}Cr, ^{54}Mn, ^{56}Mn, ^{59}Fe, ^{58}Co, ^{60}Co, ^{57}Ni, ^{64}Cu, ^{106m}Ag, ^{110m}Ag, ^{124}Sb, ^{131}Ba, ^{133}Ba, ^{135m}Ba, ^{182}Ta, ^{187}W, and ^{203}Pb.
- 20 of them are related to the SDDR at the PI area, namely: ^{42}K, ^{51}Cr, ^{54}Mn, ^{59}Fe, ^{58}Co, ^{60}Co, ^{65}Zn, ^{92m}Nb, ^{106m}Ag, ^{110m}Ag, ^{124}Sb, ^{125}Sb, ^{134}Cs, ^{152}Eu, ^{154}Eu, ^{160}Tb, ^{182}Ta, ^{181}W, ^{187}W and ^{203}Pb.
- In the case of the cask transfer to be carried to the HCF, only 4 are relevant: ^{54}Mn, ^{58}Co, ^{60}Co and ^{182}Ta.

It is worth mentioning that some of these radionuclides come from neutron activation of candidate materials, but not in the components of the current design of ITER. This is the case of ^{134}Cs, ^{152}Eu, ^{154}Eu, and ^{160}Tb that come from the L2N concrete or ^{42}K, ^{131}Ba, ^{133}Ba, and ^{135m}Ba which are produced by neutron activation of barite concrete.

Regarding the production of these radionuclides, all the relevant pathways were identified considering the information provided in both Sections 3.1 and 3.2. Thus, it is considered that all the relevant pathways involved in the SDRR at PC and PI locations were identified.

Table 4.12 provides a list of all the considered pathways for the production of each major radionuclide, which are sorted by atomic number. This table also indicates the material from which each of the radionuclides comes from, as well as their half-lives.

Therefore, to sum up, when assessing the quality of the cross sections, the considered radionuclides and pathways were taken from both previous sections. Only some major radionuclides (and therefore their pathways) of Section 3.2 were discarded because the total

SDDR, produced by the activation of the responsible material, is considerably lower than the applicable limit. That was the case of dominant radionuclides for the conventional (B-lite) and barite concrete at 12 days of cooling time and for the L2N at 1 day cooling. However, ^{24}Na and ^{60}Co (nuclides relevant at 1 day for L2N concrete) were an exception and are hereafter considered since according to reference [14] activation of this concrete produce a SDDR exceeding applicable limit in the PC (10 μSv/h). Moreover, although some radionuclide was rejected for those reasons, the same nuclide could have been taken into account in other materials or cooling times. As an example, ^{54}Mn is a dominant radionuclide in the conventional concrete (B-lite) at 12 days cooling and therefore it was rejected, but it is also given as major nuclide in the SS316LN-IG or LiPb, so it was considered in the two last cases. In brief, when there were discrepancies in the criteria to be followed, the most conservative option was chosen for the subsequent analysis.

Furthermore, it was analyzed whether the radionuclides of interest (which are almost all from 1-step reactions) come from the activation of intendent elements or impurities. In this regard it is noteworthy that the fact of considering impurities or not does not vary dominant nuclides in the cases of Cu and W whereas in the remaining cases some differences were appreciated. On the other hand, it is worth mentioning that ^{124}Sb appears as a relevant radionuclide in the Eurofer activation, coming from the Sb impurity while activation of a different Eurofer composition[18] without Sb, would not lead to this major radionuclide.

Additional points must be taken into consideration. On the one hand, in the cases of Section 3.1 where a relevant nuclide appear and did not in Section 3.2, pathways for the production of this radionuclide were identified using ACAB, as those radionuclides also appear in Section 3.2 but with a lower percentage of contribution. The same applies if a major radionuclide is given in both sections but at different cooling times: ACAB was used to identify all possible pathways at all the cooling times included in both subsections. An example is the case of ^{51}Cr which in Section 3.2, for the Eurofer, was only important at 1 day cooling while literature said (Section 3.1) it is relevant both at 1 and 12 days.

In addition to this, major radionuclides and pathways found in this work were corroborated using a handbook focused on general activation calculations [35]. This handbook reports the expected radionuclides and pathways coming from the neutron activation of different materials, taking the neutron spectra into consideration. No discrepancies were detected between the handbook data and the radionuclides and pathways considered in this chapter.

[18] Such as the one used in this thesis for the activation of the DEMO DCLL (see Chapter 6).

Table 4.12. Summary of considered pathways.

Nuclide	Half-life	Relevant Material	Main Pathways	Pathway obtained from
^{24}Na	14.95 h	LiPb, conventional, L2N and barite concrete	^{23}Na(n,g)^{24}Na	[14], ACAB
			^{24}Mg(n,p)^{24}Na	[14], ACAB
			^{27}Al(n,a)^{24}Na	[14], ACAB
^{42}K	12.4 h	Barite concrete	^{41}K(n,g)^{42}K	[14], ACAB
^{51}Cr	27.7 d	Eurofer, SS316LN-IG, SS304L, CuCrZr-IG	^{50}Cr(n,g)^{51}Cr	[10], ACAB
			^{52}Cr(n,2n)^{51}Cr	[10], ACAB
			^{54}Fe(n,a)^{51}Cr	ACAB
^{54}Mn	312.1 d	LiPb, conventional, L2N and barite concretes, Eurofer, SS316LN-IG, SS316L, SS304L, XM-19, Inconel 718, CuCrZr-IG	^{55}Mn(n,2n)^{54}Mn	[10], [11], ACAB
			^{54}Fe(n,p)^{54}Mn	[10], [11], ACAB
^{56}Mn	2.6 h	Eurofer, SS316LN-IG, SS304L	^{55}Mn(n,g)^{56}Mn	ACAB
^{59}Fe	44.5 d	Eurofer, conventional, L2N and barite concretes, SS316LN-IG, SS304L, Inconel 718, CuCrZr-IG	^{58}Fe(n,g)^{59}Fe	[10], ACAB
			^{59}Co(n,p)^{59}Fe	[10]
			^{62}Ni(n,a)^{59}Fe	ACAB
^{58}Co	70.9 d	LiPb, SS316LN-IG, SS316L, Inconel 718, XM-19, A660, CuCrZr-IG,	^{59}Co(n,2n)^{58}Co	[10], [11], ACAB
			^{58}Ni(n,p)^{58}Co	[10], [11], ACAB
^{60}Co	5.3 y	LiPb, Cu, L2N concrete, Eurofer, SS316LN-IG, SS304/316L, Inconel 718, XM-19, A660, CuCrZr	^{59}Co(n,g)^{60}Co	[10], [11], [12], ACAB
			^{60}Ni(n,p)^{60}Co	[10], [11], ACAB
			^{63}Cu(n,a)^{60}Co	[10], [11], ACAB
^{57}Ni	35.6 h	SS316LN-IG	^{58}Ni(n,2n)^{57}Ni	ACAB
^{64}Cu	12.7 h	Cu, SS316LN-IG, SS304L	^{63}Cu(n,g)^{64}Cu	ACAB
^{65}Zn	243.8 d	LiPb	^{64}Zn(n,g)^{65}Zn	ACAB
			^{66}Zn(n,2n)^{65}Zn	ACAB
^{92m}Nb	10.2 d	LiPb	^{93}Nb(n,2n)^{92m}Nb	ACAB
			^{92}Mo(n,p)^{92m}Nb	ACAB
^{106m}Ag	8.3 d	LiPb	^{107}Ag(n,2n)^{106m}Ag	ACAB
^{110m}Ag	249.8 d	LiPb, Cu	^{109}Ag(n,g)^{110m}Ag	ACAB
^{124}Sb	60.2 d	Eurofer	^{123}Sb(n,g)^{124}Sb	ACAB
^{125}Sb	9.6 d	LiPb	^{124}Sn(n,g)^{125}Sn(B$^-$)^{125}Sb	ACAB
^{134}Cs	2.1 y	L2N concrete	^{133}Cs(n,g)^{134}Cs	ACAB
^{131}Ba	11.5 d	Barite concrete	^{130}Ba(n,g)^{131}Ba	[10], ACAB
^{133}Ba	10.6 y	Barite concrete	^{132}Ba(n,g)^{133}Ba	ACAB
			^{134}Ba(n,2n)^{133}Ba	ACAB
^{135m}Ba	22.7 h	Barite concrete	^{134}Ba(n,g)^{135m}Ba	ACAB
			135Ba(n,n')^{135m}Ba	ACAB
			^{136}Ba(n,2n)^{135m}Ba	ACAB
^{152}Eu	13.5 y	L2N concrete	^{151}Eu(n,g)^{152}Eu	ACAB
^{154}Eu	8.6 y	L2N concrete	^{153}Eu(n,g)^{154}Eu	ACAB
^{160}Tb	72.3 d	L2N concrete	^{159}Tb(n,g)^{160}Tb	ACAB
^{182}Ta	114.7 d	W, L2N concrete, Eurofer, SS316LN-IG, SS304L/316L, Inconel 718, XM-19, A660, CuCrZr	^{181}Ta(n,g)^{182}Ta	[10], [11], [12], ACAB
			^{182}W(n,p)^{182}Ta	
^{181}W	121.2 d	W	^{180}W(n,g)^{181}W	ACAB
^{187}W	23.8 h	LiPb, W, Eurofer	^{186}W(n,g)^{187}W	ACAB
^{203}Pb	51.9 h	LiPb	^{204}Pb(n,2n)^{203}Pb	ACAB

4. Quality assessment of the activation cross sections pathways

This section assesses the quality of the main activation cross section, according to the previous section. In this sense, efforts had already been carried out by EAF in order to evaluate its quality, providing specific reports from 2001 version [21]-[24], [36]-[37] as it has been mentioned in Section 2. This evaluation was done validating cross sections against integral and differential data. This validation work results in a quality score (QS) for each of the reactions.

The QS magnitude is a value from 0 to 6 indicating the degree to which the EAF data are backed up by experimental data (Table 4.13). Besides the numerical score, sometimes brackets and asterisk are used, where * indicates that the score differs from the value given in the distributed EAF file due to new experimental data obtained after the library release or errors in the concerned EAF (updated score), and scores in (brackets) indicates score for total cross section.

Following this approach, the current section is divided into four parts. The first (4.1) shows the QS of the EAF-2007 cross sections for the considered reactions. Subsection 4.2 provides a quality comparison between EAF-2007 and EAF-2010 versions, to check possible updates. Subsection 4.3 is focused on those cross sections not validated according to the explained criteria, providing a comparison among EAF (2007 and 2010), TENDL (2013-2015) and experimental data from EXFOR, in order to have a first overview of TENDL quality. Finally, Subsection 4.4 is devoted to provide recommendation about the activation library to be used for the estimation of the SDDR in ITER.

Table 4.13. QS description [23].

QS	Description
0	No experimental data exists
1	Limited differential data which disagrees with the library (weak disagreement)
2	Limited differential data which agrees with the library (weak agreement)
3	Differential data which disagrees with the library (strong disagreement)
4	Differential data which agrees with the library (strong agreement)
5	Both differential and integral data exist or only integral data exist and these are not in agreement with the library
5_0	Differential data are missing and unsatisfactory agreement with integral data
5_1	Unsatisfactory agreement with differential and integral data
5_2	Satisfactory agreement with differential and unsatisfactory agreement with integral data
5_3	Differential data are missing and satisfactory agreement with integral data
5_4	Unsatisfactory agreement with differential and satisfactory agreement with integral data
6	Both differential and integral data exist and they are in agreement with the library (validation)

4.1. Quality classification of the EAF-2007 activation cross sections data for main pathways

This section is devoted to provide a quality classification of the total activation cross sections from EAF-2007 for the relevant pathways previously identified. In order to qualify these reactions, reference [24] was used, which provides QS for 470 reactions of EAF-2007. Table 4.14 shows major radionuclides and pathways justified as relevant in Sections 3.1 and 3.2 as well as the corresponding QS (taken from [24]).

As can be seen in Table 4.14, 27 reactions are scored as: 6, 6*, (6), 5, (5), (5)* and 18 reactions are not included in this reference [24]. Q=6 indicates that the reaction is validated (differential and integral) and QS=(6) signifies total cross section validated. Reactions with QS=5, 5* or (5)* means: *"reactions that should be considered for new measurements by experimentalists"*. It is important to note that for reactions classified with 5 additional scores are available. In this case, all reactions with QS=5 are classified at the same time with 5_2, which implies "*satisfactory agreement with differential and unsatisfactory agreement with integral data*" [23].

Table 4.14. QS for main cross section reactions for SDDR calculation (-, not included in [24]).

Pathway	QS	Pathway	QS	Pathway	QS
$^{23}Na(n,g)^{24}Na$	(6)	$^{59}Co(n,g)^{60}Co$	(6)	$^{132}Ba(n,g)^{133}Ba$	-
$^{24}Mg(n,p)^{24}Na$	(5)*	$^{60}Ni(n,p)^{60}Co$	(6)	$^{134}Ba(n,2n)^{133}Ba$	-
$^{27}Al(n,a)^{24}Na$	(6)	$^{63}Cu(n,a)^{60}Co$	(6)	$^{134}Ba(n,g)^{135m}Ba$	-
$^{41}K(n,g)^{42}K$	6*	$^{58}Ni(n,2n)^{57}Ni$	6	$^{135}Ba(n,n')^{135m}Ba$	-
$^{50}Cr(n,g)^{51}Cr$	-	$^{63}Cu(n,g)^{64}Cu$	5	$^{136}Ba(n,2n)\ ^{135m}Ba$	6
$^{52}Cr(n,2n)^{51}Cr$	6	$^{64}Zn(n,g)^{65}Zn$	-	$^{151}Eu(n,g)^{152}Eu$	-
$^{54}Fe(n,a)^{51}Cr$	6	$^{66}Zn(n,2n)^{65}Zn$	-	$^{153}Eu(n,g)^{154}Eu$	-
$^{55}Mn(n,2n)^{54}Mn$	6	$^{93}Nb(n,2n)^{92m}Nb$	6	$^{159}Tb(n,g)^{160}Tb$	-
$^{54}Fe(n,p)^{54}Mn$	6	$^{92}Mo(n,p)^{92m}Nb$	6	$^{181}Ta(n,g)^{182}Ta$	(6)
$^{55}Mn(n,g)^{56}Mn$	6	$^{107}Ag(n,2n)^{106m}Ag$	-	$^{182}W(n,p)^{182}Ta$	(6)
$^{58}Fe(n,g)^{59}Fe$	6	$^{109}Ag(n,g)\ ^{110m}Ag$	-	$^{183}W(n,D)^{182}Ta$	-
$^{59}Co(n,p)^{59}Fe$	6	$^{123}Sb(n,g)^{124}Sb$	-	$^{180}W(n.g)^{181}W$	-
$^{62}Ni(n,a)^{59}Fe$	6*	$^{124}Sn(n,g)^{125}Sn(B^-)^{125}Sb$	-	$^{182}W(n,2n)^{181}W$	6
$^{59}Co(n,2n)^{58}Co$	(5)	$^{133}Cs(n,g)^{134}Cs$	-	$^{186}W(n,g)^{187}W$	6
$^{58}Ni(n,p)^{58}Co$	(6)	$^{130}Ba(n,g)^{131}Ba$	-	$^{204}Pb(n,2n)^{203}Pb$	(6)

Regarding reactions appearing in Table 4.14 without any reported QS, it is necessary to underline that most of them are pathways for radionuclides coming from the activation of L2N or barite concrete, which presence in ITER is not defined yet and are only a possible option.

4.2. Quality scoring comparison between EAF-2007 and EAF-2010 for split and total reactions

Once the QS for EAF-2007 cross section provided by reference [24] had been seen, the question of whether this qualification is improved in the next version of EAF (EAF-2010) arose. In this case, there is not an EAF-2010 report providing QS for the total cross section, but one providing QS for the split reactions [37]; that is, each of the reactions that produce the same daughter nuclide but with different isomeric state. This report has an analogous one for EAF-2007 [36]. This section is devoted to compare both qualifications.

Table 4.15 provides a comparison of the QS for total reactions (taken from [24]) with those for the split ones (taken from [36]-[37]). This information can be misunderstood for that very reason, because some scores are referred to partial reactions and others to the total and, therefore, scores from [36] and [37] are sometimes different from those provided by [24]. This section also justifies which score (total or split) is the most convenient to be taking into account for each reaction.

Table 4.15. QS for EAF-2007 and EAF-2010 cross sections [24], [36]-[37] (-, not included in [24]).

Reaction	Product	Half-life	Cooling time of interest	EAF-2007	Total cross section	EAF-2010
^{50}Cr(n,g)	^{51}Cr	27.7 d	1, 12 days	4	-	4
^{64}Zn(n,g)	^{65}Zn	243.8 d	12	4	-	4
^{66}Zn(n,2n)	^{65}Zn	243.8 d	12	4	-	4
^{107}Ag(n,2n)	^{106m}Ag	8.3 d	1, 12 days	4	-	4
^{109}Ag(n,g)	^{110m}Ag	249.8 d	1, 12 days	4	-	4
^{123}Sb(n,g)	^{124g}Sb	60.2 d	1, 12 days	4	-	4
	^{124m}Sb	93 s		2		2
	^{124n}Sb	20.2 min		2		2
^{124}Sn(n,g)^{125}Sn(B$^-$)	^{125g}Sn	9.6 d	12 days	2	-	2
	^{125m}Sn	9.5 min		4		4
^{133}Cs(n,g)	^{134g}Cs	2.1 y	1, 12 days	4	-	4
	^{134m}Cs	2.9 h		3		3
^{130}Ba(n,g)	^{131g}Ba	11.5 d	1 day	2	-	2
	^{131m}Ba	14.6 min		2		2

Reaction	Product	Half-life	Cooling time of interest	EAF-2007	Total cross section	EAF-2010
^{132}Ba(n,g)	^{133g}Ba	10.6 y	1 day	2	-	2
	^{133m}Ba	38.9 h		2		2
^{134}Ba(n,2n)	^{133g}Ba	10.6 y	1 day	3	-	3
	^{133m}Ba	38.9 h		6		6
^{134}Ba(n,g)	^{135m}Ba	22.7 h	1 day	4	-	4
^{135}Ba(n,n')	^{135m}Ba	22.7 h	1 day	2	-	2
^{151}Eu(n,g)	^{152g}Eu	13.5 y	12 days	2	-	2
	^{152m}Eu	9.3 h		5	5	5
	^{152n}Eu	96 min		2	-	2
^{153}Eu(n,g)	^{154g}Eu	8.6 y	12 days	4	-	4
	^{154m}Eu	46.3 min		0		0
^{159}Tb(n,g)	^{160}Tb	72.3 d	12 days	4	-	4
^{183}W(n,D)	^{182g}Ta	114.7 d	12 days	0	-	0
	^{182m}Ta	283 ms		0		0
	^{182n}Ta	15.8 min		0		0
^{180}W(n,g)	^{181}W	121.2 d	12 days	4	-	4
^{24}Mg(n,p)	^{24g}Na	15.0 h	1 day	0	(5)*	0
	^{24m}Na	20.2 ms		0		0
^{59}Co(n,2n)	^{58g}Co	70.9 d	1, 12, 21 days	2	(5)	2
	^{58m}Co	9.1 h		5		6
^{63}Cu(n,g)	^{64}Cu	12.7 h	1 day	5	5	5
^{23}Na (n,g)	^{24g}Na	15.0 h	1 day	2	(6)	2
	^{24m}Na	20.2 ms		2		2
^{27}Al(n,a)	^{24g}Na	15.0 h	1 day	2	(6)	2
	^{24m}Na	20.2 ms		2		2
^{59}Co(n,g)	^{60g}Co	1925.3 d	1, 12, 21 days	0	(6)	0
	^{60m}Co	10.47 min		5		5
^{58}Ni(n,p)	^{58g}Co	70.9 d	1, 12, 21 days	4	(6)	4
	^{58m}Co	9.1 h		4		4
^{60}Ni(n,p)	^{60g}Co	1925.3 d	1, 12, 21 days	4	(6)	4
	^{60m}Co	10.47 min		6		6
^{63}Cu(n,a)	^{60g}Co	1925.3 d	12, 21 days	3	(6)	3
	^{60m}Co	10.47 min		4		4
^{181}Ta(n,g)	^{182g}Ta	114.7 d	1, 12, 21 days	6	(6)	6
	^{182m}Ta	283 ms		2		2

Reaction	Product	Half-life	Cooling time of interest	EAF-2007	Total cross section	EAF-2010
	^{182n}Ta	15.8 min		5		6
^{182}W(n,p)	^{182g}Ta	114.7 d	12, 21 days	2	(6)	2
	^{182m}Ta	283 ms		4		4
	^{182n}Ta	15.8 min		4		4
^{204}Pb(n,2n)	^{203g}Pb	51.9 h	1, 12 days	2	(6)	2
	^{203m}Pb	6.2 s		5		5
	^{203n}Pb	480 ms		2		2
^{41}K(n,g)	^{42}K	12.3 h	1 day	4	6*	6
^{62}Ni(n,a)	^{59}Fe	44.5 d	12 days	5	6*	6
^{52}Cr(n,2n)	^{51}Cr	27.7 d	12 days	6	6	6
^{54}Fe(n,a)	^{51}Cr	27.7 d	12 days	6	6	6
^{55}Mn(n,2n)	^{54}Mn	312.1 d	1, 12, 21 days	6	6	6
^{54}Fe(n,p)	^{54}Mn	312.1 d	1, 12, 21 days	6	6	6
^{55}Mn(n,g)	^{56}Mn	2.6 h	1 day	6	6	6
^{58}Fe(n,g)	^{59}Fe	44.5 d	1, 12 days	6	6	6
^{59}Co(n,p)	^{59}Fe	44.5 d	12 days	6	6	6
^{58}Ni(n,2n)	^{57}Ni	35.6 h	1 day	6	6	6
^{93}Nb(n,2n)	^{92m}Nb	10.2 d	12 days	6	6	6
^{92}Mo(n,p)	^{92m}Nb	10.2 d	12 days	6	6	6
^{136}Ba(n,2n)	^{135m}Ba	22.7 h	1 day	6	6	6
^{182}W(n,2n)	^{181}W	121.2 d	12 days	6	6	6
^{186}W(n,g)	^{187}W	24.0 h	1, 12 days	6	6	6

All metastable isotopes of Table 4.15 decay by isomeric transition to ground state at least in 99.76% (except in the ^{124m}Sb case, 75%). The only exceptions are ^{125m}Sn and ^{152m}Eu, which do not decay to the ground, and only the split cross section reaction for the ground state (and to the second metastable in the ^{152}Eu case) should be studied. Additionally the decay process for these radionuclides does not emit photons.

Comments regarding reactions with QS not included in [24] are given in the following paragraphs:

- ^{50}Cr(n,g)^{51}Cr: there is not production of metastable states. This reaction cross section has a score of 4 on both EAF-2007 and EAF-2010; that is, there are differential experiments which are in agreement with the library, despite having no integral data.

The same occurs for $^{64}Zn(n,g)^{65}Zn$, $^{66}Zn(n,2n)^{65}Zn$, $^{107}Ag(n,2n)^{106m}Ag$, $^{109}Ag(n,g)^{110m}Ag$, $^{159}Tb(n,g)^{160}Tb$, and $^{180}W(n,g)^{181}W$ cross sections.

- $^{123}Sb(n,g)^{124}Sb$: three final states (ground and metastable) are produced. Both EAF-2007 and EAF-2010 provide the same QS for the three split reactions, i.e. 4 for the one leading to the ground state and 3 for the two leading to both metastable isotopes. On the other hand, taking into account that the half-lives for the metastable isotopes are very low (on the order of seconds and minutes), at the cooling times considered in this chapter (from 1 day to largest cooling times) it would only be necessary to consider the total cross section, which as can be seen, does not have any QS provided. This situation is analogous to that for $^{133}Cs(n,g)^{134}Cs$ or $^{130}Ba(n,g)^{131}Ba$. In these last cases, two final states (ground and metastable) are generated and both EAF-2007 and EAF-2010 give the same QS for both cross sections leading to the two states. Moreover, as happened with the cross section for the $^{123}Sb(n,g)^{124}Sb$ reaction, taking into account the involved half-lives for the metastable states, and the cooling times of interest (1 and 12 days and even 21 days) it would only be needed to consider the total cross section.

- $^{124}Sn(n,g)^{125}Sn$: two final states are produced. However, as it has been previously said, the ^{125m}Sn do not decay to the ground, and only the split cross section reaction for the ground state should be considered, which has a QS of 2 in both EAF libraries.

- $^{132}Ba(n,g)^{133}Ba$: two final states (ground and metastable) are produced. The QS for split reactions is 2 in both EAF-2007 and EAF-2010. Taking into account that ^{133}Ba is a relevant nuclide at 1-day cooling period and the fact that the half-life for ^{133m}Ba is 38.9 hours, it is necessary to have both cross sections for split reactions very accurate, not only in the total one. Something similar occurs in the $^{134}Ba(n,2n)^{133}Ba$ reaction. However, for this last reaction, cross section for the metastable split has a QS of 6 while cross section for the reaction leading to the ground state has a poor rating (3) in both EAF libraries.

- $^{151}Eu(n,g)^{152}Eu$: three final states are generated. Taking into account that the ^{152m}Eu do not decay to the ground state, only the split cross section reaction for the ground and second metastable production should be studied. These can be considered grouped since the half-life of the second metastable is very low.

- $^{153}Eu(n,g)^{154}Eu$: two final states appear and, for each of them, the QS provided in both EAF is the same (4 for the production of the ground state and 0 for the metastable). Considering the low half-life of the ^{154m}Eu (46.3 min) compared to the cooling time of interest, only the total cross section should be taken into account.

- $^{183}W(n,D)^{182}Ta$: three final states are produced and the three split cross section reactions have the same QS (i.e. o) in both EAF versions. Once again, taken into account the half-lives of the metastable state and the fact that their isomeric transition to the ground state is almost 100%, only the total cross section must be considered.

Regarding not validated cross section reactions (QS=5, (5) and (5)* according to [24]):

- $^{24}Mg(n,p)^{24}Na$. There are two products: ^{24g}Na and ^{24m}Na. EAF-2007 and EAF-2010 provide a score of 0 (no experimental data exit) for the cross section of both split reactions. In any case, as the half-life of ^{24m}Na is milliseconds, it is not necessary to take into account the status of the split reaction, and the only important QS is that for the total reaction. This QS for the total reaction is scored as QS=(5)* according to [24] and specifically, with a 5_2, which means: satisfactory agreement with differential and unsatisfactory agreement with integral data. This statement refers to the total cross section as the QS included parentheses. Also, by having an asterisk, it is known that there has been an upgrade in the later EAF version (2010).

- $^{59}Co(n,2n)^{58}Co$: both ground and metastable states are produced. However, although Co58m decays to the ground state, its half-life (~9 hours) is relevant compared to some of our cooling times of interest (1 day cooling), so the split reactions cannot be disregarded towards the total. In this case, split reaction for the production of the ground state has QS=2; that is, there are limited differential data in agreement with the library. The QS for the split reaction leading to the metastable state has been improved from 5 (EAF-2007) to 6 (EAF-2010). Hence, some work should be done in both EAF in order to improve the split reaction producing the ground state.

- $^{63}Cu(n,g)^{64}Cu$: a single reaction appears leading to the ground state. The QS provided by EAF-2007 and EAF-2010 for the cross sections of this reaction are the same as reference [24]: 5 and, specifically, 5_2.

With regard to the reactions qualified with (6) in reference [24]; that is, total reaction validated, for all of them ground and metastable states are produced. Considering that in all cases (except for $^{58}Ni(n,p)^{58}Co$ reaction) the half-lives of the metastable nuclides are very small compared to the analyzed cooling times and these metastable nuclides decay to the ground state, it is not necessary to distinguish between the reaction leading to the ground state and that leading to metastable states. Therefore, it is only necessary to consider the total one and those are validated.

For the reaction $^{58}Ni(n,p)^{58}Co$, QS for the two isomeric states are given. Furthermore, as it has been said, ^{58m}Co has a relevant half-life compared to our times of interest. Total reaction

score (validated) should be considered for all the reports and calculations which deal with cooling times of 12 days (PI) and 21 days (HCF). For one day cooling time, split reactions need to be considered and these are scored as QS=4 in the EAF-2007 as well as in EAF-2010 libraries.

Regarding the reactions with QS=6 according to reference [24], no metastable states are produced for any of them and both EAF libraries (2007 and 2010) provide the same rating. Therefore, all the cross sections for these reactions are considered validated.

In the case of $^{41}K(n,g)^{42}K$ reaction, scored as 6*, EAF-2007 gave a QS=4 and, as expected, EAF-2010 had improved this score to a 6. This improvement is due to new integral experiments available for the validation of the EAF-2010 library. Cross section for the $^{62}Ni(n,a)^{59}Fe$ reaction is also improved in the EAF-2010 from the previous version (EAF-2007) where the QS was 5.

4.3. Status of TENDL library for considered pathways

This section is devoted to assess the status of the TENDL library (namely 2013, 2014 and 2015 versions) for those cross sections pathways selected as relevant in Section 3.3.

It is important to highlight that TENDL also started making efforts in order to provide some cross section quality in the 2009 version [38]. For later versions, specifically TENDL-2012 and TENDL-2013, there are benchmarks focused on safety. Additionally, for TENDL-2012 there is a validation report for decay heat [39]. However, for 2013, 2014 and 2015 TENDL versions there are not validation works found as relevant for maintenance activities in ITER.

For this analysis two subsections have been considered: one for the evaluation of those cross sections qualified as validated in EAF library and the second one for the remaining.

4.3.1. Status of TENDL library for those pathways validated in EAF library

This subsection is devoted to assess the status of the TENDL library (2013, 2014 and 2015 versions) for those cross sections with QS of 6 in the EAF library, in order to provide conclusions about the status of TENDL when compared to the mentioned EAF library (both versions). For this analysis, cross sections as a function of neutron energy are plotted and the different libraries are compared among themselves as well as with differential experimental data from EXFOR using the JANIS display software (version 4.0) [25].

In 20 of 25 validated cross section reactions, the use of any of the considered libraries would lead to similar results (therefore, no graph is provided). However, some differences are found between EAF and TENDL, whatever is the version used, in five of the pathways. For these cases, EAF libraries are preferred since some problems are detected in TENDL libraries:

- $^{54}Fe(n,a)^{51}Cr$ (Figure 4.4). For this reaction resonances are not included in any of the TENDL versions.
- $^{55}Mn(n,2n)^{54}Mn$ (Figure 4.5). In this case cross section reactions differences between EAF and TENDL are found to be in a factor of ~2.
- $^{58}Ni(n,p)^{58}Co$ (Figure 4.6). For this cross section, differences at low energy values are detected among the EAF and TENDL libraries.

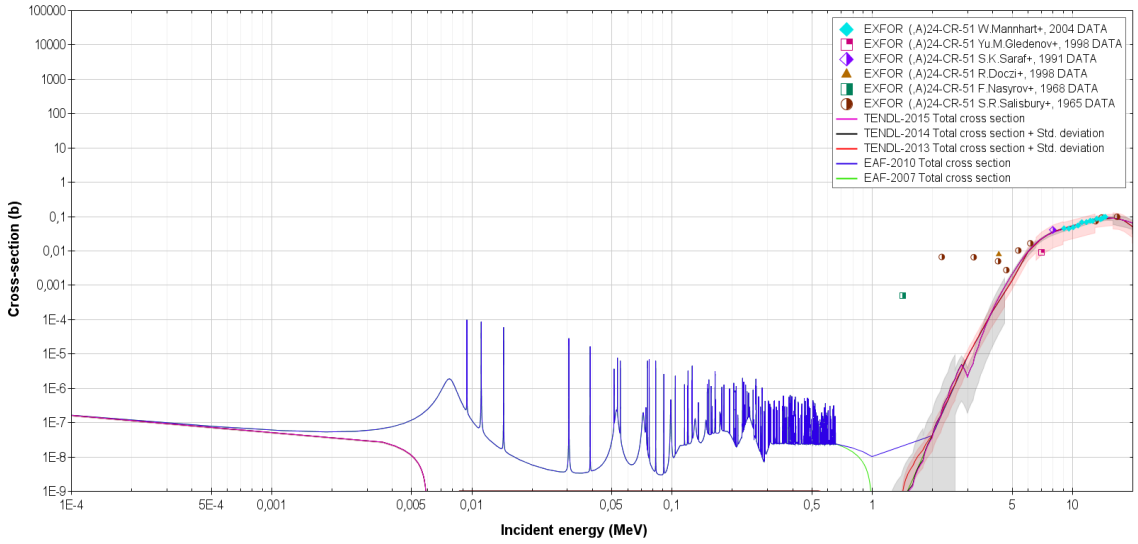

Figure 4.4. Cross section for $^{54}Fe(n,a)^{51}Cr$ reaction.

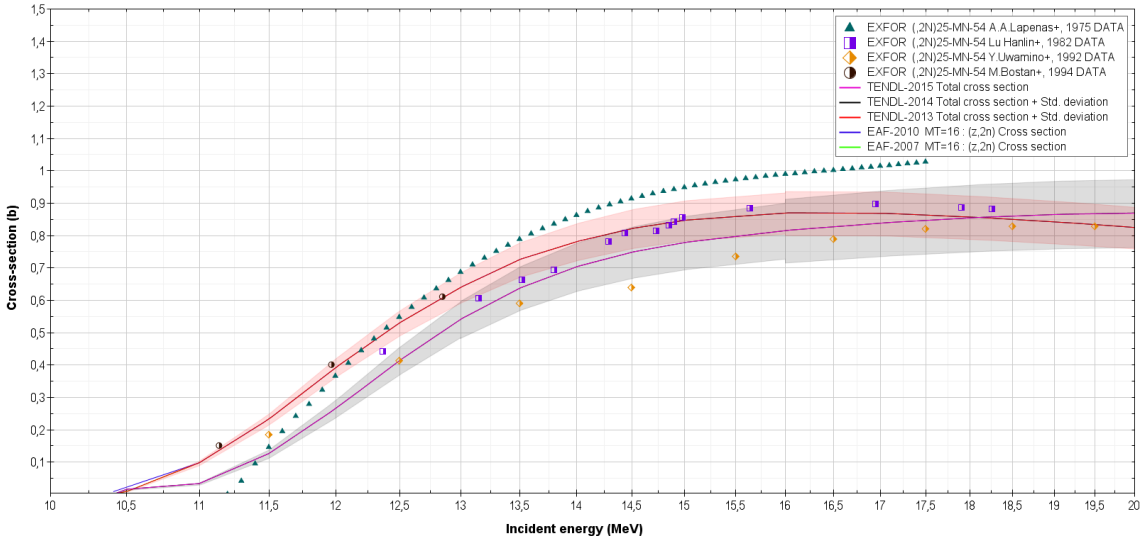

Figure 4.5. Cross section for $^{55}Mn(n,2n)^{54}Mn$ reaction.

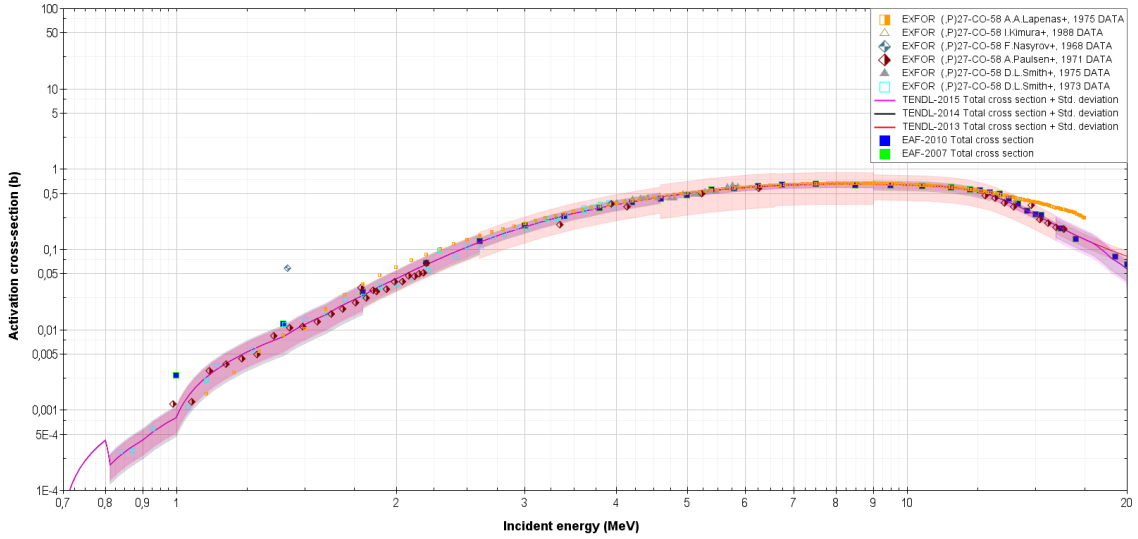

Figure 4.6. Cross section for ^{58}Ni(n,p)^{58}Co reaction.

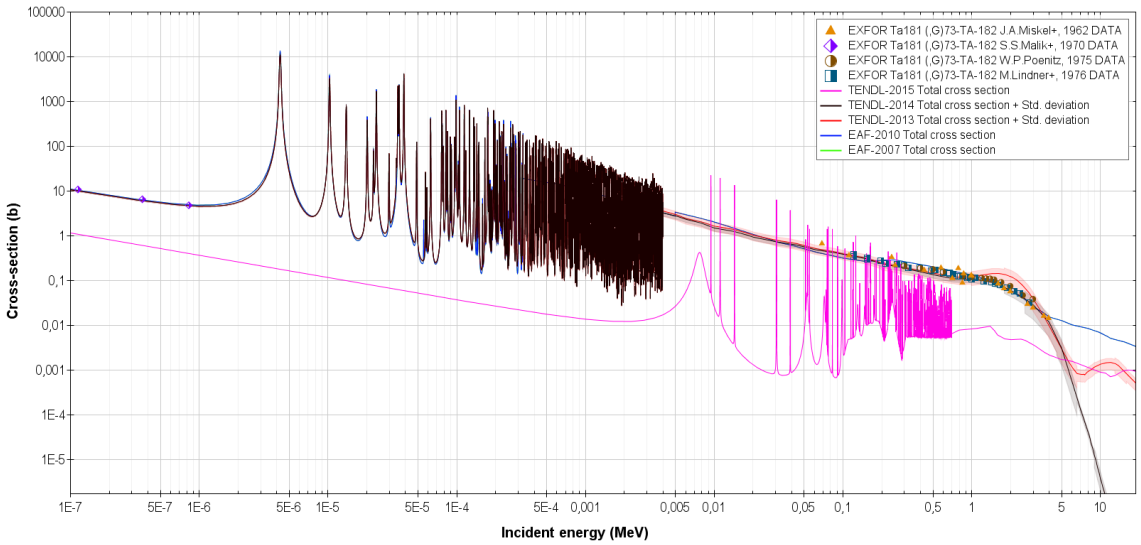

Figure 4.7. Cross section for ^{181}Ta(n,g)^{182}Ta reaction (EAF-2007 and EAF-2010 are superimposed).

- ^{181}Ta(n,g)^{182}Ta (Figure 4.7). In this case both EAF versions are coincident while TENDL versions provide significant differences among the three versions, being TENDL-2015 much lower than any of the former.

- ^{41}K(n,g)^{42}K (Figure 4.8). TENDL-2013 provides lower values than any of the other libraries in the 1/v energy range. This range is especially important since ^{42}K comes from the L2N concrete which is a bioshield plug candidate and, thus, it is exposed to low energy neutrons. For energies higher than 1 MeV EAF-2010 presents discrepancies from other libraries. However, as already mentioned, this energy range is less important from the point of view of the studied application.

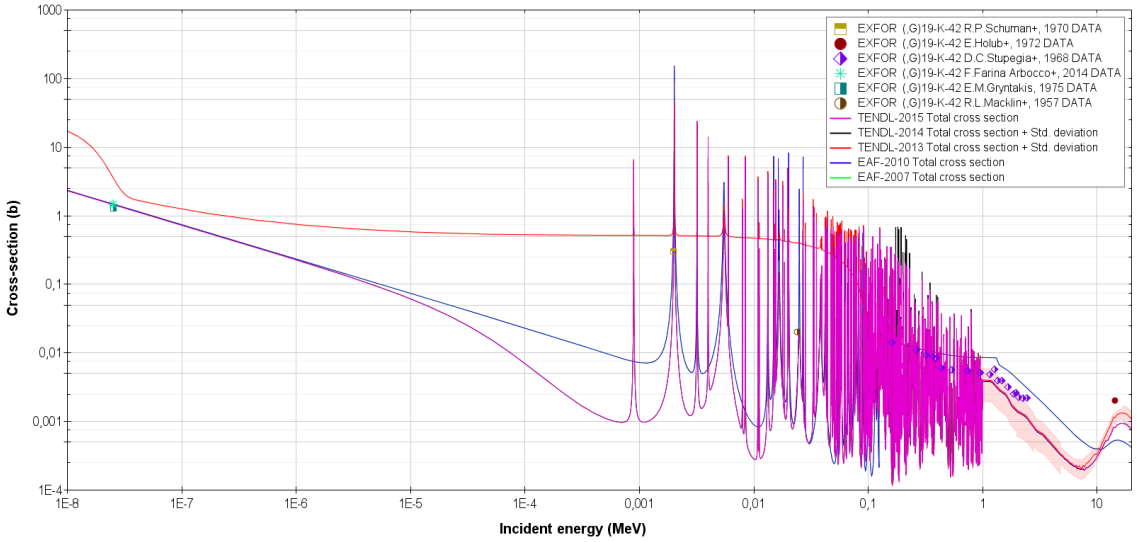

Figure 4.8. Cross section for $^{41}K(n,g)^{42}K$ reaction.

4.3.2. Status of TENDL library for those pathways with a poor or not provided QS in EAF library

The aim of this section is to give a first approach to the status of those cross sections not validated in the EAF library, in the 2013, 2014 and 2015 TENDL versions. To achieve this goal, the same procedure as in the previous section was followed: graphs for cross sections are plotted (Figure 4.9-Figure 4.32) and compared using the JANIS display software (version 4.0). Comments on Figure 4.9-Figure 4.32 are the following:

- $^{24}Mg(n,p)^{24}Na$, scored as (5)* (Figure 4.9): there are certain discrepancies between the EAF-2007 and experimental data in some energy ranges (~6.5-7 and ~8-13 MeV). However, these differences are corrected in the updated libraries EAF-2010, TENDL-2013, TENDL-2014 and TENDL-2015, which perfectly fit the experiments. Therefore, it is not necessary to work on improving the total cross section for this reaction.

- $^{59}Co(n,2n)^{58}Co$, scored as (5) (Figure 4.10): Both EAF are coincident and both have slight discrepancies with all the TENDL versions (2013, 2014 and 2015), which provide the same values. However, these differences between EAF and TENDL libraries are not significant compared to experimental data. With regard to the need of more differential experiments, for the total cross section is not necessary according to this figure. However, as the score provided was 5_2 (see Section 4.2), it is advisable to provide more integral experiments [24].

  On the other hand, and according to Section 4.2, it would be useful additional experiments for the ground state split reaction since it has a QS of 2 in both EAF

libraries and its contribution to the total production of ^{58}Co is relevant (around 30%). In order to corroborate this necessity, Figure 4.11 represents the cross section for the production of the ground state. As it can be seen, experimental values are lower than EAF and TENDL libraries. Furthermore, differences are appreciated between the different versions of TENDL as well as between EAF and TENDL libraries.

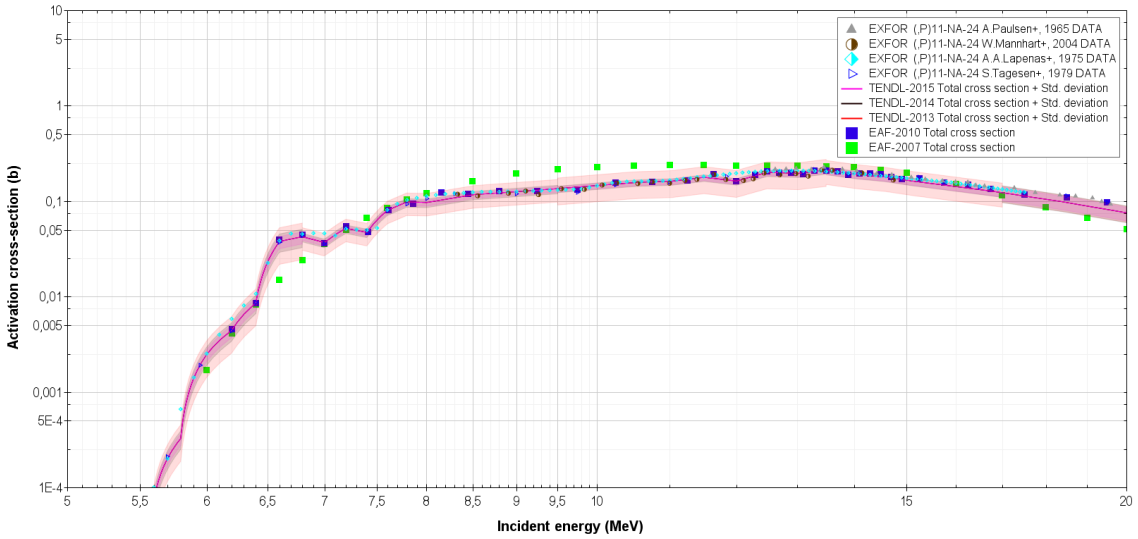

Figure 4.9. Cross section for ^{24}Mg(n,p)^{24}Na reaction: (5) (TENDL-2013, TENDL-2014 and TENDL-2015 are superimposed) [18].*

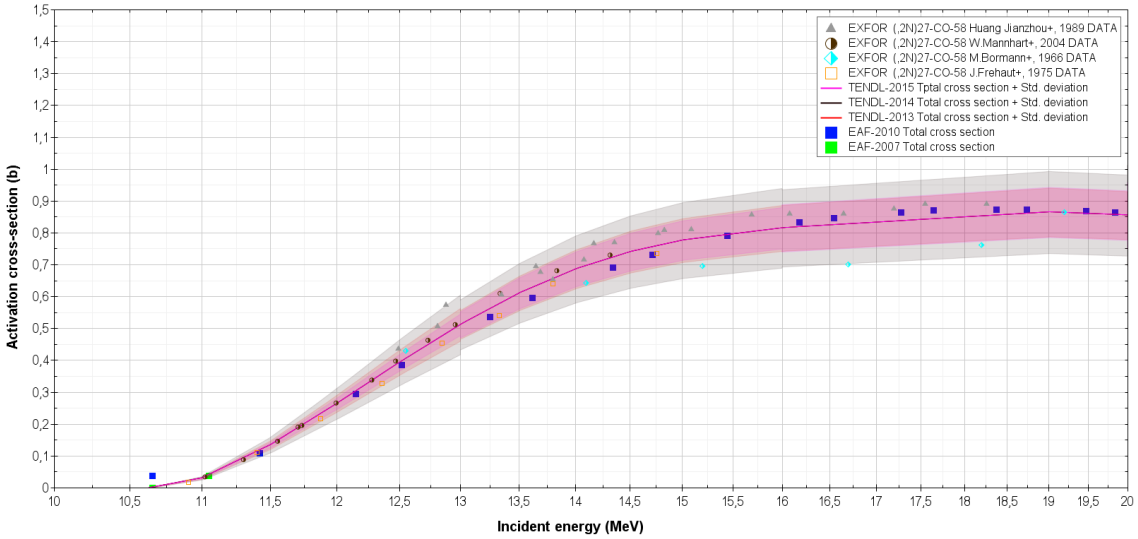

Figure 4.10. Cross section for ^{59}Co(n,2n)^{58}Co reaction: (5) (EAF-2007 and EAF-2010 are superimposed; TENDL-2013, TENDL-2014 and TENDL-2015 are superimposed) [18].

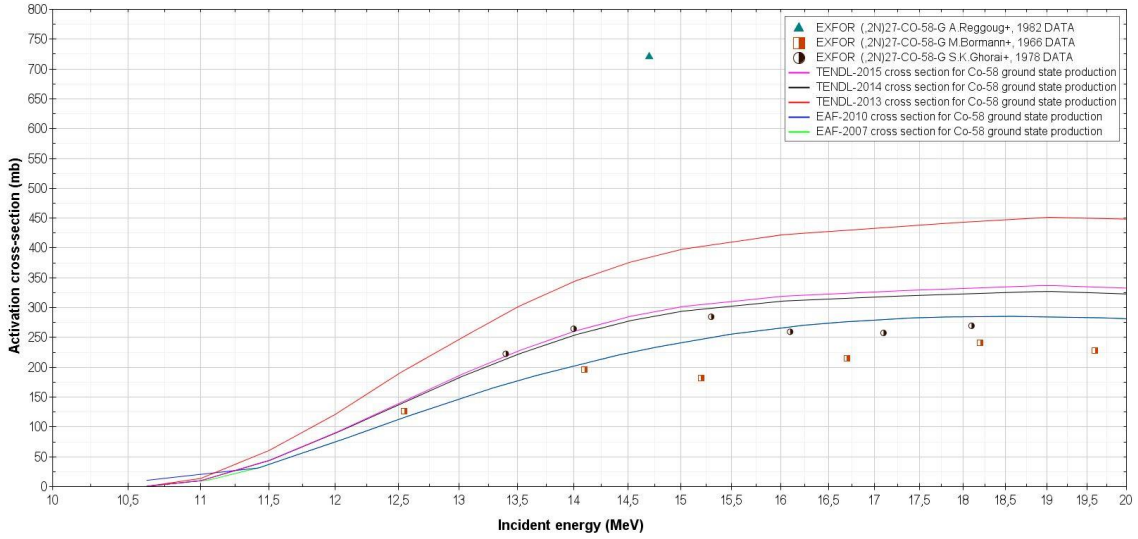

Figure 4.11. Cross section for $^{59}Co(n,2n)^{58g}Co$ reaction (EAF-2007 and EAF-2010 are superimposed) [18].

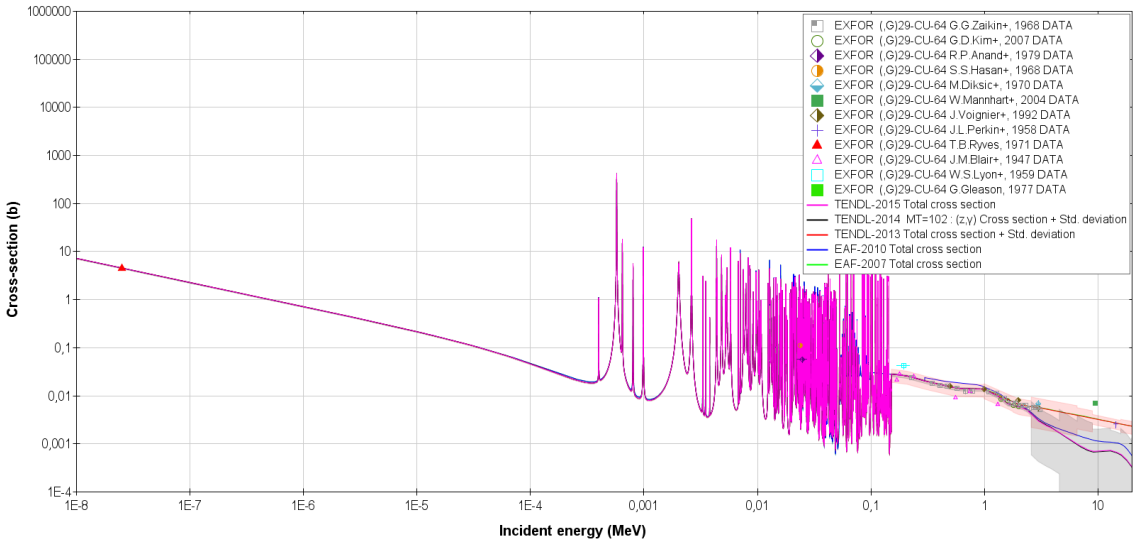

Figure 4.12. Cross section for $^{63}Cu(n,g)^{64}Cu$ reaction: 5 (EAF-2007 and TENDL-2013 are superimposed; TENDL-2014 and TENDL-2015 are superimposed) [18].

- $^{63}Cu(n,g)^{64}Cu$, scored as 5: Figure 4.12 shows that there are few measurements above 5 MeV. Also, for energies higher than 3 MeV there are differences between EAF-2007, EAF-2010 and TENDL-2014 (TENDL-2015 coincides with TENDL-2014). Furthermore TENDL-2013 matches EAF-2007 in the whole range of energies up to 20 MeV, adjusting better to the experimental data above 3 MeV than EAF-2010 and TENDL-2014 (and thus TENDL-2015) do. In conclusion, additional experimental data are recommended.

Regarding reactions with no QS provided by reference [24], it is worth mentioning that in most of the cases, they are reactions for the production of radionuclides such as ^{133}Cs, ^{131}Ba or

^{160}Tb, which come from the activation of candidate materials to be part of the shielding, and only a few are for the production radionuclides, such as ^{51}Cr, coming from the activation of materials that are currently in the ITER model. The following comments are underlined for these reactions:

- ^{50}Cr(n,g)^{51}Cr. Figure 4.13 shows that EAF-2007 and EAF-2010 are coincident while TENDL-2013 and TENDL-2014 differ from 0.8 MeV and 4 MeV, respectively. TENDL-2015 perfectly matches TENDL-2014. Worth mentioning that both EAF-2007 and EAF-2010 are not even in the band of standard deviation for TENDL-2013 but all libraries are included in the band of standard deviation for TENDL-2014. On the other hand, there is a good agreement with data lower than 1 MeV and significant uncertainties in experiments. There is a lack of experimental data for energies higher than 1 MeV. Therefore, it is advisable to work on improving this cross section.

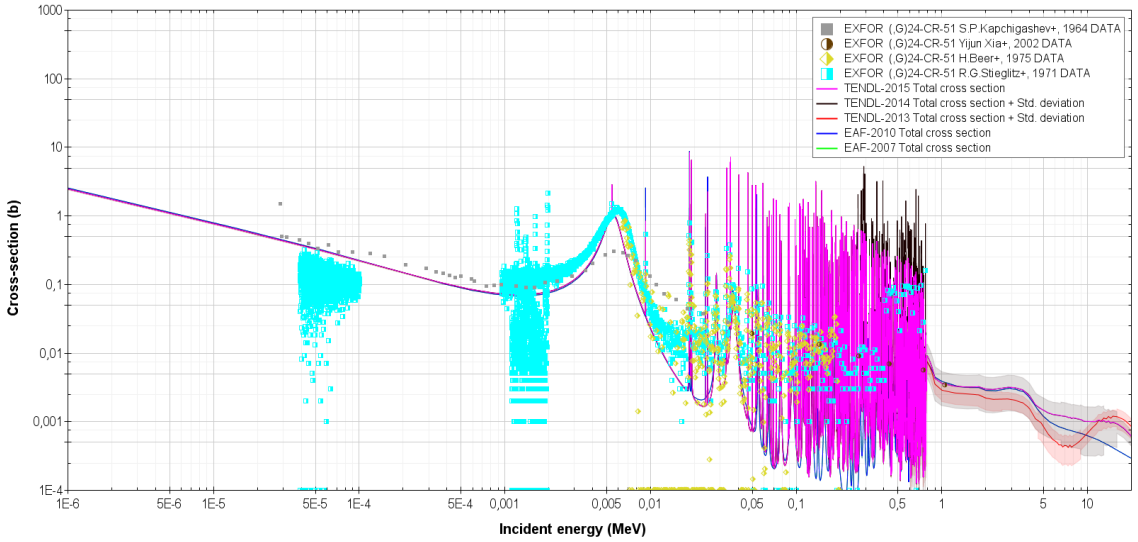

Figure 4.13. Cross section for ^{50}Cr(n,g)^{51}Cr reaction (EAF-2007 and EAF-2010 are superimposed; TENDL-2014 and TENDL-2015 are superimposed) [18].

- ^{64}Zn(n,g)^{65}Zn. It is plain to see in Figure 4.14 that EAF (both versions) and TENDL (2013-2015 versions) provide similar values until 1.3 MeV, value from which libraries start to differ, providing TENDL higher rates. Despite available experiments are in agreement with all the libraries, no experimental data are found for energies higher than 1 MeV, making difficult to draw any conclusion about the best evaluated cross section.

- ^{66}Zn(n,2n)^{65}Zn. In this case Figure 4.15 reveals that both EAF are coincident from 12 MeV onwards. Meanwhile all TENDL versions are coincident and provide lower values for this cross section than EAF does. Regarding the available experiments, they are

enough and in agreement with the libraries. However, since some of them fit better to one library than to another and vice versa, they are not conclusive when it comes to decide which is better.

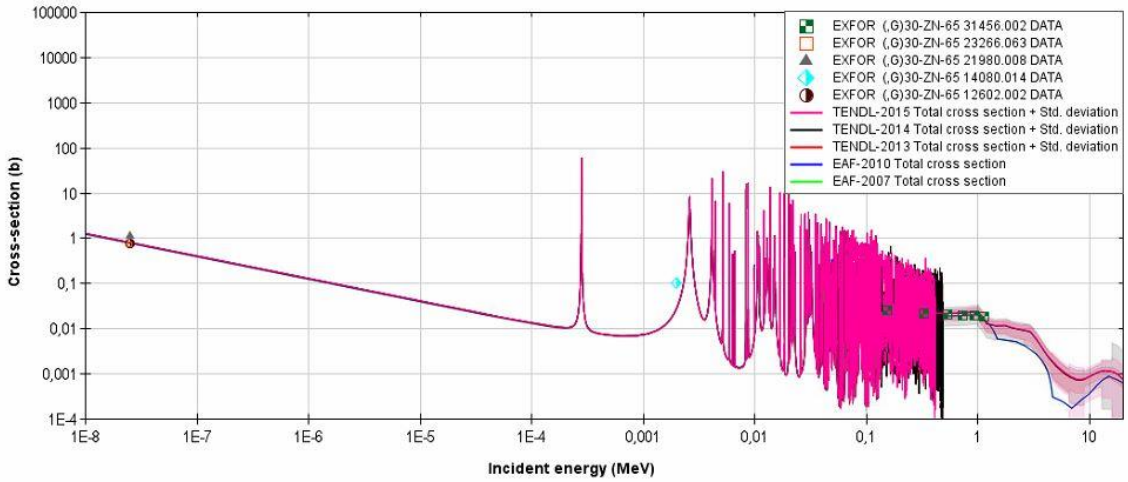

Figure 4.14. Cross section for $^{64}Zn(n,g)^{65}Zn$ reaction (EAF-2007 and EAF-2010 are superimposed; TENDL-2013, TENDL-2014 and TENDL-2015 are superimposed).

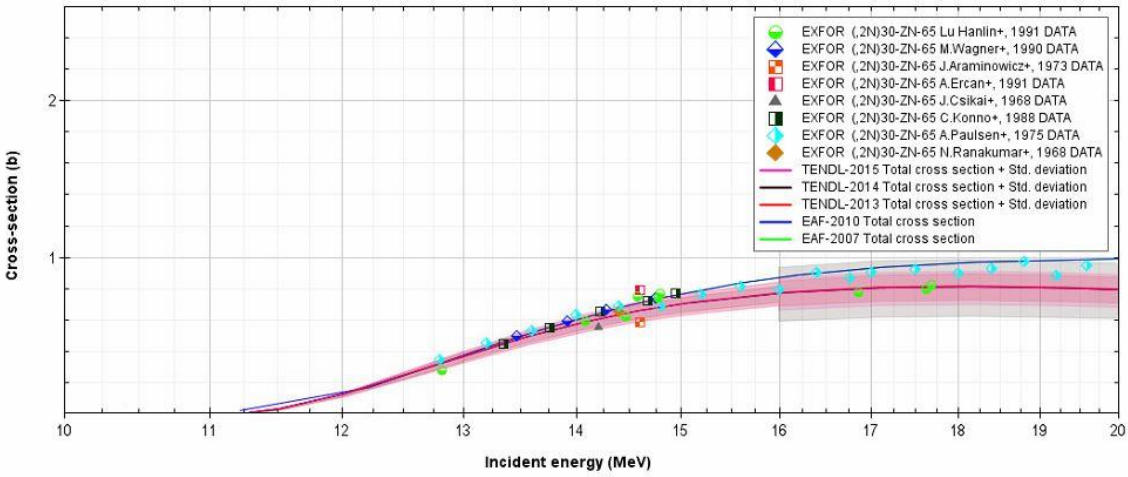

Figure 4.15. Cross section for $^{66}Zn(n,2n)^{65}Zn$ reaction (TENDL-2013, TENDL-2014 and TENDL-2015 are superimposed).

- $^{107}Ag(n,2n)^{106m}Ag$. Figure 4.16 shows both EAF are coincident from 10.3 MeV onwards while EAF-2007 and TENDL-2013 are coincident in all the energy range. There are differential experimental data at all energies but, those below 13 MeV, are few and lower than the values provided by the library.

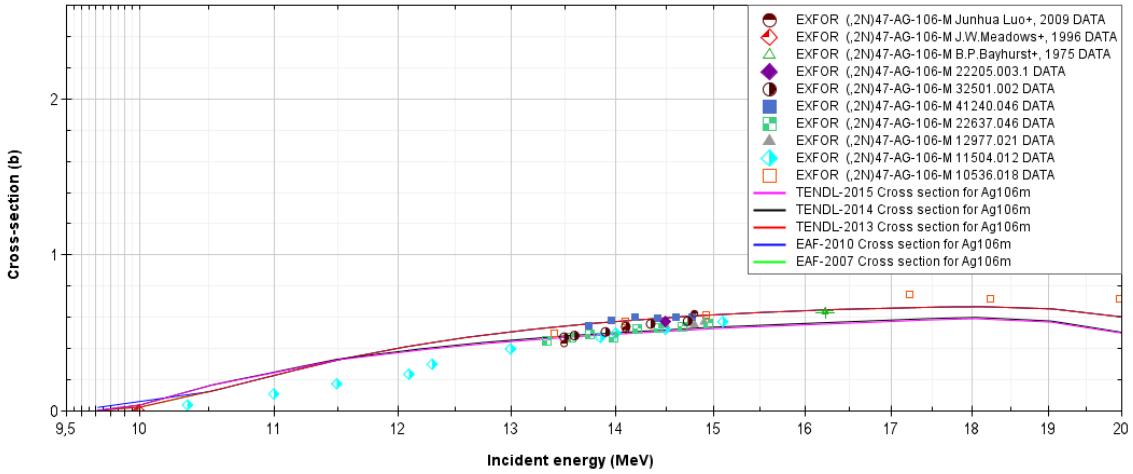

Figure 4.16. Cross section for $^{107}Ag(n,2n)^{106m}Ag$ reaction (EAF-2007 and TENDL-2013 are superimposed).

- $^{109}Ag(n,g)^{110m}Ag$. Figure 4.17 exposes that in general, TENDL-2013 is the library with the lowest values for this cross section, except at 5 MeV and around values, when TENDL-2014 (and 2015) replaces it. On the other hand, both TENDL-2014 and 2015 give the highest values in the range 0.01-3 MeV. Experiments in the 1/v area show better agreement with all the libraries but TENDL-2013 while there are not experiments in the resonance area. For higher energies experiments are not concluding.

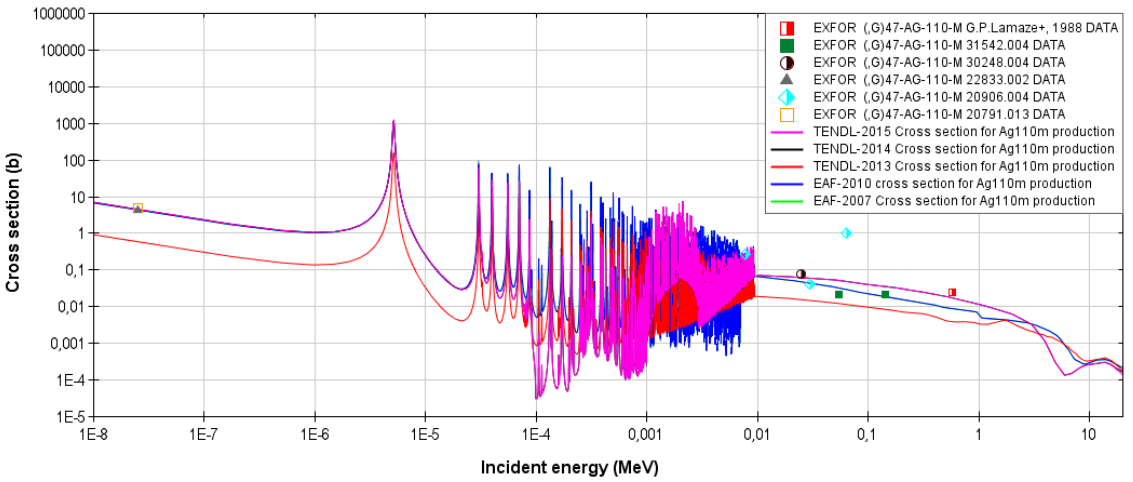

Figure 4.17. Cross section for $^{109}Ag(n,g)^{110m}Ag$ reaction (TENDL-2014 and TENDL-2015 are superimposed).

- $^{123}Sb(n,g)^{124}Sb$. Figure 4.18 indicates that there is practically no difference among the libraries. With regard to the experimental data, a need of additional differential experiments for energies higher than 3 MeV is detected since there is only one, with a much higher value. The remaining experiments are in good agreement with the libraries.

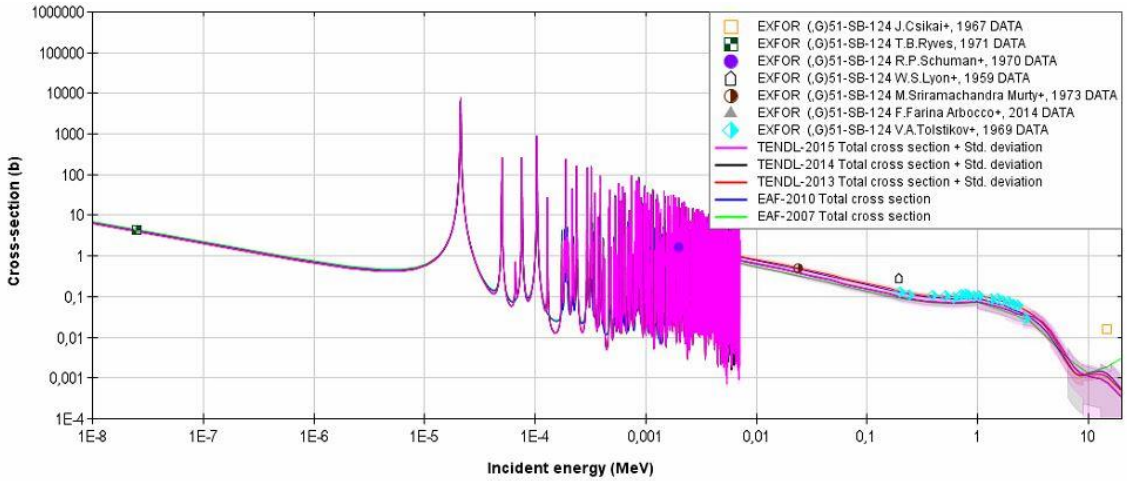

Figure 4.18. Cross section for $^{123}Sb(n,g)^{124}Sb$ reaction (TENDL-2014 and TENDL-2015 are superimposed).

- $^{124}Sn(n,g)^{125}Sn$ (for subsequent β- to produce ^{125}Sb). As it has been previously commented (see Section 4.2), only the cross section for the production of the ground state should be considered since the 125mSn do not decay to the ground state. Figure 4.19 shows that there are limited differential data and that the higher differences among the different libraries are located for energies higher than 1 MeV.

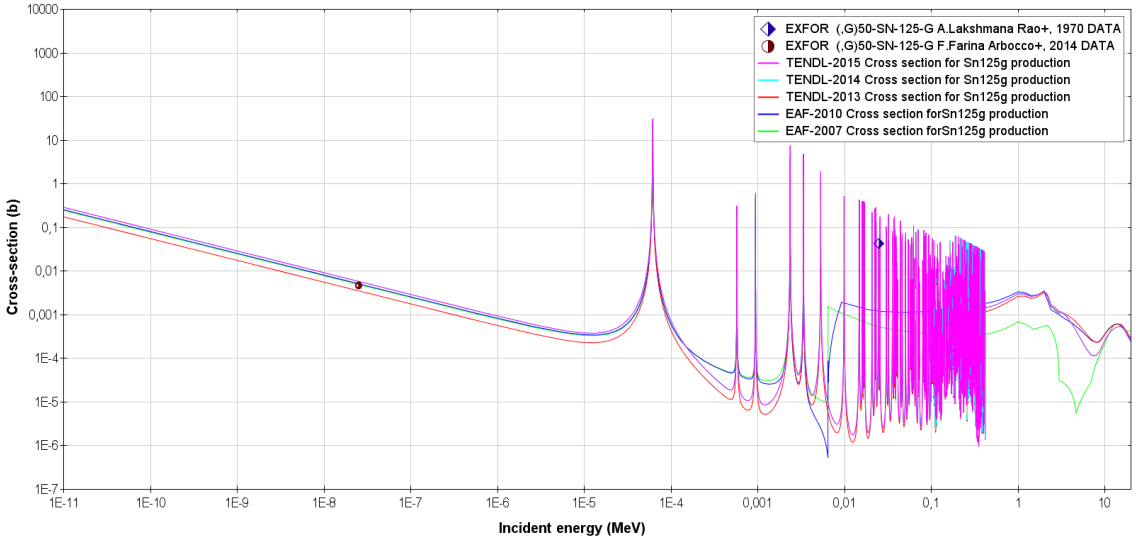

Figure 4.19. Cross section for $^{124}Sn(n,g)^{125}Sn$ reaction (TENDL-2014 and TENDL-2015 are superimposed).

- $^{133}Cs(n,g)^{134}Cs$. The plot given in Figure 4.20 shows that there is no appreciable differences among all the libraries until an energy value of 1 MeV. From then on, EAF-2010 is the library presenting the highest values, up to 7 times higher. The available differential experiments are in agreement with the libraries but, however, they do not make possible to discern what is the best library when they begin to give different

values (from 1 MeV) because the only two experiments at 14 MeV are one in perfect agreement with the EAF-2010 and, the other one, with the TENDL-2015.

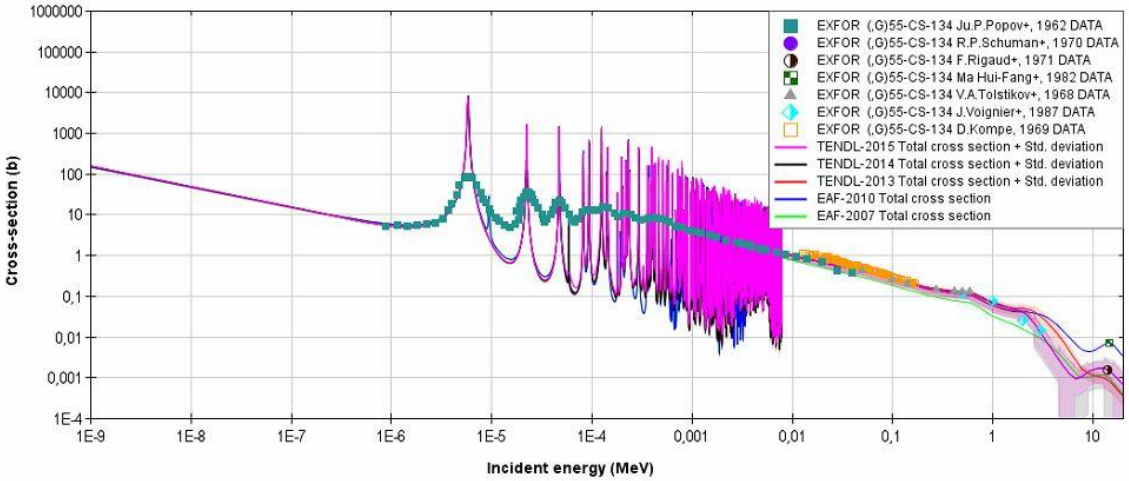

Figure 4.20. Cross section for $^{133}Cs(n,g)^{134}Cs$ reaction (TENDL-2014 and TENDL-2015 are superimposed).

- $^{130}Ba(n,g)^{131}Ba$. Limited data are shown in Figure 4.21, with satisfactory agreement between ~ 10^{-5} and ~$5 \cdot 10^{-2}$ MeV. Furthermore, a lack of experimental data for higher energies is observed. EAF-2007 and EAF-2010 are coincident and, in addition, TENDL (2013, 2014 and 2015) shows lower values in the 1/v energy range, having a good agreement with one of the experiments at these energies.

  For energies higher than 10 keV there is only one experiment and libraries overestimate by far that value. There are not experiments neither for the production of split reactions nor for the total reaction around this energy. Furthermore, for the energy of this experiment (1 MeV), discrepancies between both EAF (2007 and 2010) and TENDL (2013, 2014 and 2015) can be observed, being the EAF values lower than those from TENDL. Moreover, TENDL-2014 and TENDL-2015 are identical and at this range TENDL-2013 provides slight lower values. Therefore, in case the barite concrete is expected to be used in ITER, it would be necessary to work in the production of additional experiments for the improvement of this cross section.

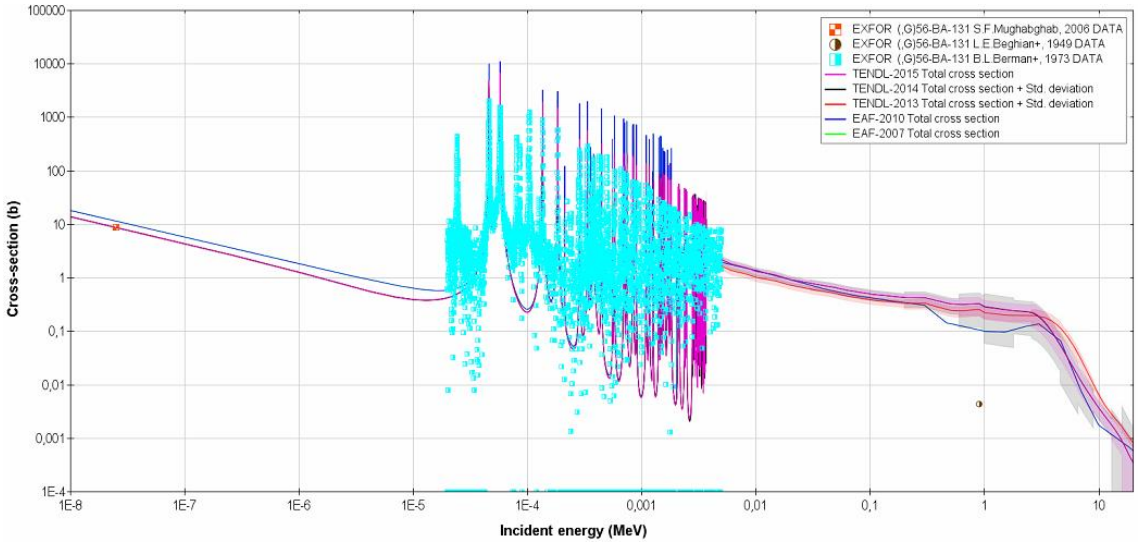

Figure 4.21. Cross section for $^{130}Ba(n,g)^{131}Ba$ reaction (EAF-2007 and EAF-2010 are superimposed; TENDL-2014 and TENDL-2015 are superimposed) [18].

- $^{132}Ba(n,g)^{133}Ba$ (Figure 4.22). There are very few experiments and only for the ground or the metastable state, not for the total. Furthermore, all of them are in the 1/v area. Metastable values are much lower than ground ones. Furthermore there are differences among all the libraries except for TENDL-2014 and TENDL-2015 which are coincident. From that resonance area, TENDL-2013 fits best to EAF-2010, while EAF-2007 disagrees and shows higher values; TENDL-2014 (and thus TENDL-2015) differs from TENDL-2013 (and therefore with EAF-2010) and EAF-2007 and considers intermediate values between them until 3 MeV where it begins to have the lowest values. Therefore, if barite concrete is used in ITER, it would be necessary to dedicate extended effort for the improvement of this cross section.

  Taking into account that it is necessary to consider split reactions separately due to the half-life of ^{133m}Ba (see Section 4.2), although both reactions have a QS of 2, it is specially necessary to work on improving the cross section producing the ground state since its contribution to the total production of ^{133}Ba is around 98%.

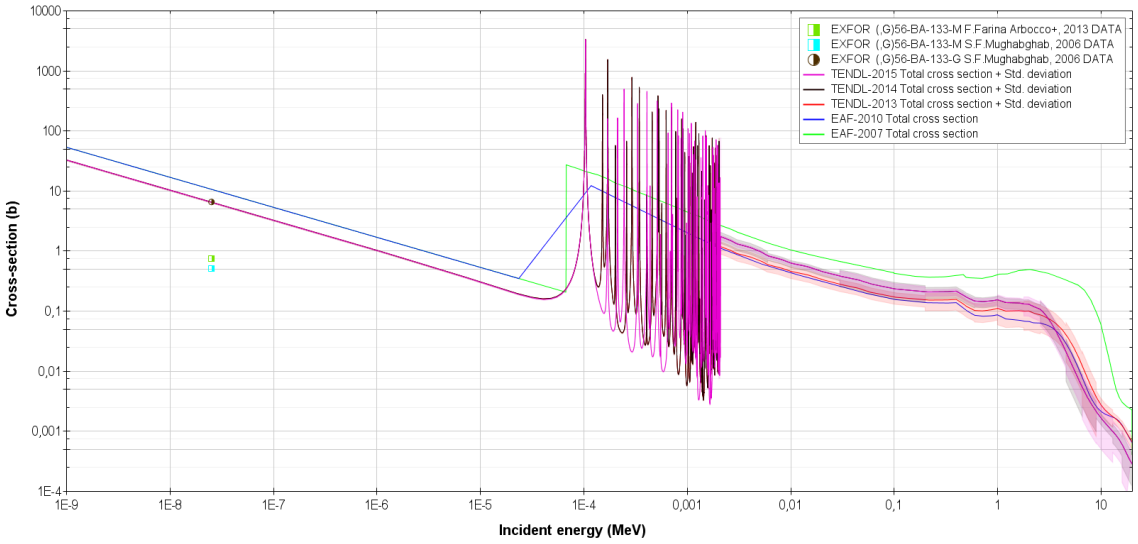

Figure 4.22. Cross section for $^{132}Ba(n,g)^{133}Ba$ reaction (TENDL-2014 and TENDL-2015 are superimposed) [18].

- $^{134}Ba(n,2n)^{133}Ba$ (Figure 4.23). Both EAF and TENDL libraries in any of the versions give very similar values for the cross section for this reaction with little discrepancies in the range of 10-14 MeV. The experimental data for the total cross section are higher than those of the libraries.

  Considering the information of the previous section; that is cross section for the metastable split in both EAF has a QS of 6, while cross section for the reaction leading to the ground state has a poor rating (3), work should only be done for the cross section of the reaction producing the ground state, taking also into account that the split reaction producing the ground state contributes between 47-76% to the total production of ^{133}Ba. This is confirmed by Figure 4.24, where some differences between libraries and experiments are observed.

- $^{134}Ba(n,g)^{135m}Ba$. From the plot of Figure 4.25 comes out that there are differences regarding the libraries for this cross section reaction. EAF provides higher values at low energies while TENDL (all versions) does at higher ones. The lack of experiments is noted; those available at high energies seem to fit better with the TENDL-2014 and TENDL-2015. However, it is important to keep in mind that this reaction is important in the barite concrete case and, therefore, reliability is particularly needed at low energies.

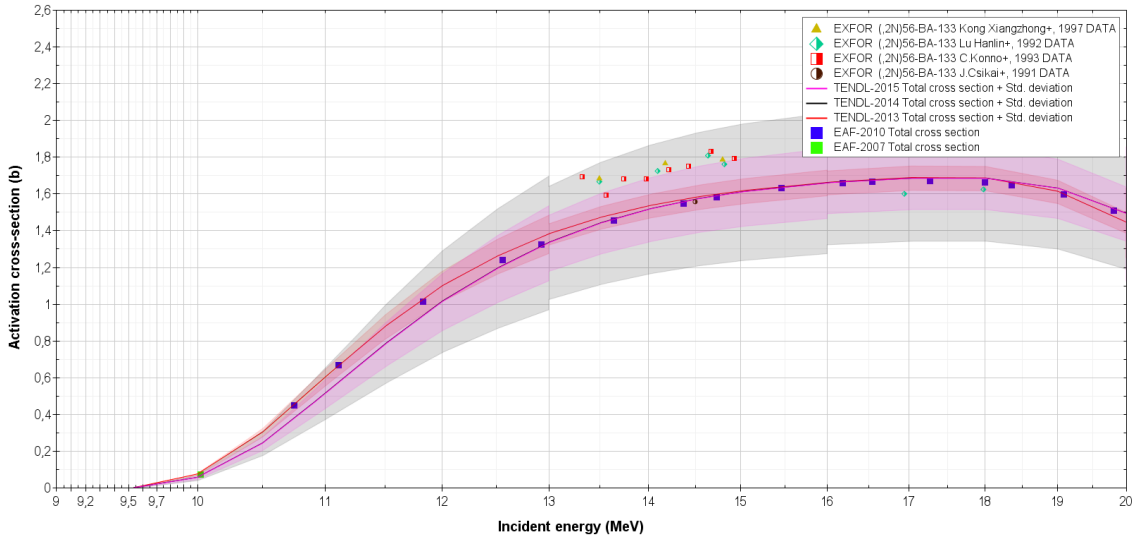

Figure 4.23. Cross section for $^{134}Ba(n,2n)^{133}Ba$ reaction (EAF-2007 and EAF-2010 are superimposed; TENDL-2014 and TENDL-2015 are superimposed) [18].

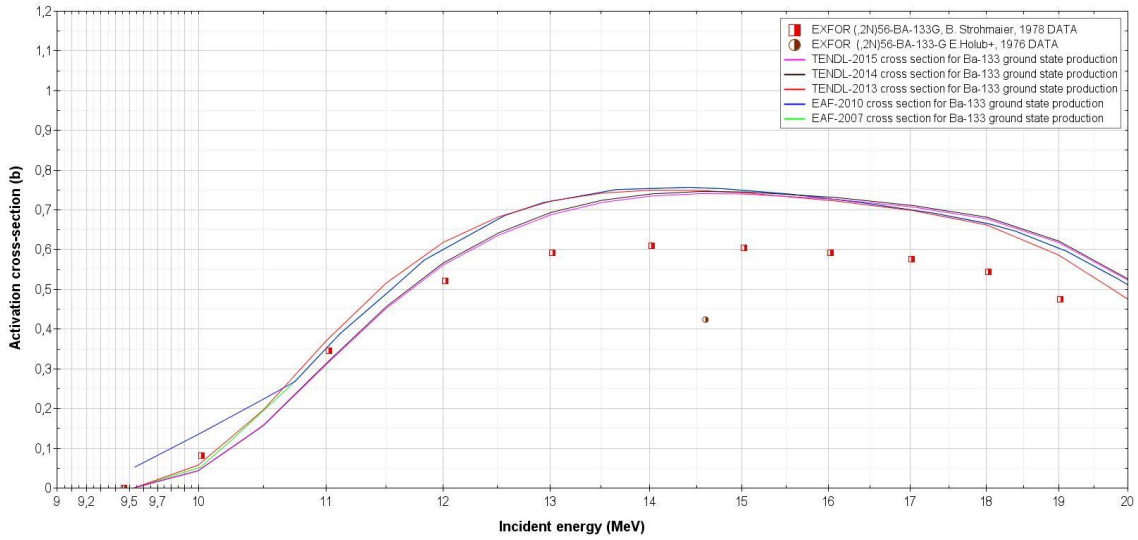

Figure 4.24. Cross section for $^{134}Ba(n,2n)^{133g}Ba$ reaction [18].

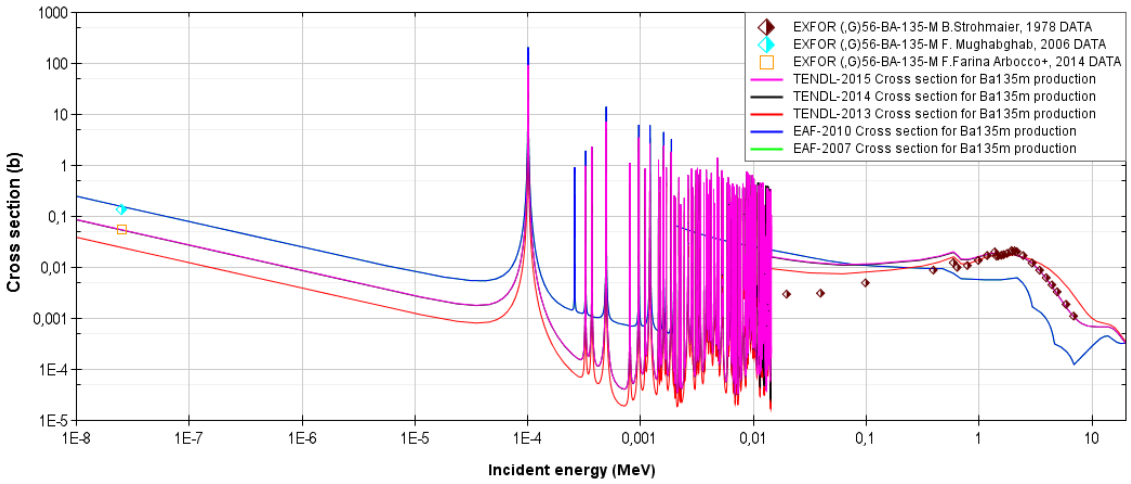

Figure 4.25. Cross section for $^{134}Ba(n,g)^{135m}Ba$ reaction (EAF-2007 and EAF-2010 are superimposed; TENDL-2014 and TENDL-2015 are superimposed).

- $^{135}Ba(n,n')^{135m}Ba$. As it is shown in Figure 4.26, there are significant differences in the values provided by each library up to 10 MeV. Furthermore, a need for additional differential experiments is detected.

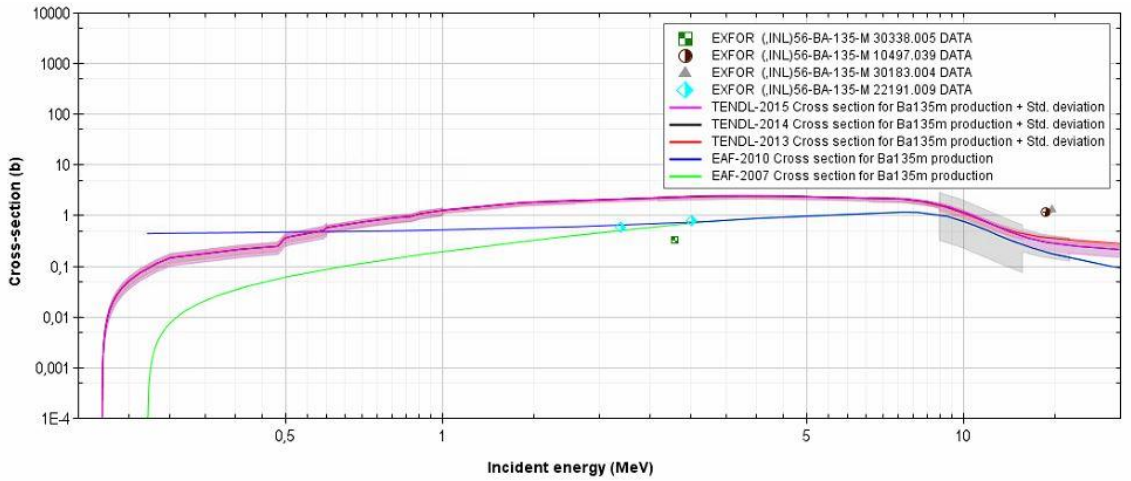

Figure 4.26. Cross section for $^{135}Ba(n,n')^{135m}Ba$ reaction (TENDL-2014 and TENDL-2015 are superimposed).

- $^{151}Eu(n,g)^{152}Eu$. As it has been said, for the purpose of this chapter, only the split reactions leading to the ground and the second metastable states of ^{152}Eu need to be taken into account, leaving the cross section for the production of the first metastable to one side. Therefore, the total reaction Figure 4.27 shows the cross section for the production of the ground sate and Figure 4.28 for the production of the second metastable.

Generally speaking, it can be seen in all these figures that TENDL-2013 is more different to the other versions of TENDL than the 2014 or 2015 one. From Figure 4.27, one can see that differences among EAF and TENDL libraries are appreciated for energy values higher than 1 MeV. Furthermore, there are data in all the energy range and all the libraries provide lower values than those achieved by experiments. For what concerns to the second metastable production, it is plain to see that few experimental data are found and, also, differences among the EAF and TENDL libraries are detected, providing the EAF ones lower results.

- $^{153}Eu(n,g)^{154}Eu$. Figure 4.29 reveals that all the libraries are very similar but TENDL (all versions) has a largest resonance area since it ends at higher energies. From 0.5 MeV onwards, libraries begin to diverge, especially appreciating this in the 2.5-10 MeV range. In this area TENDL-2013 provides the highest values.

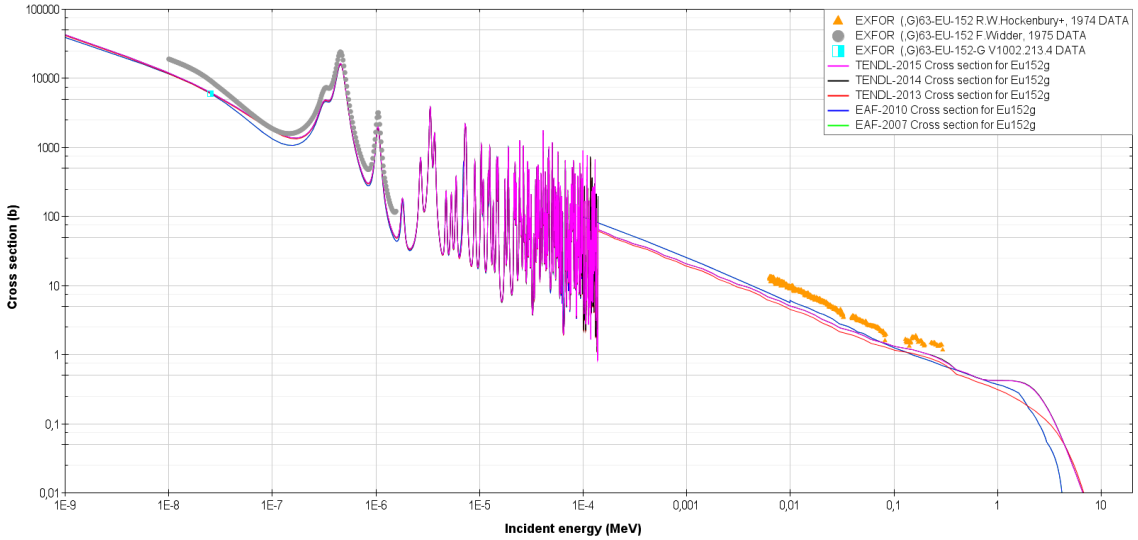

Figure 4.27. Cross section for $^{151}Eu(n,g)^{152g}Eu$ reaction (EAF-2007 and EAF-2010 are superimposed).

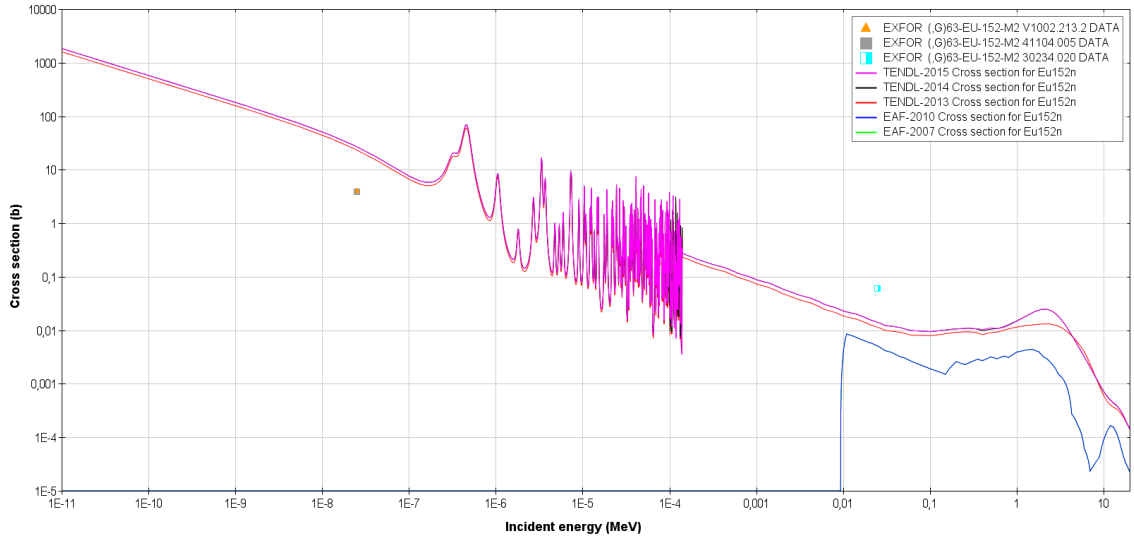

Figure 4.28. Cross section for ^{151}Eu(n,g)^{152n}Eu reaction (EAF-2007 and EAF-2010 are superimposed).

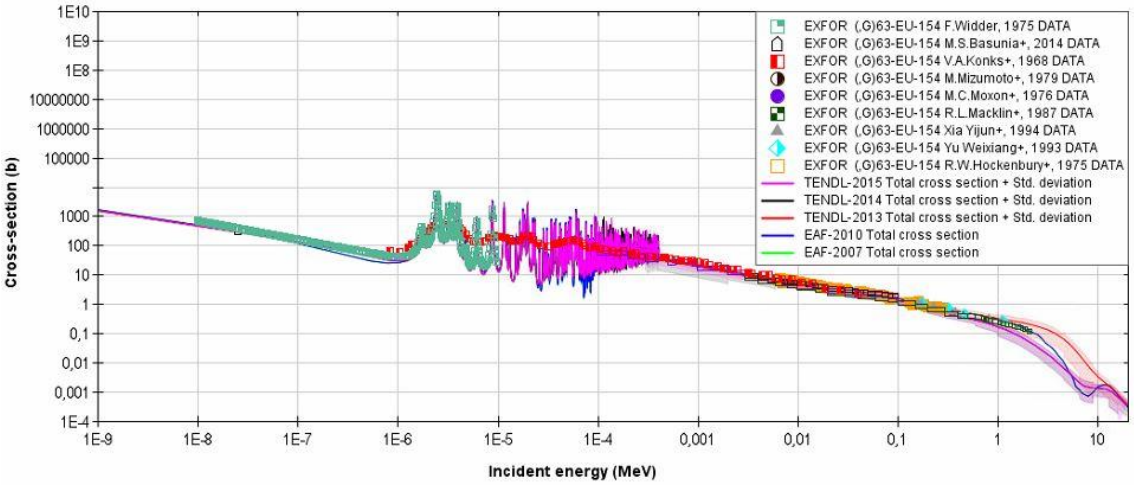

Figure 4.29. Cross section for ^{153}Eu(n,g)^{154}Eu reaction (EAF-2007 and EAF-2010 are superimposed).

- ^{159}Tb(n,g)^{160}Tb. In this case (Figure 4.30) there are many experiments and in agreement with the libraries. Major differences between the libraries are observed from 1 MeV onwards, although these differences are not notable until 12 MeV, where EAF (both versions) provides higher values which are in agreement with the only available experiment at that energy.

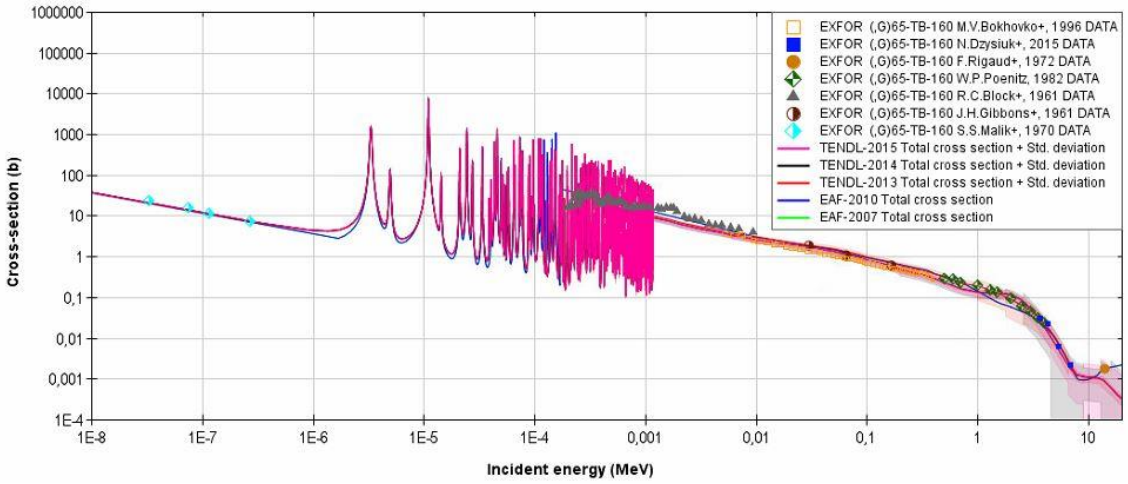

Figure 4.30. Cross section for $^{159}Tb(n,g)^{160}Tb$ reaction (EAF-2007 and EAF-2010 are superimposed).

- $^{183}W(n,D)^{182}Ta$. As can be seen in Figure 4.31, there are not differential data in the energy range of interest, as expected from Section 4.2. TENDL-2013 is the library providing higher values along the whole energy range.

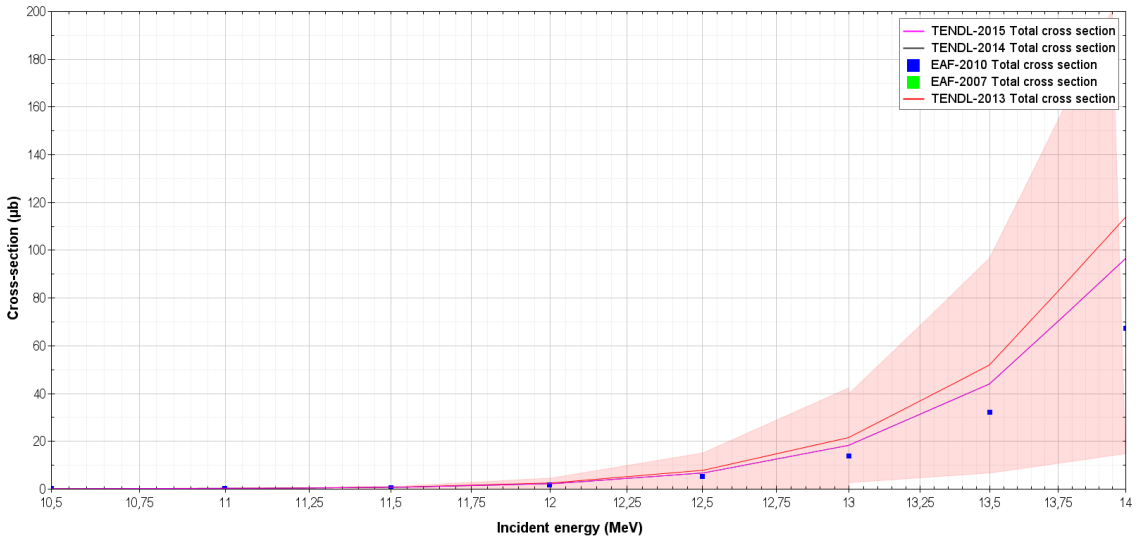

Figure 4.31. Cross section for $^{183}W(n,D)^{182}Ta$ reaction (EAF-2007 and EAF-2010 are superimposed; TENDL-2014 and TENDL-2015 are superimposed).

- $^{180}W(n,g)^{181}W$. One can see in Figure 4.32 that there are differences among the libraries in the 1/v area and that experiments in that zone are in agreement with the EAF library. On the other hand, there is a lack of experiments in the high energy area from 500 keV onwards. From then to 3 MeV, TENDL-2013 is the library with the highest values. On the contrary, TENDL-2014 and TENDL-2015 provides the lowest. From 3-14 MeV, EAF library (both versions, as they are coincident) shows the lowest values.

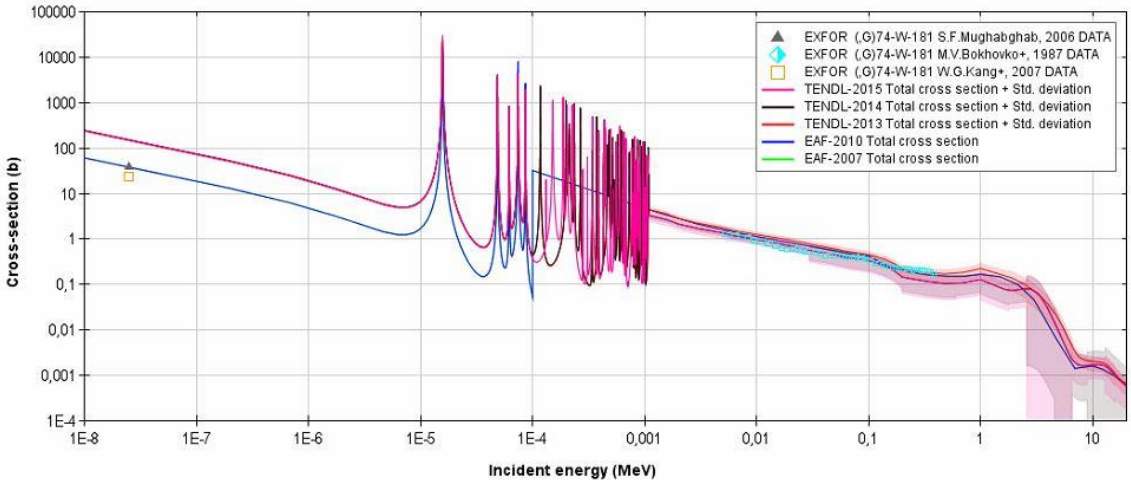

Figure 4.32. Cross section for $^{180}W(n,g)^{181}W$ reaction (EAF-2007 and EAF-2010 are superimposed; TENDL-2014 and TENDL-2015 are superimposed).

4.4. Recommendation on the activation library to be used for SDDR prediction in ITER

Three different sets of relevant cross sections were found using the EAF validation procedure:

- Not validated but with satisfactory agreement with differential and unsatisfactory agreement with integral data (QS=5_2).
- Validated: both differential and integral data exist and they are in agreement with the library (QS=6).
- QS not provided.

With regard to the first set (3 reactions), that is reactions with QS=5_2, no significant differences between EAF and TENDL versions were found.

For those validated reactions, that is QS=6, in most of the cases (20 reactions out of 25) the use of any of the considered libraries would lead to similar results. However, differences were found in 5 reactions between EAF and TENDL whatever is the version used.

Regarding those reactions without provided QS (a total number of 18), a considerable lack of experimental data was found. In cross sections via (n,g) reactions, this lack of data is detected in the high energy area, precisely where the libraries differ most among themselves and, therefore, no recommendation can be provided between EAF and TENDL libraries. It is worth noting that most of these reactions are related to the activation of potential materials for ITER, which are not currently included in the model. In this sense, for instance, some slight

differences would be expected when using EAF libraries instead of TENDL in the activation of the barite concrete, producing the former higher values.

As a conclusion, the use of any of the analyzed EAF and TENDL libraries would lead to similar results in the SDDR calculation in ITER with slight discrepancies.

5. Summary and conclusions

The feasibility to carry out manual maintenance activities in ITER requires that certain SDDR limits are met in different areas. Also, an accurate estimation of SDDR requires reliable activation cross sections.

This chapter provides relevant information about the quality of available activation cross sections data for maintenance activities in ITER, mainly in the PC and PI areas as well as for the cask transfer transportation. For this purpose, EAF-2007 and 2010 versions, that are the reference activation libraries within ITER and the EUROFusion Programme, were explored.

In order to assess the quality of activation cross sections, relevant materials that will be placed in ITER and producing most of the SDDR in the PC and PI areas were selected, as well as some other concrete candidates for the bioshield plug (L2N and barite concretes). Then, major radionuclides and related pathways were found. This information comes both from previous works as well as own calculations, all of them using EAF-2007 and ITER SA2 irradiation scenario.

As a conclusion, a total number of 27 radionuclides were found as relevant.

- 19 of them are relevant for the SDDR analysis at the ITER PC, namely: ^{24}Na, ^{42}K, ^{51}Cr, ^{54}Mn, ^{56}Mn, ^{59}Fe, ^{58}Co, ^{60}Co, ^{57}Ni, ^{64}Cu, ^{106m}Ag, ^{110m}Ag, ^{124}Sb, ^{131}Ba, ^{133}Ba, ^{135m}Ba, ^{182}Ta, ^{187}W and ^{203}Pb.

- 20 of them are related to the SDDR at PI, namely: ^{42}K, ^{51}Cr, ^{54}Mn, ^{59}Fe, ^{58}Co, ^{60}Co, ^{65}Zn, ^{92m}Nb, ^{106m}Ag, ^{110m}Ag, ^{124}Sb, ^{125}Sb, ^{134}Cs, ^{152}Eu, ^{154}Eu, ^{160}Tb, ^{182}Ta, ^{181}W, ^{187}W and ^{203}Pb.

In the case of the cask transfer to be carried to the HCF, only 4 are relevant: ^{54}Mn, ^{58}Co, ^{60}Co and ^{182}Ta. Furthermore, it is necessary to highlight that ^{134}Cs, ^{152}Eu, ^{154}Eu and ^{160}Tb were taken into account only in the case that L2N concrete is used in ITER. The same happened for ^{42}K, ^{131}Ba, ^{133}Ba and ^{135m}Ba and the barite concrete.

A total number of 45 pathways appear for the production of these dominant radionuclides. For these pathways the quality of the cross sections involved can be break down into the following categories:

- 25 cross section reactions are differential and integral validated. Hence, no further work is needed for them. Herein are most of the cross section reactions which give rise to those nuclides that contribute most to the SDDR. For these reactions, EAF and TENDL libraries provide similar results, except for 5 of them where some discrepancies were detected.

- 20 cross section reactions are not validated and should be considered for betterment since a lack of integral experimental data, and also of differential data in some cases, is detected. Also, slight discrepancies among the EAF (2007 and 2010) and TENDL are found for some cross sections, but it is not clear which one fits better with the available differential experiments, or the differences are found in the energy range without experiments. This fact makes difficult any conclusion about the best evaluated cross section library to be used for the SDDR estimation in ITER, indicating that further work to determine their reliability degree is needed, priorized as follows:

  - ✓ Efforts on improvement should be focused on $^{59}Co(n,2n)^{58}Co$, $^{63}Cu(n,g)^{64}Cu$ and $^{50}Cr(n,g)^{51}Cr$ cross section reactions as these production pathways appear for radionuclides contributing more and/or in the activation of more than one material.

    For $^{59}Co(n,2n)^{58}Co$ and $^{63}Cu(n,g)^{64}Cu$ reactions additional integral experiments are needed. Furthermore, for $^{63}Cu(n,g)^{64}Cu$ differential experiments for energies higher than 3 MeV would be useful since discrepancies have been found among the analyzed libraries. Also, for $^{59}Co(n,2n)^{58g}Co$ integral and differential experiments are recommended. In the case of $^{50}Cr(n,g)^{51}Cr$ reaction, no experimental data are found for energies higher than 1 MeV which are suggested to be carried out.

  - ✓ 8 more cross sections require further work (less priority): $^{64}Zn(n,g)^{65}Zn$, $^{66}Zn(n,2n)^{65}Zn$, $^{107}Ag(n,2n)^{106m}Ag$, $^{109}Ag(n,g)^{110m}Ag$, $^{123}Sb(n,g)^{124}Sb$, $^{124}Sn(n,g)^{125}Sn(B-)^{125}Sb$, $^{183}W(n,D)^{182}Ta$ and $^{180}W(n,g)^{181}W$.

  - ✓ If L2N and barite concretes are used in ITER some other cross section reactions require betterment, especially at low energies since these materials should not be exposed to the neutrons produced in the high energy range of the D-T fusion spectrum:

    - For the L2N concrete case: $^{133}Cs(n,g)^{134}Cs$, $^{151}Eu(n,g)^{152}Eu$, $^{153}Eu(n,g)^{154}Eu$ and $^{159}Tb(n,g)^{160}Tb$.

- For the barite concrete case: $^{130}Ba(n,g)^{131}Ba$, $^{132}Ba(n,g)^{133}Ba$, $^{134}Ba(n,2n)^{133}Ba$, $^{134}Ba(n,g)^{135m}Ba$ and $^{135}Ba(n,n')^{135m}Ba$.

In conclusion, to date, without any further work and considering radionuclides and pathways with contributions higher than 1%, the calculated CDR (produced by the activation of each of the materials) with EAF validated cross sections is, at least: SS316LN-IG (91%), SS304L (97%), Eurofer (95%), LiPb (85%), W (98%), conventional concrete from B-lite (98%), and L2N concrete (94%).

This indicates that most of the cross sections involved in the ITER SDDR calculation are validated and therefore, the safety factors that should be taken into account may be minimum. However, it should be noted that the SDDR coming from the Cu activation is not overall trustworthy. Thus, validation work is recommended for those cross section involved in the SDDR coming from Cu. Regarding the potential candidate materials studied, only the cross sections related to the barite concrete are found to be not validated. In this sense, if the barite concrete is finally used in ITER, validation work is suggested too.

6. References

[1] H. Iida, V. Khripunov, L. Petrizzi, G. Federici. *Nuclear Analysis Report* (NAR). ITER IDM location https://user.iter.org/?uid=22F2ST (**2004**).

[2] J. How, R. Reichle. *Plant Description (PD)*. ITER IDM location: https://user.iter.org/?uid=2X6K67 (**2009**).

[3] *Technical specification for the engineering support in the area of Test Blanket Module (TBM) systems design and technological demonstration* (**2011**).

[4] R. Forrest. *Data requirements for neutron activation. Part I: Cross sections*. Fusion Engineering and Design, Vol. 81, pp. 2143 – 2156 (**2006**). Doi: http://dx.doi.org/10.1016/j.fusengdes.2006.01.001

[5] U. Fischer, P. Batistoni, R. Forrest, C. Konno, R.L. Perel, K. Seidel, S.P. Simakov. *Development needs of nuclear data for fusion technology*. International Conference on Nuclear Data for Science and Technology (**2007**). Doi: http://dx.doi.org/10.1051/ndata:07494

[6] P. Batistoni, U. Fischer, K. Ochiai, L. Petrizzi, K. Seidel, M. Youssef. *Neutronics and nuclear data issues in ITER and their validation*. Fusion Engineering and Design, Vol. 83, nº 7 – 9, pp. 834 – 841 (**2008**). Doi: http://dx.doi.org/10.1016/j.fusengdes.2008.04.009

[7] R. Forrest. *Nuclear science and data needs for advanced nuclear systems*. Energy Procedia, Vol. 7, pp. 540 – 552 (**2011**). Doi: http://dx.doi.org/10.1016/j.egypro.2011.06.075

[8] J.P. Catalán, A. Suárez, L. Bertalot, T. Giacomin, J. Sanz, V. Udintsev, M. Walsh. *Neutronics in support of the bioshield plug design of equatorial port 12 for ITER*. Fusion Engineering and Design, Vols. 96 – 97, pp. 231 – 235 (**2015**). Doi: http://dx.doi.org/10.1016/j.fusengdes.2015.06.015

[9] R. Pampin, A. Davis, S. Lilley. *European ITER TBS neutronics, activation and shutdown dose preliminary mapping.* F4E-2008-OPE-02-01 v1.0 (**2010**).

[10] B.Y. Kim. *Final report on neutronic analysis of the ITER TBM PP (CDR)*. ITER IDM location: https://user.iter.org/?uid=JR5EZH (**2013**).

[11] H. Liu. Final report on the ITER automated transfer cask biological and absorbed dose rate analysis. ITER IDM location: https://user.iter.org/?uid=N6DH9T (**2014**).

[12] R. Juárez, P. Sauvan, J.P. Catalán, L. Pérez, R. García, A.J. López. *Shielding proposal to reduce the neutron cross talk between EP and LP of ITER*. ITER IDM location: https://user.iter.org/?uid=QPYYNV (**2015**).

[13] A. Davis, S. Zheng, L.W. Parker, A. Turner. *Neutronics and activation analysis for the european TBS with improved nuclear shielding*. F4E-2008-OPE-02-01-04 deliverables 4 & 5 (**2012**).

[14] J. Li, S. Liu, P. Zhao, Y. Li, Y. Peng. *Activation analysis and comparison of bio-shield under ITER and ASP neutron irradiation*. Journal of Fusion Energy, Vol. 34, pp. 727 – 732 (**2015**). Doi: http://dx.doi.org/10.1007/s10894-015-9850-6

[15] A. Serikov, L. Bertalot, U. Fischer, C.S. Pitcher, A. Suárez, V.S. Udintsev, B. Weinhorst. *Shut-down dose rate analysis for ITER diagnostic equatorial and upper ports*. Fusion Engineering and Design, Vol. 89, pp. 1964 – 1968 (**2014**). Doi: http://dx.doi.org/10.1016/j.fusengdes.2014.01.025

[16] M.S. Cheon, S. Pak, C.R. Seon, H.G. Lee, L. Bertalot, R. Barnsley. *Evaluation of the neutron flux effect on the ITER VUV diagnostic system in the upper port*. Journal of the Korean Physical Society, Vol. 59, nº 3, pp. 2228 – 2232 (**2011**). Doi: http://dx.doi.org/10.1016/j.fusengdes.2016.02.009

[17] M. Loughlin. *Guidelines for Nuclear Analyses*. ITER IDM location: https://user.iter.org/?uid=R7XRXB (**2015**).

[18] R. García. M. García, R. Pampin, J. Sanz. *Status of reliability in determining SDDR for manual maintenance activities in ITER: Quality assessment of relevant activation cross sections involved*. Fusion Engineering and Design, Vol. 112, pp. 177 – 191 (**2016**). Doi: http://dx.doi.org/10.1016/j.fusengdes.2016.08.016

[19] R. García, M. García, F. Ogando, R. Pampin, J. Sanz. *Reliability of activation cross sections for estimation of shutdown dose rate in the ITER port cell and port interspace*. Proceeding of ND 2016 International Conference on Nuclear Data for Science and Technology. EPJ Web of Conferences (**submitted**).

[20] J. Sanz, O. Cabellos, N. García-Herranz. *ACAB Inventory code for nuclear applications. User's manual* (**2008**).

[21] R.A. Forrest, M. Pillon, U. Von Möllendorff, K. Seidel. *Validation of EASY-2001 using integral measurements*. UKAEA FUS 467 report (**2001**).

[22] R.A. Forrest, M. Pillon, U. Von Möllendorff, K. Seidel, J. Kopecky, J-Ch. Sublet. *Validation of EASY-2003 using integral measurements*. UKAEA FUS 500 report (**2003**).

[23] R.A. Forrest, J. Kopecky, M. Pillon, K. Seidel. *Validation of EASY-2005 using integral measurements.* UKAEA FUS 526 report (**2006**).

[24] R.A. Forrest, J. Kopecky, M. Pillon, A. Klix, S.P. Simakov, J-Ch. Sublet, P. Bém, M. Honusek, E. Simeckova. *Validation of EASY-2007 using integral measurements*. UKAEA FUS 547 report (**2008**).

[25] N. Soppera, M. Bossant, E. Dupont. JANIS 4: An Improved Version of the NEA Java-based Nuclear Data Information System. Nuclear Data Sheets, Vol. 120, pp. 294 – 296 (**2014**). Doi: http://dx.doi.org/10.1016/j.nds.2014.07.071

[26] M. Loughlin, E. Polunovskiy. *ITER neutronic model: A-lite.* ITER IDM location: https://user.iter.org/?uid=2NEZZS (**2009**).

[27] E. Polunovskiy, A. Serikov, A. Suarez*. ITER neutronic model: B-lite R121217*. ITER IDM location: https://user.iter.org/?uid=9KKVQR (**2012**).

[28] E. Polunovskiy. *ITER neutronic model: C-lite, R.131031*. ITER IDM location: https://user.iter.org/?uid=M2TKBE (**2013**).

[29] M.J. Loughlin, N.P. Taylor. *Recommendation on plasma scenarios*. ITER IDM location: https://user.iter.org/?uid=2V3V8G (**2009**).

[30] A. Serikov, U. Fischer, D. Leichtle, C.S. Pitcher. *Monte Carlo radiation shielding and activation analyses for the Diagnostic Equatorial Port Plug in ITER*. Fusion Engineering and Design, Vol. 87, pp. 690 – 694 (**2012**). Doi: http://dx.doi.org/10.1016/j.fusengdes.2012.02.003

[31] R. Juárez, L. Pérez, F. Ogando, J. P. Catalán, R. García, A.J. López. *HCLL/HCPB nuclear analysis - Second run of calculations* (**2014**).

[32] R. Juárez, P. Sauvan, L. Pérez, D. Panayotov, J. Vallory, M. Zmitko, Y. Poitevin, J. Sanz. *Shudown dose rate analysis of european test blanket modules shields in ITER equatorial port #16*. Fusion Engineering and Design, Vols. 109 – 111, Part B, pp. 1554 – 1558 (**2016**). Doi: http://dx.doi.org/10.1016/j.fusengdes.2015.11.023

[33] V. Barabash. *Chemical compositions of materials representing the components included into basic model for nuclear analysis of ITER* (**2015**).

[34] X-5 Monte Carlo Team. *MCNP – A General Monte Carlo N-Particle Transport Code Version 5*, LA-CP-03-0245, Los Alamos National Laboratory (**2005**).

[35] R.A. Forrest, A. Tabasso, C. Danani, S. Jakhar, A.K. Shaw. *Handbook of activation data calculated using EASY-2007*. UKAEA FUS 552 report (**2009**).

[36] R. Forrest. *The European Activation File: EAF-2007 neutron-induced cross section library* (**2007**).

[37] J-Ch. Sublet, L.W. Packer, J. kopecky, R.A. Forrest, A.J. Koning, D.A. Rochman. *The European Activation File: EAF-2010 neutron-induced cross section library* (**2010**).

[38] J. Kopecky. *Validation of TENDL-2009 using integral measurements* (**2010**).

[39] J-Ch. Sublet, M.R. Gilber. *Decay heat validation, FISPACT-II & TENDL-2012,-2011 and EAF-2010 nuclear data libraries* (**2013**).

Chapter 5

Impact of ITER in-vessel diagnostic systems on the radiation loads of the vacuum vessel and toroidal field coils

This chapter describes the analysis of the impact of some in-vessel diagnostic systems (reflectometry, NAS, FWS and bolometers) on the radiation loads on the VV and the TFCs of the ITER reactor. These radiation loads correspond to nuclear heating and neutron induced damage on different components that can endanger the appropriate functioning of the VV and TFCs by different ways.

1. Introduction

The diagnostic systems to be installed in ITER are needed to provide the necessary tools to control, evaluate and optimize the plasma performance. They are also needed to help in the understanding of the plasma physics. These systems include measurements of temperature, density, concentration, particle impurities and energy confinement times.

ITER will have a set of approximately 60 diagnostics to ensure a controlled operation of the tokamak [1]-[2]. The diagnostics design for ITER is currently under development in Cadarache, France. This progress is a challenge due to the harsh conditions they must tolerate, strict engineering requirements and the need for high reliability in measurements.

The in-vessel diagnostics, which are the focus of this chapter, cut the BSMs system out due to their position and, in some cases, because they require special cutouts in the BSMs in order to meet the measurement requirements [3]. As a result, two effects are produced. On the one hand, the shielding material is removed and, on the other hand, streaming paths are generated. These effects concern both to TFCs and the VV, since both share the BSMs as a radiation barrier.

As it has been commented in Chapter 1, during the operation of ITER reactor the VV and the TFCs are under high levels of neutron and gamma radiation. This radiation can endanger their appropriate functioning and, consequently, the plasma confinement. Specifically, the power deposited by this radiation, commonly known as nuclear heating, on the superconducting

TFCs has to be under the limits imposed by the capacity of the cryogenic cooling system designed for ITER and the quenching of the superconductor state. In addition, the radiation damage induced by neutrons on the winding pack insulator has to be in such levels that guarantee the preservation of its insulating capacity. Finally, thermal stresses due to a non-uniformly nuclear heating on the VV impose also limits to this magnitude. All these issues are evaluated by a set of radiation loads which limits will be described further (Section 3.2.1). On the other hand, there is some concern within ITER IO, since the analyses carried out some years ago reflected radiation load values very close to the design limits, or even above [4]. Therefore, any contribution leading to an increase of these radiation loads must be studied.

This is where the diagnostic systems come into play, since the modification of the BSMs due to the diagnostics needs to be evaluated. The measurement of these radiation loads considering the inclusion of diagnostics is a major task for ITER, since if the required limits are not met the diagnostics have to be redesigned. Thus, previous works on B-lite model, evaluating the impact of the cutouts necessary for the in-vessel bolometer cameras in the nuclear shielding of the VV and TFC, can be found in the literature [5].

This chapter collects a series of nuclear analyses carried out to evaluate the full impact of different ITER in-vessel diagnostic systems on the radiation loads of the VV and the TFCs. Specifically, Reflectometry, NAS, FWS and bolometers diagnostics are studied. In order to measure the impact of these diagnostics a case without diagnostics (the current ITER reference model for neutron analysis, C-lite) was used as a baseline case and compared to those cases where the different diagnostics were included. This work, during the development of the thesis, has given rise to several reports within the ITER framework [6]-[10] and there is also a prepared publication, which at present is under the ITER review [11].

The most relevant features for the neutronic analysis of the studied diagnostics, with special focus on the geometry, are described in Section 2. The computational procedure and assumptions as well as the criteria used for the radiations loads are described in Section 3. Finally, the results were breakdown following the different analyzed radiation loads and are detailed in Section 4 and Section 5 is devoted to summarize the main conclusions.

2. Description of the in-vessel diagnostic systems

This section describes the studied diagnostic systems and their location in the reactor. For the sake of clarity, Figure 5.1 shows a Y-cut of the neutronic reactor model displaying the numeration of the blankets, so the position of each diagnostic system can be easily identified. As can be seen, blankets are numbered clockwise from #1-#18, starting from the one close to the divertor following the inboard (#1-#8) and then downwards along the outboard (#9-#18).

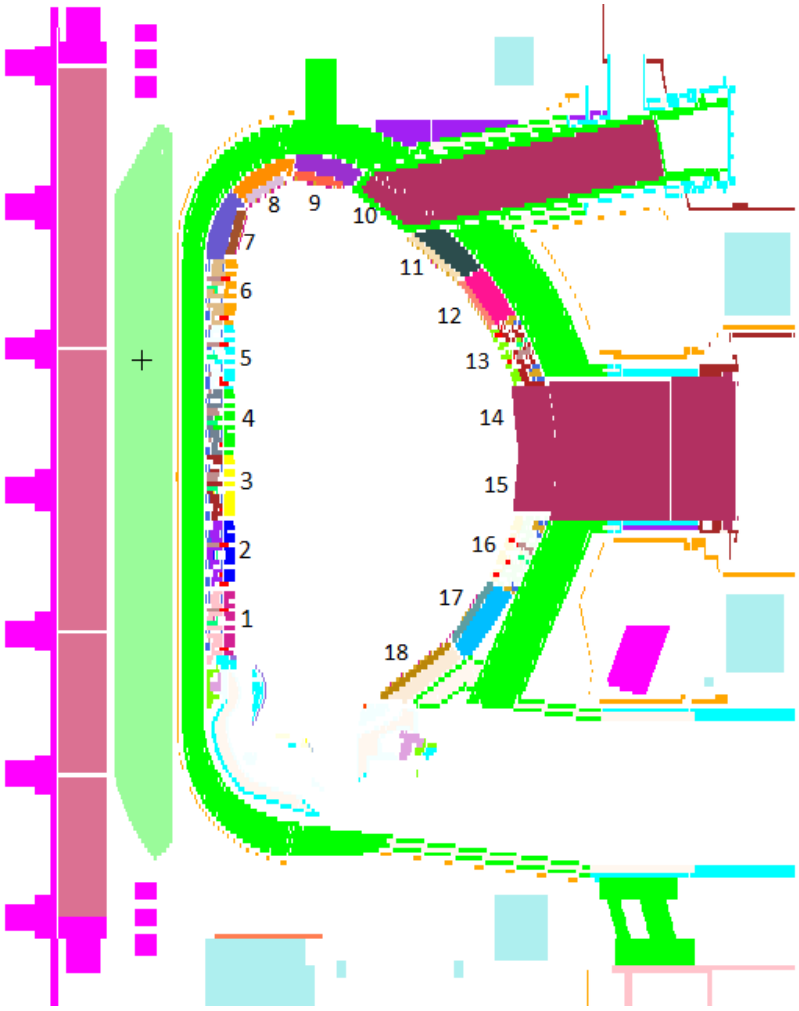

Figure 5.1. Y-cut of the C-lite model [11].

2.1. Reflectometry

In order to measure the density profile in the main plasma and the plasma position and shape in ITER, the reflectometry diagnostic will be used, providing a reference for the magnetic diagnostic in long pulses [12].

Five of the nine sectors (40º) in which the ITER tokamak is divided contain reflectometry antennas. However, not all antennas from the different sectors are identical, but there are three different types (Figure 5.2): a single inboard antenna (contained in three sectors), a double inboard antenna (contained in one sector) and a single outboard antenna (contained in one sector). Although there are three different types of sectors, the CAD model is very similar for all cases. Figure 5.3 shows this CAD model and its cutout.

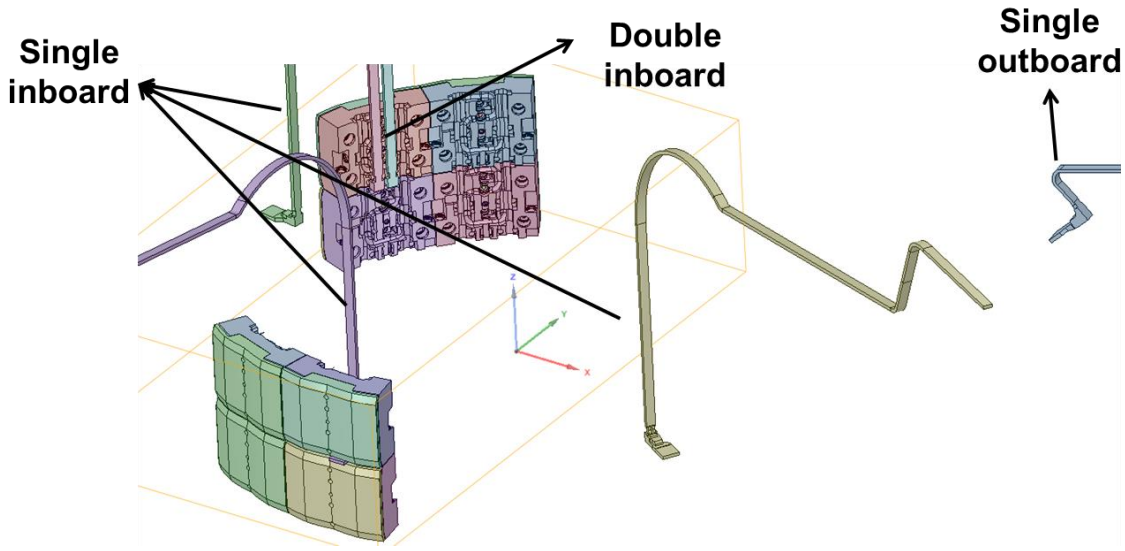

Figure 5.2. Different types of reflectometry antennas inside the ITER tokamak [11].

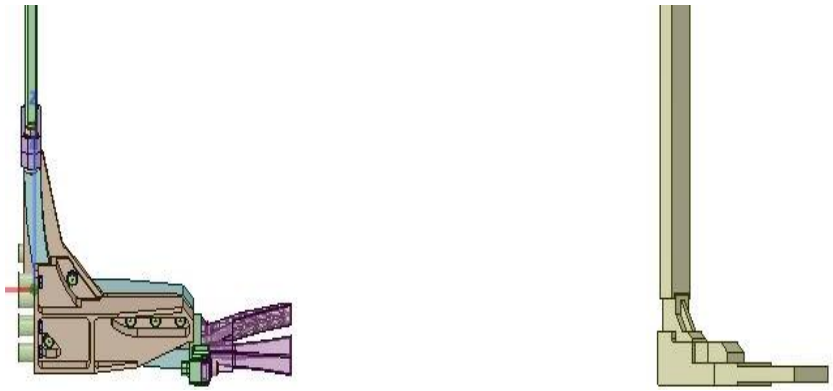

(a) (b)

Figure 5.3. 3D CAD model of the reflectometry diagnostic: (a), the diagnostic components; (b) its cutout.

2.2. Neutron Activation System (NAS)

The NAS is part of the category of «neutron diagnostic» category. It uses a pneumatic tube system for transporting a material sample within a capsule to the VV, where it is irradiated by the reaction neutron flux. Then, the sample is returned to a counting station where its radioactivity is measured and thus, the incident neutron flux is determined [13]. Hence, this diagnostic system (NAS) provides time integrated measurements of the neutron fluence at the first wall and evaluates total fusion power from ITER plasma [14]-[15].

The NAS diagnostic is placed in two of the nine tokamak sectors. In each of the sectors, it is located in the inboard region and it consists of three measurement points located in the vertical gaps of blankets #1, #4 and #8 (see Figure 5.1) as can be seen in Figure 5.4.

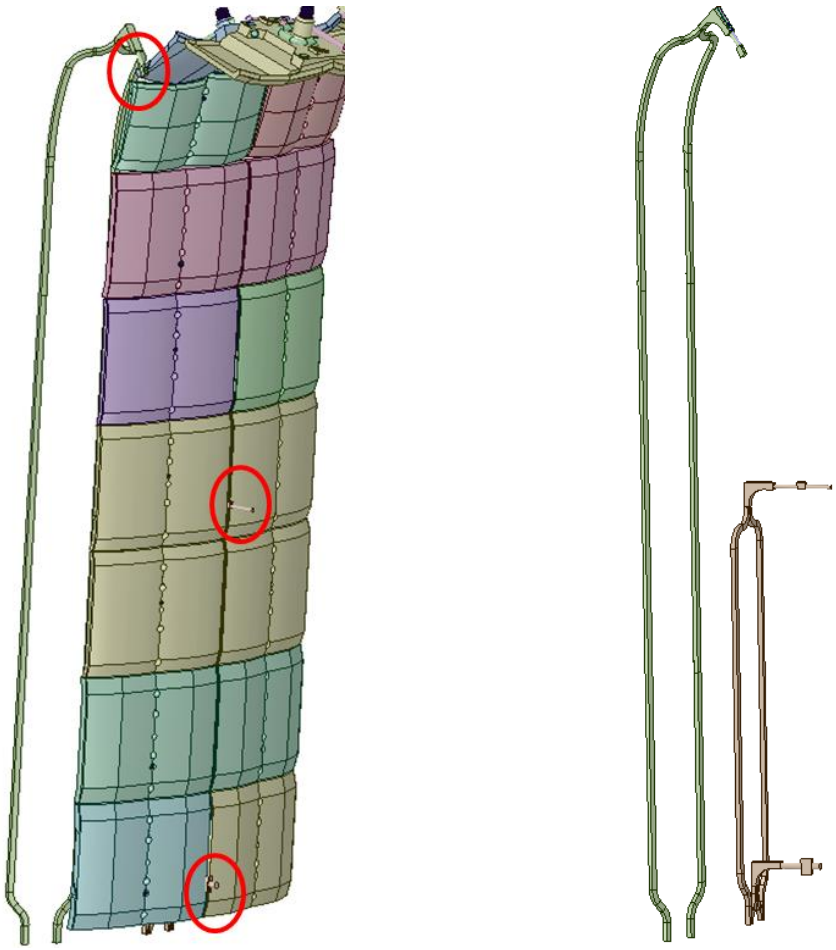

(a) (b)

Figure 5.4. (a), Location of the measurement points of NAS diagnostic; (b), NAS diagnostic model.

2.3. First Wall Samples (FWS)

FWS are a one of the plasma facing components in ITER. The primary role for FWS is to measure erosion. Additionally, dust accumulation, deposition effects and T retention are also measured by this diagnostic [16].

There are two types of FWS located in the slots between blanket module blocks of ITER (Figure 5.5, Table 5.1). The first type (L) is the most critical one since it goes completely through the blanket FW. The type S only removes some material in the plasma facing zone of the blanket FW having, therefore, lower impact than the type L in the reduction of the shielding capability of the blanket.

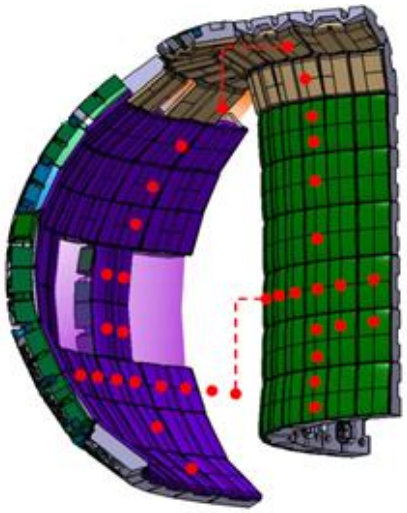

Figure 5.5. FWS location in ITER [17].

Table 5.1. Location of the FWS by type.

# Blanket	FWS	# Blanket	FWS
1	3 L	11	2 L
2	3 L	12	0
3	3 S	13	3 L
4	3 S	14	2 S
5	3 S	15	2 S
6	3 L	16	5 S
7,8,9	9 S	17	5 S
10	0	18	4 L, 1S

Figure 5.6 shows the 3D original CAD model for both type of FWS (L and S). Materials defined for the FWS are shown in Figure 5.7.

(a) (b)

Figure 5.6. 3D original CAD model for the FWS: (a), type L; (b), type S [11].

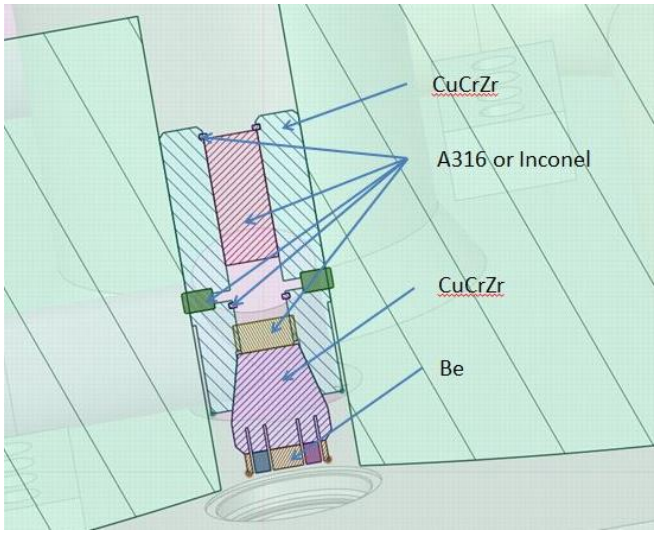

Figure 5.7. Materials used for the FWS [11].

2.4. Bolometers

Bolometers (Figure 5.8) are one of the basic diagnostics in all fusion devices. Bolometers provide measurement of the plasma radiation. The radiation power loss measured using them is crucial to the understanding of power balance of the plasma and its spatial distribution [3],[18].

Bolometers are located at sectors #1, #3, #4, #6, #8 and #9 (see Figure 5.1), even though each of these sectors contains a different number of them and with different cutout widths, as reported in Table 5.2. Figure 5.9 shows the CAD model for bolometers including the space reservation used to make the customized cutout on the blanket.

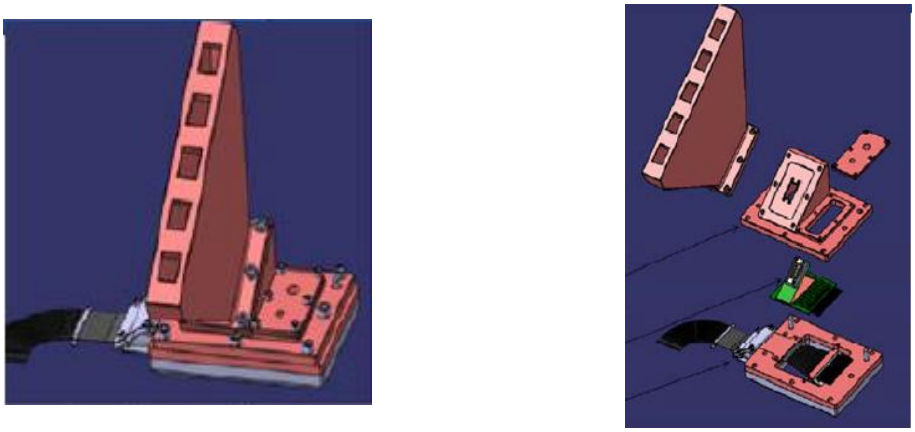

(a) (b)

Figure 5.8. (a), Bolometer complete assembly; (b), exploded view [19].

Table 5.2. Bolometers location [11].

# Sector	# Blanket	Bolometers	Cutout width (cm)
1	1	2	14 and 30
	5	1	30
	7	1	30
	8	1	30
	18	1	30
3	1	1	30
	8	1	20
	18	1	20
4	1	1	30
	18	1	20
6	8	1	20
	9	1	20
	18	1	20
8	1	1	30
	8	1	20
	18	1	30
9	1	1	30
	7	2	20 and 30
	9	1	30

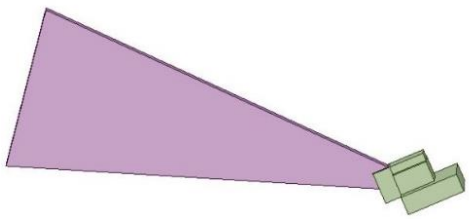

Figure 5.9. Bolometer diagnostic model [11].

3. Procedure, computational tools and assumptions

This section is devoted to describe the procedure and computational tools used for the evaluation of the impact of the four considered in-vessel diagnostics in the shielding capability of the blanket. Subsections are dedicated to the computational procedure, radiation loads criteria, and geometry simplification process.

3.1. Computational procedure

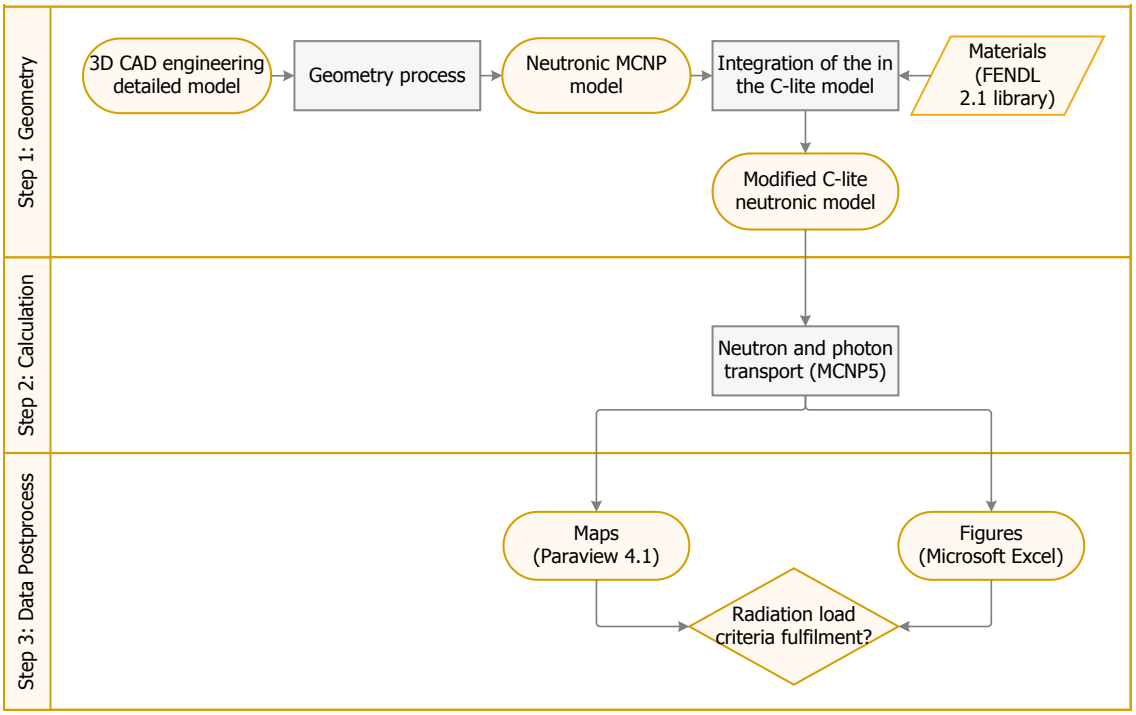

Figure 5.10. Flowchart for the methodology procedure (; starts and ends of processes; , process/actions; , data; , question/decision).

The different steps followed in the computational procedure are represented by a flowchart in Figure 5.10 and they are described in the following lines.

The procedure starts with a 3D geometric model in CAD format provided by the ITER Technology & Diagnostics division design engineers, for each of the four diagnostic systems. In a first step each of the four mentioned models must be simplified, according to the methodology for the geometry process described in Chapter 3[19]. Most of the needed simplifications had to do with splines and one solid defined as a surface. All these simplification actions are performed using the SpaceClaim2014 3D CAD-modeling software [20] and subsequently the model is translated using MCAM 4.8 [21].

Upon achieving a suitable neutronic model, materials and densities for the diagnostics are included using FENDL 2.1 [22] and MCNPLIB04P [23] as cross section libraries for neutron and gammas respectively. Then, MCNP is run again without the void mode. Afterwards, the

[19] In Figure 5.10 this Step 1: geometry has been simplified for the sake of clarity. The complete description can be found in Chapter 3, Section 2.1.

neutronic models in MCNP format are introduced in the current ITER standard neutronic model (C-lite) obtaining an integrated model.

In a second step, different radiation (neutron and gamma) transport calculations, mainly focused on energy deposition and radiation damage, using MCNP5 code are carried out in order to obtain the radiation loads results needed to be compared to the defined criteria in Section 3.2.1. Finally, for the last step, Paraview 4.1 visualization tool [24] is used to obtain maps.

3.2. Computational assumptions

This section deals with the computational assumptions that have been made in the nuclear analyses performed to evaluate the impact of the different diagnostic systems on the radiation shielding of the VV and the TFCs.

3.2.1. Radiation load criteria

The radiation load limits, related to the VV and TFCs, required for ITER are exposed in Table 5.3. As it can be seen, within the six imposed criteria, five of them are linked to the different components of the TFC (Figure 5.11) and only one to the VV.

Table 5.3. Radiation load limits for the VV and TFC in ITER [11], [25].

Radiation Load	Limit
Nuclear heating on the VV surface	0.6 W/m^3
Integral TFC nuclear heating	14 kW
Maximal nuclear heating in the conductor/winding pack	1 kW/m^3
Maximal nuclear heating in the coil case	2 kW/m^3
Peak of absorbed dose in coil insulator	10 MGy
Peak of neutron fluence in coil insulator	10^{22} n/m^2

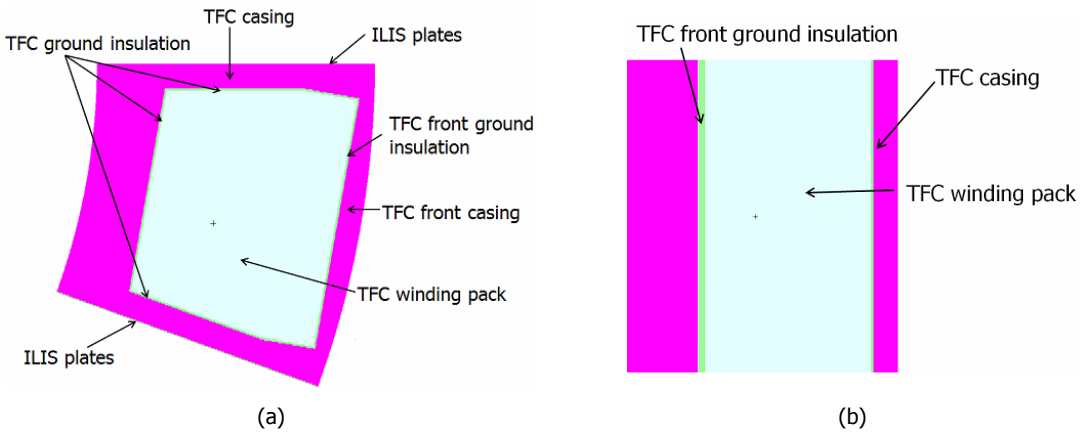

Figure 5.11. (a) TFC components; (b) front ground insualtion.

3.2.2. Geometry correction factors/tally definition

In this paper, all the results related with the TFC are given for the inboard straight leg (blankets #1-#6 corresponding to segments #1-#20) shown in Figure 5.12, except for the integral nuclear heating of the TFC in the FWS and bolometers cases, where the outboard segments (#21-#44) have been also considered.

On the other hand, it is important to note that, for all these results related with TFCs (except for those corresponding to neutron fluence, Section 4.6) several correction factors are used in order to take into account simplifications in the geometry [5]:

- Factor of 1.05 for taking into account the steel-water heterogeneity in blanket shield block.
- Factor of 1.10 for considering the void space inside the housings for the blanket flexible.
- Factor of 1.20 in order to consider the steel-water heterogeneity in the inner-wall shield between VV shells.

In summary, the total correction factor to be used is 1.3992.

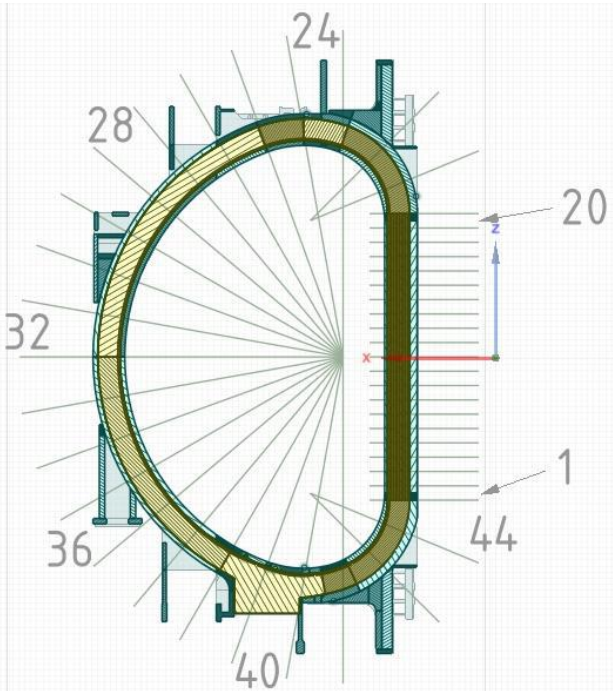

Figure 5.12. Tally segmentation of the TFC [11], [26].

3.3. Neutronic models

Each of the 3D models in CAD for the in-vessel diagnostic systems (Section 2) was simplified according to the procedure described in Section 3.1. This section is devoted to provide information about the simplified neutronic models used to perform the transport calculations.

3.3.1. Reflectometry

For this system, taking into account that there are three types of antennas (Section 2.1), three different neutronic models to simulate each type of sector are required.

Furthermore, for the inboard antennas (single and double cases), after the simplification process and before introducing the diagnostic model into the C-lite reference model, some parts of C-lite have been modified since they interfere with the diagnostic. Specifically, the first wall (FW) of blanket #4 (see Figure 5.1) was modified increasing the cutout from 10 mm to 40 mm. This modification can be appreciated in Figure 5.13, where the original C-lite model is compared with the one containing the diagnostic. Figure 5.14 compares the neutronic model of a single inboard antenna with the one with double. Regarding the diagnostic materials, the reflectometry system is made of SS316L(N)-IG.

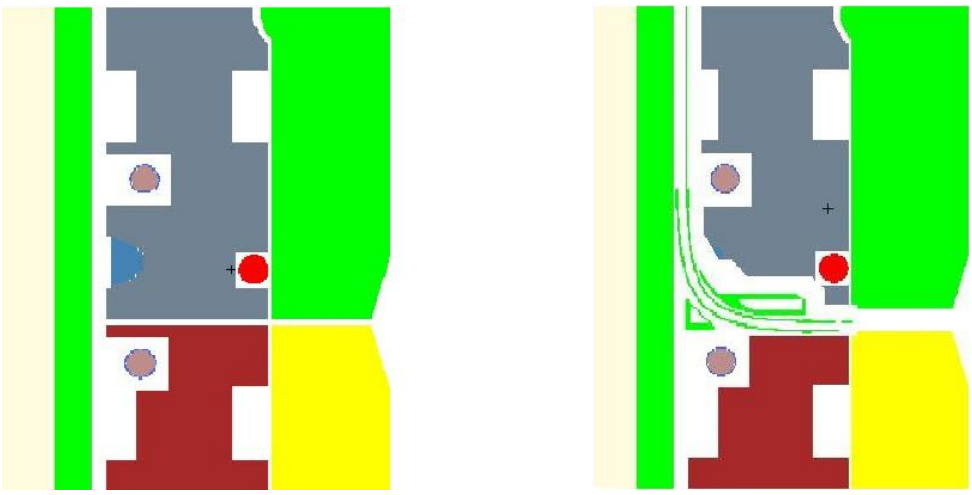

Figure 5.13. MCNP plotter view corresponding to py=8 cut of C-lite model: (a), without diagnostic; (b), with diagnostic.

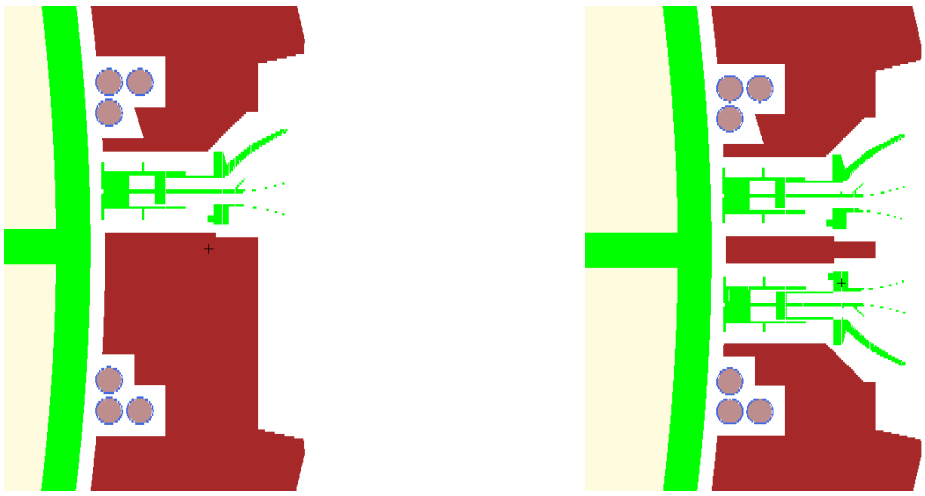

Figure 5.14. C-lite view at plane Z=52 cm for the (a), single and (b), double reflectometry diagnostic case.

3.3.2. Neutron Activation System

For this diagnostic, a single neutronic model was needed since the two sectors that include this diagnosis are identical. Figure 5.15 shows the simplified model used in the radiation transport calculation. The material used for this diagnostic is SS316L(N)-IG.

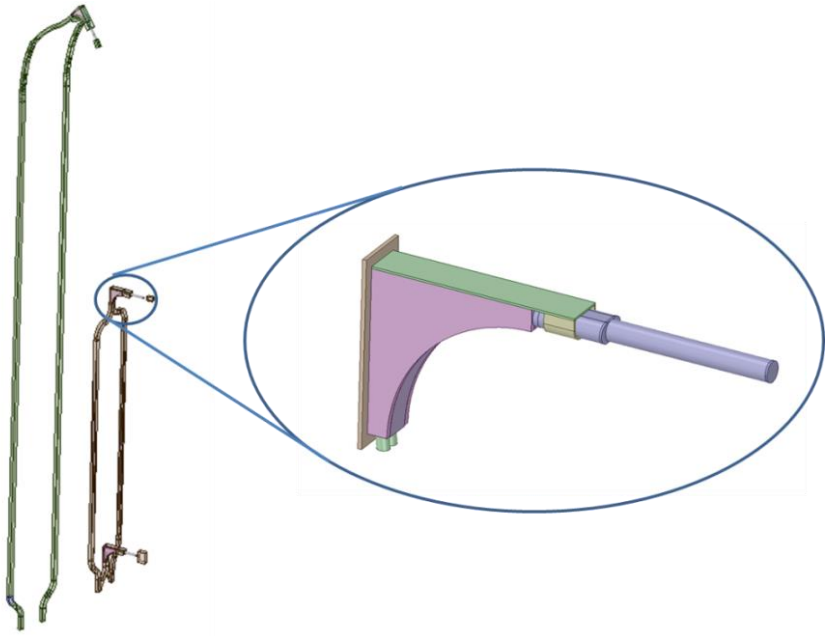

Figure 5.15. 3D CAD simplified model of NAS diagnostic.

3.3.3. First Wall Samples

For the FWS, the neutronic model used in this paper only contemplates the cutouts due to the type L of the FWS. In addition, these cutouts are considered completely empty, as it is a most conservative case.

3.3.4. Bolometers

In this case, as there are six sector with this diagnostic included an each of them with different cutout and number of bolometers, six different neutronic models have been used, one for each sector. Furthermore, for this diagnostic a homogenized material (SS316LN-IG, 48.9%; Mo, 14.8% and void, 36.3%) was used.

4. Radiation load results and analysis

This section is devoted to provide the results achieved in this work for each of the four diagnostic systems. These results are displayed in six different subsections corresponding to the six different radiation loads limits exposed in Section 3.2.1. In each subsection, the results obtained for the different radiation loads are compared between a baseline case, consisting in C-lite without any modification, and the four diagnostic cases in which the respective diagnostics were included in the C-lite model.

Furthermore, for the bolometers case, except for the TFC nuclear heating, results are only provided for sector #1, which is the most critical one since, as it has been shown in Table 5.2, it is the sector with the highest number of bolometers and worse positions.

4.1. VV nuclear heating

The results corresponding to nuclear heating on the VV surface are shown in Figure 5.16 and Figure 5.17 for the baseline and the different diagnostic cases. The calculations were performed using a mesh of around 1.5 cm x 1.5 cm on the surface and 0.5 cm in depth inside the VV for the inboard straight leg, and a rectangular mesh with 2 cm x 2 cm x 2 cm for the outboard region in order to simulate the superficial nuclear heating. Neutron and gamma contributions were taken into account.

In the inboard region (Figure 5.16) the design limit of 0.6 W/m^3 was fulfilled for the all the analyzed cases. In the case of nuclear heating due to neutrons the worst region corresponds to the interblanket gaps due to the direct streaming while, in the case due to photons, the worst region coincides with that behind the manifold cutouts as already reported in [5].

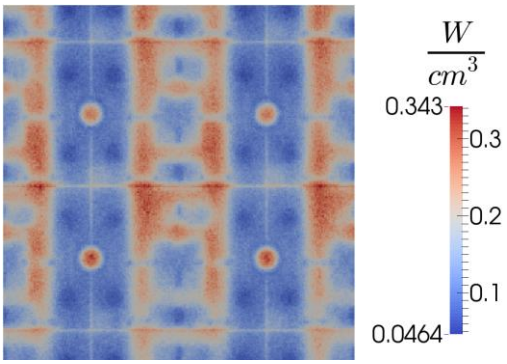
$\frac{W}{cm^3}$
0.343
0.3
0.2
0.1
0.0464

(a)

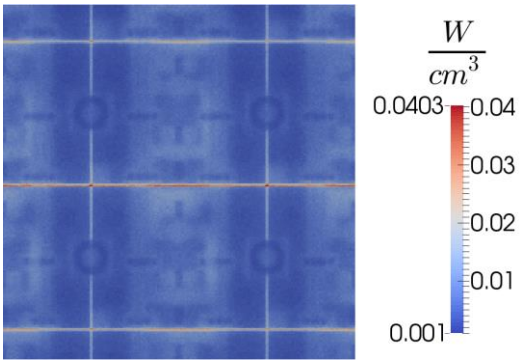
$\frac{W}{cm^3}$
0.0403
0.04
0.03
0.02
0.01
0.001

(e)

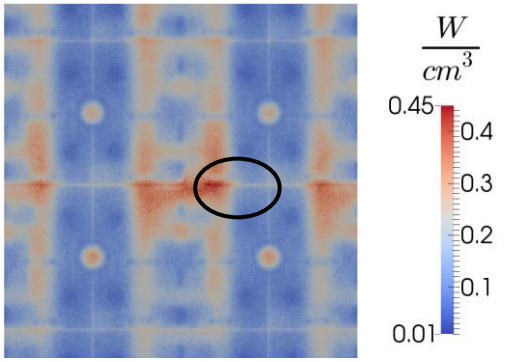
$\frac{W}{cm^3}$
0.45
0.4
0.3
0.2
0.1
0.01

(b)

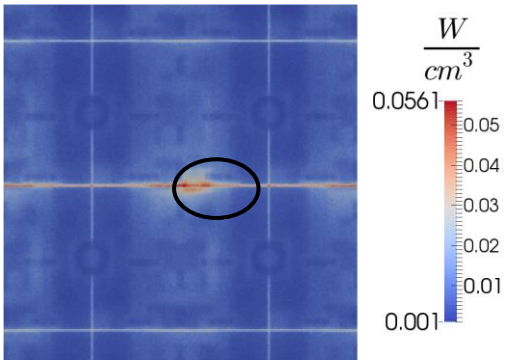
$\frac{W}{cm^3}$
0.0561
0.05
0.04
0.03
0.02
0.01
0.001

(f)

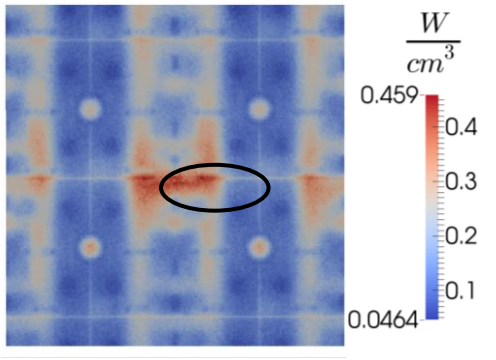
$\frac{W}{cm^3}$
0.459
0.4
0.3
0.2
0.1
0.0464

(c)

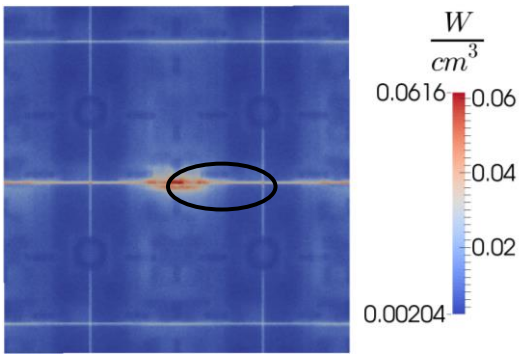
$\frac{W}{cm^3}$
0.0616
0.06
0.04
0.02
0.00204

(g)

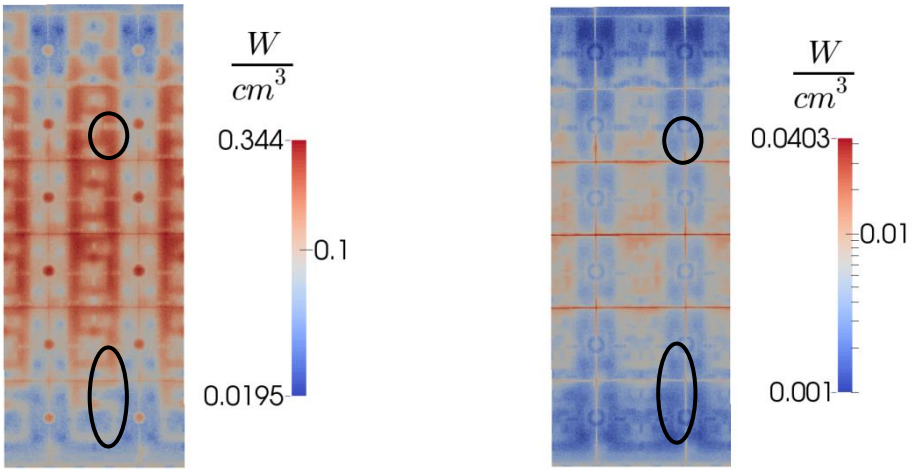

(d) (h)

Figure 5.16. Volumetric nuclear heating in the VV for the baseline (a and e), reflectometry (single: b and f; double: c and g) and bolometers (sector #1) cases due to photons (a, b, c and d) and neutrons (e, f, g and h). Regions enclosed in a black circle correspond to the zone just behind diagnostics [11].

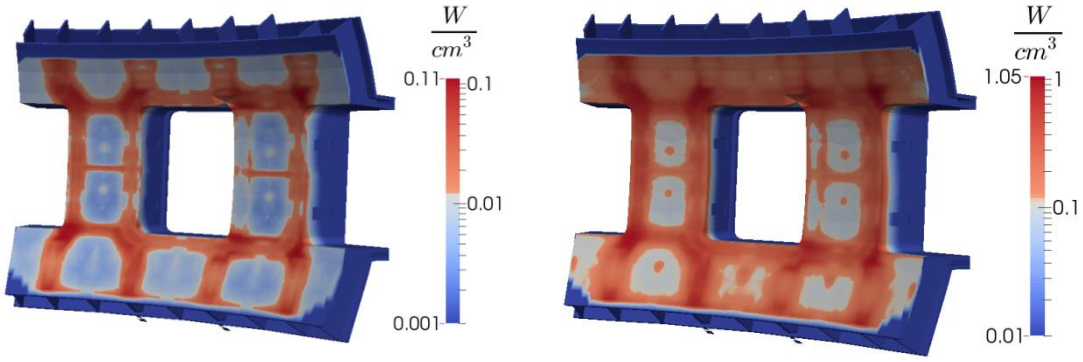

(a) (b)

Figure 5.17. Volumetric nuclear heating in the VV for the baseline case for the outboard around the equatorial port due to: (a), neutrons; (b), photons [11].

In the outboard region (Figure 5.17) the baseline case is already above the required design limit. For the FWS case, the calculated volumetric nuclear heating in the surface of the VV is very similar to the baseline case and thus, it does not fulfillthe required limit. This high value in the outboard region is due to the current design of the blankets and thus, FWS has no noticeable impact on the VV nuclear heating.

The maximum error obtained in these calculations is close to a 10% that is the limit considered for a reliable calculation for this kind of tally in MCNP. In the regions with higher nuclear heating this error is below of a 5%.

4.2. Integral TFCs nuclear heating

In this section the integrated nuclear heating on the TFC in the baseline and the different diagnostic systems is compared. For the evaluation of the integrated nuclear heating the contributions of steel casing, winding pack and ground insulator were taken into account.

For the reflectometry diagnostic, the total nuclear heating in the inboard leg (that is considering the three single and the double antenna sectors) is 9.01 kW, while the total nuclear heating for the baseline case is 8.77 kW (Figure 5.18). Therefore, the difference for the inboard region is 240 W. The highest differences are found in those segments located around the level of blanket #4. On the other hand, the single outboard antenna has an impact of less than 8 W. Thus, the total increment for the whole reactor due to this diagnostic is close to 250 W.

The total nuclear heating in the inboard straight leg due to the NAS system (located in two tokamak sectors) is 8.79 kW (Figure 5.18). Therefore, the inclusion of the NAS diagnostic produces 15 W of increment (around 0.2% of increment) in this magnitude.

Regarding the impact of the FWS, Figure 5.18 and Figure 5.19 show the nuclear heating for the whole reactor in the inboard straight leg and outboard segments, respectively. The total nuclear heating for one sector is 1.931 kW for the baseline, while for the FWS it is 1.934 kW. Therefore, the additional nuclear heating is 2.37 W per sector and 21.3 W for the entire reactor.

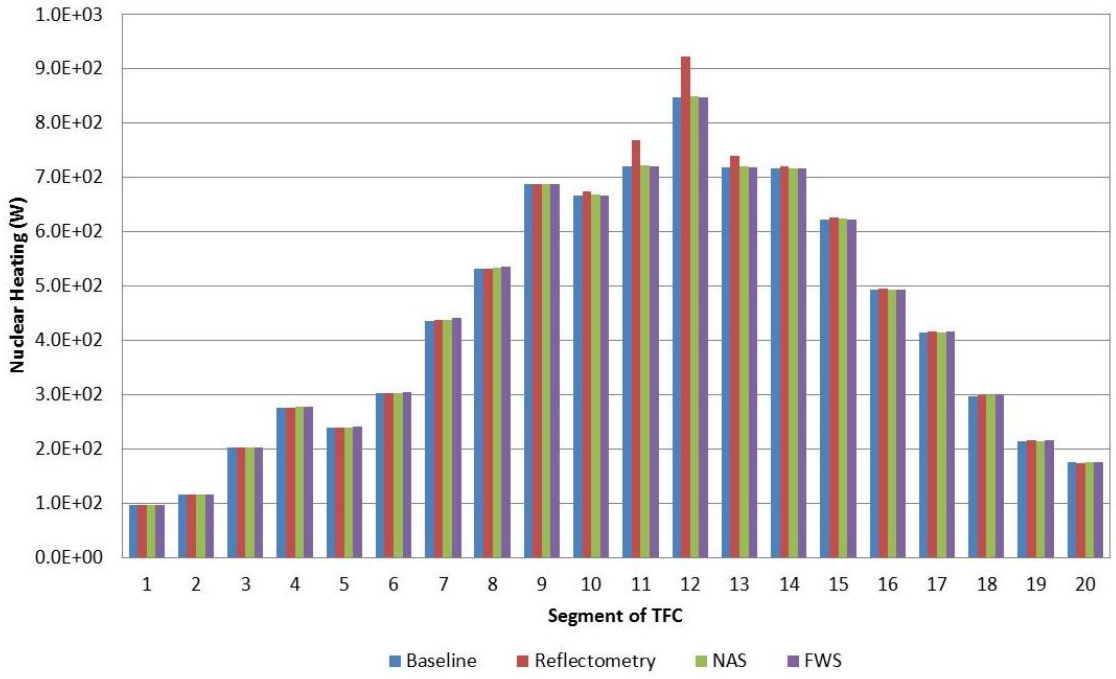

Figure 5.18. Nuclear heating in the TFC inboard straight leg segments for the baseline, reflectometry, NAS and FWS cases [11].

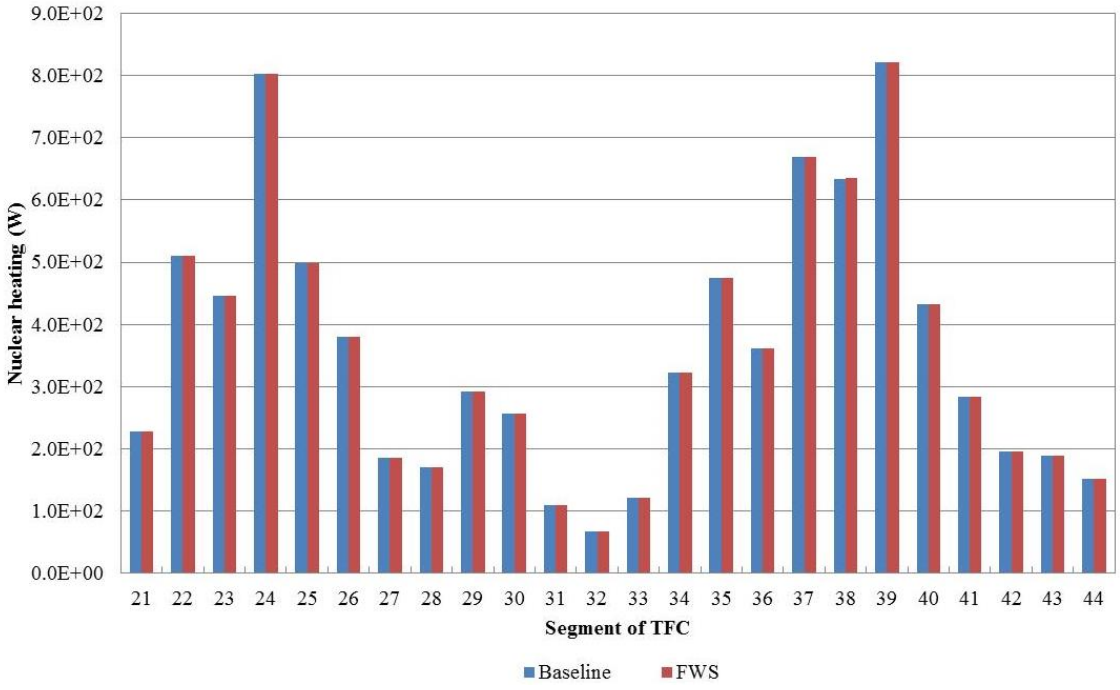

Figure 5.19. Nuclear heating in the outboard TFC segments for the baseline and FWS cases [11].

Figure 5.20 displays the total nuclear heating for the whole reactor for both baseline and bolometers cases. The total nuclear heating for the bolometers case is 17.39 kW and, therefore, their inclusion implies about 20 W of increment in the nuclear heating of TFC.

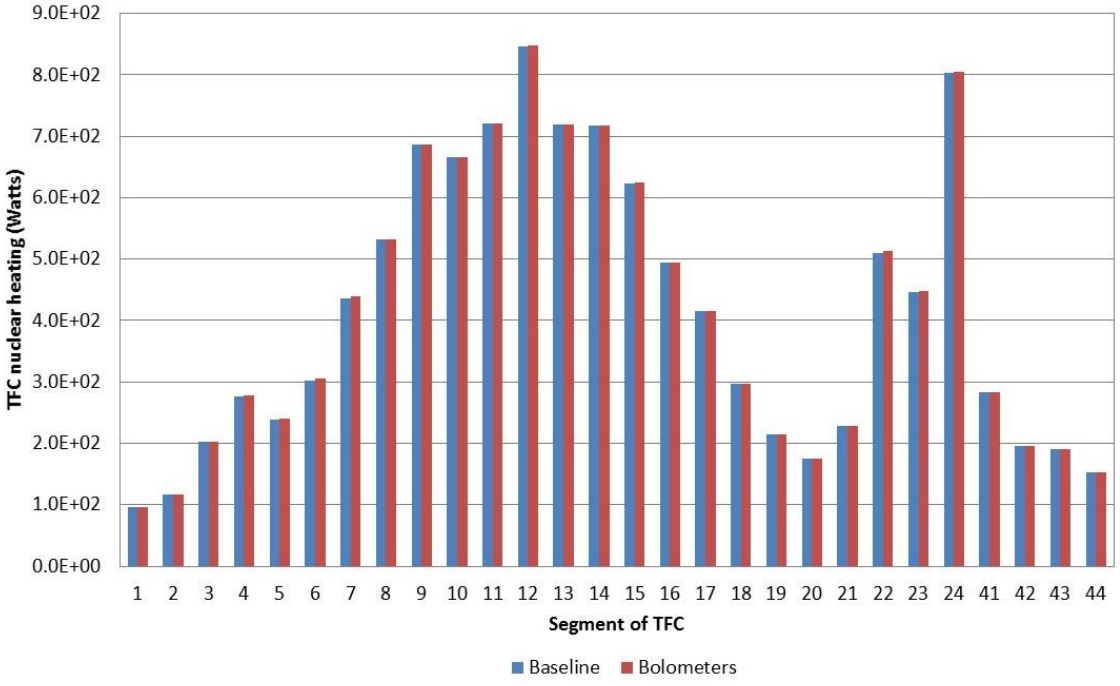

Figure 5.20. Nuclear heating in the outboard TFC segments for the baseline and bolometers cases [11].

Table 5.4. Increment in the integral TFC nuclear heating of the diagnostics systems compared to the baseline [11].

Reflectometry	NAS	FWS	Bolometers
250 W	15 W	21.3 W	20 W

Table 5.4 provides a summary about the difference in the integral TFC nuclear heating when including each of the diagnostics systems, compared to the baseline. On the other hand, the integral nuclear heating for the baseline is 17.37 kW, which is higher than the design limit of 14 kW.

4.3. Volumetric heating of the TFCs windings

This section is devoted to supply volumetric nuclear heating data in the whole winding pack of the inboard straight leg of the TFC, for the 7 mm situated closer to the plasma, for one tokamak sector. Figure 5.21 shows the volumetric nuclear heating for the baseline, reflectometry (single and double antenna), NAS, FWS and bolometers cases. As expected, the NAS, FWS and bolometers cases do not provide significant differences from the baseline case, while the reflectometry case induces a higher nuclear heating. Furthermore, all the different bolometers cases (depending on the considered sector) provide similar results.

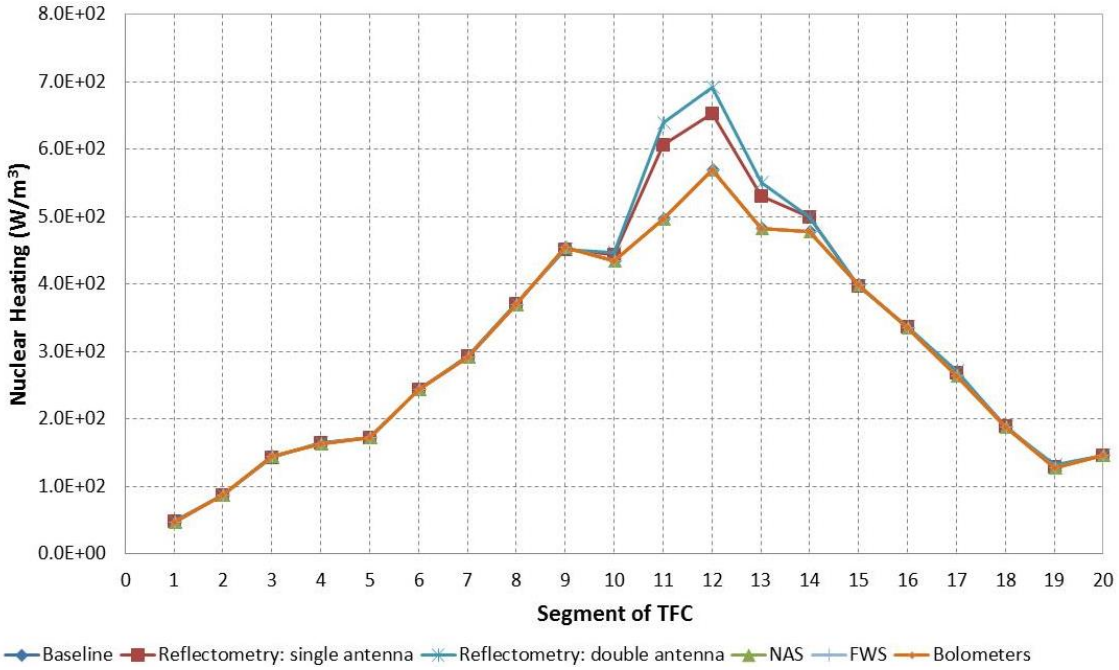

Figure 5.21. Volumetric nuclear heating for the winding pack (for the 7 mm situated closer to the plasma) of the inboard straight leg of the TFC for the baseline, reflectometry (single and double antennas), NAS, FWS and bolometers (sector #1) cases [11].

4.4. Volumetric heating of the TFCs casing

The volumetric nuclear heating for the front steel casing of the inboard straight leg of the TFC can be seen in Figure 5.22 for the baseline, reflectometry, NAS, FWS and bolometers cases. The differences between the values for each of the diagnostic cases compared to the baseline case are equal than in section 4.3. Hence, the highest difference is found for the reflectometry case around the segment #12. As a conclusion, the target design limit of 2 kW/m^3 is not reached in any case.

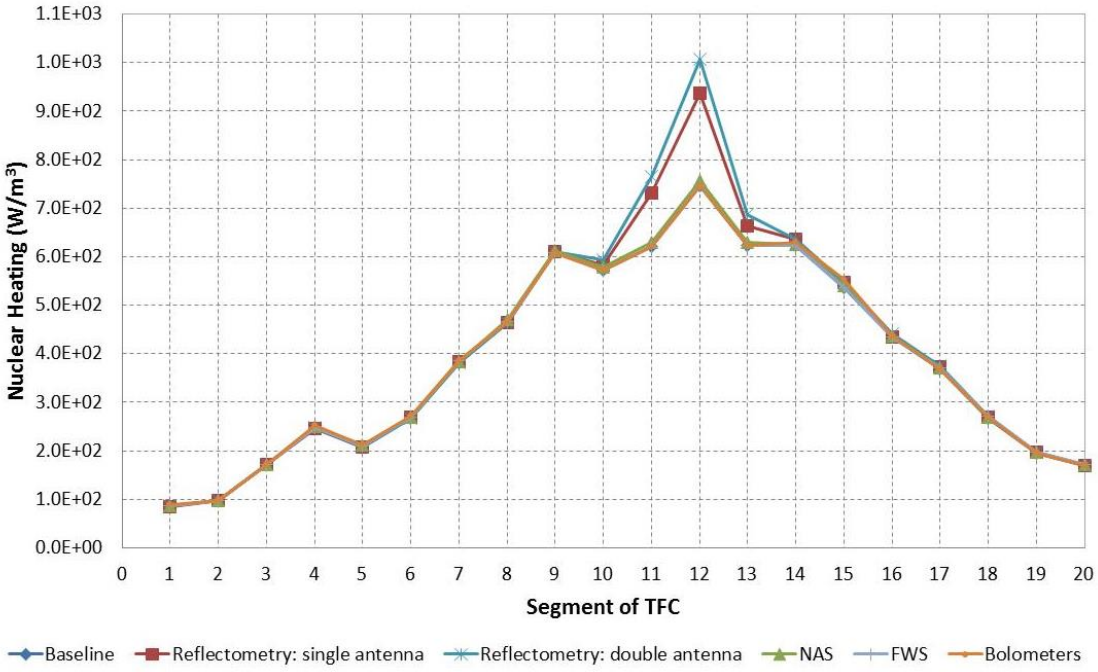

Figure 5.22. Volumetric nuclear heating to the front casing of the inboard straight leg of the TFC for the baseline, reflectometry (single and double antennas), NAS, FWS and bolometers (sector #1) cases [11].

4.5. Dose in TFCs ground insulator

In Figure 5.23 the absorbed dose in the ground insulator of the inboard straight leg of the TFC is shown for all the diagnostic systems cases contrast with the baseline. As it can be seen, the differences among all the cases compared to the baseline are also slight, following the behavior shown in the other magnitudes. Appreciable differences are only detected for the reflectometry case in segments #11-#13. The target design value for this magnitude (10 MGy) is fulfilled in all the studied cases.

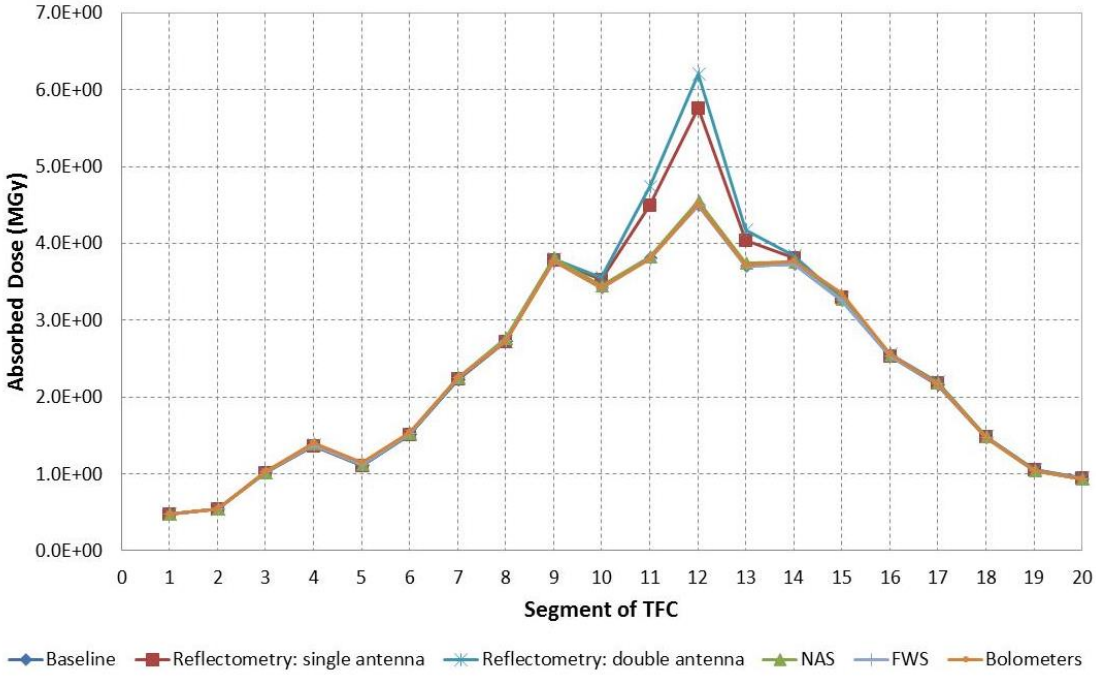

Figure 5.23. Absorbed dose in the TFC frontal ground insulator for the baseline, reflectometry (single and double antennas), NAS, FWS and bolometers (sector #1) cases [11].

4.6. Neutron fluence in the TFCs ground insulator

Although the radiation load limit regarding the neutron fluence in the TFC ground insulator is referred to the total value, in this section the fast (E>0.1 MeV) neutron fluence in the front ground insulator of the inboard straight leg of TFC is also calculated since it is an important magnitude regarding material damage. As it has been commented, for these calculations the correction factors are not used.

Figure 5.24 and Figure 5.25 show the fast and total neutron fluence in the front ground insulator of the inboard straight leg of TFC for the baseline, reflectometry, NAS and FWS and bolometers cases. The relative differences between all the cases for both fast and total neutron fluence are equal to the other magnitudes. The target limit of 10^{22} n/m^2 is fulfilled for either case.

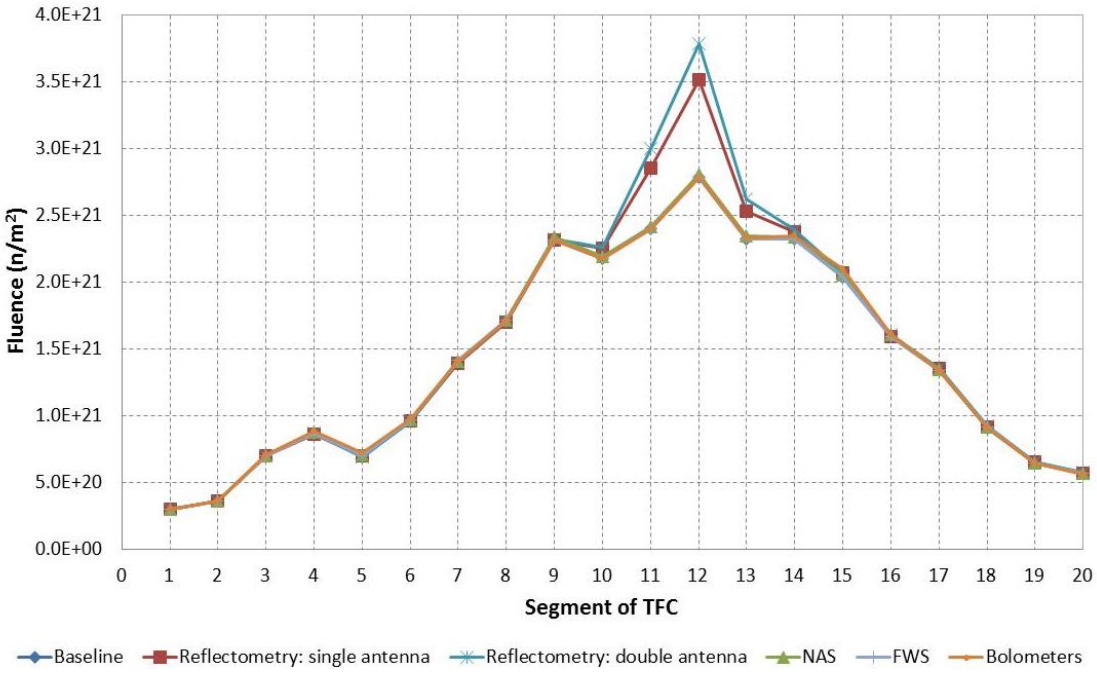

Figure 5.24. Fast neutron fluence in the front insulator of the inboard straight leg for the baseline, reflectometry (single and double antennas), NAS, FWS and bolometers (sector #1) cases [11].

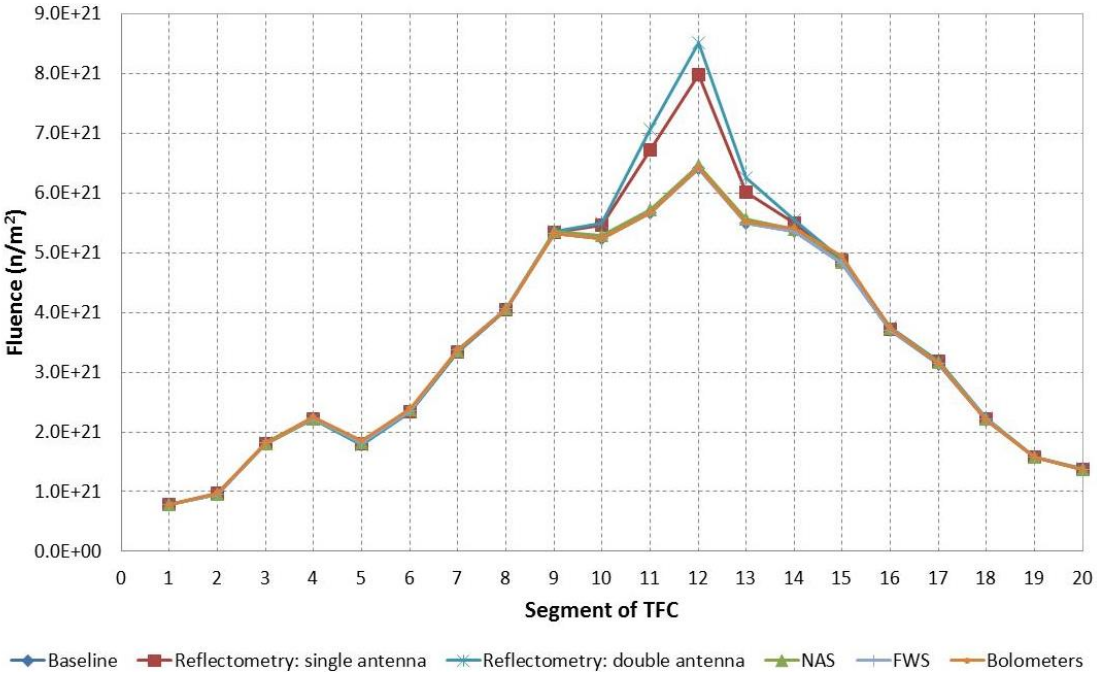

Figure 5.25. Total neutron fluence in the insulator of the inboard straight leg for the baseline, reflectometry (single and double antennas), NAS, FWS and bolometers (sector #1) cases [11].

5. Summary and conclusions

In this chapter the impact of reflectometry, NAS, FWS and bolometers in-vessel diagnostics on the radiation loads on the VV and TFC was evaluated. For this purpose, a baseline case (C-lite model without any diagnostic system included) and four different cases (each one with each of the diagnostics included) were compared. Results revealed that all the studied radiation loads present a similar behavior for all the cases.

The NAS, FWS and bolometers systems present a negligible impact on the radiation loads when compared to the baseline case. However, the reflectometry system has a maximum difference of 35% on the radiation loads on the TFC (located at segment #12 of the TFC inboard straight leg) compared to the baseline case, corresponding with the region where the double antenna is situated. For the remaining segments, there are no significant differences (none above 5%) except for the two adjacent segments (i.e. segments #11 and #13, where differences are 13% and 25% respectively). To give a figure of this impact, in the case of the integral nuclear heating in the TFC the impact of the inclusion of the NAS, bolometer and FWS systems in one ITER sector is ~20 W while the impact of reflectometry system is one order of magnitude higher (~250 W).

With regard to the compliance of the radiation limits, the obtained results are summarized in Table 5.5 where it can be seen that, all the radiation loads except the nuclear heating on the outboard VV surface and the integral nuclear heating in the TFC are under the design limits.

The contribution of the in-vessel systems to the integral nuclear heating on the TFC is aroundt 2% of the target limit (~2800 W above the baseline case). The nuclear heating on the VV surface the excess is found in the outboard region, where all the systems provide almost the same values than the baseline case. Hence, these results rule out that the analyzed systems are the cause of overcoming the limits. In fact, the excess on nuclear heating in both cases, already present in the baseline case, is a well-known problem for the current configuration of the blankets system of ITER, which modification is part of the ongoing ITER design tasks.

Table 5.5. Summary of the radiation loads limits compliance of the in-vessel diagnostic systems [11].

	Reflectometry	**NAS**	**FWS**	**Bolometers**
Nuclear heating on the VV surface Outboard/Inboard	×/✓	×/✓	×/✓	×/✓
Integral TFC nuclear heating	×	×	×	×
Maximal nuclear heating in the TFC winding pack	✓	✓	✓	✓
Maximal nuclear heating in the TFC casing	✓	✓	✓	✓
Peak of absorbed dose in TFC ground insulator	✓	✓	✓	✓
Peak of neutron fluence in the TFC ground insulator	✓	✓	✓	✓

✓ means that the limit is met, and × means that the limit is not fulfilled.

Under these conditions and taking into account that the reconfiguration of the blankets is going to improve their shielding capability, the contribution of the in-vessel diagnostics systems to the VV and TFC radiation loads seems not critical for these components.

6. References

[1] ITER Organization. *ITER. Diagnostics*. Available: https://www.iter.org/mach/diagnostics [Accessed 5 October 2016].

[2] R. A. Pitts. *ITER status and challengues*. ITER IDM location: https://user.iter.org/?uid=S3W8V7 (**2015**).

[3] A. Encheva, L. Bertalot, B. Macklin, G. Vayakis, C. Walker. *Integration of ITER in-vessel diagnostic components in the vacuum vessel.* Fusion Engineering and Design, Vol. 84, pp. 736 – 742 (**2009**). Doi: http://dx.doi.org/10.1016/j.fusengdes.2008.12.101

[4] H. Iida, V. Khripunov, L. Petrizzi, G. Federici. *Nuclear Analysis Report*. ITER IDM location: https://user.iter.org/?uid=22F2ST (**2004**).

[5] A. Suárez. *Impact of blanket cutouts for bolometers in VV and TFC neutronics.* ITER IDM location: https://user.iter.org/?uid=LADD8Q (**2014**).

[6] J.P. Catalán, R. García, A. Suárez. *Nuclear heating in the antenna of the reflectometry diagnostic*. ITER Neutronics Report. ITER IDM location: https://user.iter.org/?uid=Q5MJSQ (**2014**).

[7] J.P. Catalán, R. García, A. Suárez*. Impact of reflectometry diagnostic on the radiation loads of the Vacuum Vessel and Toroidal Field Coils*. ITER Neutronics Report. ITER IDM location: https://user.iter.org/?uid=QEJYFF (**2015**).

[8] J.P. Catalán, R. García, A. Suárez. *Impact of Neutron Activation System (NAS) diagnostic on the radiation loads of the Vacuum Vessel and Toroidal Field Coils.* ITER Neutronics Report. ITER IDM location: https://user.iter.org/?uid=QEKTWA (**2014**).

[9] J.P. Catalán, R. García, A. Suárez. *Neutronics for the First Wall Diagnostics and impact on toroidal field coils (TFC) and vacuum vessel (VV) heating*. ITER Neutronics Report. ITER IDM location: https://user.iter.org/?uid=QN66Q7 (**2015**).

[10] J.P. Catalán, R. García, A. Suárez. *Impact of blanket cutouts for bolometers on the radiation loads of the Vacuum Vessel and Toroidal Field Coils*. ITER Neutronics Report. ITER IDM location: https://user.iter.org/?uid=QEYKCW (**2015**).

[11] J.P. **Catalán**, R. García, A. Suarez, L. Bertalot, J. Sanz, G. Vayakis, V. Krasilnikov, P. Shigin, R. Reichle, V. Udintsev, M. Walsh. *Impact of ITER in-vessel diagnostics on the radiation loads of the Vacuum Vessel and Toroidal Field Coils* (**under ITER review**).

[12] G. Vayakis, C.I. Walker, F. Clairet, R. Sabot, V. Tribaldos, T. Estrada, E. Blanco, J. Sánchez, G.G. Denisov, V.I. Belousov, F. Da Silva, P. Varela, M.E. Manso, L. Cupido, J. Dias, N. Valverde, V.A. Vershkov, D.A. Shelukhin, S.V. Solda. *Status and prospects for mm-wave reflectometry in ITER*. Nuclear Fusion, Vol. 46, nº 9, pp. 836 – 845 (**2006**). Doi: http://dx.doi.org/10.1088/0029-5515/46/9/S20

[13] D. Haikney. *CPD - Install Diagnostics, Instrumentation and Fuelling Installation - Lower Port Extensions*. ITER IDM location: https://user.iter.org/?uid=Q3ZES6 (**2014**).

[14] L. Bertalot, R. Barnsley, M.F. Direz, J.M. Drevon, A. Encheva, S. Jakhar, Y. Kashchuk, K.M. Patel, A.P. Arumugam, V. Udintsev, C. Walker and M. Walsh. *Fusion neutron diagnostics on ITER tokamak*. Journal of Instrumentation, Vol. 7, nº 4 (**2012**). Doi: http://dx.doi.org/10.1088/1748-0221/7/04/C04012

[15] M.S. Cheon, C.R. Seon, S. Pak, H.G. Lee, L. Bertalot, R.A. Forrest. *Operational Radioactivity Evaluation of ITER Diagnostic Neutron Activation System*. IEEE Transactions on Plasma Science, Vol. 38, nº 3, pp. 274 – 277 (**2010**). Doi: http://dx.doi.org/10.1109/TPS.2009.2036917

[16] G. Martínez, A. Martina, C. Watts, E. Veshcheva, R. Reichlea, P. Shigina, F. Sabourinc, S. Gicquela, R. Mitteaua, J. González. *Diagnostic integration solutions in the ITER first wall*. Fusion Engineering and Design, Vols. 98 – 99, pp. 1548 – 1551 (**2015**). Doi: http://dx.doi.org/10.1016/j.fusengdes.2015.06.046

[17] V. Udintsev, M. Walsh. *ITER Diagnostics. First Wall Samples* (**2014**). Available: http://www.bigscience.dk/media/46778/iter_diagnostics_udintsev_v1_0.pdf [Accessed: 10 December 2015].

[18] K. Tahiliani, R. Jha. *Chapter 7: Bolometers for Fusion Plasma Diagnostics*. India, Institute for Plasma Reserach (**2012**). Doi: http://dx.doi.org/10.5772/33466

[19] F. Sánchez. *EU contribution to the Diagnostics of ITER*. Danish Big Science Network Meeting 2014: Fusion for Energy (**2014**). Available: https://industryportal.f4e.europa.eu/IP_EXT_REFERENCE_DOCUMENTS/F4E%20-%20Diagnostics%20-%20Counsell%20IBF-13.pdf [Accessed: 10 December 2015].

[20] *SpaceClaim*. Available: http://www.spaceclaim.com/

[21] Y. Wu. *CAD-based interface programs for fusion neutron transport simulation FDS Team*. Fusion Engineering and Design, Vol. 84, pp. 1987 – 1992 (**2009**). Doi: http://dx.doi.org/10.1016/j.fusengdes.2008.12.041

[22] D. López Aldama, A. Trkov. *FENDL-2.1 Update of an evaluated nuclear data library for fusion applications*, INDC(NDS)-467 Distr. FE. IAEA.

[23] X-5 Monte Carlo Team. *MCNP – A General Monte Carlo N-Particle Transport Code Version 5*, LA-CP-03-0245, Los Alamos National Laboratory (**2005**).

[24] *Paraview*. Available: http://www.paraview.org/

[25] M. Loughlin, E. Polunovskiy, K. Ioki, M. Merola, G. Sannazzaro, M. Sawan. *Nuclear Shielding for the Toroidal Field Coils of ITER*. Fusion Science and Technology, Vol. 60, nº 1, pp. 81 – 86 (**2011**).

[26] E. Polunovskiy. *Nuclear responses in TFC*. ITER IDM location: https://user.iter.org/?uid=BP6B8V (**2015**).

Chapter 6
Characterization of the DCLL DEMO model for safety and environment purposes

This chapter is intended to characterize the DCLL DEMO breeder blanket for safety and environment purposes, on the basis of using the 3D neutronic models developed during 2014 and 2015. Additionally, a comparison among the four BB concepts is done. Finally, radioactive waste management assessment was carried out focused on the analysis of the needed impurities mitigation for disposing these wastes in El Cabril near-surface facility.

1. Introduction

The main goal of the DEMO reactors is to demonstrate the commercial viability of a power plant based on magnetic confinement fusion. A DEMO reactor is conceived to be the step between ITER and a commercial reactor. The DEMO construction is planned to begin by 2030, in order to allow the start of operation in the early 2040s and reaching the goal of fusion electricity in the grid by 2050 [1].

Currently four BB concepts are being considered: HCPB, HCLL, WCLL and DCLL (see Chapter 2, Section 4). Due to the differences in materials and construction of the four BB concepts, differences in nuclear responses when exposed under neutron irradiation are detected. This is of particular importance to safety, maintenance or waste management calculations. In particular, activity inventories are fundamental for decommissioning and waste disposal since higher activities and longer lived isotopes affect the disposal route for irradiated material, while the decay heat values are particularly important for safety analysis where the amount of decay heat will play an important role in the assessment of Loss Of Coolant Accidents (LOCA) and or determining the cooling needs. In this frame, the aim of this chapter is to characterize the DEMO DCLL for further safety and/or environment assessments.

DCLL is basically characterized by the use of self-cooled breeding zones with the liquid metal LiPb serving as T breeder, neutron multiplier and coolant. He is used for cooling the FW and other supporting structures made of the ferritic–martensitic steel Eurofer-97. Taking into account that the LiPb flows at a higher velocity than it does in other blankets that use is, such as HCLL or WCLL (but lower than self-cooled LiPb), it extracts most of the reactor power while

the He cooling extracts the remaining. In addition, FCI are used for thermal and electrical insulation since the intense magnetic field causes important MHD and thermal-hydraulic effects. Figure 6.1 presents a scheme for the equatorial outboard model (in the 2014 DCLL model design) [2].

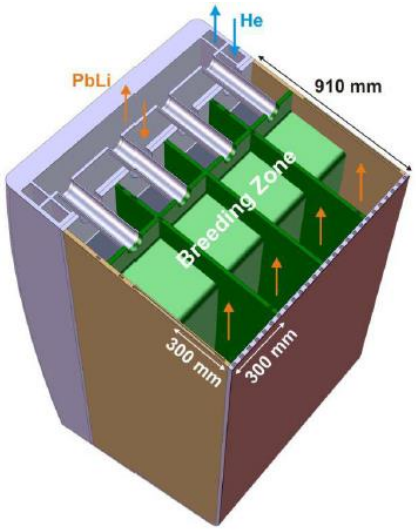

Figure 6.1. DCLL equatorial outboard scheme [2].

This chapter presents the results of performed calculations to ascertain the decay heat and activity for both the entire reactor and from each blanket module separately, as well as for the entire manifold/Back Supporting Structure (BSS). These calculations were carried out in the *SAE-2.17.1-T01-D04* task during the 2015 and 2016 years, with the 2014 and 2015 models, respectively, under the Eurofusion programme. Within these activities, and in the framework of this thesis, part of the work described in this chapter for the 2014 model has given rise to a report [3] and two papers [4]-[5], and one more report colleting the results obtained for the 2015 model is also being prepared.

Previously to this work, there was a participation within the *WP13-SYS-02-T08* task of EFDA related to activation calculation in the HCLL model [6]. This task was especially important in order to learn how to deal with this kind of work and the obtained results turned out to be part of a publication [7].

The organization of the present chapter is as follows. First, the analysis corresponding to 2014 model (and therefore performed during 2015) is collected in Section 2. Section 3 is devoted to provide the update corresponding to the model of 2015 (carried out during 2016). This two mentioned sections, in turn, are subdivided in the same way: description of the model, computational assumptions and methodology and results. Section 4 compares the results for

the 2014 DCLL to other BB concepts, since analogous calculations were carried out for the other three BB concepts[20] in the framework of Eurofusion[21].

On the other hand, it is known that one of the main presuppositions for the global interest in nuclear fusion is that it should be cleaner and safer compared to traditional nuclear technology. This implies, among other considerations, that the produced radioactive waste in a fusion power plant is expected to be categorized as LLW after no more than 100 year of cooling time. In fact, it is desired to fulfillthis goal at 50 years, in the effort to reduce the radiological impact of fusion energy as soon as possible, on the road to be not a burden for future generations. For this reason, Section 5 is devoted to determine the composition limits for different materials to minimize the radiological impact of waste and achieve the LLW at the mentioned cooling time. It is worth mentioning that previous work on radioactive waste for a DCLL model was performed in [8]. Finally, Section 6 highlights the main conclusions of this chapter.

2. Analysis on the 2014 DEMO DCLL model

This section is devoted to provide the description and results of the activation analysis performed on the 2014 DEMO DCLL model. For this purpose, Section 2.1 describes the generation and characteristics of the model. Section 2.2 is devoted both to describe the neutronic model used, specifying materials as well as the irradiation scenario selected, and to explain the calculation methodology followed. The last subsection (2.3) shows the achieved activation results.

Aside from the calculations to obtain the decay heat and activity both from the blanket modules for the entire reactor, each blanket module separately, and the entire manifold, an additional analysis on the equatorial outboard module was done in order to i) study the contribution from the different components to both activation responses (decay heat and activity) and ii) identify major radionuclides contributing to the decay heat in the different components.

[20] CCFE is in charge of the HCLL, KIT of the HCPB, and the Lithuanian Energy Institute (LEI) of the WCLL concept.

[21] For 2015, a similar comparison is expected. However, at the time of presentation of this thesis the results corresponding to the other models were not yet widespread.

2.1. Description of the 2014 DEMO DCLL model

Under the Eurofusion Programme, the process for generation of computational models for neutron transport and transmutation analyses is being undertaken. As a first step, a generic neutronic model of DEMO (Figure 6.2) was developed by KIT within the Breeder Blanket Work Package (WPBB) of the PPPT Programme as the basis for the integration of the different blankets [9]-[10].

Table 1 summarizes some of the related machine and plasma parameters that were used for the generation of the model. According to the fusion power, the neutron source for the total reactor is $5.580 \cdot 10^{20}$ n/s.

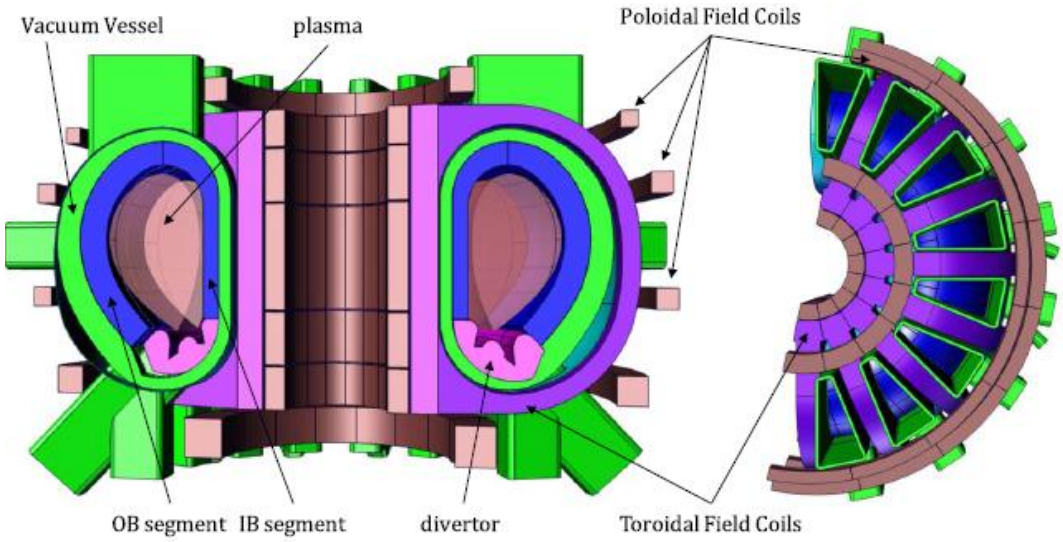

Figure 6.2. 2014 DEMO CAD generic model [2].

Table 6.1. DEMO parameters [11].

Parameter	Value
Major radius (m)	9.0
Minor radius (m)	2.25
Plasma elongation	1.56
Plasma triangularity	0.33
Plasma peaking factor	1.7
Fusion power (MW)	1572
Net electric power (MW)	500

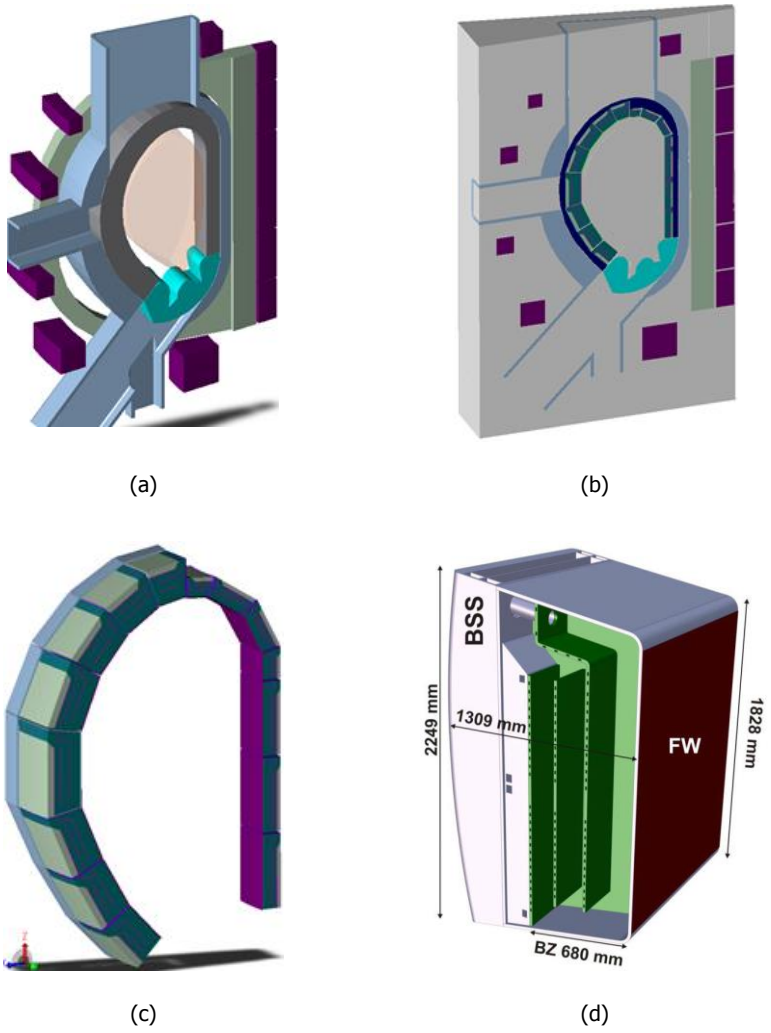

Figure 6.3. (a), Neutronic CAD DEMO generic model; (b), Complete neutronic 2014 DEMO DCLL model; (c), Detailed neutronic model of the DCLL blankets segment (hiding lateral walls and BP); (d), Dimensions for the DCLL equatorial outboard [5].

The geometric modelling of the different blankets and their integration into the DEMO generic neutronic model is also being accomplished by different institutions. Spain, and more specifically CIEMAT, is leading the development of a DCLL BB within the agreement between European institutions for the period 2014-2018, under the mentioned Eurofusion Programme [2],[12]. As a result, the 2014 3D DEMO DCLL reactor neutronic model was produced [13]. Figure 6.3 shows the CAD model (generic and for DCLL), the module's segmentation inside a sector and the main dimensions for the equatorial outboard module.

Regarding the blanket description, the generic model can be divided into 32 sectors of 22.5º. However, since every inboard sector can be divided into two segments (of 11.25º) and every outboard into three, the blanket is composed of 48 outboard and 32 inboard segments [2].

Each of the blanket modules in the model has a similar structure but with different dimensions, containing the following components (Figure 6.4): armour (coating of the first wall), first wall (FW), side, top and bottom walls, stiffenings, LiPb, inner collector and Back Plate (BP). FCI were not yet included in this neutronic model. The material compositions for each of the components are displayed in Table 6.2.

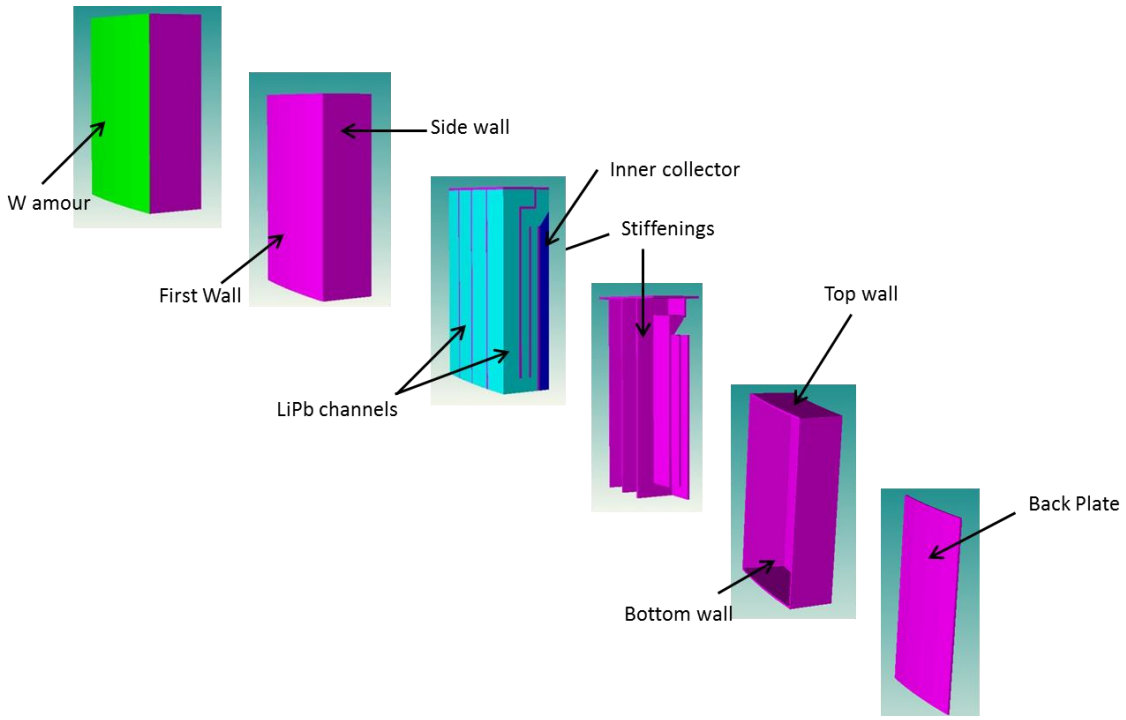

Figure 6.4. Components of the blanket modules in the DCLL neutronic model.

Table 6.2. Material composition for the components of the blanket modules in the DCLL neutronic model.

		Composition (% vol.)			
Component		**Eurofer**	**He**	**LiPb**	**W**
FW	FW coating				100
	FW	85.54	14.46		
Breeder zone+ Helium collector	1^{st}, 2^{nd} and 3^{rd} radial stiffening	91.33	8.67		
	LiPb channels			100	
	He	53	47		
	Eurofer walls				
Walls	Side walls	85.54	14.46		
	Top Wall	85.54	14.46		
	Bottom Wall	85.54	14.46		
	BP	85.54	14.46		

2.2. Computational assumptions and methodology for decay heat and activity calculations

This section is devoted to describe the computational model (2.2.1), the irradiation scenario (2.2.2), and the methodology followed for the calculations, including computational assumptions and material compositions (2.2.3).

2.2.1. Computational model: blanket description

An MCNP model of the fusion power DEMO reactor with DCLL blanket modules was used for the activation calculations. The MCNP model consists of a DCLL torus sector of 11.25º and includes blanket modules, manifolds, shields, vacuum vessel, coils and divertor (Figure 6.5).

Blanket modules in the model are numbered anti-clockwise from 1 to 15 (Figure 6.5), starting from the one close to the divertor following the inboard (1-7) and then downwards along the outboard (8-15). Since the torus sector is 11.25º (not 22.5º) it includes one complete module for those numbered 1-7 and one and a half modules for those named 8-15. Therefore, the complete model consists of 224 inboard modules and 384 outboard modules, giving rise a total number of 608 modules.

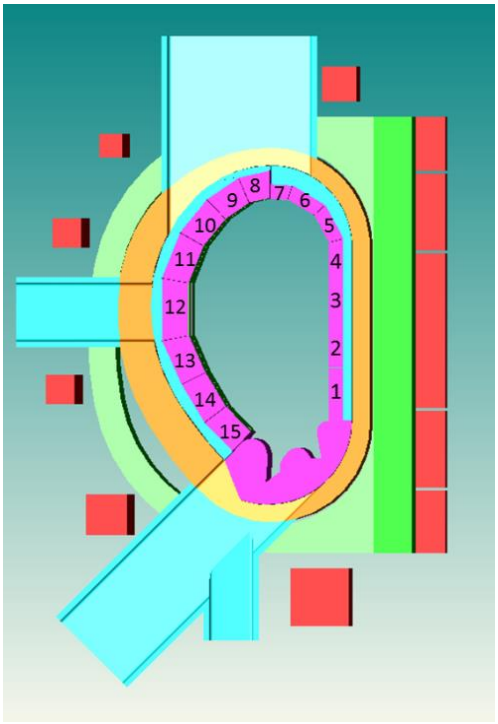

Figure 6.5. MCNP plot of 2014 DEMO DCLL model with numbered blanket modules (vertical cut).

2.2.2. Irradiation scenario and cooling times of interest

The assumed irradiation scenario for the activation calculations is based on the first DEMO operation phase: Continuous operation over 5.2 years (CY) minus 10 days at 30% of the nominal fusion power followed by 10 days pulsed operation with 48 pulses of 4 hours at full power and 1 hour dwell time in between (Figure 6.6). The after shutdown times considered for the calculation of the activity inventories and the decay heat are the following: 1 s, 5 min, 30 min, 1 hr, 3 hr, 5 hr, 10 hr, 1 day, 3 days, 1 week, 2 weeks, 4 weeks, 8 weeks, 6 months, 1 year, 10 years, 100 years, 300 years and 1000 years. 300 years of cooling time is considered as it is a fixed time to fulfillrequirements for El Cabril Spanish near surface facility for the disposal of radioactive wastes [14].

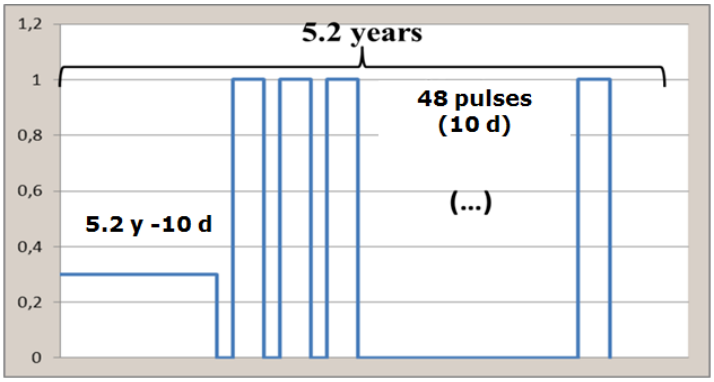

Figure 6.6. Irradiation scenario [14].

2.2.3. Calculation methodology

Firstly, the structure of the blanket modules was simplified into five components (Figure 6.7): W armour, FW, caps (both side/lateral walls as well as the top and bottom walls; i.e. the casing without the FW and BP), breeder module (the whole interior of the blanket module; i.e. stiffenings, LiPb channels and inner collector) and BP.

Secondly, the volume averaged neutron flux spectra were calculated for each of these components in each blanket module, after some slight adaptation of the reference neutronic model provided by CIEMAT. Finally, the activation calculations were performed for each component using the obtained average neutron flux and an average representative material defined from the volume fractions of the materials and voids in the component. Table 6.3 describes the material composition (in volume fraction) used for each of the components of the blanket modules.

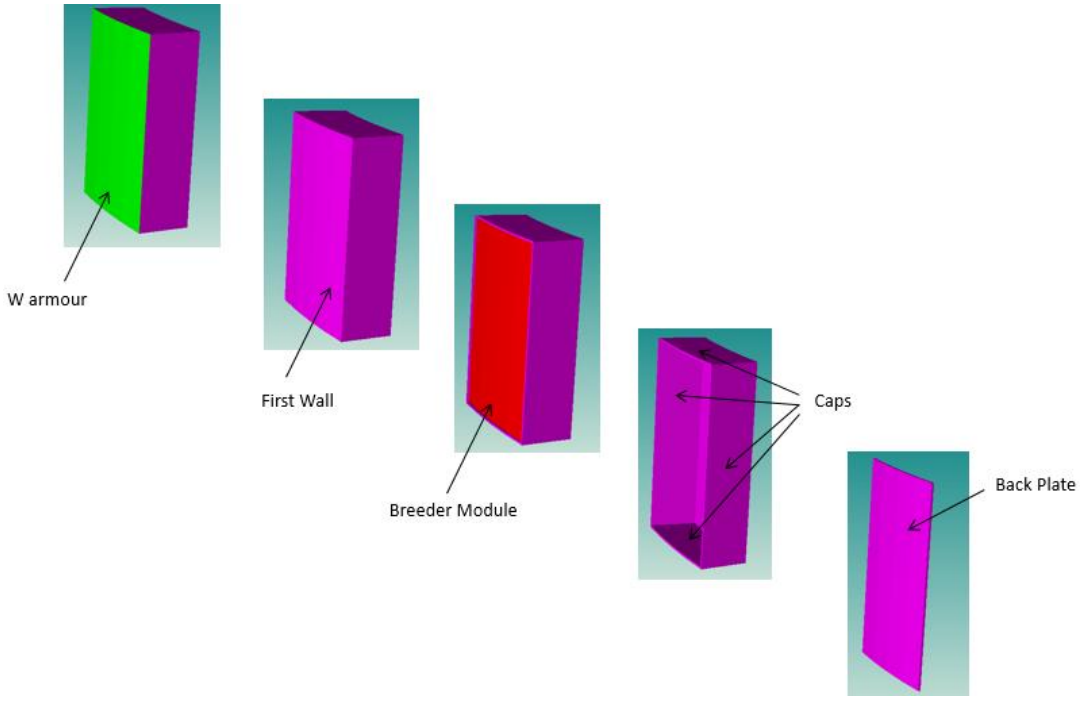

Figure 6.7. Components used in the activation calculations for each of the blanket modules.

Table 6.3. Material composition for activated components.

Volume (%)	Eurofer	LiPb (90% ^{6}Li)	Tungsten	Void (He @ 80bar)	Total
W armour (W) (2mm)			100		100
FW (t=20mm)	85.54			14.46	100
Breeder module	17.85	73		9.15	100
Caps	85.54			14.46	100
BP	85.54			14.46	100
Manifold	51.29	44.36		4.35	100

The material elemental compositions used to perform activation calculations contain impurities as it can be seen in Table 6.4, and were taken from [15]-[17]. It is worth noting that in the LiPb there is a ^{6}Li enrichment of 90%.

The simulation procedure starts with the calculation of the volumes for the materials and voids using the stochastic volume determination method. Afterwards, average neutron fluxes were computed with MCNP5 code [23] in each of the material cells; i.e. five cells in each blanket module corresponding with each of the components, and two cells in the manifold: one corresponding to the inboard (behind the inboard modules 1-7) and the second one corresponding to the outboard (behind the outboard modules 8-15).

Table 6.4. Elemental composition of the materials in the 2014 DEMO DCLL reactor blanket [15]-[17].

Element	% weight		
	Tungsten	**Eurofer**	**LiPb**
H	0.0005	-	-
Li	-	-	0.620
B	-	0.001	-
C	0.003	0.105	-
N	0.0005	0.04	-
O	0.002	0.001	-
Na	0.001	-	-
Mg	0.0005	-	-
Al	0.0015	0.004	0.010
Si	0.002	0.026	0.010
P	0.002	0.002	-
S	0.0005	0.003	-
K	0.001	-	-
Ca	0.0005	-	-
Ti	0.0005	0.001	-
V	-	0.2	0.005
Cr	0.002	9.0	0.005
Mn	0.0005	0.550	0.005
Fe	0.003	88.821	0.005
Co	0.001	0.005	-
Ni	0.0005	0.01	0.005
Cu	0.001	0.003	0.001
Zn	0.0005	-	0.001
As	0.0005	-	-
Zr	0.0005	-	-
Nb	0.001	0.005	0.001
Mo	0.01	0.003	0.005
Pd	-	-	0.001
Ag	0.001	-	0.001
Cd	0.0005	-	-
Sn	-	-	0.020
Ba	0.0005	-	-
Ta	0.002	0.12	-
W	99.9595	1.1	0.020
Pb	0.0005	-	99.265
Bi	-	-	0.020
Density (g/cc)	19.24	7.87	9.54

The DEMO neutron source used is represented in a FORTRAN source routine that is compiled with the MCNP code and the model was run for 10^9 source neutrons. Once the volumes and fluxes are obtained, activation is accomplished.

The complete simulation procedure is carried out automatically for all the cells belonging to the blanket which are a total of 75 complete material zones for the 11.25º torus sector, as well as for the two cells of the manifold. For automatized calculation some coupling schemes developed by F. Ogando were used (see Chapter 3, Section 6). It is worth noting that although in the outboard (blanket modules 8-15) the 11.25º torus sector contains 1.5 blanket modules, the contribution of these halves modules was estimated multiplying the values obtained for the complete ones by 0.5. Finally, in order to obtain the activity and decay heat for all the blanket modules and manifold for the entire reactor (360º), results for the 11.25º torus sector were multiplied by 32.

Library used for transport is the JEFF-3.1.1, according to the "*Guidelines for Neutronic Analyses*" recommendations [14]. Nevertheless, for a very limited number of nuclides FENDL (3.0 and 2.1) which is also recommended, is used when no data for these nuclides are found in the JEFF library, namely ^{12}C, ^{18}O, ^{180}W, sulphur and tin. Average neutron fluxes are obtained in the standard VITAMIN-J 175 group structure and then activation calculations are carried out with the ACAB code [19], using EAF-2007 library.

Library used for transport is the JEFF-3.1.1, according to the "*Guidelines for Neutronic Analyses*" recommendations [14]. Nevertheless, for a very limited number of nuclides FENDL (3.0 and 2.1) which is also recommended, is used when no data for these nuclides are found in the JEFF library, namely ^{12}C, ^{18}O, ^{180}W, sulphur and tin. Average neutron fluxes are obtained in the standard VITAMIN-J 175 group structure and then activation calculations are carried out with the ACAB code [19], using EAF-2007 library.

Finally, it is worth to underline that for the additional calculations on the equatorial outboard module #12 (Sections 2.3.3 and 2.3.4), materials of the breeder module (i.e. Eurofer, LiPb and He) were considered separately.

2.3. Activation results and analysis

The results presented in this section are divided into five parts. The first four compile the results related with the blanket modules and the last one to the manifold.

Section 2.3.1 shows the computed volumes and neutron fluxes over the blanket components that will be used for the activation calculations. The second section (2.3.2) displays the results of decay heat and activity in the blanket modules. The third one (Section 2.3.3) is

devoted to provide component contribution to the decay heat and activity in the equatorial outboard module (#12) while Section 2.3.4 identifies major radionuclides contributing to decay heat in each of the components of the blanket module. The last section (2.3.5) presents the decay heat and activity results in the manifold.

It is important to mention that a complete irradiation of the LiPb during the entire operation phase was considered. Since the LiPb is moving in and out of the blankets, it would be exposed to a lower flux. The assumption of the remaining LiPb inside the blankets during the full reactor operation is not very realistic and, therefore, the obtained results are conservative but, however it is reasonable considering the current state of DEMO design. Regarding T produced as a consequence of the LiPb activation, it is excluded from all the following results.

2.3.1. Volumes and neutron fluxes over the blanket components

Table 6.5 summarizes the volumes over all the blankets modules in the reactor (360º), separated into components. The statistical error for all the volumes sampling is below 0.3%. Neutron fluxes computed for all the 5 component of the 15 different blanket modules are shown in Table 6.6. The statistical error of calculation in the vast majority of the energy groups is lower than 1%.

Table 6.5. Volumes for the components in the blanket modules for the entire reactor (cm^3).

# Blanket Modules	W	FW	Caps	Breeder	BP	Total
1	$1.48\cdot10^{5}$	$1.41\cdot10^{6}$	$1.88\cdot10^{6}$	$3.10\cdot10^{7}$	$1.31\cdot10^{6}$	$3.57\cdot10^{7}$
2	$1.48\cdot10^{5}$	$1.42\cdot10^{6}$	$1.88\cdot10^{6}$	$3.09\cdot10^{7}$	$1.31\cdot10^{6}$	$3.57\cdot10^{7}$
3	$1.48\cdot10^{5}$	$1.41\cdot10^{6}$	$1.89\cdot10^{6}$	$3.10\cdot10^{7}$	$1.31\cdot10^{6}$	$3.57\cdot10^{7}$
4	$5.34\cdot10^{4}$	$5.04\cdot10^{5}$	$1.20\cdot10^{6}$	$1.18\cdot10^{7}$	$5.54\cdot10^{5}$	$1.42\cdot10^{7}$
5	$8.79\cdot10^{4}$	$8.41\cdot10^{5}$	$1.54\cdot10^{6}$	$2.07\cdot10^{7}$	$9.85\cdot10^{5}$	$2.41\cdot10^{7}$
6	$9.54\cdot10^{4}$	$9.12\cdot10^{5}$	$1.63\cdot10^{6}$	$2.27\cdot10^{7}$	$1.10\cdot10^{6}$	$2.65\cdot10^{7}$
7	$5.93\cdot10^{4}$	$5.62\cdot10^{5}$	$1.40\cdot10^{6}$	$1.41\cdot10^{7}$	$7.05\cdot10^{5}$	$1.68\cdot10^{7}$
8	$7.89\cdot10^{4}$	$7.46\cdot10^{5}$	$3.52\cdot10^{6}$	$4.02\cdot10^{7}$	$1.15\cdot10^{6}$	$4.57\cdot10^{7}$
9	$1.15\cdot10^{5}$	$1.09\cdot10^{6}$	$4.10\cdot10^{6}$	$5.59\cdot10^{7}$	$1.53\cdot10^{6}$	$6.28\cdot10^{7}$
10	$1.51\cdot10^{5}$	$1.45\cdot10^{6}$	$4.61\cdot10^{6}$	$7.15\cdot10^{7}$	$1.90\cdot10^{6}$	$7.96\cdot10^{7}$
11	$1.85\cdot10^{5}$	$1.77\cdot10^{6}$	$5.13\cdot10^{6}$	$8.84\cdot10^{7}$	$2.36\cdot10^{6}$	$9.79\cdot10^{7}$
12	$2.52\cdot10^{5}$	$2.52\cdot10^{6}$	$5.79\cdot10^{6}$	$1.19\cdot10^{8}$	$3.22\cdot10^{6}$	$1.31\cdot10^{8}$
13	$1.87\cdot10^{5}$	$1.80\cdot10^{6}$	$5.09\cdot10^{6}$	$8.75\cdot10^{7}$	$2.29\cdot10^{6}$	$9.68\cdot10^{7}$
14	$1.72\cdot10^{5}$	$1.65\cdot10^{6}$	$4.78\cdot10^{6}$	$7.77\cdot10^{7}$	$1.99\cdot10^{6}$	$8.63\cdot10^{7}$
15	$1.44\cdot10^{5}$	$1.37\cdot10^{6}$	$4.35\cdot10^{6}$	$6.42\cdot10^{7}$	$1.64\cdot10^{6}$	$7.17\cdot10^{7}$
Total (cm^3)	$2.02\cdot10^{6}$	$1.95\cdot10^{7}$	$4.88\cdot10^{7}$	$7.67\cdot10^{8}$	$2.34\cdot10^{7}$	$8.60\cdot10^{8}$
Total (m^3)	$2.02\cdot10^{0}$	$1.95\cdot10^{1}$	$4.88\cdot10^{1}$	$7.67\cdot10^{2}$	$2.34\cdot10^{1}$	$8.60\cdot10^{2}$

Table 6.6. Total average neutron fluxes over the different components (10^{14} n/cm^2·s).

# Blanket Module	W	FW	Caps	Breeder	BP
1	7.67	7.58	4.52	4.86	2.10
2	9.02	9.18	6.46	6.67	3.12
3	9.37	9.53	6.70	6.90	3.23
4	9.07	9.06	5.97	6.05	2.72
5	8.96	8.93	5.64	5.94	2.66
6	8.93	8.93	5.63	5.93	2.68
7	8.99	8.96	5.66	5.85	2.70
8	9.00	8.96	3.65	3.78	0.66
9	9.12	9.13	3.98	4.13	0.77
10	9.31	9.38	4.18	4.40	0.83
11	9.47	9.59	4.31	4.58	0.87
12	9.57	9.72	4.38	4.77	0.89
13	9.50	9.73	4.52	4.81	0.91
14	9.01	9.20	4.34	4.53	0.87
15	8.43	8.57	3.56	3.87	0.66

2.3.2. Decay heat and activity in the blanket modules for the entire reactor

This section summarizes the decay heat and activity results for all the blanket modules and the entire reactor. Results do not include T produced by the activation of the LiPb in the breeder module since it is assumed to be continuously drained.Table 6.7 shows the decay heat (W) in the each of the blanket modules for the entire reactor (360º). As it can be seen, the total decay heat falls as the decay time increases, being 22.5 – 11.7 MW up to 1 hour; just below 1 MW at 2 months and about 0.3 MW up to ~ 1 year; then it drops to 4.5 W at 100 years and it finally reaches around 3 W after 1000 years of cooling.

Furthermore, module #12 (equatorial outboard) shows the highest values (in W) with a difference, depending on the cooling time, up to 1 order of magnitude with the lowest module #4 (inboard module just close and above equatorial inboard #3). However, analyzing volumetric values (W/cc), module #3 (equatorial inboard) is the one with highest value of decay heat (module #12 is about 63% of module #3 in specific values).

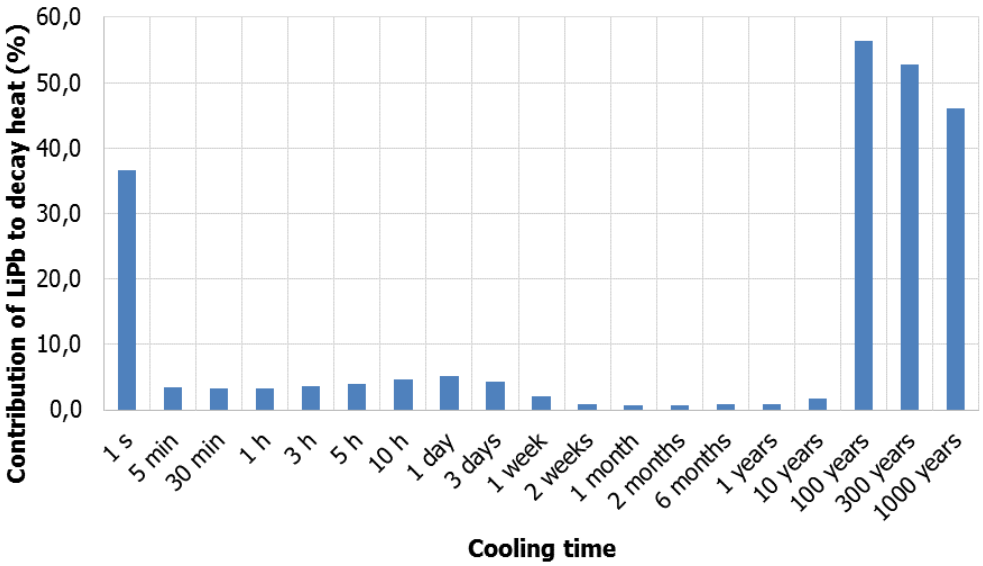

Figure 6.8. Contribution of LiPb to the decay heat in the equatorial outboard module (#12).

Figure 6.8 shows the contribution of the LiPb (as said, with T excluded) to the decay heat in a single complete equatorial outboard module (#12). As it is shown, the LiPb contribution is especially relevant after 100 years of cooling time, as well as at the time immediately after the shutdown (1 second of cooling time).

Table 6.8 shows activity results in the blanket modules for the entire reactor (360º). As it is shown, total activity is between $1.3 \cdot 10^{14}$ and $1.1 \cdot 10^{12}$ MBq up to 10 years; $1.6 \cdot 10^{8}$ MBq at 100 years and then it drops to $\sim 10^{7}$ for longer cooling times.

On the other hand, as in the case of the decay heat, module #12 (outboard equatorial) shows highest values (in Bq) with around one order of magnitude difference with lowest module value. However, analyzing volumetric values (Bq/cc), module #3 (equatorial inboard) is the one with highest values of activity (module #12 is about 60% of module #3 in specific values).

Table 6.7. Total decay heat (W) from the blanket for the entire reactor separated into the individual blanket modules (excluding T from activated LiPb).

Time (years)	Blanket module (360º)															Total (W)	Total (MW)
	1	2	3	4	5	6	7	8	9	10	11	12	13	14	15		
$3.17\cdot10^{-8}$	$1.05\cdot10^{6}$	$1.44\cdot10^{6}$	$1.45\cdot10^{6}$	$4.51\cdot10^{5}$	$7.73\cdot10^{5}$	$8.81\cdot10^{5}$	$5.82\cdot10^{5}$	$8.78\cdot10^{5}$	$1.33\cdot10^{6}$	$1.84\cdot10^{6}$	$2.39\cdot10^{6}$	$3.35\cdot10^{6}$	$2.48\cdot10^{6}$	$2.07\cdot10^{6}$	$1.53\cdot10^{6}$	$2.25\cdot10^{7}$	$2.25\cdot10^{1}$
$9.51\cdot10^{-6}$	$7.26\cdot10^{5}$	$8.82\cdot10^{5}$	$8.77\cdot10^{5}$	$2.94\cdot10^{5}$	$4.88\cdot10^{5}$	$5.49\cdot10^{5}$	$3.64\cdot10^{5}$	$5.67\cdot10^{5}$	$8.53\cdot10^{5}$	$1.16\cdot10^{6}$	$1.47\cdot10^{6}$	$2.03\cdot10^{6}$	$1.52\cdot10^{6}$	$1.30\cdot10^{6}$	$9.97\cdot10^{6}$	$1.41\cdot10^{7}$	$1.41\cdot10^{1}$
$5.71\cdot10^{-5}$	$6.69\cdot10^{5}$	$7.99\cdot10^{5}$	$7.92\cdot10^{5}$	$2.66\cdot10^{5}$	$4.43\cdot10^{5}$	$4.99\cdot10^{5}$	$3.30\cdot10^{5}$	$5.15\cdot10^{5}$	$7.74\cdot10^{5}$	$1.05\cdot10^{6}$	$1.33\cdot10^{6}$	$1.84\cdot10^{6}$	$1.37\cdot10^{6}$	$1.18\cdot10^{6}$	$9.08\cdot10^{5}$	$1.28\cdot10^{7}$	$1.28\cdot10^{1}$
$1.14\cdot10^{-4}$	$6.24\cdot10^{5}$	$7.33\cdot10^{5}$	$7.24\cdot10^{5}$	$2.45\cdot10^{5}$	$4.07\cdot10^{5}$	$4.59\cdot10^{5}$	$3.03\cdot10^{5}$	$4.73\cdot10^{5}$	$7.12\cdot10^{5}$	$9.62\cdot10^{5}$	$1.22\cdot10^{6}$	$1.69\cdot10^{6}$	$1.26\cdot10^{6}$	$1.08\cdot10^{6}$	$8.38\cdot10^{5}$	$1.17\cdot10^{7}$	$1.17\cdot10^{1}$
$3.42\cdot10^{-4}$	$4.90\cdot10^{5}$	$5.41\cdot10^{5}$	$5.29\cdot10^{5}$	$1.81\cdot10^{5}$	$3.04\cdot10^{5}$	$3.43\cdot10^{5}$	$2.25\cdot10^{5}$	$3.53\cdot10^{5}$	$5.30\cdot10^{5}$	$7.13\cdot10^{5}$	$9.02\cdot10^{5}$	$1.24\cdot10^{6}$	$9.24\cdot10^{5}$	$8.04\cdot10^{5}$	$6.34\cdot10^{5}$	$8.71\cdot10^{6}$	$8.71\cdot10^{0}$
$5.71\cdot10^{-4}$	$4.07\cdot10^{5}$	$4.25\cdot10^{5}$	$4.12\cdot10^{5}$	$1.43\cdot10^{5}$	$2.41\cdot10^{5}$	$2.72\cdot10^{5}$	$1.78\cdot10^{5}$	$2.79\cdot10^{5}$	$4.20\cdot10^{5}$	$5.62\cdot10^{5}$	$7.08\cdot10^{5}$	$9.69\cdot10^{5}$	$7.22\cdot10^{5}$	$6.34\cdot10^{5}$	$5.08\cdot10^{5}$	$6.88\cdot10^{6}$	$6.88\cdot10^{0}$
$1.14\cdot10^{-3}$	$3.02\cdot10^{5}$	$2.90\cdot10^{5}$	$2.76\cdot10^{5}$	$9.83\cdot10^{4}$	$1.67\cdot10^{5}$	$1.89\cdot10^{5}$	$1.23\cdot10^{5}$	$1.94\cdot10^{5}$	$2.91\cdot10^{5}$	$3.87\cdot10^{5}$	$4.83\cdot10^{5}$	$6.56\cdot10^{5}$	$4.89\cdot10^{5}$	$4.36\cdot10^{5}$	$3.60\cdot10^{5}$	$4.74\cdot10^{6}$	$4.74\cdot10^{0}$
$2.74\cdot10^{-3}$	$2.07\cdot10^{5}$	$1.95\cdot10^{5}$	$1.85\cdot10^{5}$	$6.68\cdot10^{4}$	$1.13\cdot10^{5}$	$1.28\cdot10^{5}$	$8.26\cdot10^{4}$	$1.32\cdot10^{5}$	$1.98\cdot10^{5}$	$2.63\cdot10^{5}$	$3.28\cdot10^{5}$	$4.44\cdot10^{5}$	$3.31\cdot10^{5}$	$2.97\cdot10^{5}$	$2.47\cdot10^{5}$	$3.22\cdot10^{6}$	$3.22\cdot10^{0}$
$8.21\cdot10^{-3}$	$1.01\cdot10^{5}$	$1.08\cdot10^{5}$	$1.05\cdot10^{5}$	$3.77\cdot10^{4}$	$6.25\cdot10^{4}$	$6.98\cdot10^{4}$	$4.52\cdot10^{4}$	$7.48\cdot10^{4}$	$1.12\cdot10^{5}$	$1.49\cdot10^{5}$	$1.88\cdot10^{5}$	$2.56\cdot10^{5}$	$1.92\cdot10^{5}$	$1.68\cdot10^{5}$	$1.35\cdot10^{5}$	$1.80\cdot10^{6}$	$1.80\cdot10^{0}$
$1.92\cdot10^{-2}$	$6.50\cdot10^{4}$	$7.61\cdot10^{4}$	$7.63\cdot10^{4}$	$2.75\cdot10^{4}$	$4.45\cdot10^{4}$	$4.92\cdot10^{4}$	$3.19\cdot10^{4}$	$5.45\cdot10^{4}$	$8.18\cdot10^{4}$	$1.09\cdot10^{5}$	$1.37\cdot10^{5}$	$1.88\cdot10^{5}$	$1.41\cdot10^{5}$	$1.22\cdot10^{5}$	$9.58\cdot10^{4}$	$1.30\cdot10^{6}$	$1.30\cdot10^{0}$
$3.84\cdot10^{-2}$	$5.69\cdot10^{4}$	$6.83\cdot10^{4}$	$6.89\cdot10^{4}$	$2.49\cdot10^{4}$	$4.01\cdot10^{4}$	$4.42\cdot10^{4}$	$2.87\cdot10^{4}$	$4.96\cdot10^{4}$	$7.43\cdot10^{4}$	$9.90\cdot10^{4}$	$1.25\cdot10^{5}$	$1.70\cdot10^{5}$	$1.28\cdot10^{5}$	$1.10\cdot10^{5}$	$8.63\cdot10^{4}$	$1.17\cdot10^{6}$	$1.17\cdot10^{0}$
$7.67\cdot10^{-2}$	$5.10\cdot10^{4}$	$6.18\cdot10^{4}$	$6.26\cdot10^{4}$	$2.26\cdot10^{4}$	$3.64\cdot10^{4}$	$4.01\cdot10^{4}$	$2.61\cdot10^{4}$	$4.50\cdot10^{4}$	$6.75\cdot10^{4}$	$8.99\cdot10^{4}$	$1.13\cdot10^{5}$	$1.55\cdot10^{5}$	$1.17\cdot10^{5}$	$1.00\cdot10^{5}$	$7.81\cdot10^{4}$	$1.07\cdot10^{6}$	$1.07\cdot10^{0}$
$1.53\cdot10^{-1}$	$4.31\cdot10^{4}$	$5.27\cdot10^{4}$	$5.33\cdot10^{4}$	$1.92\cdot10^{4}$	$3.09\cdot10^{4}$	$3.41\cdot10^{4}$	$2.22\cdot10^{4}$	$3.82\cdot10^{4}$	$5.73\cdot10^{4}$	$7.64\cdot10^{4}$	$9.64\cdot10^{4}$	$1.32\cdot10^{5}$	$9.91\cdot10^{4}$	$8.50\cdot10^{4}$	$6.62\cdot10^{4}$	$9.06\cdot10^{5}$	$9.06\cdot10^{-1}$
$5.01\cdot10^{-1}$	$2.20\cdot10^{4}$	$2.81\cdot10^{4}$	$2.85\cdot10^{4}$	$1.00\cdot10^{4}$	$1.62\cdot10^{4}$	$1.79\cdot10^{4}$	$1.18\cdot10^{4}$	$1.98\cdot10^{4}$	$2.98\cdot10^{4}$	$3.99\cdot10^{4}$	$5.06\cdot10^{4}$	$6.94\cdot10^{4}$	$5.22\cdot10^{4}$	$4.44\cdot10^{4}$	$3.43\cdot10^{4}$	$4.75\cdot10^{5}$	$4.75\cdot10^{-1}$
$9.99\cdot10^{-1}$	$1.00\cdot10^{4}$	$1.37\cdot10^{4}$	$1.40\cdot10^{4}$	$4.74\cdot10^{3}$	$7.67\cdot10^{4}$	$8.55\cdot10^{3}$	$5.70\cdot10^{3}$	$9.24\cdot10^{3}$	$1.39\cdot10^{4}$	$1.88\cdot10^{4}$	$2.40\cdot10^{4}$	$3.31\cdot10^{4}$	$2.49\cdot10^{4}$	$2.10\cdot10^{4}$	$1.58\cdot10^{4}$	$2.25\cdot10^{5}$	$2.25\cdot10^{-1}$
$9.99\cdot10^{0}$	$3.41\cdot10^{3}$	$4.00\cdot10^{2}$	$4.08\cdot10^{2}$	$1.58\cdot10^{2}$	$2.50\cdot10^{2}$	$2.75\cdot10^{2}$	$1.76\cdot10^{2}$	$3.37\cdot10^{2}$	$5.12\cdot10^{2}$	$6.73\cdot10^{2}$	$8.46\cdot10^{2}$	$1.15\cdot10^{3}$	$8.67\cdot10^{2}$	$7.50\cdot10^{2}$	$5.68\cdot10^{2}$	$7.71\cdot10^{3}$	$7.71\cdot10^{-3}$
$9.99\cdot10^{1}$	$1.84\cdot10^{-1}$	$2.46\cdot10^{-1}$	$2.53\cdot10^{-1}$	$8.96\cdot10^{-2}$	$1.45\cdot10^{-1}$	$1.64\cdot10^{-1}$	$1.04\cdot10^{-1}$	$1.90\cdot10^{-1}$	$2.85\cdot10^{-1}$	$4.14\cdot10^{-1}$	$4.59\cdot10^{-1}$	$6.82\cdot10^{-1}$	$5.14\cdot10^{-1}$	$3.86\cdot10^{-1}$	$3.10\cdot10^{-1}$	$4.43\cdot10^{0}$	$4.43\cdot10^{-4}$
$3.00\cdot10^{2}$	$1.55\cdot10^{-1}$	$2.03\cdot10^{-1}$	$2.09\cdot10^{-1}$	$7.45\cdot10^{-2}$	$1.23\cdot10^{-1}$	$1.35\cdot10^{-1}$	$8.49\cdot10^{-2}$	$1.61\cdot10^{-1}$	$2.43\cdot10^{-1}$	$3.26\cdot10^{-1}$	$4.15\cdot10^{-1}$	$5.73\cdot10^{-1}$	$4.29\cdot10^{-1}$	$3.64\cdot10^{-1}$	$2.60\cdot10^{-1}$	$3.76\cdot10^{0}$	$3.76\cdot10^{-6}$
$9.99\cdot10^{2}$	$1.29\cdot10^{-1}$	$1.67\cdot10^{-1}$	$1.72\cdot10^{-1}$	$6.26\cdot10^{-2}$	$1.03\cdot10^{-1}$	$1.12\cdot10^{-1}$	$7.06\cdot10^{-2}$	$1.35\cdot10^{-1}$	$2.03\cdot10^{-1}$	$2.71\cdot10^{-1}$	$3.44\cdot10^{-1}$	$4.73\cdot10^{-1}$	$3.55\cdot10^{-1}$	$3.02\cdot10^{-1}$	$2.16\cdot10^{-1}$	$3.12\cdot10^{0}$	$3.12\cdot10^{-6}$

Table 6.8. Total activity (Bq) from the blanket for the entire reactor separated into the individual blanket modules (excluding T from activated LiPb).

Time (years)	Blanket module (360º)															Total (Bq)	Total (MBq)
	1	2	3	4	5	6	7	8	9	10	11	12	13	14	15		
$3.17\cdot10^{-8}$	$6.85\cdot10^{18}$	$8.48\cdot10^{18}$	$8.42\cdot10^{18}$	$2.67\cdot10^{18}$	$4.56\cdot10^{18}$	$5.17\cdot10^{18}$	$3.38\cdot10^{18}$	$5.04\cdot10^{18}$	$7.63\cdot10^{18}$	$1.05\cdot10^{19}$	$1.35\cdot10^{19}$	$1.88\cdot10^{19}$	$1.40\cdot10^{19}$	$1.18\cdot10^{19}$	$9.02\cdot10^{18}$	$1.30\cdot10^{20}$	$1.30\cdot10^{14}$
$9.51\cdot10^{-6}$	$5.10\cdot10^{18}$	$5.81\cdot10^{18}$	$5.71\cdot10^{18}$	$1.91\cdot10^{18}$	$3.20\cdot10^{18}$	$3.60\cdot10^{18}$	$2.36\cdot10^{18}$	$3.58\cdot10^{18}$	$5.38\cdot10^{18}$	$7.29\cdot10^{18}$	$9.27\cdot10^{18}$	$1.28\cdot10^{19}$	$9.54\cdot10^{18}$	$8.25\cdot10^{18}$	$6.44\cdot10^{18}$	$9.03\cdot10^{19}$	$9.03\cdot10^{13}$
$5.71\cdot10^{-5}$	$4.90\cdot10^{18}$	$5.53\cdot10^{18}$	$5.43\cdot10^{18}$	$1.82\cdot10^{18}$	$3.05\cdot10^{18}$	$3.43\cdot10^{18}$	$2.25\cdot10^{18}$	$3.41\cdot10^{18}$	$5.12\cdot10^{18}$	$6.94\cdot10^{18}$	$8.82\cdot10^{18}$	$1.22\cdot10^{19}$	$9.07\cdot10^{18}$	$7.86\cdot10^{18}$	$6.15\cdot10^{18}$	$8.60\cdot10^{19}$	$8.60\cdot10^{13}$
$1.14\cdot10^{-4}$	$4.75\cdot10^{18}$	$5.34\cdot10^{18}$	$5.23\cdot10^{18}$	$1.75\cdot10^{18}$	$2.94\cdot10^{18}$	$3.31\cdot10^{18}$	$2.17\cdot10^{18}$	$3.28\cdot10^{18}$	$4.93\cdot10^{18}$	$6.68\cdot10^{18}$	$8.49\cdot10^{18}$	$1.17\cdot10^{19}$	$8.73\cdot10^{18}$	$7.57\cdot10^{18}$	$5.93\cdot10^{18}$	$8.28\cdot10^{19}$	$8.28\cdot10^{13}$
$3.42\cdot10^{-4}$	$4.31\cdot10^{18}$	$4.75\cdot10^{18}$	$4.65\cdot10^{18}$	$1.56\cdot10^{18}$	$2.62\cdot10^{18}$	$2.96\cdot10^{18}$	$1.93\cdot10^{18}$	$2.91\cdot10^{18}$	$4.38\cdot10^{18}$	$5.93\cdot10^{18}$	$7.52\cdot10^{18}$	$1.04\cdot10^{19}$	$7.72\cdot10^{18}$	$6.71\cdot10^{18}$	$5.30\cdot10^{18}$	$7.36\cdot10^{19}$	$7.36\cdot10^{13}$
$5.71\cdot10^{-4}$	$4.00\cdot10^{18}$	$4.37\cdot10^{18}$	$4.27\cdot10^{18}$	$1.43\cdot10^{18}$	$2.41\cdot10^{18}$	$2.72\cdot10^{18}$	$1.77\cdot10^{18}$	$2.67\cdot10^{18}$	$4.02\cdot10^{18}$	$5.43\cdot10^{18}$	$6.89\cdot10^{18}$	$9.51\cdot10^{18}$	$7.07\cdot10^{18}$	$6.16\cdot10^{18}$	$4.87\cdot10^{18}$	$6.76\cdot10^{19}$	$6.76\cdot10^{13}$
$1.14\cdot10^{-3}$	$3.52\cdot10^{18}$	$3.85\cdot10^{18}$	$3.75\cdot10^{18}$	$1.26\cdot10^{18}$	$2.12\cdot10^{18}$	$2.39\cdot10^{18}$	$1.56\cdot10^{18}$	$2.34\cdot10^{18}$	$3.51\cdot10^{18}$	$4.75\cdot10^{18}$	$6.02\cdot10^{18}$	$8.31\cdot10^{18}$	$6.18\cdot10^{18}$	$5.39\cdot10^{18}$	$4.26\cdot10^{18}$	$5.92\cdot10^{19}$	$5.92\cdot10^{13}$
$2.74\cdot10^{-3}$	$2.85\cdot10^{18}$	$3.24\cdot10^{18}$	$3.19\cdot10^{18}$	$1.06\cdot10^{18}$	$1.77\cdot10^{18}$	$1.99\cdot10^{18}$	$1.30\cdot10^{18}$	$1.94\cdot10^{18}$	$2.92\cdot10^{18}$	$3.96\cdot10^{18}$	$5.04\cdot10^{18}$	$6.98\cdot10^{18}$	$5.19\cdot10^{18}$	$4.49\cdot10^{18}$	$3.52\cdot10^{18}$	$4.94\cdot10^{19}$	$4.94\cdot10^{13}$
$8.21\cdot10^{-3}$	$1.91\cdot10^{18}$	$2.45\cdot10^{18}$	$2.46\cdot10^{18}$	$7.98\cdot10^{17}$	$1.31\cdot10^{18}$	$1.47\cdot10^{18}$	$9.66\cdot10^{17}$	$1.43\cdot10^{18}$	$2.14\cdot10^{18}$	$2.94\cdot10^{18}$	$3.78\cdot10^{18}$	$5.27\cdot10^{18}$	$3.93\cdot10^{18}$	$3.34\cdot10^{18}$	$2.52\cdot10^{18}$	$3.67\cdot10^{19}$	$3.67\cdot10^{13}$
$1.92\cdot10^{-2}$	$1.54\cdot10^{18}$	$2.11\cdot10^{18}$	$2.14\cdot10^{18}$	$6.87\cdot10^{17}$	$1.12\cdot10^{18}$	$1.24\cdot10^{18}$	$8.22\cdot10^{17}$	$1.21\cdot10^{18}$	$1.83\cdot10^{18}$	$2.51\cdot10^{18}$	$3.24\cdot10^{18}$	$4.53\cdot10^{18}$	$3.38\cdot10^{18}$	$2.84\cdot10^{18}$	$2.11\cdot10^{18}$	$3.13\cdot10^{19}$	$3.13\cdot10^{13}$
$3.84\cdot10^{-2}$	$1.40\cdot10^{18}$	$1.96\cdot10^{18}$	$2.00\cdot10^{18}$	$6.42\cdot10^{17}$	$1.04\cdot10^{18}$	$1.16\cdot10^{18}$	$7.66\cdot10^{17}$	$1.14\cdot10^{18}$	$1.70\cdot10^{18}$	$2.34\cdot10^{18}$	$3.02\cdot10^{18}$	$4.23\cdot10^{18}$	$3.16\cdot10^{18}$	$2.65\cdot10^{18}$	$1.96\cdot10^{18}$	$2.92\cdot10^{19}$	$2.92\cdot10^{13}$
$7.67\cdot10^{-2}$	$1.28\cdot10^{18}$	$1.82\cdot10^{18}$	$1.85\cdot10^{18}$	$5.93\cdot10^{17}$	$9.65\cdot10^{17}$	$1.07\cdot10^{18}$	$7.10\cdot10^{17}$	$1.05\cdot10^{18}$	$1.57\cdot10^{18}$	$2.17\cdot10^{18}$	$2.80\cdot10^{18}$	$3.92\cdot10^{18}$	$2.93\cdot10^{18}$	$2.45\cdot10^{18}$	$1.80\cdot10^{18}$	$2.70\cdot10^{19}$	$2.70\cdot10^{13}$
$1.53\cdot10^{-1}$	$1.12\cdot10^{18}$	$1.61\cdot10^{18}$	$1.64\cdot10^{18}$	$5.23\cdot10^{17}$	$8.50\cdot10^{17}$	$9.46\cdot10^{17}$	$6.30\cdot10^{17}$	$9.27\cdot10^{17}$	$1.39\cdot10^{18}$	$1.92\cdot10^{18}$	$2.48\cdot10^{18}$	$3.48\cdot10^{18}$	$2.60\cdot10^{18}$	$2.17\cdot10^{18}$	$1.59\cdot10^{18}$	$2.39\cdot10^{19}$	$2.39\cdot10^{13}$
$5.01\cdot10^{-1}$	$7.34\cdot10^{17}$	$1.12\cdot10^{18}$	$1.15\cdot10^{18}$	$3.58\cdot10^{17}$	$5.85\cdot10^{17}$	$6.50\cdot10^{17}$	$4.43\cdot10^{17}$	$6.44\cdot10^{17}$	$9.61\cdot10^{17}$	$1.34\cdot10^{18}$	$1.74\cdot10^{18}$	$2.45\cdot10^{18}$	$1.83\cdot10^{18}$	$1.51\cdot10^{18}$	$1.09\cdot10^{18}$	$1.66\cdot10^{19}$	$1.66\cdot10^{13}$
$9.99\cdot10^{-1}$	$5.28\cdot10^{17}$	$8.47\cdot10^{17}$	$8.70\cdot10^{17}$	$2.65\cdot10^{17}$	$4.32\cdot10^{17}$	$4.85\cdot10^{17}$	$3.31\cdot10^{17}$	$4.82\cdot10^{17}$	$7.17\cdot10^{17}$	$1.00\cdot10^{18}$	$1.31\cdot10^{18}$	$1.84\cdot10^{18}$	$1.38\cdot10^{18}$	$1.13\cdot10^{18}$	$8.07\cdot10^{17}$	$1.24\cdot10^{19}$	$1.24\cdot10^{13}$
$9.99\cdot10^{0}$	$4.64\cdot10^{16}$	$7.60\cdot10^{16}$	$7.81\cdot10^{16}$	$2.38\cdot10^{16}$	$3.88\cdot10^{16}$	$4.36\cdot10^{16}$	$3.02\cdot10^{16}$	$4.30\cdot10^{16}$	$6.47\cdot10^{16}$	$9.02\cdot10^{16}$	$1.23\cdot10^{17}$	$1.67\cdot10^{17}$	$1.25\cdot10^{17}$	$1.02\cdot10^{17}$	$7.26\cdot10^{16}$	$1.12\cdot10^{18}$	$1.12\cdot10^{12}$
$9.99\cdot10^{1}$	$7.94\cdot10^{12}$	$8.64\cdot10^{12}$	$5.48\cdot10^{12}$	$2.05\cdot10^{12}$	$3.27\cdot10^{12}$	$6.84\cdot10^{12}$	$5.67\cdot10^{12}$	$8.62\cdot10^{12}$	$1.04\cdot10^{13}$	$7.29\cdot10^{12}$	$5.71\cdot10^{13}$	$1.22\cdot10^{13}$	$9.28\cdot10^{12}$	$8.01\cdot10^{12}$	$1.18\cdot10^{1}$	$1.64\cdot10^{14}$	$1.64\cdot10^{8}$
$3.00\cdot10^{2}$	$3.41\cdot10^{12}$	$4.60\cdot10^{12}$	$4.73\cdot10^{12}$	$1.63\cdot10^{12}$	$2.70\cdot10^{12}$	$2.99\cdot10^{12}$	$1.94\cdot10^{12}$	$3.26\cdot10^{12}$	$4.88\cdot10^{12}$	$6.59\cdot10^{12}$	$8.41\cdot10^{12}$	$1.16\cdot10^{13}$	$8.71\cdot10^{12}$	$7.33\cdot10^{12}$	$5.42\cdot10^{12}$	$7.82\cdot10^{13}$	$7.82\cdot10^{7}$
$9.99\cdot10^{2}$	$2.71\cdot10^{12}$	$3.64\cdot10^{12}$	$3.75\cdot10^{12}$	$1.30\cdot10^{12}$	$2.15\cdot10^{12}$	$2.37\cdot10^{12}$	$1.55\cdot10^{12}$	$2.58\cdot10^{12}$	$3.85\cdot10^{12}$	$5.18\cdot10^{12}$	$6.61\cdot10^{12}$	$9.13\cdot10^{12}$	$6.84\cdot10^{12}$	$5.76\cdot10^{12}$	$4.27\cdot10^{12}$	$6.17\cdot10^{13}$	$6.17\cdot10^{7}$

2.3.3. Contribution of the different components to decay heat and activity

A single complete blanket module #12 in a torus sector of 11.25º (located in the equatorial zone of the outboard and therefore where the blanket receives highest neutron fluxes of all outboard modules) was selected for a further study. In this analysis, the contribution of the 5 different components to the activation responses (decay heat and activity) was assessed. Furthermore, the breeder module component was broken down in the different materials that compose it: Eurofer, LiPb and He.

Figure 6.9 shows the total decay heat for the equatorial outboard module (#12) as well as the contribution of the components. Contribution of the He in the breeder is not shown since its values are several orders of magnitude lower than those corresponding to other components.

It is important to note that LiPb contribution is given again excluding the contribution of T. Had it been considered, LiPb would have been the main contributor both at 1 second after shutdown and from 1 year cooling. Without T considered, LiPb is the main contributor both at the time of the shutdown and after 100 years of cooling time. At the remaining times listed, Eurofer from the breeder module is the component with the highest values of decay heat. As it would be expected, the BP is the component with the lowest contribution to decay heat in almost all the considered times. As it can be seen some differences are detected between the caps and the FW, in terms of time evolution. This is due to the effect of the spectrum in the production of radionuclides.

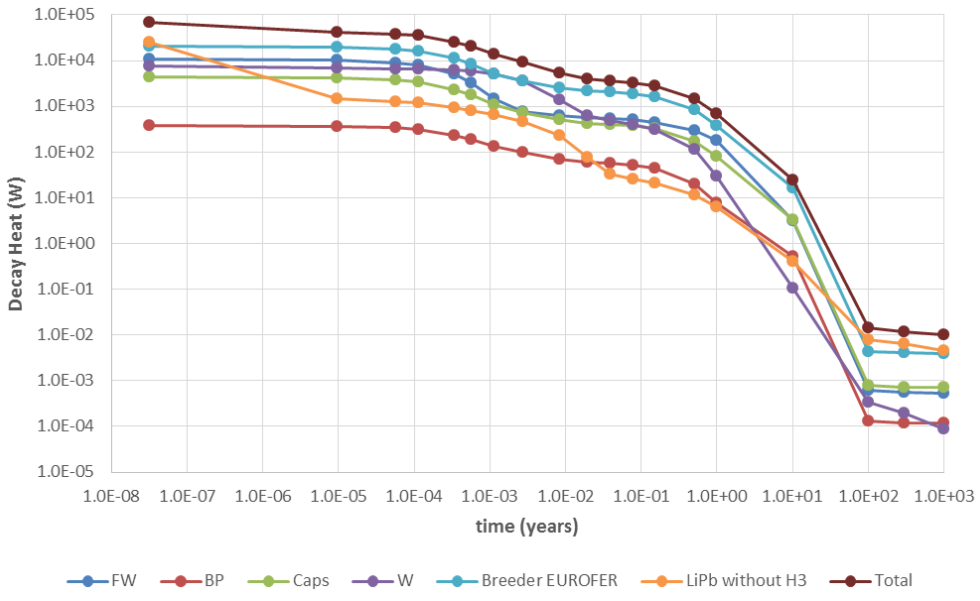

Figure 6.9. Decay heat for equatorial outboard blanket module (#12): Total and contribution from W, FW, caps, BP components and breeder module materials.

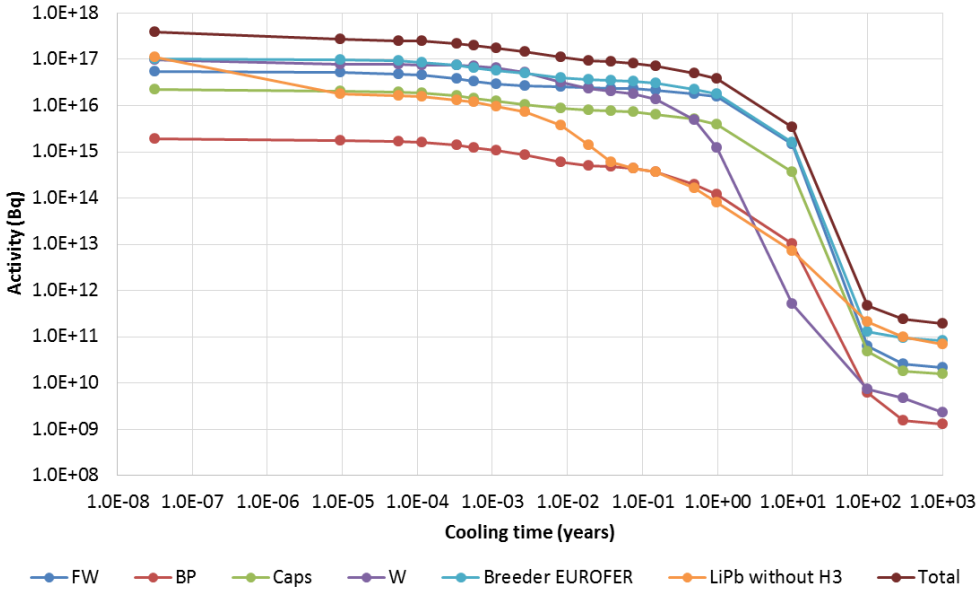

Figure 6.10. Activity for equatorial outboard blanket module (#12): Total and contribution from W, FW, caps, BP components and breeder module materials.

A similar figure (Figure 6.10) is given for the activity response. Contribution of He in the breeder was again excluded, as it is negligible. LiPb contribution is also given excluding the T. If it had been considered, LiPb would have been the main contributor at all the cooling times. However, without T, LiPb is only the main contributor both at the time of the shutdown and at 100 and 300 years of cooling time. As it happened in the decay heat, in the remaining times listed, Eurofer from the breeder module (coming from both stiffenings and inner collector) is the component with the highest values. Finally, BP is the component with the lowest contribution to activity up to one year and after 100 years. At intermediate times, W armour is the one with the lowest contribution.

2.3.4. Main radionuclides contributing to the decay heat in the blanket components

The main radionuclides contributing to decay heat were identified using the same single complete equatorial outboard blanket module #12 as reference. Once again, results for the breeder module component were separated into materials. Figure 6.11-Figure 6.16 represent the major contributors in each of the components.

- W armour (Figure 6.11). ^{187}W (half-life 24 h) is dominant up to 3 days, when ^{185}W (half-life 75.1 days) turns into the largest contributor until a year. At the end times, impurities determine the critical radionuclides. So, at 10 years ^{60}Co (half-life 1925.3 days) is the main contributor. From 100 years, and until 300 years, ^{39}Ar (half-life 269 years) becomes the most relevant isotope and, in the last period, ^{94}Nb (half-life $2.0 \cdot 10^4$ years) replaces it.

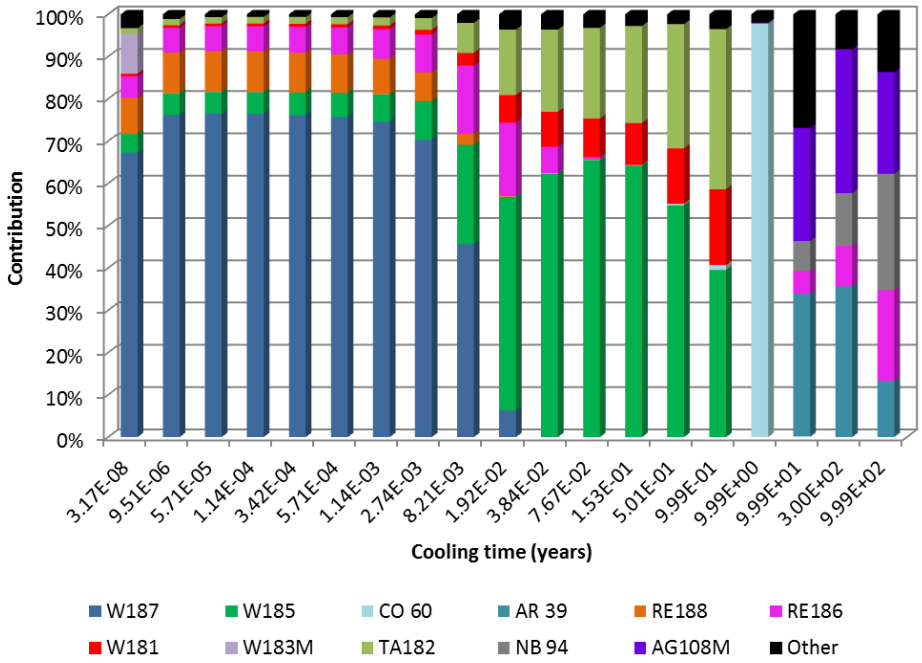

Figure 6.11. Main radionuclides for decay heat in the W armour.

- FW (Figure 6.12). It can be seen that ^{56}Mn (half-life 2.6 h) is dominant up to 10 hours of cooling time. After this time, ^{54}Mn (half-life 312.1 days) is the main contributor until 1 year after shutdown, when ^{60}Co (half-life 1925.3 days) replaces it as main contributor to decay heat until 10 years. In the last period ^{94}Nb ($2.0 \cdot 10^4$ years) is dominant.

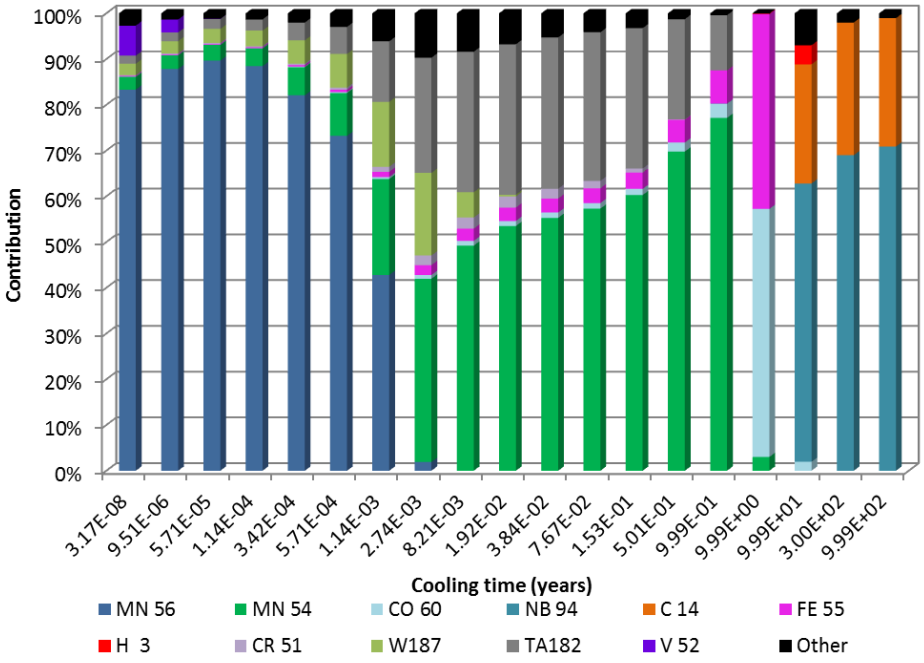

Figure 6.12. Main radionuclides for decay heat in the FW.

- Caps (Figure 6.13). ^{56}Mn (half-life 2.6 h) is dominant up to 5 hours of cooling time. After this time, ^{187}W (half-life 24 h) is the main contributor until 10 hours after shutdown. Then, ^{182}Ta (half-life 114.7 days) becomes the major radionuclide up to 6 months. Immediately ^{54}Mn (half-life 312.1 days) replaces it until 1 year. ^{60}Co (half-life 1925.3 days) is the major contributor at 10 years and ^{94}Nb (half-life $2.0 \cdot 10^4$ years) from then to 100 years.

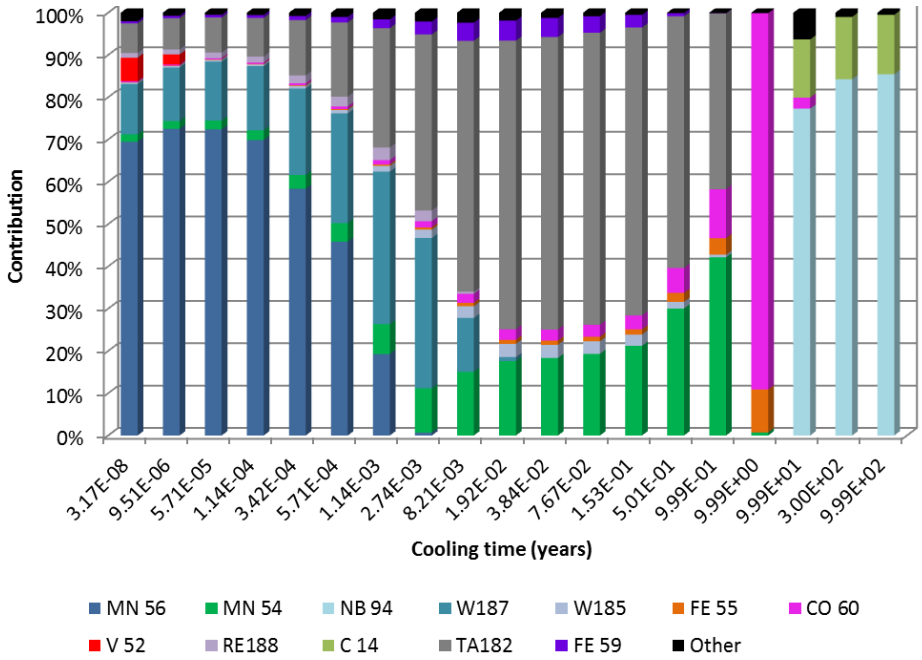

Figure 6.13. Main radionuclides for decay heat in the caps.

- Eurofer from the breeder (Figure 6.14). In this case ^{56}Mn (half-life 2.6 h) is the main contributor to decay heat up to 5 hours of cooling. Then, ^{187}W (half-life 24 h) is dominant until 10 hours when, ^{182}Ta (half-life 114.7 days) replaces it until one year. At 10 years of cooling time ^{60}Co (half-life 1925.3 days) is the major contributor. Finally, ^{94}Nb (half-life $2.0 \cdot 10^4$ years) is the main contributor from 100 years of cooling time.

- LiPb from the breeder[22] (Figure 6.15). In this case, ^{207m}Pb (half-life 0.8 seconds) is the major radionuclide at the time close to the shutdown (1 second). Immediately after, ^{203}Pb (half-life 51.9 h) is the main contributor up to one week, when ^{210}Po (half-life 138.4 days) is dominant (until 1 year). ^{204}Tl (half-life 3.8 years) replaces it as major radionuclide at 10 years while ^{94}Nb (half-life $2.0 \cdot 10^4$ years) is the main contributor up to 1000 years of cooling time.

[22] Note that T has not been taken into consideration.

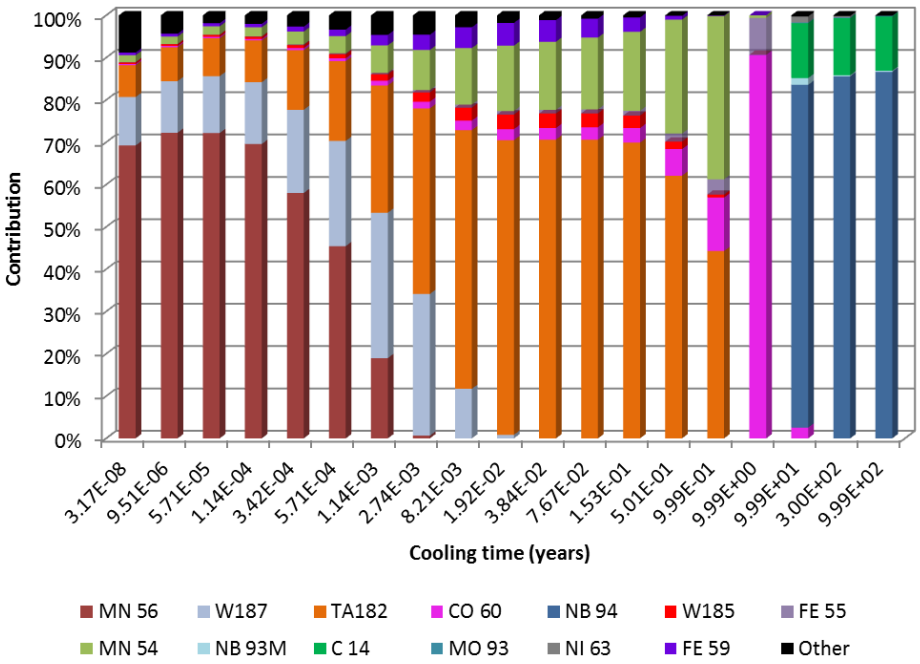

Figure 6.14. Main radionuclides for decay heat in the Eurofer breeder.

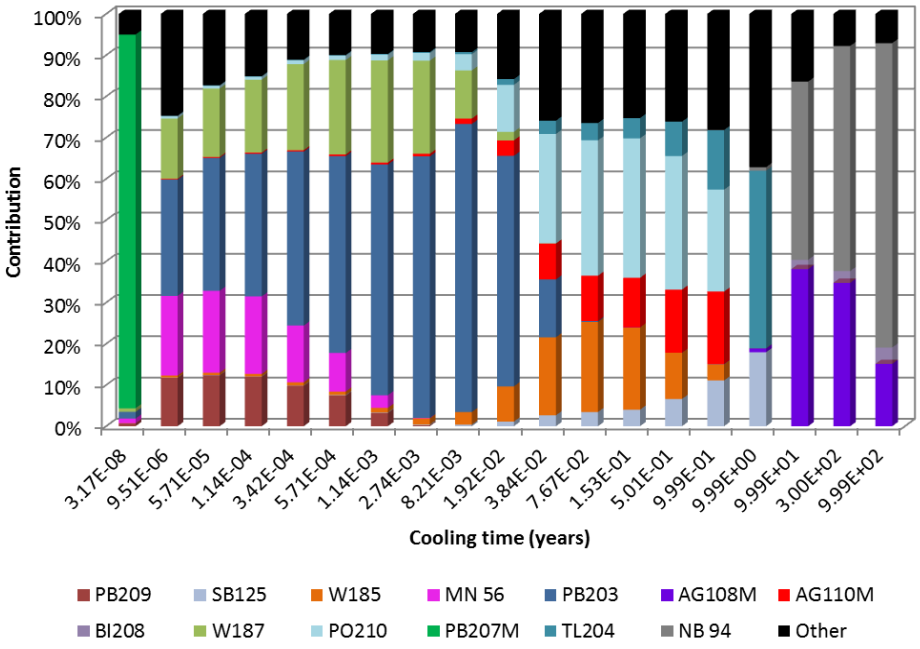

Figure 6.15. Main radionuclides for decay heat in the LiPb breeder.

- BP (Figure 6.16). Dominant radionuclides are almost the same as in the case of the caps. The only difference is found in regard to ^{56}Mn (half-life 2.6 h), which in this case is only dominant until 3 hours, instead of 5 hours.

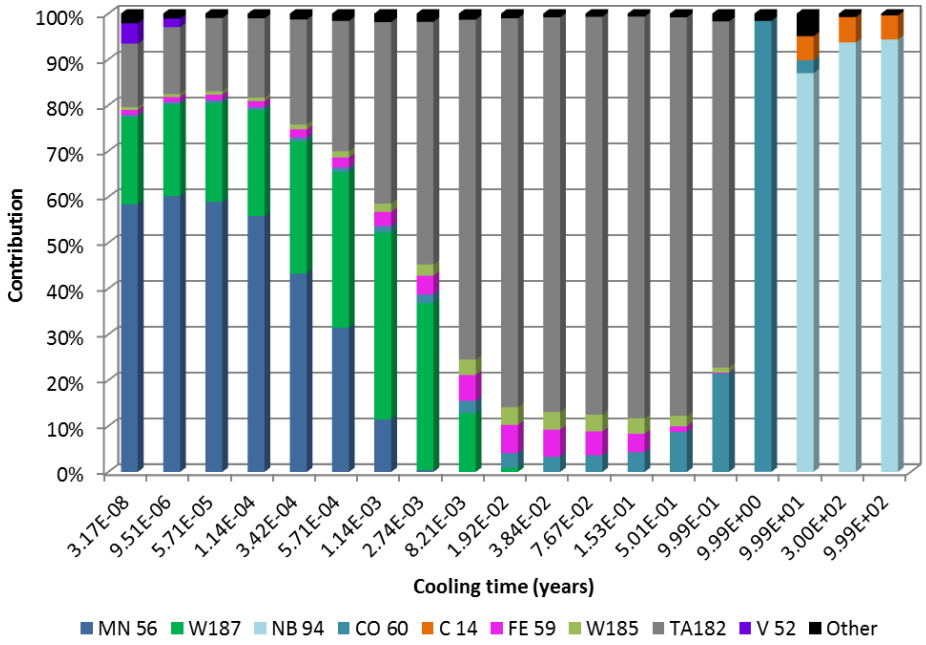

Figure 6.16. Main radionuclides for decay heat in the BP.

2.3.5. Decay heat and activity in the manifold

Table 6.9 shows volumes for the two regions in which the manifold has been divided (inboard and outboard), for the entire reactor (360º) and fluxes calculated for the two regions in which the manifold has been divided (inboard and outboard).

Table 6.10-Table 6.11 display the evolution of the decay heat and activity responses for the two regions, as well as for the whole manifold. For decay heat, total values are between $5.9 \cdot 10^{2}$ and $1.2 \cdot 10^{2}$ kW up to 1 day; about 10 kW up to 1 year and finally, it drops to $2.8 \cdot 10^{-4}$ kW at 1000 years. In the case of activity, total value is $2.8 \cdot 10^{12}$-$1.2 \cdot 10^{12}$ MBq up to 1 day; just over $2.7 \cdot 10^{11}$ MBq at 1 year and then it drops to $3.8 \cdot 10^{6}$ MBq at 1000 years of cooling. As it can be seen the inboard area shows, in the vast majority of the times, higher values than the outboard with the only exception for the decay heat for 10 and 100 years of cooling times.

Regarding major radionuclides contributing to decay heat are: ^{56}Mn up to 5 hours (half-life 2.6 h), ^{182}Ta up to one year (half-life 114.7 days), ^{60}Co up to 100 years (half-life 1925.3 days) and ^{94}Nb for larger cooling times (half-life $2.0 \cdot 10^{4}$ years).

Table 6.9. Volume (cm^3) and total neutron flux for the manifold (10^{12} $n/cm^2 \cdot s$).

Manifold	Volume	Total neutron flux
Inboard	$1.48 \cdot 10^8$	29.8
Outboard	$3.02 \cdot 10^8$	7.64
Total	$4.51 \cdot 10^8$	

Table 6.10. Total decay heat from the manifold for the entire reactor (T excluded).

Time (years)	Inboard (W)	Outboard (W)	Total (W)	Total (kW)
$3.17 \cdot 10^{-8}$	$3.51 \cdot 10^5$	$2.38 \cdot 10^5$	$5.88 \cdot 10^5$	$5.88 \cdot 10^2$
$9.51 \cdot 10^{-6}$	$3.12 \cdot 10^5$	$2.15 \cdot 10^5$	$5.27 \cdot 10^5$	$5.27 \cdot 10^2$
$5.71 \cdot 10^{-5}$	$2.79 \cdot 10^5$	$1.93 \cdot 10^5$	$4.72 \cdot 10^5$	$4.72 \cdot 10^2$
$1.14 \cdot 10^{-4}$	$2.55 \cdot 10^5$	$1.77 \cdot 10^5$	$4.31 \cdot 10^5$	$4.31 \cdot 10^2$
$3.42 \cdot 10^{-4}$	$1.85 \cdot 10^5$	$1.29 \cdot 10^5$	$3.15 \cdot 10^5$	$3.15 \cdot 10^2$
$5.71 \cdot 10^{-4}$	$1.44 \cdot 10^5$	$1.01 \cdot 10^5$	$2.45 \cdot 10^5$	$2.45 \cdot 10^2$
$1.14 \cdot 10^{-3}$	$9.82 \cdot 10^5$	$6.94 \cdot 10^4$	$1.68 \cdot 10^5$	$1.68 \cdot 10^2$
$2.74 \cdot 10^{-3}$	$7.32 \cdot 10^4$	$5.22 \cdot 10^4$	$1.25 \cdot 10^5$	$1.25 \cdot 10^2$
$8.21 \cdot 10^{-3}$	$5.63 \cdot 10^4$	$4.05 \cdot 10^4$	$9.67 \cdot 10^4$	$9.67 \cdot 10^1$
$1.92 \cdot 10^{-2}$	$4.99 \cdot 10^4$	$3.61 \cdot 10^4$	$8.60 \cdot 10^4$	$8.60 \cdot 10^1$
$3.84 \cdot 10^{-2}$	$4.72 \cdot 10^4$	$3.43 \cdot 10^4$	$8.15 \cdot 10^4$	$8.15 \cdot 10^1$
$7.67 \cdot 10^{-2}$	$4.30 \cdot 10^4$	$3.14 \cdot 10^4$	$7.44 \cdot 10^4$	$7.44 \cdot 10^1$
$1.53 \cdot 10^{-1}$	$3.58 \cdot 10^4$	$2.65 \cdot 10^4$	$6.24 \cdot 10^4$	$6.24 \cdot 10^1$
$5.01 \cdot 10^{-1}$	$1.67 \cdot 10^4$	$1.34 \cdot 10^4$	$3.01 \cdot 10^4$	$3.01 \cdot 10^1$
$9.99 \cdot 10^{-1}$	$6.29 \cdot 10^3$	$6.26 \cdot 10^3$	$1.26 \cdot 10^4$	$1.26 \cdot 10^1$
$9.99 \cdot 10^0$	$2.79 \cdot 10^2$	$1.41 \cdot 10^3$	$1.69 \cdot 10^3$	$1.69 \cdot 10^0$
$9.99 \cdot 10^1$	$1.95 \cdot 10^{-1}$	$7.76 \cdot 10^0$	$7.96 \cdot 10^0$	$7.96 \cdot 10^{-3}$
$3.00 \cdot 10^2$	$1.83 \cdot 10^{-1}$	$1.14 \cdot 10^{-1}$	$2.98 \cdot 10^{-1}$	$2.98 \cdot 10^{-4}$
$9.99 \cdot 10^2$	$1.70 \cdot 10^{-1}$	$1.06 \cdot 10^{-1}$	$2.76 \cdot 10^{-1}$	$2.76 \cdot 10^{-4}$

Table 6.11. Total activity from the manifold for the entire reactor (T excluded).

Time (years)	Inboard (Bq)	Outboard (Bq)	Total (Bq)	Total (MBq)
$3.17 \cdot 10^{-8}$	$1.71 \cdot 10^{18}$	$1.11 \cdot 10^{18}$	$2.81 \cdot 10^{18}$	$2.81 \cdot 10^{12}$
$9.51 \cdot 10^{-6}$	$1.53 \cdot 10^{18}$	$1.00 \cdot 10^{18}$	$2.53 \cdot 10^{18}$	$2.53 \cdot 10^{12}$
$5.71 \cdot 10^{-5}$	$1.43 \cdot 10^{18}$	$9.38 \cdot 10^{17}$	$2.36 \cdot 10^{18}$	$2.36 \cdot 10^{12}$
$1.14 \cdot 10^{-4}$	$1.36 \cdot 10^{18}$	$8.91 \cdot 10^{17}$	$2.25 \cdot 10^{18}$	$2.25 \cdot 10^{12}$
$3.42 \cdot 10^{-4}$	$1.16 \cdot 10^{18}$	$7.59 \cdot 10^{17}$	$1.92 \cdot 10^{18}$	$1.92 \cdot 10^{12}$
$5.71 \cdot 10^{-4}$	$1.04 \cdot 10^{18}$	$6.77 \cdot 10^{17}$	$1.72 \cdot 10^{18}$	$1.72 \cdot 10^{12}$
$1.14 \cdot 10^{-3}$	$8.90 \cdot 10^{17}$	$5.75 \cdot 10^{17}$	$1.46 \cdot 10^{18}$	$1.46 \cdot 10^{12}$
$2.74 \cdot 10^{-3}$	$7.58 \cdot 10^{17}$	$4.85 \cdot 10^{17}$	$1.24 \cdot 10^{18}$	$1.24 \cdot 10^{12}$
$8.21 \cdot 10^{-3}$	$6.11 \cdot 10^{17}$	$3.85 \cdot 10^{17}$	$9.96 \cdot 10^{17}$	$9.96 \cdot 10^{11}$
$1.92 \cdot 10^{-2}$	$5.54 \cdot 10^{17}$	$3.46 \cdot 10^{17}$	$8.99 \cdot 10^{17}$	$8.99 \cdot 10^{11}$
$3.84 \cdot 10^{-2}$	$5.22 \cdot 10^{17}$	$3.27 \cdot 10^{17}$	$8.48 \cdot 10^{17}$	$8.48 \cdot 10^{11}$
$7.67 \cdot 10^{-2}$	$4.80 \cdot 10^{17}$	$2.98 \cdot 10^{17}$	$7.78 \cdot 10^{17}$	$7.78 \cdot 10^{11}$
$1.53 \cdot 10^{-1}$	$4.10 \cdot 10^{17}$	$2.53 \cdot 10^{17}$	$6.62 \cdot 10^{17}$	$6.62 \cdot 10^{11}$
$5.01 \cdot 10^{-1}$	$2.53 \cdot 10^{17}$	$1.50 \cdot 10^{17}$	$4.03 \cdot 10^{17}$	$4.03 \cdot 10^{11}$
$9.99 \cdot 10^{-1}$	$1.73 \cdot 10^{17}$	$9.82 \cdot 10^{16}$	$2.71 \cdot 10^{17}$	$2.71 \cdot 10^{11}$
$9.99 \cdot 10^{0}$	$1.54 \cdot 10^{16}$	$8.32 \cdot 10^{15}$	$2.37E \cdot 10^{16}$	$2.37 \cdot 10^{10}$
$9.99 \cdot 10^{1}$	$3.20 \cdot 10^{12}$	$2.31 \cdot 10^{12}$	$5.51 \cdot 10^{12}$	$5.51 \cdot 10^{6}$
$3.00 \cdot 10^{2}$	$3.05 \cdot 10^{12}$	$1.60 \cdot 10^{12}$	$4.64 \cdot 10^{12}$	$4.64 \cdot 10^{6}$
$9.99 \cdot 10^{2}$	$2.55 \cdot 10^{12}$	$1.30 \cdot 10^{12}$	$3.85 \cdot 10^{12}$	$3.85 \cdot 10^{6}$

3. Analysis on the 2015 DEMO DCLL model

This section is devoted to provide the description and results of the activation analysis performed on the 2015 DEMO DCLL model. For this purpose, Section 3.1 describes the generation and characteristics of the model. Section 3.2 is devoted both to describe the neutronic model used, specifying materials as well as the irradiation scenario selected, and to explain the calculation methodology followed. The last subsection (3.3) shows the achieved activation calculations.

3.1. Description of the 2015 DEMO DCLL model

As a continuation of the work carried out during 2014 for the development of a generic DEMO model and the resultant particular models for each of the concepts, during 2015, a new generic neutronic DEMO model was developed by (KIT) [20]. Table 6.12 summarizes some of the machine

and plasma parameters that were used for the generation of the model. According to the fusion power, the neutron source for the total reactor is now $7.323 \cdot 10^{20}$ n/s.

Based on the new generic model, the corresponding models for the specific blanket concepts, including DEMO were developed too [21]. In this frame, this Section 3 is intended to continue the activation characterization of the DCLL breeder blanket, which was begun last year. Calculations and analysis were performed to obtain the decay heat and activity both from the blanket modules for the entire reactor and from each blanket module separately, as well as for the entire manifold. Results are provided for a range of decay times of interest for maintenance activities, safety and waste management assessments. In addition, nuclear heating is also provided, which was not calculated for the former 2014 model.

It is important to remember that the previous model (used in the 2015 task) had 1572 MW fusion power ($5.581 \cdot 10^{20}$ n/s), with a plasma major radius of 9 m, minor radius of 2.25 m and an elongation of 1.56 (see Section 2.1). These differences can be appreciated in Figure 6.17. Furthermore, in the 2014 model the torus was divided into 16 sectors of 22.5º, each having 3 outboard and 2 inboard blanket segments, although for neutronic purposes, an 11.25º half-sector was used. In addition, each sector contained 15 blanket modules.

However, in the 2015 configuration the torus is divided into 18 sectors of 20º. However, as in the previous model, every inboard sector can be divided into two segments (of 10º) and every outboard into three; thus, the blanket is composed of 54 outboard and 36 inboard segments. The total number of blanket modules per 10º sector is 16.

Table 6.12. DEMO parameters of the 2015 baseline configuration [14], [22].

Parameter	Value
No of TF coils	18
Major radius (m)	9.072
Minor radius (m)	2.927
Aspect ratio	3.1
Plasma elongation	1.59
Plasma triangularity	0.33
Fusion power (MW)	2037
Average neutron wall loading (PROCESS code)	1.05
Net electric power	500

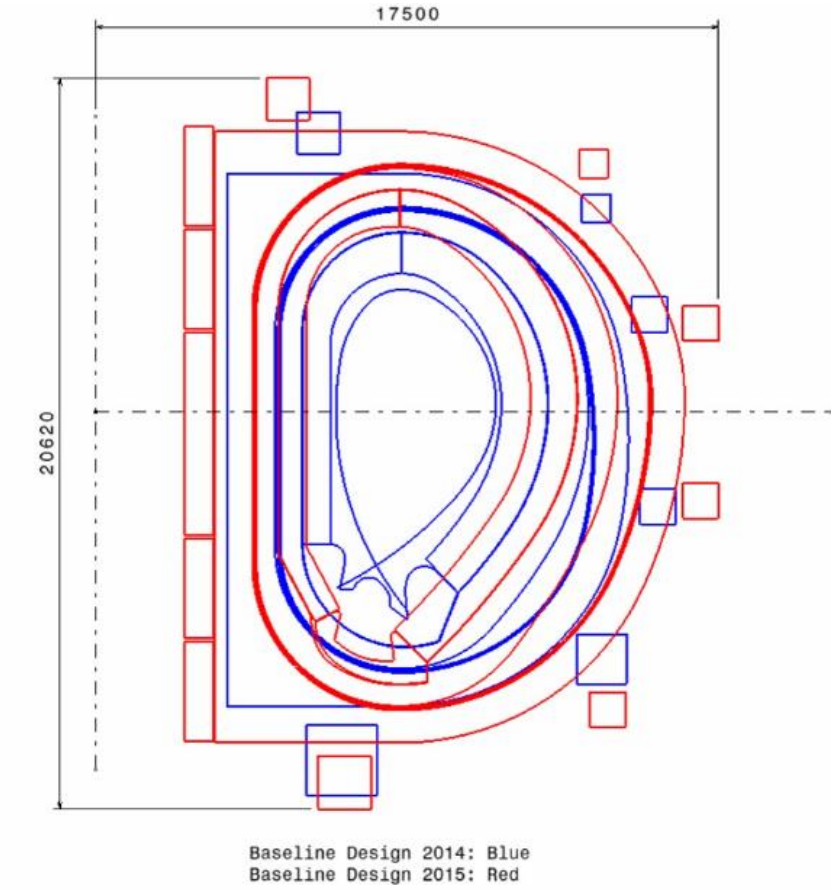

Figure 6.17. 2014 vs. 2015 DEMO generic models [23].

Moreover, the current model is quasi-heterogenized (except for the equatorial OB module, which is fully heterogenized) but even so, it is important to note that it already includes the FCI (in the homogenized composition), which were not taken into account in the previous model from 2014.

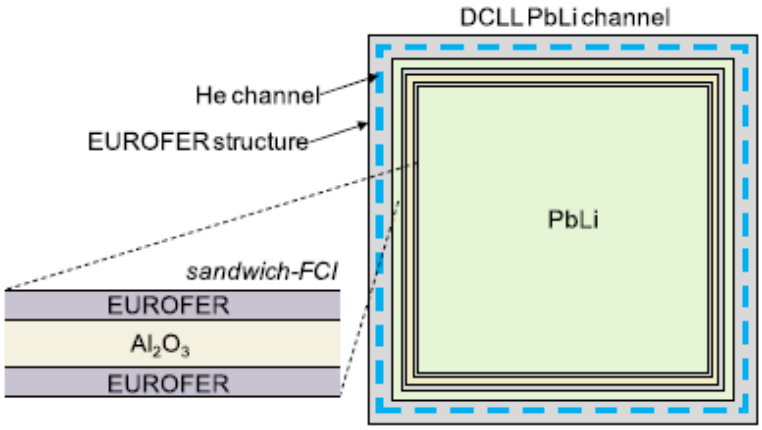

Figure 6.18. FCI scheme [2].

In this sense, FCI need to be made of composites or ceramic structures in order to ensure a proper thermal and electrical insulation. In the last years, DCLL used to have FCI made of silicon carbide (SiC). Nonetheless, in the 2015 design, a Eurofer – alumina (Al_2O_3) – Eurofer sandwich was proposed for FCI (Figure 6.18). The main advantage from the former is that the cost is reduced but, however, corrosion problems may appear, especially in those zones with high LiPb temperatures. Hence, depending on its final design, corrosion barriers may also be considered. However, since the velocity of the LiPb in the DCLL is high, low concentration of T is predicted and therefore, T permeation to He is not expected so barriers could not be necessary [2], [24].

Regarding the blanket description, each of the blanket modules considered in the model has a similar structure but with different dimensions. Each of them contains the following components (Figure 6.19): armour (coating of the first wall), FW, lateral walls, stiffenings, breeder zone general (which corresponds to the LiPb, FCI and Eurofer) and BP. The material compositions for each of the components are displayed in Table 6.13.

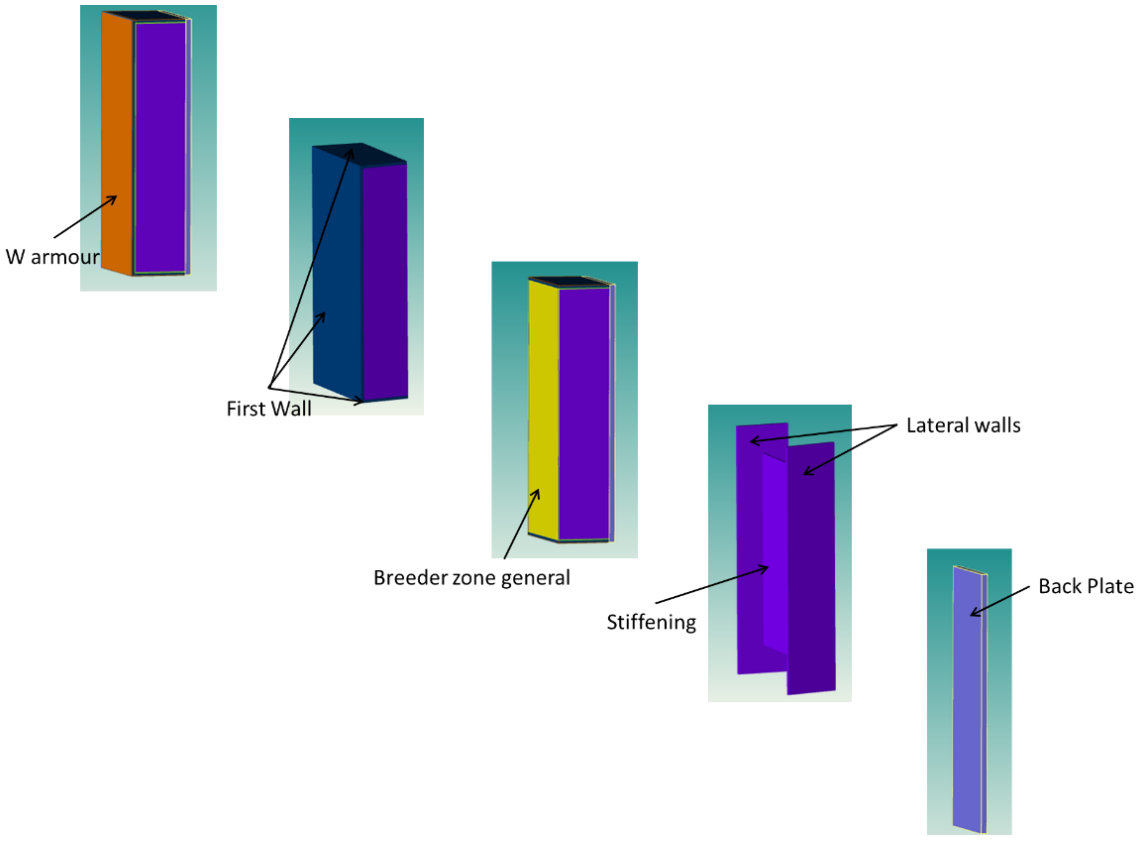

Figure 6.19. Components of the blanket modules in the 2015 DEMO DCLL neutronic model.

Table 6.13. Material composition for the components of the blanket modules in the DCLL neutronic model.

Component		Composition (% vol.)				
		Eurofer	**He**	**LiPb**	**W**	**Al_2O_3**
FW	FW coating/armour				100	
	FW	70.5		29.5		
Breeder zone	Stiffenings	100				
	Breeder zone general	10.9	1.5	87.4		0.2
Walls	Lateral walls	100				
	BP	88.5		11.5		

3.2. Computational assumptions and methodology for decay heat and activity calculations

This section is devoted to describe the computational model (3.2.1), the irradiation scenario (3.2.2), and the methodology followed for the calculations, including computational assumptions and material compositions (3.2.3).

3.2.1. Computational model: blanket description

An MCNP model of the fusion power demonstration reactor with DCLL blanket modules was used for the activation calculations. As it was previously mentioned, the MCNP model consists of a DCLL torus sector of 10º. Blanket modules in the model are numbered clockwise from 1 to 16 (Figure 6.20), starting from the one close to the divertor following the inboard (1-8) and then downwards along the outboard (9-16).

The torus sector of 10º includes one complete module for those numbered 1-8 and one and a half modules for those named 9-16. Therefore, the complete model consists of 288 inboard modules and 432 outboard modules, giving rise to a total number of 720 modules.

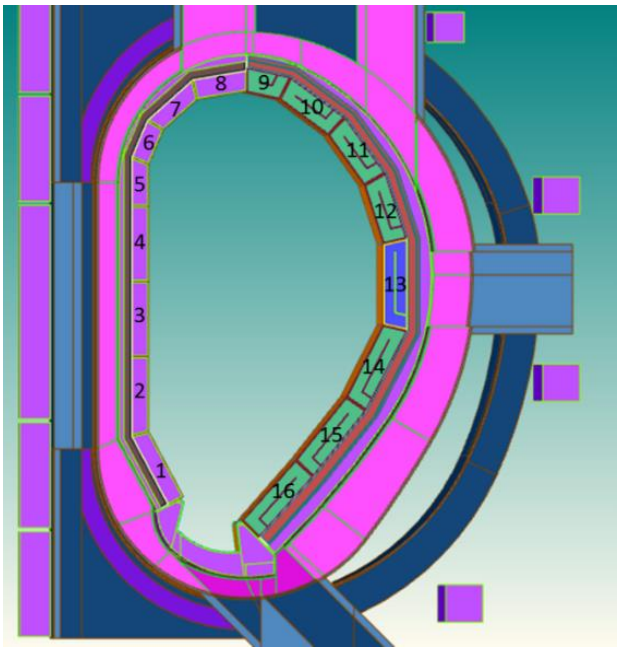

Figure 6.20. MCNP plot of DCLL DEMO blanket model (vertical cut).

3.2.2. Irradiation scenario and cooling times of interest

The assumed irradiation scenario for the activation calculations is the same as for the 2014 DEMO DCLL model, i.e. continuous operation over 5.2 years (CY) minus 10 days at 30% of the nominal fusion power followed by 10 days pulsed operation with 48 pulses of 4 hours at full power and 1 hour dwell time in between (see Figure 6.6). However, aside from the considered cooling times in the mentioned model, for the 2015 two more are taken into account, namely, 0 s (i.e. shutdown) and 50 years.

3.2.3. Calculation methodology

The calculation methodology is basically the same as the exposed in Section 2.2.3. The only difference is that the structure of the blanket modules is divided into six components (instead of five), according to Figure 6.21: W armour, FW, top and bottom walls (separated from the FW), lateral walls, breeder module (the whole interior of the blanket module; i.e. breeder zone and stiffenings) and BP. Hence, the average representative material defined from the volume fractions of the materials is quite different too and for these calculations corresponds to Table 6.14.

The manifold was divided into two cells, as in the 2014 model: one corresponding to the inboard (behind the inboard modules 1-8) and the second one corresponding to the outboard (behind the outboard modules 9-16).

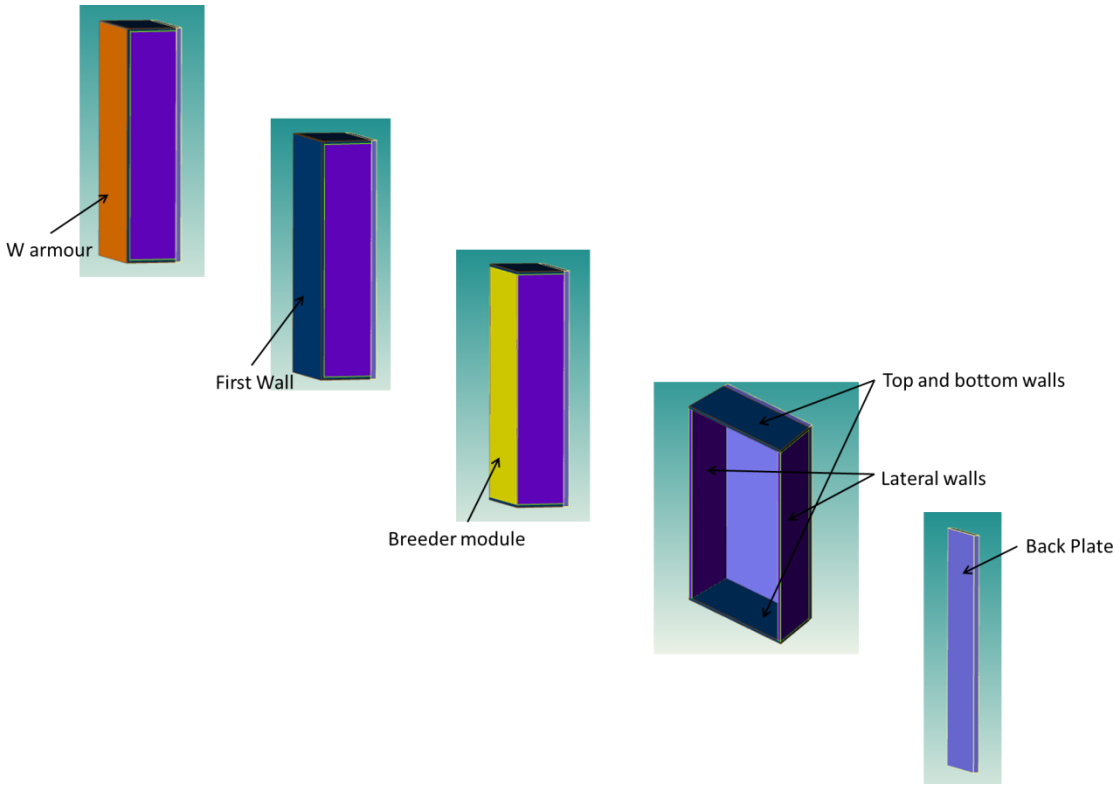

Figure 6.21. Components used in the activation calculations for each of the blanket modules.

Table 6.14. Material composition for activated components.

	Composition (% vol.)				
Component	**Eurofer**	**He**	**LiPb**	**W**	**Al_2O_3**
FW coating/armour				100	
FW	70.50		29.50		
Top and bottom walls	70.50		29.50		
Lateral walls	100				
Breeder module	13.31	1.46	85.04		0.19
BP	88.50		11.5		
Manifold Inboard	49.63	9.49	40.88		
Manifold Outboard	52.72	4.86	42.43		

The material elemental compositions used to perform activation calculations are the same as those used to carry out the calculations on the 2014 DEMO DCLL model (see Table 6.4), which means that impurities are considered for W, LiPb and Eurofer. Note that, once again, there is a ^{6}Li enrichment of 90% in the LiPb. However, the Al_2O_3 was considered pure.

Libraries and codes used were exactly the same as those mentioned in Section 2.2.3 (libraries: JEFF-3.1.1, FENDL-3.0 and FENDL-2.1 for transport simulations and EAF-2007 for activation; codes: MCNP5 for transport and ACAB for activation), according to the recommendations provided in the "*Guidelines for Neutronic Analyses*" [14]. Also, the DEMO neutron source used was again represented in a FORTRAN source routine that is compiled with the MCNP code and the model was run, as in the 2014 model, for 10^9 source neutrons.

In the same way, the contribution of the halves modules for the outboard was estimated multiplying the values obtained for the complete ones by 0.5. Finally, in this case, for obtaining the response functions results in all the blanket modules and manifold for the entire reactor (360º), results for the 10º torus sector are multiplied by 36.

Finally, it is worth to underline that for the additional calculations on the equatorial outboard module #13 (Sections 3.3.3, 3.3.4 and 3.3.5), materials of the breeder module (i.e. Eurofer, LiPb, Al_2O_3 and He) were considered separately.

3.3. Activation results and analysis

The results of this work are presented in six sections. The first five collect the results related with the blanket modules and the last one to those for the manifold.

The first one shows the computed volumes and neutron fluxes over the blanket components that will be used for the activation calculations (section 3.3.1). The second one (section 3.3.2) displays the results of decay heat and activity in the blanket modules. The third one (section 3.3.3) is devoted to provide component contribution to the decay heat and activity in the equatorial outboard module (#13) while Section 3.3.4 identifies major radionuclides contributing to decay heat in each of the components of the blanket module. Section 3.3.5 provides the radial decay heat profile across the blanket for different components, namely breeder module, top and bottom walls and lateral walls. The last section (3.3.6) presents the decay heat and activity results for the manifold.

Regarding the irradiation of LiPb, a complete irradiation during the entire operation phase has been considered. The fact is that the LiPb is exposed to a lower flux and thus, lower results are expected, since it is moving in and out of the blankets. The assumption of the remaining LiPb inside the blankets during the full reactor operation is not a very realistic estimation and, therefore, the obtained results are conservative but, however it is reasonable considering the current state of DEMO design.

Moreover, it is important to underline that, as in the case of results coming from the 2014 model, hereafter T coming from the activation of LiPb was removed from all the results, since it will be extracted from the breeder material throughout the blankets life time. Note that LiPb is present, aside from the breeder module, in the FW, top and bottom wall and BP, as well as in the manifold.

3.3.1. Volumes and neutron fluxes over the blanket components

Table 6.15 summarizes the volumes over all the blankets modules in the reactor (360º), separated into the different components. In all the component volumes, the statistical error for the volume sampling is lower than 0.3%.

Neutron fluxes computed for all the 6 component of the 16 different blanket modules are shown in Table 6.16. The statistical error of calculation in the vast majority of the energy groups is lower than 1%.

Table 6.15. Volumes for the components in the blanket modules for the entire reactor (cm^3).

# Blanket Modules	W	FW	Top and bottom walls	Lateral walls	Breeder module	BP	Total
1	$1.55\cdot10^{5}$	$1.93\cdot10^{6}$	$8.15\cdot10^{5}$	$1.81\cdot10^{6}$	$2.99\cdot10^{7}$	$3.43\cdot10^{6}$	$3.80\cdot10^{7}$
2	$1.46\cdot10^{5}$	$1.83\cdot10^{6}$	$7.36\cdot10^{5}$	$1.80\cdot10^{6}$	$2.73\cdot10^{7}$	$3.21\cdot10^{6}$	$3.50\cdot10^{7}$
3	$1.46\cdot10^{5}$	$1.82\cdot10^{6}$	$7.24\cdot10^{5}$	$1.74\cdot10^{6}$	$2.65\cdot10^{7}$	$3.03\cdot10^{6}$	$3.40\cdot10^{7}$
4	$1.46\cdot10^{5}$	$1.82\cdot10^{6}$	$7.25\cdot10^{5}$	$1.74\cdot10^{6}$	$2.65\cdot10^{7}$	$1.96\cdot10^{6}$	$3.29\cdot10^{7}$
5	$8.05\cdot10^{4}$	$1.01\cdot10^{6}$	$7.55\cdot10^{5}$	$1.03\cdot10^{6}$	$1.56\cdot10^{7}$	$1.96\cdot10^{6}$	$2.04\cdot10^{7}$
6	$7.56\cdot10^{4}$	$9.44\cdot10^{5}$	$8.26\cdot10^{5}$	$9.65\cdot10^{5}$	$1.52\cdot10^{7}$	$1.68\cdot10^{6}$	$1.97\cdot10^{7}$
7	$1.00\cdot10^{5}$	$1.26\cdot10^{6}$	$9.72\cdot10^{5}$	$1.27\cdot10^{6}$	$2.27\cdot10^{7}$	$2.92\cdot10^{6}$	$2.93\cdot10^{7}$
8	$1.29\cdot10^{5}$	$1.62\cdot10^{6}$	$1.23\cdot10^{6}$	$1.46\cdot10^{6}$	$3.12\cdot10^{7}$	$3.16\cdot10^{6}$	$3.88\cdot10^{7}$
9	$8.65\cdot10^{4}$	$1.09\cdot10^{6}$	$1.50\cdot10^{6}$	$2.30\cdot10^{6}$	$2.72\cdot10^{7}$	$2.67\cdot10^{6}$	$3.48\cdot10^{7}$
10	$1.86\cdot10^{5}$	$2.33\cdot10^{6}$	$1.83\cdot10^{6}$	$3.77\cdot10^{6}$	$5.57\cdot10^{7}$	$4.97\cdot10^{6}$	$6.88\cdot10^{7}$
11	$2.25\cdot10^{5}$	$2.83\cdot10^{6}$	$2.17\cdot10^{6}$	$3.86\cdot10^{6}$	$6.85\cdot10^{7}$	$6.07\cdot10^{6}$	$8.37\cdot10^{7}$
12	$2.48\cdot10^{5}$	$3.11\cdot10^{6}$	$2.40\cdot10^{6}$	$3.87\cdot10^{6}$	$7.61\cdot10^{7}$	$6.70\cdot10^{6}$	$9.24\cdot10^{7}$
13	$3.36\cdot10^{5}$	$4.21\cdot10^{6}$	$2.51\cdot10^{6}$	$5.15\cdot10^{6}$	$1.05\cdot10^{8}$	$9.24\cdot10^{6}$	$1.26\cdot10^{8}$
14	$3.16\cdot10^{5}$	$3.96\cdot10^{6}$	$2.34\cdot10^{6}$	$5.09\cdot10^{6}$	$9.72\cdot10^{7}$	$8.52\cdot10^{6}$	$1.17\cdot10^{8}$
15	$2.69\cdot10^{5}$	$3.36\cdot10^{6}$	$1.96\cdot10^{6}$	$4.92\cdot10^{6}$	$7.91\cdot10^{7}$	$6.80\cdot10^{6}$	$9.64\cdot10^{7}$
16	$2.12\cdot10^{5}$	$2.66\cdot10^{6}$	$1.55\cdot10^{6}$	$4.82\cdot10^{6}$	$6.07\cdot10^{7}$	$5.24\cdot10^{6}$	$7.52\cdot10^{7}$
Total (cm^3)	$3.35\cdot10^{6}$	$4.19\cdot10^{7}$	$2.64\cdot10^{7}$	$5.15\cdot10^{7}$	$8.62\cdot10^{8}$	$8.22\cdot10^{7}$	$9.43\cdot10^{8}$
Total (m^3)	$3.35\cdot10^{0}$	$4.19\cdot10^{1}$	$2.64\cdot10^{1}$	$5.15\cdot10^{1}$	$8.62\cdot10^{2}$	$8.22\cdot10^{1}$	$9.43\cdot10^{2}$

Table 6.16. Total average neutron fluxes over the different components (10^{14} n/cm^2·s).

# Blanket Module	W	FW	Top and bottom walls	Lateral walls	Breeder module	BP
1	9.59	9.63	5.60	6.25	6.33	2.49
2	9.91	9.89	6.52	6.59	6.68	2.74
3	10.64	10.75	7.52	7.57	7.70	3.31
4	10.66	10.75	7.46	7.50	7.63	3.27
5	10.26	10.21	6.65	6.70	6.76	2.78
6	10.19	10.16	6.14	6.43	6.53	2.40
7	10.28	10.27	6.04	6.43	6.57	2.52
8	10.38	10.42	5.68	6.24	6.46	2.16
9	10.47	10.49	5.50	5.15	5.64	1.47
10	10.63	10.69	5.57	5.35	5.99	1.55
11	10.81	10.91	5.86	5.50	6.25	1.65
12	10.96	11.10	6.07	5.63	6.47	1.73
13	11.08	11.26	6.01	5.73	6.61	1.77
14	11.07	11.26	6.09	5.81	6.65	1.78
15	10.69	10.88	6.09	5.65	6.38	1.70
16	9.75	9.80	5.08	4.82	5.32	1.33

3.3.2. Decay heat, activity and nuclear heating in the blanket modules for the entire reactor

This section summarizes the decay heat, activity and nuclear heating results for all the blanket modules and the entire reactor. Results for the decay heat and the activity do not include T produced by the activation of the LiPb in the breeder module since it is assumed to be continuously drained.

2.3.2.1. Decay heat in the blanket modules for the entire reactor

Table 6.17 shows the decay heat (W) in the blanket modules for the entire reactor (360º). As it can be seen, total decay heat is 47.9 – 14.7 MW up to 1 hour; around 1 MW at 2 months and around 0.3 MW up to ~ 1 year; then it drops to 7 W at 100 years and it finally reaches 4.6 W after 1000 years of cooling.

Module #13 (equatorial outboard) shows highest values (in W) which are around 6 times higher than those of the module with the lowest values (#6). However, analyzing volumetric values

(W/cc), modules #3 and #4 are those with highest values of decay heat (module #13 is about 76% of module #3 and #4 in specific values).

Table 6.18 shows activity results in the blanket modules for the entire reactor (360º). As it is shown, total activity is between $2.4 \cdot 10^{14}$ and $1.7 \cdot 10^{13}$ MBq up to 1 year; $5.1 \cdot 10^{8}$ MBq at 50 years and then it drops until 10^{7} at 1000 years.

On the other hand, as in the case of the decay heat, module #13 (equatorial outboard) shows highest values (in Bq) which are around 6.5 times higher than those of the module with the lowest values (#6). Once again, analyzing volumetric values (Bq/cc), it is found that modules #3 and #4 are those with highest values of activity (module #13 is about 70% of module #3 and #4 in specific values).

Table 6.17. Total decay heat (W) from the blanket for the entire reactor separated into the individual blanket modules (excluding T from activated LiPb).

Time (years)	Blanket module (360º)																Total (W)	Total (MW)
	1	2	3	4	5	6	7	8	9	10	11	12	13	14	15	16		
$0.00\cdot10^{0}$	$1.68\cdot10^{6}$	$1.78\cdot10^{6}$	$2.39\cdot10^{6}$	$2.31\cdot10^{6}$	$1.02\cdot10^{6}$	$9.59\cdot10^{5}$	$1.22\cdot10^{6}$	$1.89\cdot10^{6}$	$1.45\cdot10^{6}$	$3.13\cdot10^{6}$	$4.10\cdot10^{6}$	$4.83\cdot10^{6}$	$6.86\cdot10^{6}$	$6.44\cdot10^{6}$	$4.94\cdot10^{6}$	$2.86\cdot10^{6}$	$4.79\cdot10^{7}$	$4.79\cdot10^{1}$
$3.17\cdot10^{-8}$	$1.16\cdot10^{6}$	$1.22\cdot10^{6}$	$1.58\cdot10^{6}$	$1.53\cdot10^{6}$	$7.07\cdot10^{5}$	$6.58\cdot10^{5}$	$8.15\cdot10^{5}$	$1.26\cdot10^{6}$	$9.84\cdot10^{5}$	$2.08\cdot10^{6}$	$2.69\cdot10^{6}$	$3.14\cdot10^{6}$	$4.42\cdot10^{6}$	$4.16\cdot10^{6}$	$3.24\cdot10^{6}$	$1.96\cdot10^{6}$	$3.16\cdot10^{7}$	$3.16\cdot10^{1}$
$9.51\cdot10^{-6}$	$7.03\cdot10^{5}$	$7.34\cdot10^{5}$	$8.90\cdot10^{5}$	$8.71\cdot10^{5}$	$4.32\cdot10^{5}$	$4.00\cdot10^{5}$	$4.71\cdot10^{5}$	$7.17\cdot10^{5}$	$5.90\cdot10^{5}$	$1.19\cdot10^{6}$	$1.50\cdot10^{6}$	$1.72\cdot10^{6}$	$2.38\cdot10^{6}$	$2.26\cdot10^{6}$	$1.81\cdot10^{6}$	$1.19\cdot10^{6}$	$1.79\cdot10^{7}$	$1.79\cdot10^{1}$
$5.71\cdot10^{-5}$	$6.35\cdot10^{5}$	$6.62\cdot10^{5}$	$7.99\cdot10^{5}$	$7.82\cdot10^{5}$	$3.90\cdot10^{5}$	$3.61\cdot10^{5}$	$4.29\cdot10^{5}$	$6.46\cdot10^{5}$	$5.31\cdot10^{5}$	$1.07\cdot10^{6}$	$1.35\cdot10^{6}$	$1.54\cdot10^{6}$	$2.14\cdot10^{6}$	$2.02\cdot10^{6}$	$1.63\cdot10^{6}$	$1.07\cdot10^{6}$	$1.61\cdot10^{7}$	$1.61\cdot10^{1}$
$1.14\cdot10^{-4}$	$5.82\cdot10^{5}$	$6.06\cdot10^{5}$	$7.27\cdot10^{5}$	$7.12\cdot10^{5}$	$3.57\cdot10^{5}$	$3.30\cdot10^{5}$	$3.96\cdot10^{5}$	$5.90\cdot10^{5}$	$4.85\cdot10^{5}$	$9.80\cdot10^{5}$	$1.23\cdot10^{6}$	$1.40\cdot10^{6}$	$1.94\cdot10^{6}$	$1.84\cdot10^{6}$	$1.48\cdot10^{6}$	$9.80\cdot10^{5}$	$1.46\cdot10^{7}$	$1.46\cdot10^{1}$
$3.42\cdot10^{-4}$	$4.30\cdot10^{5}$	$4.43\cdot10^{5}$	$5.21\cdot10^{5}$	$5.12\cdot10^{5}$	$2.61\cdot10^{5}$	$2.42\cdot10^{5}$	$3.00\cdot10^{5}$	$4.29\cdot10^{5}$	$3.51\cdot10^{5}$	$7.09\cdot10^{5}$	$8.84\cdot10^{5}$	$1.01\cdot10^{6}$	$1.39\cdot10^{6}$	$1.31\cdot10^{6}$	$1.06\cdot10^{6}$	$7.16\cdot10^{5}$	$1.06\cdot10^{7}$	$1.06\cdot10^{1}$
$5.71\cdot10^{-4}$	$3.38\cdot10^{5}$	$3.45\cdot10^{5}$	$3.97\cdot10^{5}$	$3.91\cdot10^{5}$	$2.03\cdot10^{5}$	$1.89\cdot10^{5}$	$2.42\cdot10^{5}$	$3.32\cdot10^{5}$	$2.71\cdot10^{5}$	$5.46\cdot10^{5}$	$6.78\cdot10^{5}$	$7.68\cdot10^{5}$	$1.06\cdot10^{6}$	$9.99\cdot10^{5}$	$8.14\cdot10^{5}$	$5.57\cdot10^{5}$	$8.13\cdot10^{6}$	$8.13\cdot10^{0}$
$1.14\cdot10^{-3}$	$2.31\cdot10^{5}$	$2.32\cdot10^{5}$	$2.58\cdot10^{5}$	$2.55\cdot10^{5}$	$1.37\cdot10^{5}$	$1.28\cdot10^{5}$	$1.73\cdot10^{5}$	$2.21\cdot10^{5}$	$1.80\cdot10^{5}$	$3.61\cdot10^{5}$	$4.44\cdot10^{5}$	$4.99\cdot10^{5}$	$6.82\cdot10^{5}$	$6.45\cdot10^{5}$	$5.31\cdot10^{5}$	$3.75\cdot10^{5}$	$5.35\cdot10^{6}$	$5.35\cdot10^{0}$
$2.74\cdot10^{-3}$	$1.58\cdot10^{5}$	$1.58\cdot10^{5}$	$1.72\cdot10^{5}$	$1.71\cdot10^{5}$	9.30·104	$8.69\cdot10^{4}$	$1.21\cdot10^{5}$	$1.50\cdot10^{5}$	$1.22\cdot10^{5}$	$2.44\cdot10^{5}$	$2.99\cdot10^{5}$	$3.35\cdot10^{5}$	$4.57\cdot10^{5}$	$4.32\cdot10^{5}$	$3.57\cdot10^{5}$	$2.55\cdot10^{5}$	$3.61\cdot10^{6}$	$3.61\cdot10^{0}$
$8.21\cdot10^{-3}$	$9.22\cdot10^{4}$	$9.31\cdot10^{4}$	$1.04\cdot10^{5}$	$1.03\cdot10^{5}$	$5.53\cdot10^{4}$	$5.14\cdot10^{4}$	$7.07\cdot10^{4}$	$8.95\cdot10^{4}$	$7.45\cdot10^{4}$	$1.48\cdot10^{5}$	$1.82\cdot10^{5}$	$2.05\cdot10^{5}$	$2.81\cdot10^{5}$	$2.66\cdot10^{5}$	$2.18\cdot10^{5}$	$1.53\cdot10^{5}$	$2.19\cdot10^{6}$	$2.19\cdot10^{0}$
$1.92\cdot10^{-2}$	$6.89\cdot10^{4}$	$7.00\cdot10^{4}$	$7.93\cdot10^{4}$	$7.83\cdot10^{4}$	$4.19\cdot10^{4}$	$3.87\cdot10^{4}$	$5.29\cdot10^{4}$	$6.77\cdot10^{4}$	$5.74\cdot10^{4}$	$1.13\cdot10^{5}$	$1.40\cdot10^{5}$	$1.58\cdot10^{5}$	$2.16\cdot10^{5}$	$2.04\cdot10^{5}$	$1.67\cdot10^{5}$	$1.16\cdot10^{5}$	$1.67\cdot10^{6}$	$1.67\cdot10^{0}$
$3.84\cdot10^{-2}$	$6.30\cdot10^{4}$	$6.40\cdot10^{4}$	$7.25\cdot10^{4}$	$7.16\cdot10^{4}$	$3.83\cdot10^{4}$	$3.55\cdot10^{4}$	$4.83\cdot10^{4}$	$6.19\cdot10^{4}$	$5.28\cdot10^{4}$	$1.04\cdot10^{5}$	$1.28\cdot10^{5}$	$1.44\cdot10^{5}$	$1.98\cdot10^{5}$	$1.87\cdot10^{5}$	$1.53\cdot10^{5}$	$1.06\cdot10^{5}$	$1.53\cdot10^{6}$	$1.53\cdot10^{0}$
$7.67\cdot10^{-2}$	$5.73\cdot10^{4}$	$5.82\cdot10^{4}$	$6.61\cdot10^{4}$	$6.52\cdot10^{4}$	$3.49\cdot10^{4}$	$3.23\cdot10^{4}$	$4.38\cdot10^{4}$	$5.64\cdot10^{4}$	$4.82\cdot10^{4}$	$9.46\cdot10^{4}$	$1.17\cdot10^{5}$	$1.32\cdot10^{5}$	$1.80\cdot10^{5}$	$1.71\cdot10^{5}$	$1.39\cdot10^{5}$	$9.69\cdot10^{4}$	$1.39\cdot10^{6}$	$1.39\cdot10^{0}$
$1.53\cdot10^{-1}$	$4.84\cdot10^{4}$	$4.94\cdot10^{4}$	$5.63\cdot10^{4}$	$5.55\cdot10^{4}$	2.9610^{4}	$2.73\cdot10^{4}$	$3.68\cdot10^{4}$	$4.78\cdot10^{4}$	$4.09\cdot10^{4}$	$8.04\cdot10^{4}$	$9.92\cdot10^{4}$	$1.12\cdot10^{5}$	$1.54\cdot10^{5}$	$1.45\cdot10^{5}$	$1.19\cdot10^{5}$	$8.21\cdot10^{5}$	$1.18\cdot10^{6}$	$1.18\cdot10^{0}$
$5.01\cdot10^{-1}$	$2.48\cdot10^{4}$	$2.56\cdot10^{4}$	$3.00\cdot10^{4}$	$2.95\cdot10^{4}$	$1.53\cdot10^{4}$	$1.41\cdot10^{4}$	$1.82\cdot10^{4}$	$2.50\cdot10^{4}$	$2.13\cdot10^{4}$	$4.21\cdot10^{4}$	$5.23\cdot10^{4}$	$5.93\cdot10^{4}$	$8.17\cdot10^{4}$	$7.74\cdot10^{4}$	$6.27\cdot10^{4}$	$4.24\cdot10^{4}$	$6.22\cdot10^{5}$	$6.22\cdot10^{-1}$
$9.99\cdot10^{-1}$	$1.14\cdot10^{4}$	$1.20\cdot10^{4}$	$1.47\cdot10^{4}$	$1.44\cdot10^{4}$	$7.16\cdot10^{3}$	$6.60\cdot10^{3}$	$7.92\cdot10^{3}$	$1.18\cdot10^{4}$	$1.00\cdot10^{4}$	$2.00\cdot10^{4}$	$2.51\cdot10^{4}$	$2.87\cdot10^{4}$	$3.97\cdot10^{4}$	$3.77\cdot10^{4}$	$3.02\cdot10^{4}$	$1.97\cdot10^{4}$	$2.97\cdot10^{5}$	$2.97\cdot10^{-1}$
$9.99\cdot10^{0}$	$3.96\cdot10^{2}$	$3.98\cdot10^{2}$	$4.35\cdot10^{2}$	$4.31\cdot10^{2}$	$2.44\cdot10^{2}$	$2.28\cdot10^{2}$	$3.33\cdot10^{2}$	$3.92\cdot10^{2}$	$3.55\cdot10^{2}$	$6.77\cdot10^{2}$	$8.25\cdot10^{2}$	$9.20\cdot10^{2}$	$1.25\cdot10^{3}$	$1.18\cdot10^{3}$	$9.77\cdot10^{2}$	$6.97\cdot10^{2}$	$9.74\cdot10^{3}$	$9.74\cdot10^{-3}$
$5.00\cdot10^{1}$	$2.07\cdot10^{0}$	$2.04\cdot10^{0}$	$2.12\cdot10^{0}$	$2.16\cdot10^{0}$	$1.26\cdot10^{0}$	$1.18\cdot10^{0}$	$1.80\cdot10^{0}$	$2.03\cdot10^{0}$	$1.84\cdot10^{0}$	$3.50\cdot10^{0}$	$4.25\cdot10^{0}$	$4.72\cdot10^{0}$	$6.39\cdot10^{0}$	$6.02\cdot10^{0}$	$5.01\cdot10^{0}$	$3.63\cdot10^{0}$	$5.00\cdot10^{1}$	$5.00\cdot10^{-5}$
$9.99\cdot10^{1}$	$2.64\cdot10^{-1}$	$2.60\cdot10^{-1}$	$2.63\cdot10^{-1}$	$2.90\cdot10^{-1}$	$1.54\cdot10^{-1}$	$1.44\cdot10^{-1}$	$2.06\cdot10^{-1}$	$2.74\cdot10^{-1}$	$2.22\cdot10^{-1}$	$4.60\cdot10^{-1}$	$5.81\cdot10^{-1}$	$6.63\cdot10^{-1}$	$9.22\cdot10^{-1}$	$8.63\cdot10^{-1}$	$6.86\cdot10^{-1}$	$4.56\cdot10^{-1}$	$6.71\cdot10^{0}$	$6.71\cdot10^{-6}$
$3.00\cdot10^{2}$	$2.24\cdot10^{-1}$	$2.18\cdot10^{-1}$	$2.16\cdot10^{-1}$	$2.39\cdot10^{-1}$	$1.30\cdot10^{-1}$	$1.21\cdot10^{-1}$	$1.76\cdot10^{-1}$	$2.29\cdot10^{-1}$	$1.88\cdot10^{-1}$	$3.86\cdot10^{-1}$	$4.84\cdot10^{-1}$	$5.49\cdot10^{-1}$	$7.61\cdot10^{-1}$	$7.13\cdot10^{-1}$	$5.70\cdot10^{-1}$	$3.86\cdot10^{-1}$	$5.59\cdot10^{0}$	$5.59\cdot10^{-6}$
$9.99\cdot10^{2}$	$1.88\cdot10^{-1}$	$1.82\cdot10^{-1}$	$1.76\cdot10^{-1}$	$1.97\cdot10^{-1}$	$1.09\cdot10^{-1}$	$1.02\cdot10^{-1}$	$1.48\cdot10^{-1}$	$1.90\cdot10^{-1}$	$1.57\cdot10^{-1}$	$3.20\cdot10^{-1}$	$4.00\cdot10^{-1}$	$4.52\cdot10^{-1}$	$6.24\cdot10^{-1}$	$5.84\cdot10^{-1}$	$4.70\cdot10^{-1}$	$3.23\cdot10^{-1}$	$4.62\cdot10^{0}$	$4.62\cdot10^{-6}$

Table 6.18. Total activity (Bq) from the blanket for the entire reactor separated into the individual blanket modules (excluding T from activated LiPb).

Time (years)	Blanket module (360º)																Total (Bq)	Total (MBq)
	1	2	3	4	5	6	7	8	9	10	11	12	13	14	15	16		
$0.00\cdot10^{0}$	$8.70\cdot10^{18}$	$9.17\cdot10^{18}$	$1.19\cdot10^{19}$	$1.15\cdot10^{19}$	$5.27\cdot10^{18}$	$4.84\cdot10^{18}$	$6.71\cdot10^{18}$	$9.43\cdot10^{18}$	$7.17\cdot10^{18}$	$1.54\cdot10^{19}$	$2.01\cdot10^{19}$	$2.35\cdot10^{19}$	$3.32\cdot10^{19}$	$3.12\cdot10^{19}$	$2.42\cdot10^{19}$	$1.45\cdot10^{19}$	$2.37\cdot10^{20}$	$2.37\cdot10^{14}$
$3.17\cdot10^{-8}$	$6.65\cdot10^{18}$	$6.97\cdot10^{18}$	$8.73\cdot10^{18}$	$8.50\cdot10^{18}$	$4.03\cdot10^{18}$	$3.67\cdot10^{18}$	$4.98\cdot10^{18}$	$6.95\cdot10^{18}$	$5.37\cdot10^{18}$	$1.14\cdot10^{19}$	$1.46\cdot10^{19}$	$1.69\cdot10^{19}$	$2.37\cdot10^{19}$	$2.24\cdot10^{19}$	$1.76\cdot10^{19}$	$1.10\cdot10^{19}$	$1.73\cdot10^{20}$	$1.73\cdot10^{14}$
$9.51\cdot10^{-6}$	$4.56\cdot10^{18}$	$4.74\cdot10^{18}$	$5.66\cdot10^{18}$	$5.55\cdot10^{18}$	$2.76\cdot10^{18}$	$2.49\cdot10^{18}$	$3.28\cdot10^{18}$	$4.56\cdot10^{18}$	$3.63\cdot10^{18}$	$7.45\cdot10^{18}$	$9.37\cdot10^{18}$	$1.^{7}\cdot10^{19}$	$1.49\cdot10^{19}$	$1.41\cdot10^{19}$	$1.13\cdot10^{19}$	$7.49\cdot10^{18}$	$1.12\cdot10^{20}$	$1.12\cdot10^{14}$
$5.71\cdot10^{-5}$	$4.34\cdot10^{18}$	$4.50\cdot10^{18}$	$5.36\cdot10^{18}$	$5.26\cdot10^{18}$	$2.62\cdot10^{18}$	$2.36\cdot10^{18}$	$3.12\cdot10^{18}$	$4.33\cdot10^{18}$	$3.44\cdot10^{18}$	$7.07\cdot10^{18}$	$8.87\cdot10^{18}$	$1.02\cdot10^{19}$	$1.41\cdot10^{19}$	$1.33\cdot10^{19}$	$1.07\cdot10^{19}$	$7.11\cdot10^{18}$	$1.07\cdot10^{20}$	$1.07\cdot10^{14}$
$1.14\cdot10^{-4}$	$4.18\cdot10^{18}$	$4.34\cdot10^{18}$	$5.15\cdot10^{18}$	$5.06\cdot10^{18}$	$2.53\cdot10^{18}$	$2.27\cdot10^{18}$	$3.00\cdot10^{18}$	$4.16\cdot10^{18}$	$3.30\cdot10^{18}$	$6.79\cdot10^{18}$	$8.53\cdot10^{18}$	$9.75\cdot10^{18}$	$1.35\cdot10^{19}$	$1.28\cdot10^{19}$	$1.03\cdot10^{19}$	$6.84\cdot10^{18}$	$1.02\cdot10^{20}$	$1.02\cdot10^{14}$
$3.42\cdot10^{-4}$	$3.72\cdot10^{18}$	$3.85\cdot10^{18}$	$4.55\cdot10^{18}$	$4.47\cdot10^{18}$	$2.24\cdot10^{18}$	$2.01\cdot10^{18}$	$2.66\cdot10^{18}$	$3.68\cdot10^{18}$	$2.91\cdot10^{18}$	$5.98\cdot10^{18}$	$7.50\cdot10^{18}$	$8.57\cdot10^{18}$	$1.19\cdot10^{19}$	$1.12\cdot10^{19}$	$9.06\cdot10^{18}$	$6.05\cdot10^{18}$	$9.03\cdot10^{19}$	$9.03\cdot10^{13}$
$5.71\cdot10^{-4}$	$3.41\cdot10^{18}$	$3.53\cdot10^{18}$	$4.16\cdot10^{18}$	$4.09\cdot10^{18}$	$2.05\cdot10^{18}$	$1.83\cdot10^{18}$	$2.44\cdot10^{18}$	$3.37\cdot10^{18}$	$2.65\cdot10^{18}$	$5.47\cdot10^{18}$	$6.85\cdot10^{18}$	$7.82\cdot10^{18}$	$1.08\cdot10^{19}$	$1.02\cdot10^{19}$	$8.28\cdot10^{18}$	$5.54\cdot10^{18}$	$8.26\cdot10^{19}$	$8.26\cdot10^{13}$
$1.14\cdot10^{-3}$	$3.00\cdot10^{18}$	$3.10\cdot10^{18}$	$3.66\cdot10^{18}$	$3.60\cdot10^{18}$	$1.80\cdot10^{18}$	$1.60\cdot10^{18}$	$2.13\cdot10^{18}$	$2.95\cdot10^{18}$	$2.32\cdot10^{18}$	$4.78\cdot10^{18}$	$6.00\cdot10^{18}$	$6.85\cdot10^{18}$	$9.48\cdot10^{18}$	$8.97\cdot10^{18}$	$7.25\cdot10^{18}$	$4.85\cdot10^{18}$	$7.24\cdot10^{19}$	$7.24\cdot10^{13}$
$2.74\cdot10^{-3}$	$2.54\cdot10^{18}$	$2.64\cdot10^{18}$	$3.15\cdot10^{18}$	$3.09\cdot10^{18}$	$1.53\cdot10^{18}$	$1.35\cdot10^{18}$	$1.80\cdot10^{18}$	$2.51\cdot10^{18}$	$1.97\cdot10^{18}$	$4.08\cdot10^{18}$	$5.13\cdot10^{18}$	$5.87\cdot10^{18}$	$8.15\cdot10^{18}$	$7.71\cdot10^{18}$	$6.21\cdot10^{18}$	$4.12\cdot10^{18}$	$6.18\cdot10^{19}$	$6.18\cdot10^{13}$
$8.21\cdot10^{-3}$	$1.95\cdot10^{18}$	$2.06\cdot10^{18}$	$2.53\cdot10^{18}$	$2.47\cdot10^{18}$	$1.19\cdot10^{18}$	$1.03\cdot10^{18}$	$1.37\cdot10^{18}$	$1.96\cdot10^{18}$	$1.54\cdot10^{18}$	$3.20\cdot10^{18}$	$4.05\cdot10^{18}$	$4.67\cdot10^{18}$	$6.52\cdot10^{18}$	$6.17\cdot10^{18}$	$4.93\cdot10^{18}$	$3.19\cdot10^{18}$	$4.88\cdot10^{19}$	$4.88\cdot10^{13}$
$1.92\cdot10^{-2}$	$1.69\cdot10^{18}$	$1.80\cdot10^{18}$	$2.24\cdot10^{18}$	$2.18\cdot10^{18}$	$1.05\cdot10^{18}$	$8.90\cdot10^{17}$	$1.18\cdot10^{18}$	$1.72\cdot10^{18}$	$1.35\cdot10^{18}$	$2.81\cdot10^{18}$	$3.57\cdot10^{18}$	$4.12\cdot10^{18}$	$5.76\cdot10^{18}$	$5.46\cdot10^{18}$	$4.35\cdot10^{18}$	$2.79\cdot10^{18}$	$4.30\cdot10^{19}$	$4.30\cdot10^{13}$
$3.84\cdot10^{-2}$	$1.59\cdot10^{18}$	$1.69\cdot10^{18}$	$2.11\cdot10^{18}$	$2.06\cdot10^{18}$	$9.81\cdot10^{17}$	$8.31\cdot10^{17}$	$1.10\cdot10^{18}$	$1.61\cdot10^{18}$	$1.27\cdot10^{18}$	$2.64\cdot10^{18}$	$3.36\cdot10^{18}$	$3.88\cdot10^{18}$	$5.42\cdot10^{18}$	$5.14\cdot10^{18}$	$4.09\cdot10^{18}$	$2.62\cdot10^{18}$	$4.04\cdot10^{19}$	$4.04\cdot10^{13}$
$7.67\cdot10^{-2}$	$1.46\cdot10^{18}$	$1.56\cdot10^{18}$	$1.96\cdot10^{18}$	$1.91\cdot10^{18}$	$9.07\cdot10^{17}$	$7.63\cdot10^{17}$	$1.01\cdot10^{18}$	$1.49\cdot10^{18}$	$1.18\cdot10^{18}$	$2.45\cdot10^{18}$	$3.11\cdot10^{18}$	$3.60\cdot10^{18}$	$5.04\cdot10^{18}$	$4.78\cdot10^{18}$	$3.80\cdot10^{18}$	$2.42\cdot10^{18}$	$3.75\cdot10^{19}$	$3.75\cdot10^{13}$
$1.53\cdot10^{-1}$	$1.28\cdot10^{18}$	$1.38\cdot10^{18}$	$1.74\cdot10^{18}$	$1.69\cdot10^{18}$	$7.99\cdot10^{17}$	$6.64\cdot10^{17}$	$8.82\cdot10^{17}$	$1.32\cdot10^{18}$	$1.04\cdot10^{18}$	$2.17\cdot10^{18}$	$2.76\cdot10^{18}$	$3.20\cdot10^{18}$	$4.48\cdot10^{18}$	$4.25\cdot10^{18}$	$3.37\cdot10^{18}$	$2.13\cdot10^{18}$	$3.32\cdot10^{19}$	$3.32\cdot10^{13}$
$5.01\cdot10^{-1}$	$8.54\cdot10^{17}$	$9.34\cdot10^{17}$	$1.22\cdot10^{18}$	$1.18\cdot10^{18}$	$5.42\cdot10^{17}$	$4.31\cdot10^{17}$	$5.75\cdot10^{17}$	$9.07\cdot10^{17}$	$7.27\cdot10^{17}$	$1.51\cdot10^{18}$	$1.93\cdot10^{18}$	$2.25\cdot10^{18}$	$3.17\cdot10^{18}$	$3.01\cdot10^{18}$	$2.37\cdot10^{18}$	$1.45\cdot10^{18}$	$2.31\cdot10^{19}$	$2.31\cdot10^{13}$
$9.99\cdot10^{-1}$	$6.22\cdot10^{17}$	$6.88\cdot10^{17}$	$9.21\cdot10^{17}$	$8.90\cdot10^{17}$	$4.00\cdot10^{17}$	$3.03\cdot10^{17}$	$4.09\cdot10^{17}$	$6.75\cdot10^{17}$	$5.45\cdot10^{17}$	$1.13\cdot10^{18}$	$1.46\cdot10^{18}$	$1.71\cdot10^{18}$	$2.40\cdot10^{18}$	$2.28\cdot10^{18}$	$1.79\cdot10^{18}$	$1.07\cdot10^{18}$	$1.73\cdot10^{19}$	$1.73\cdot10^{13}$
$9.99\cdot10^{0}$	$5.54\cdot10^{16}$	$6.15\cdot10^{16}$	$8.31\cdot10^{16}$	$8.02\cdot10^{16}$	$3.58\cdot10^{16}$	$2.70\cdot10^{16}$	$3.65\cdot10^{16}$	$6.07\cdot10^{16}$	$4.92\cdot10^{16}$	$1.02\cdot10^{17}$	$1.32\cdot10^{17}$	$1.54\cdot10^{17}$	$2.18\cdot10^{17}$	$2.07\cdot10^{17}$	$1.62\cdot10^{17}$	$9.64\cdot10^{16}$	$1.56\cdot10^{18}$	$1.56\cdot10^{12}$
$5.00\cdot10^{1}$	$1.99\cdot10^{13}$	$2.03\cdot10^{13}$	$2.42\cdot10^{13}$	$2.38\cdot10^{13}$	$1.20\cdot10^{13}$	$9.13\cdot10^{12}$	$1.24\cdot10^{13}$	$2.08\cdot10^{13}$	$1.71\cdot10^{13}$	$3.49\cdot10^{13}$	$4.39\cdot10^{13}$	$5.02\cdot10^{13}$	$7.36\cdot10^{13}$	$6.58\cdot10^{13}$	$5.23\cdot10^{13}$	$3.38\cdot10^{13}$	$5.14\cdot10^{14}$	$5.14\cdot10^{8}$
$9.99\cdot10^{1}$	$7.37\cdot10^{12}$	$7.40\cdot10^{12}$	$8.79\cdot10^{12}$	$8.64\cdot10^{12}$	$4.36\cdot10^{12}$	$3.31\cdot10^{12}$	$4.50\cdot10^{12}$	$7.78\cdot10^{12}$	$6.20\cdot10^{12}$	$1.29\cdot10^{13}$	$1.65\cdot10^{13}$	$1.89\cdot10^{13}$	$2.66\cdot10^{13}$	$2.48\cdot10^{13}$	$1.95\cdot10^{13}$	$1.25\cdot10^{13}$	$1.90\cdot10^{14}$	$1.90\cdot10^{8}$
$3.00\cdot10^{2}$	$4.52\cdot10^{12}$	$4.52\cdot10^{12}$	$5.25\cdot10^{12}$	$5.18\cdot10^{12}$	$2.68\cdot10^{12}$	$2.49\cdot10^{12}$	$3.47\cdot10^{12}$	$4.68\cdot10^{12}$	$3.78\cdot10^{12}$	$7.77\cdot10^{12}$	$9.80\cdot10^{12}$	$1.12\cdot10^{13}$	$1.55\cdot10^{13}$	$1.46\cdot10^{13}$	$1.16\cdot10^{13}$	$7.57\cdot10^{12}$	$1.15\cdot10^{14}$	$1.15\cdot10^{8}$
$9.99\cdot10^{2}$	$3.57\cdot10^{12}$	$3.57\cdot10^{12}$	$4.13\cdot10^{12}$	$4.08\cdot10^{12}$	$2.13\cdot10^{12}$	$1.97\cdot10^{12}$	$2.73\cdot10^{12}$	$3.67\cdot10^{12}$	$2.99\cdot10^{12}$	$6.09\cdot10^{12}$	$7.66\cdot10^{12}$	$8.71\cdot10^{12}$	$1.21\cdot10^{13}$	$1.14\cdot10^{13}$	$9.07\cdot10^{12}$	$5.94\cdot10^{12}$	$8.98\cdot10^{13}$	$8.98\cdot10^{7}$

2.3.2.2. Nuclear heating in the blanket modules for the entire reactor

Nuclear heating due to neutrons, for the different components of the blanket and the total is shown in Table 6.19, whereas Table 6.20 collects analogous results, but due to photons. Table 6.21 summarizes the total nuclear heating, taking into account both contributions. One can see that the contribution of photons is higher than the corresponding to neutrons.

As it can be seen, module #13 is the one with the highest values, which are around 6.5 times higher than those of the module with the lowest values (#6). With regard to volumetric values, values for module #13 are about 78% of those for modules #3 and #4, which are those with the highest values.

Table 6.19. Nuclear heating due to neutrons for the different components in the blanket modules for the entire reactor (W).

# Blanket Modules	W	FW	Top and bottom walls	Lateral walls	Breeder module	BP	Total (W)	Total (MW)
1	$6.60\cdot10^{4}$	$2.22\cdot10^{6}$	$1.96\cdot10^{5}$	$6.06\cdot10^{5}$	$1.24\cdot10^{7}$	$9.27\cdot10^{5}$	$1.64\cdot10^{7}$	$1.64\cdot10^{1}$
2	$7.21\cdot10^{4}$	$2.46\cdot10^{6}$	$2.36\cdot10^{5}$	$6.68\cdot10^{5}$	$1.21\cdot10^{7}$	$9.46\cdot10^{5}$	$1.64\cdot10^{7}$	$1.64\cdot10^{1}$
3	$8.83\cdot10^{4}$	$3.19\cdot10^{6}$	$3.10\cdot10^{5}$	$8.95\cdot10^{5}$	$1.39\cdot10^{7}$	$1.06\cdot10^{6}$	$1.94\cdot10^{7}$	$1.94\cdot10^{1}$
4	$8.64\cdot10^{4}$	$3.10\cdot10^{6}$	$3.02\cdot10^{5}$	$8.67\cdot10^{5}$	$1.37\cdot10^{7}$	$6.81\cdot10^{5}$	$1.88\cdot10^{7}$	$1.88\cdot10^{1}$
5	$4.09\cdot10^{4}$	$1.38\cdot10^{6}$	$2.47\cdot10^{5}$	$3.80\cdot10^{5}$	$6.97\cdot10^{6}$	$5.89\cdot10^{5}$	$9.61\cdot10^{6}$	$9.61\cdot10^{0}$
6	$3.65\cdot10^{4}$	$1.24\cdot10^{6}$	$2.36\cdot10^{5}$	$3.45\cdot10^{5}$	$6.61\cdot10^{6}$	$4.38\cdot10^{5}$	$8.90\cdot10^{6}$	$8.90\cdot10^{0}$
7	$4.83\cdot10^{4}$	$1.67\cdot10^{6}$	$2.94\cdot10^{5}$	$4.66\cdot10^{5}$	$9.90\cdot10^{6}$	$7.92\cdot10^{5}$	$1.32\cdot10^{7}$	$1.32\cdot10^{1}$
8	$6.33\cdot10^{4}$	$2.25\cdot10^{6}$	$3.83\cdot10^{5}$	$5.38\cdot10^{5}$	$1.34\cdot10^{7}$	$7.41\cdot10^{5}$	$1.74\cdot10^{7}$	$1.74\cdot10^{1}$
9	$4.31\cdot10^{4}$	$1.57\cdot10^{6}$	$4.66\cdot10^{5}$	$6.89\cdot10^{5}$	$1.04\cdot10^{7}$	$4.43\cdot10^{5}$	$1.36\cdot10^{7}$	$1.36\cdot10^{1}$
10	$9.69\cdot10^{4}$	$3.57\cdot10^{6}$	$5.20\cdot10^{5}$	$1.25\cdot10^{6}$	$2.26\cdot10^{7}$	$8.58\cdot10^{5}$	$2.89\cdot10^{7}$	$2.89\cdot10^{1}$
11	$1.24\cdot10^{5}$	$4.65\cdot10^{6}$	$6.65\cdot10^{5}$	$1.38\cdot10^{6}$	$2.92\cdot10^{7}$	$1.11\cdot10^{6}$	$3.71\cdot10^{7}$	$3.71\cdot10^{1}$
12	$1.44\cdot10^{5}$	$5.48\cdot10^{6}$	$7.88\cdot10^{5}$	$1.46\cdot10^{6}$	$3.35\cdot10^{7}$	$1.27\cdot10^{6}$	$4.27\cdot10^{7}$	$4.27\cdot10^{1}$
13	$2.04\cdot10^{5}$	$7.82\cdot10^{6}$	$8.32\cdot10^{5}$	$2.02\cdot10^{6}$	$4.74\cdot10^{7}$	$1.79\cdot10^{6}$	$6.00\cdot10^{7}$	$6.00\cdot10^{1}$
14	$1.93\cdot10^{5}$	$7.44\cdot10^{6}$	$7.84\cdot10^{5}$	$2.01\cdot10^{6}$	$4.42\cdot10^{7}$	$1.66\cdot10^{6}$	$5.62\cdot10^{7}$	$5.62\cdot10^{1}$
15	$1.52\cdot10^{5}$	$5.80\cdot10^{6}$	$6.21\cdot10^{5}$	$1.80\cdot10^{6}$	$3.43\cdot10^{7}$	$1.27\cdot10^{6}$	$4.40\cdot10^{7}$	$4.40\cdot10^{1}$
16	$9.65\cdot10^{4}$	$3.50\cdot10^{6}$	$3.76\cdot10^{5}$	$1.29\cdot10^{6}$	$2.18\cdot10^{7}$	$7.93\cdot10^{5}$	$2.78\cdot10^{7}$	$2.78\cdot10^{1}$
Total (W)	$1.56\cdot10^{6}$	$5.74\cdot10^{7}$	$7.25\cdot10^{6}$	$1.67\cdot10^{7}$	$3.32\cdot10^{8}$	$1.54\cdot10^{7}$	$4.31\cdot10^{8}$	$4.31\cdot10^{2}$
Total (MW)	$1.56\cdot10^{0}$	$5.74\cdot10^{1}$	$7.25\cdot10^{0}$	$1.67\cdot10^{1}$	$3.32\cdot10^{2}$	$1.54\cdot10^{1}$	$4.31\cdot10^{2}$	-

Table 6.20. Nuclear heating due to photons for the different components in the blanket modules for the entire reactor (W).

# Blanket Modules	W	FW	Top and bottom walls	Lateral walls	Breeder module	BP	Total (W)	Total (MW)
1	$3.29\cdot10^{6}$	$7.37\cdot10^{6}$	$1.06\cdot10^{6}$	$2.92\cdot10^{6}$	$2.95\cdot10^{7}$	$1.07\cdot10^{6}$	$4.52\cdot10^{7}$	$4.52\cdot10^{1}$
2	$3.29\cdot10^{6}$	$7.60\cdot10^{6}$	$9.49\cdot10^{5}$	$3.13\cdot10^{6}$	$2.96\cdot10^{7}$	$1.07\cdot10^{6}$	$4.57\cdot10^{7}$	$4.57\cdot10^{1}$
3	$3.72\cdot10^{6}$	$9.11\cdot10^{6}$	$1.18\cdot10^{6}$	$3.89\cdot10^{6}$	$3.80\cdot10^{7}$	$1.22\cdot10^{6}$	$5.71\cdot10^{7}$	$5.71\cdot10^{1}$
4	$3.69\cdot10^{6}$	$8.93\cdot10^{6}$	$1.15\cdot10^{6}$	$3.80\cdot10^{6}$	$3.69\cdot10^{7}$	$7.78\cdot10^{5}$	$5.53\cdot10^{7}$	$5.53\cdot10^{1}$
5	$1.87\cdot10^{6}$	$4.31\cdot10^{6}$	$9.89\cdot10^{5}$	$1.81\cdot10^{6}$	$1.70\cdot10^{7}$	$6.64\cdot10^{5}$	$2.66\cdot10^{7}$	$2.66\cdot10^{1}$
6	$1.75\cdot10^{6}$	$3.97\cdot10^{6}$	$9.56\cdot10^{5}$	$1.64\cdot10^{6}$	$1.60\cdot10^{7}$	$4.87\cdot10^{5}$	$2.48\cdot10^{7}$	$2.48\cdot10^{1}$
7	$2.37\cdot10^{6}$	$5.40\cdot10^{6}$	$1.14\cdot10^{6}$	$2.19\cdot10^{6}$	$2.40\cdot10^{7}$	$8.89\cdot10^{5}$	$3.60\cdot10^{7}$	$3.60\cdot10^{1}$
8	$3.13\cdot10^{6}$	$7.21\cdot10^{6}$	$1.45\cdot10^{6}$	$2.50\cdot10^{6}$	$3.27\cdot10^{7}$	$8.23\cdot10^{5}$	$4.78\cdot10^{7}$	$4.78\cdot10^{1}$
9	$2.15\cdot10^{6}$	$5.03\cdot10^{6}$	$1.77\cdot10^{6}$	$3.28\cdot10^{6}$	$2.44\cdot10^{7}$	$4.90\cdot10^{5}$	$3.71\cdot10^{7}$	$3.71\cdot10^{1}$
10	$4.74\cdot10^{6}$	$1.12\cdot10^{7}$	$2.05\cdot10^{6}$	$5.80\cdot10^{6}$	$5.35\cdot10^{7}$	$9.19\cdot10^{5}$	$7.82\cdot10^{7}$	$7.82\cdot10^{1}$
11	$5.94\cdot10^{6}$	$1.42\cdot10^{7}$	$2.60\cdot10^{6}$	$6.29\cdot10^{6}$	$7.00\cdot10^{7}$	$1.18\cdot10^{6}$	$1.00\cdot10^{8}$	$1.00\cdot10^{2}$
12	$6.74\cdot10^{6}$	$1.63\cdot10^{7}$	$3.01\cdot10^{6}$	$6.57\cdot10^{6}$	$8.17\cdot10^{7}$	$1.35\cdot10^{6}$	$1.16\cdot10^{8}$	$1.16\cdot10^{2}$
13	$9.31\cdot10^{6}$	$2.28\cdot10^{7}$	$3.16\cdot10^{6}$	$9.01\cdot10^{6}$	$1.16\cdot10^{8}$	$1.90\cdot10^{6}$	$1.62\cdot10^{8}$	$1.62\cdot10^{2}$
14	$8.73\cdot10^{6}$	$2.15\cdot10^{7}$	$3.00\cdot10^{6}$	$8.99\cdot10^{6}$	$1.09\cdot10^{8}$	$1.76\cdot10^{6}$	$1.53\cdot10^{8}$	$1.53\cdot10^{2}$
15	$7.01\cdot10^{6}$	$1.71\cdot10^{7}$	$2.44\cdot10^{6}$	$8.18\cdot10^{6}$	$8.30\cdot10^{7}$	$1.35\cdot10^{6}$	$1.19\cdot10^{8}$	$1.19\cdot10^{2}$
16	$4.82\cdot10^{6}$	$1.12\cdot10^{7}$	$1.84\cdot10^{6}$	$6.35\cdot10^{6}$	$4.92\cdot10^{7}$	$8.69\cdot10^{5}$	$7.42\cdot10^{7}$	$7.42\cdot10^{1}$
Total (W)	$7.25\cdot10^{7}$	$1.73\cdot10^{8}$	$2.88\cdot10^{7}$	$7.64\cdot10^{7}$	$8.10\cdot10^{8}$	$1.68\cdot10^{7}$	$1.18\cdot10^{9}$	$1.18\cdot10^{3}$
Total (MW)	$7.25\cdot10^{1}$	$1.73\cdot10^{2}$	$2.88\cdot10^{1}$	$7.64\cdot10^{1}$	$8.10\cdot10^{2}$	$1.68\cdot10^{1}$	$1.18\cdot10^{3}$	-

Table 6.21. Nuclear heating for the different components in the blanket modules for the entire reactor (W).

# Blanket Modules	W	FW	Top and bottom walls	Lateral walls	Breeder module	BP	Total (W)	Total (MW)
1	$3.35\cdot10^{6}$	$9.59\cdot10^{6}$	$1.25\cdot10^{6}$	$3.53\cdot10^{6}$	$4.19\cdot10^{7}$	$2.00\cdot10^{6}$	$6.16\cdot10^{7}$	$6.16\cdot10^{1}$
2	$3.36\cdot10^{6}$	$1.01\cdot10^{7}$	$1.19\cdot10^{6}$	$3.80\cdot10^{6}$	$4.17\cdot10^{7}$	$2.01\cdot10^{6}$	$6.21\cdot10^{7}$	$6.21\cdot10^{1}$
3	$3.81\cdot10^{6}$	$1.23\cdot10^{7}$	$1.49\cdot10^{6}$	$4.79\cdot10^{6}$	$5.19\cdot10^{7}$	$2.28\cdot10^{6}$	$7.66\cdot10^{7}$	$7.66\cdot10^{1}$
4	$3.77\cdot10^{6}$	$1.20\cdot10^{7}$	$1.45\cdot10^{6}$	$4.67\cdot10^{6}$	$5.06\cdot10^{7}$	$1.46\cdot10^{6}$	$7.40\cdot10^{7}$	$7.40\cdot10^{1}$
5	$1.91\cdot10^{6}$	$5.69\cdot10^{6}$	$1.24\cdot10^{6}$	$2.19\cdot10^{6}$	$2.39\cdot10^{7}$	$1.25\cdot10^{6}$	$3.62\cdot10^{7}$	$3.62\cdot10^{1}$
6	$1.78\cdot10^{6}$	$5.21\cdot10^{6}$	$1.19\cdot10^{6}$	$1.99\cdot10^{6}$	$2.26\cdot10^{7}$	$9.25\cdot10^{5}$	$3.37\cdot10^{7}$	$3.37\cdot10^{1}$
7	$2.41\cdot10^{6}$	$7.08\cdot10^{6}$	$1.44\cdot10^{6}$	$2.65\cdot10^{6}$	$3.39\cdot10^{7}$	$1.68\cdot10^{6}$	$4.92\cdot10^{7}$	$4.92\cdot10^{1}$
8	$3.20\cdot10^{6}$	$9.46\cdot10^{6}$	$1.83\cdot10^{6}$	$3.04\cdot10^{6}$	$4.61\cdot10^{7}$	$1.56\cdot10^{6}$	$6.52\cdot10^{7}$	$6.52\cdot10^{1}$
9	$2.19\cdot10^{6}$	$6.60\cdot10^{6}$	$2.24\cdot10^{6}$	$3.97\cdot10^{6}$	$3.48\cdot10^{7}$	$9.33\cdot10^{5}$	$5.07\cdot10^{7}$	$5.07\cdot10^{1}$
10	$4.84\cdot10^{6}$	$1.47\cdot10^{7}$	$2.57\cdot10^{6}$	$7.05\cdot10^{6}$	$7.61\cdot10^{7}$	$1.78\cdot10^{6}$	$1.07\cdot10^{8}$	$1.07\cdot10^{2}$
11	$6.06\cdot10^{6}$	$1.88\cdot10^{7}$	$3.26\cdot10^{6}$	$7.66\cdot10^{6}$	$9.91\cdot10^{7}$	$2.29\cdot10^{6}$	$1.37\cdot10^{8}$	$1.37\cdot10^{2}$
12	$6.88\cdot10^{6}$	$2.18\cdot10^{7}$	$3.80\cdot10^{6}$	$8.03\cdot10^{6}$	$1.15\cdot10^{8}$	$2.62\cdot10^{6}$	$1.58\cdot10^{8}$	$1.58\cdot10^{2}$
13	$9.51\cdot10^{6}$	$3.06\cdot10^{7}$	$3.99\cdot10^{6}$	$1.10\cdot10^{7}$	$1.64\cdot10^{8}$	$3.69\cdot10^{6}$	$2.22\cdot10^{8}$	$2.22\cdot10^{2}$
14	$8.92\cdot10^{6}$	$2.90\cdot10^{7}$	$3.79\cdot10^{6}$	$1.10\cdot10^{7}$	$1.53\cdot10^{8}$	$3.43\cdot10^{6}$	$2.09\cdot10^{8}$	$2.09\cdot10^{2}$
15	$7.16\cdot10^{6}$	$2.29\cdot10^{7}$	$3.06\cdot10^{6}$	$9.99\cdot10^{6}$	$1.17\cdot10^{8}$	$2.62\cdot10^{6}$	$1.63\cdot10^{8}$	$1.63\cdot10^{2}$
16	$4.91\cdot10^{6}$	$1.47\cdot10^{7}$	$2.21\cdot10^{6}$	$7.64\cdot10^{6}$	$7.09\cdot10^{7}$	$1.66\cdot10^{6}$	$1.02\cdot10^{8}$	$1.02\cdot10^{2}$
Total (W)	$7.41\cdot10^{7}$	$2.30\cdot10^{8}$	$3.60\cdot10^{7}$	$9.30\cdot10^{7}$	$1.14\cdot10^{9}$	$3.22\cdot10^{7}$	$1.61\cdot10^{9}$	$1.61\cdot10^{3}$
Total (MW)	$7.41\cdot10^{1}$	$2.30\cdot10^{2}$	$3.60\cdot10^{1}$	$9.30\cdot10^{1}$	$1.14\cdot10^{3}$	$3.22\cdot10^{1}$	$1.61\cdot10^{3}$	-

3.3.3. Contribution of the different components to decay heat, activity and nuclear heating

A complete blanket module #13 in a torus sector of 10º (located in the equatorial zone of the outboard and, therefore, where the blanket receives highest neutron fluxes of all outboard modules; see Figure 6.20) was selected for a further study.

In this analysis, the contribution of the 6 different components to the activation responses (decay heat and activity) is assessed. Furthermore, the breeder module component is broken down in the different materials that compose it: Eurofer, LiPb, Al_2O_3, and He.

Figure 6.22 shows the total decay heat for the equatorial outboard module (#13) as well as the contribution of the components (considering the breeder module separated into materials). Contribution of the He in the breeder is not shown since its values are several orders

of magnitude lower than those corresponding to other components. It is important to note that LiPb contribution in all the components is given again excluding the contribution of T.

As it can be seen, LiPb is the main contributor both at the time of the shutdown and after 100 years of cooling time. At the remaining times listed, Eurofer from the breeder module is the component with the highest values of decay heat. The Al_2O_3 from the FCI is the component with the lowest contribution to decay heat at all the considered times, followed by the BP. As it can be seen some differences are detected between the values corresponding to both top and bottom walls and the FW (which are the two components with the same composition). This is due to the effect of the spectrum in the production of radionuclides.

A similar figure (Figure 6.23) is given for the activity response. Once again, contribution of the He in the breeder is excluded as it is negligible. LiPb is only the main contributor both at the time of the shutdown and from 50 years of cooling time. At the remaining times listed, Eurofer from the breeder module and FW are the components with the highest values. Finally, as happened with the decay heat, Al_2O_3 is the material with the lowest contribution.

With regard to the nuclear heating, Figure 6.24 shows that the breeder module is the component contributing most while the BP is the one with the lowest contribution.

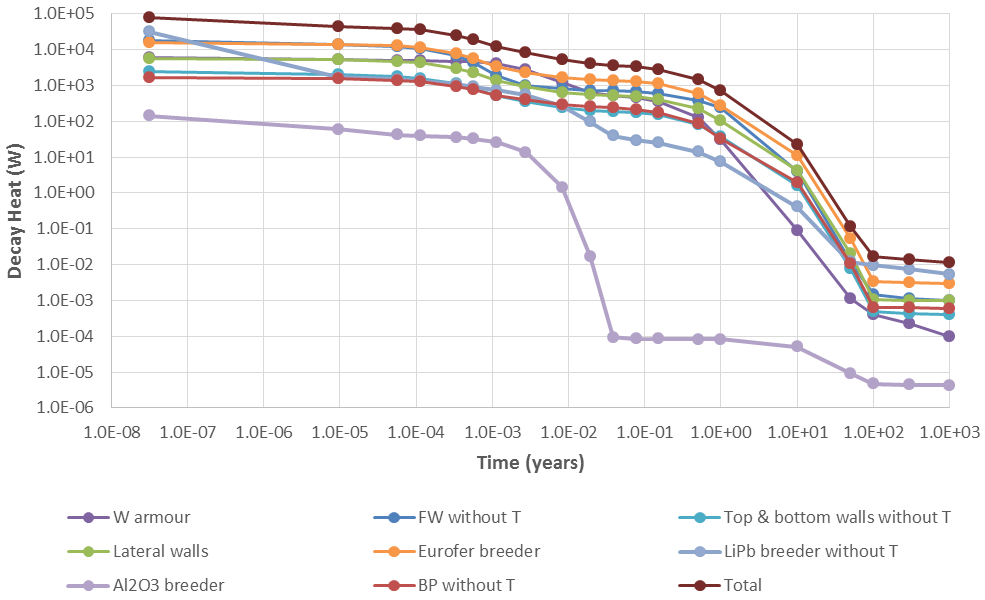

Figure 6.22. Decay heat for equatorial outboard blanket module (#13): Total and contribution from components (W, FW, top and bottom walls, lateral walls and BP) and breeder module materials.

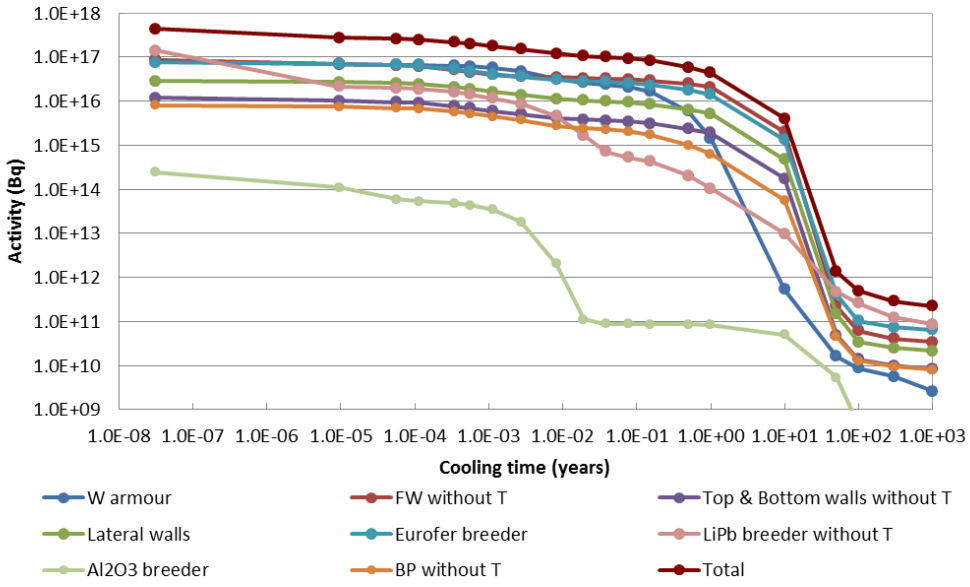

Figure 6.23. Activity for equatorial outboard blanket module (#13): Total and contribution from components (W, FW, top and bottom walls, lateral walls and BP) and breeder module materials.

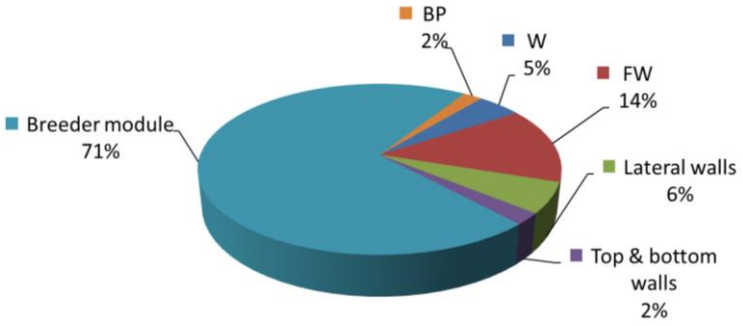

Figure 6.24. Contribution of the different components to the nuclear heating.

3.3.4. Main radionuclides contributing to the decay heat in the blanket components

The main radionuclides contributing to decay heat have been identified using the same complete equatorial outboard blanket module #13 as a reference. As in the case of the previous section, the breeder module component is divided into its materials. Figure 6.25 - Figure 6.32 shows the major contributors in each of the components.

- W armour (Figure 6.25). ^{187}W (half-life 24 h) is dominant up to 3 days of cooling time when ^{185}W (half-life 75.1 days) turns into the largest contributor until a year. In the end times, impurities determine the critical nuclides. So, at 10 years ^{60}Co (half-life 1925.3 days) is the main contributor. However, from 100 years and until 300 years ^{39}Ar (half-life 269 years) becomes the most relevant isotope and in the last period, ^{94}Nb (half-life $2.03 \cdot 10^4$ years) develop into the most relevant isotope to decay heat.

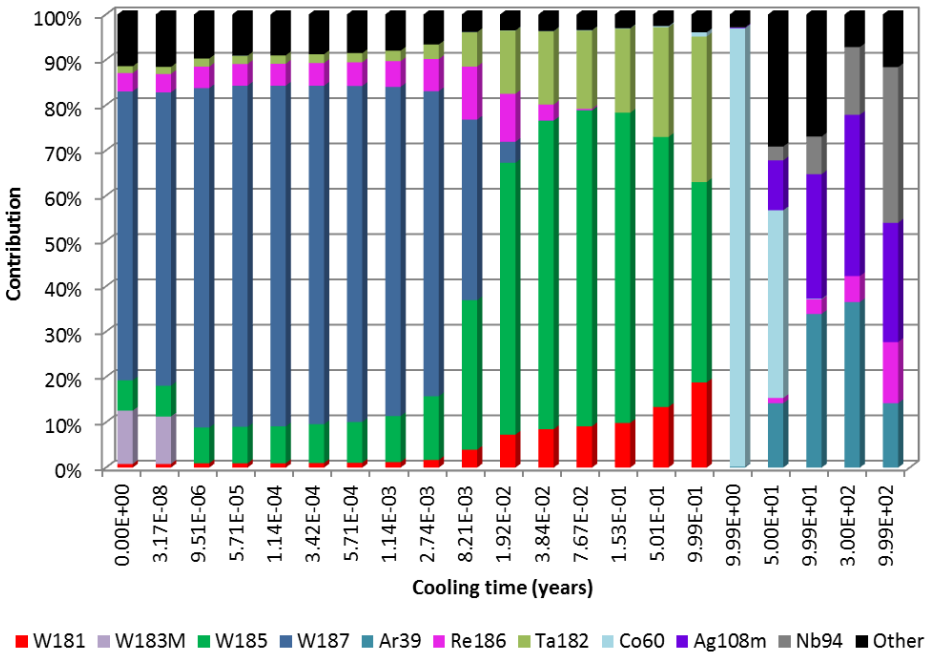

Figure 6.25. Main radionuclides for decay heat in the W armour.

- FW (Figure 6.26). It can be seen that ^{56}Mn (half-life 2.6 h) is dominant up to 10 hours of cooling time. After this time, ^{54}Mn (half-life 312.1 days) is the main contributor until 1 year after shutdown. Then, ^{55}Fe (half-life 2.7 years) replaces it as main contributor to decay heat up to 1 year, At 10 years, ^{60}Co (half-life 1925.3 days) is the radionuclide contributing most to this response while, in the last period ^{94}Nb ($2.0 \cdot 10^4$ years) is dominant.

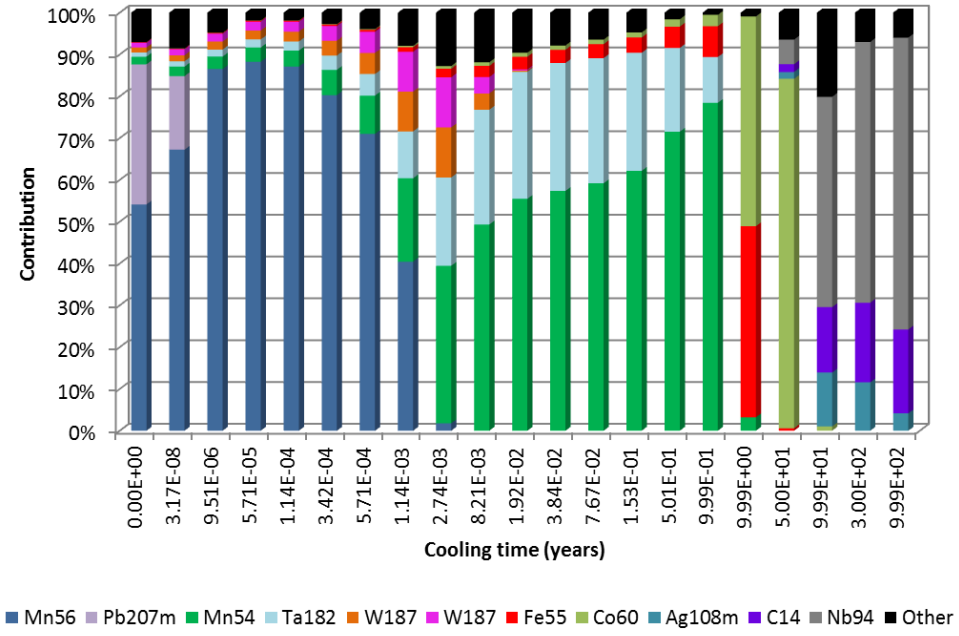

Figure 6.26. Main radionuclides for decay heat in the FW.

- Top and bottom walls (Figure 6.27). ^{56}Mn (half-life 2.6 h) is dominant up to 5 hours of cooling time. After this time, ^{187}W (half-life 24 h) is the main contributor until 10 hours after shutdown. Then, ^{182}Ta (half-life 114.7 days) becomes the major radionuclide up to 6 months. Immediately ^{54}Mn (half-life 312.1 days) replaces it until 1 year. ^{60}Co (half-life 1925.3 days) is the major contributor up to 50 years and ^{94}Nb (half-life $2.0 \cdot 10^4$ years) from then to 100 years.

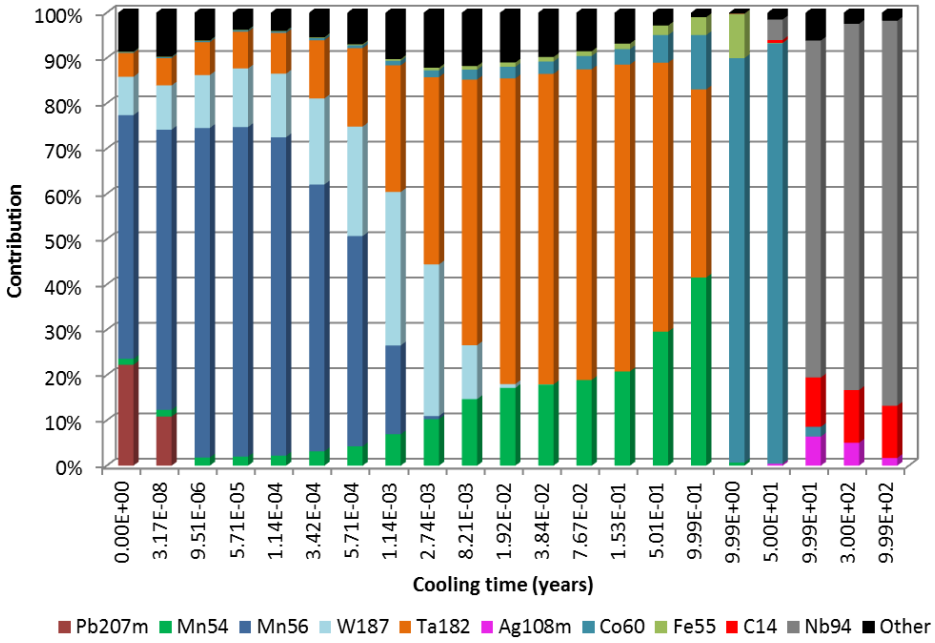

Figure 6.27. Main radionuclides for decay heat in the top and bottom walls.

- Lateral walls (Figure 6.28). ^{56}Mn (half-life 2.58 h) is dominant up to 5 hours of cooling time. After this time, ^{187}W (half-life 24 h) is the main contributor until 1 day after shutdown. Then, ^{182}Ta (half-life 114.7 days) becomes the major radionuclide up to 6 months. At 1 year, ^{54}Mn (half-life 312.1 days) replaces it. ^{60}Co (half-life 1925.3 days) is the major contributor up to 50 years and ^{94}Nb (half-life $2.0 \cdot 10^4$ years) from then to 100 years.

- Eurofer from the breeder (Figure 6.29). In this case, ^{56}Mn (half-life 2.6 h) is the main contributor to decay heat up to 5 hours of cooling. At 10 hours, ^{187}W (half-life 24 h) and ^{182}Ta (half-life 114.7 days) replace it, with practically the same contribution. Then, ^{182}Ta remains dominant up to 6 months. ^{54}Mn (half-life 312.1 days) appears as the major contributor at 1 year and, both at 10 and 50 years of cooling time ^{60}Co (half-life 1925.3 days) is dominant. Finally, ^{94}Nb (half-life $2.0 \cdot 10^4$ years) is the main contributor from 100 years of cooling time.

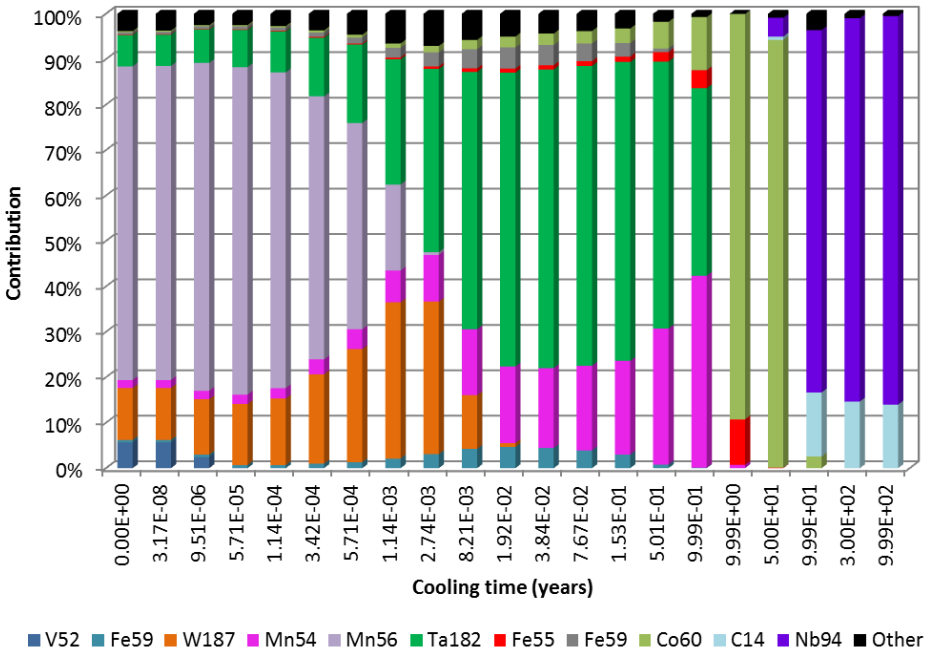

Figure 6.28. Main radionuclides for decay heat in the lateral walls.

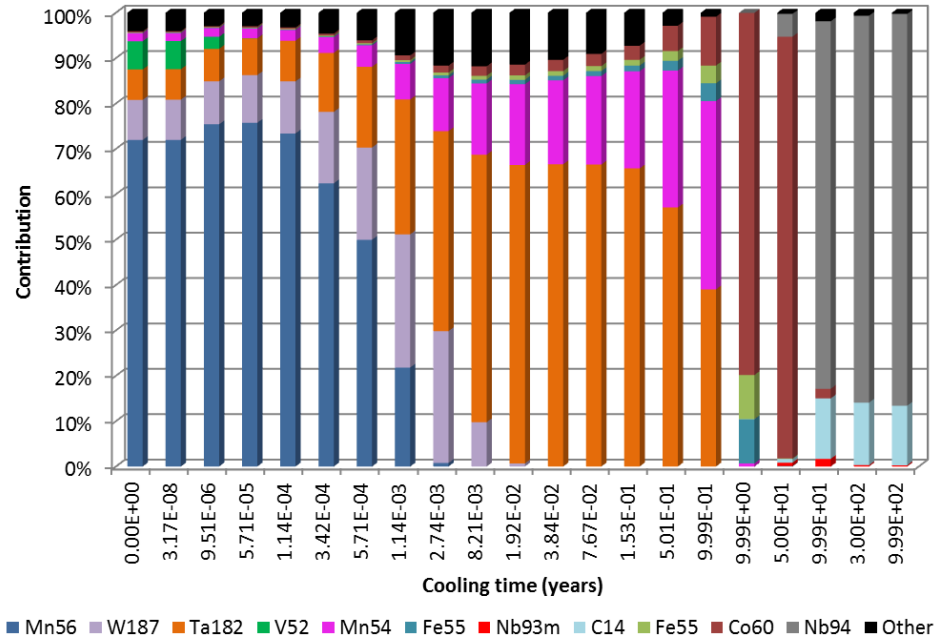

Figure 6.29. Main radionuclides for decay heat in the Eurofer from the breeder.

- LiPb from the breeder (Figure 6.30). ^{207m}Pb (half-life 0.81 seconds) is the major radionuclide at the time close to the shutdown (1 second). Immediately after, ^{203}Pb (half-life 51.9 h) is the main contributor up to one week, when ^{210}Po (half-life 138.4 days) is dominant (until 1 year). ^{204}Tl (half-life 3.8 years) replaces it as major radionuclide at 10 years while ^{94}Nb (half-life $2.0 \cdot 10^4$ years) is the main contributor up to 1000 years of cooling time.

- Al_2O_3 from the FCI (Figure 6.31). At the shutdown (and at 1 second of cooling time), ^{28}Al (half-live 2.2 minutes) is dominant. Since then, ^{24}Na (half-life 15 h) becomes the main contributor up to 1 week, when T (half-life 12.3 years) replaces it up to 50 years. At the end timed (from 100 years) ^{26}Al (half-life $7.2 \cdot 10^5$ years) is the main contributor.

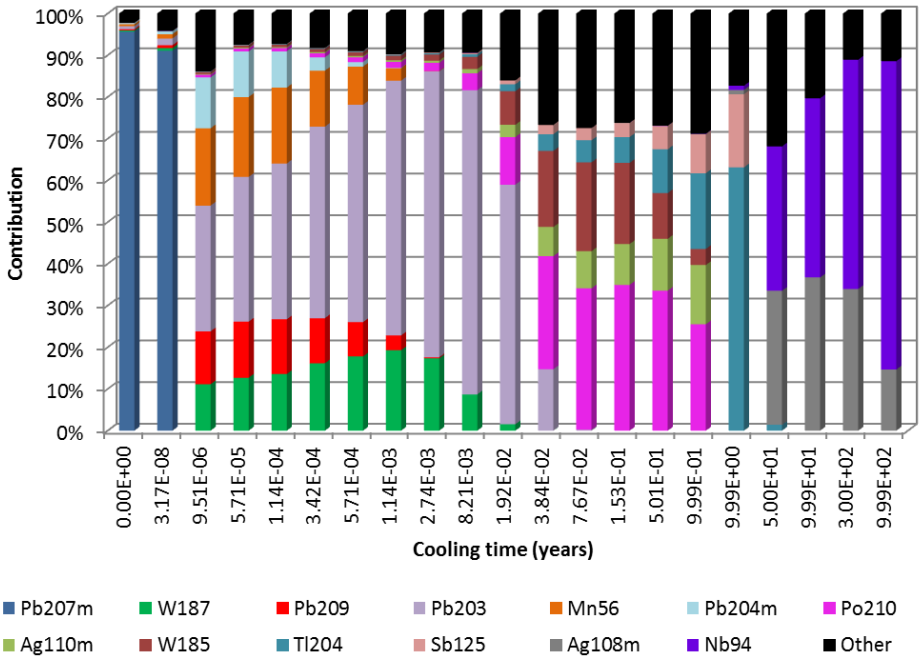

Figure 6.30. Main radionuclides for decay heat in the LiPb from the breeder.

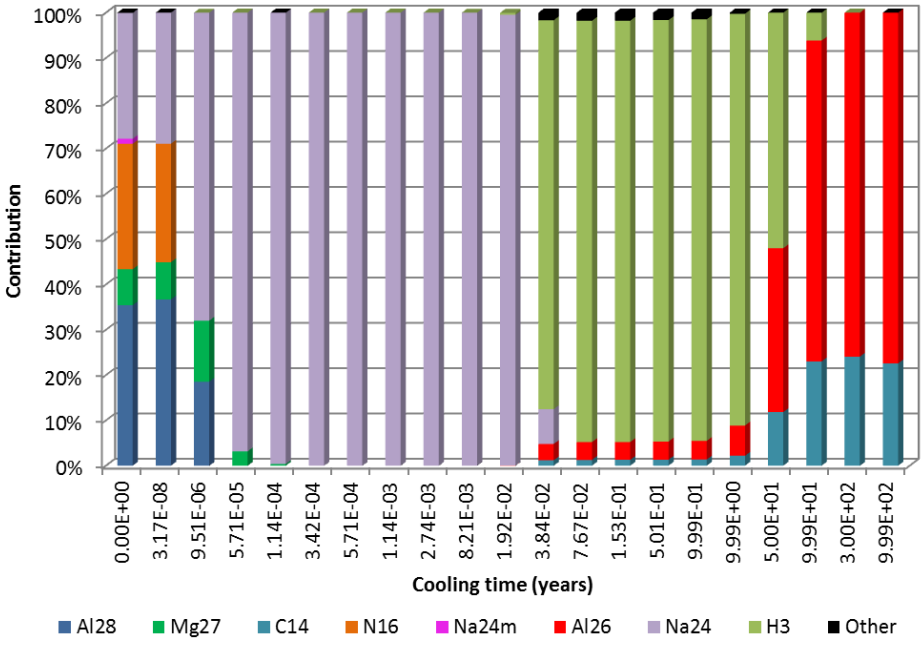

Figure 6.31. Main radionuclides for decay heat in the Al_2O_3 from the breeder.

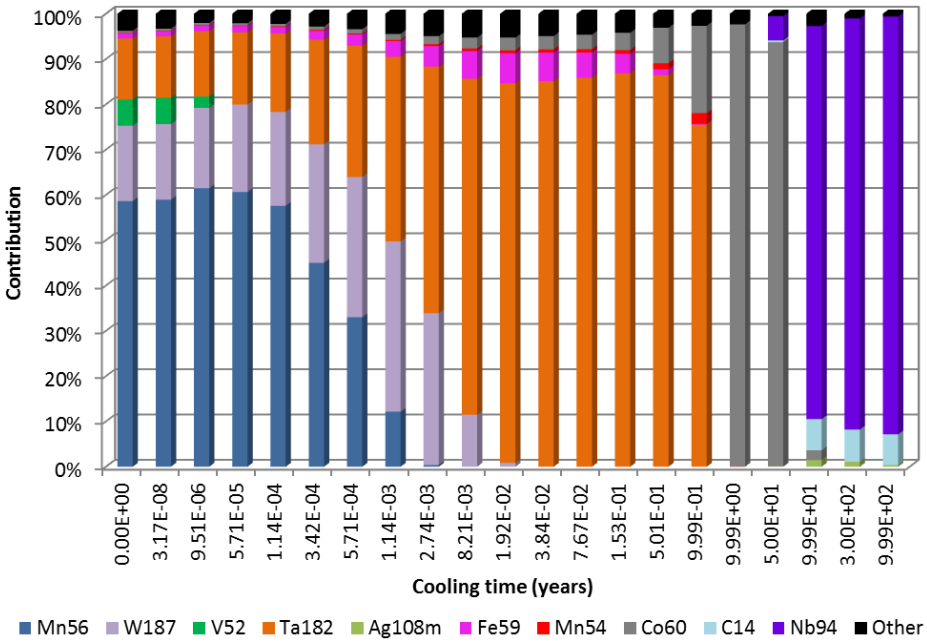

Figure 6.32. Main radionuclides for decay heat in the BP.

- BP (Figure 6.32). This case is similar to the top and bottom walls. Thus, ^{56}Mn (half-life 2.6 h) is dominant up to 5 hours of cooling time, while ^{187}W (half-life 24 h) is the main contributor until 10 hours. Then, ^{182}Ta (half-life 114.7 days) becomes the major radionuclide up to 6 months, when ^{54}Mn (half-life 312.1 days) replaces it until 1 year. ^{60}Co (half-life 1925.3 days) is the major contributor up to 50 years and ^{94}Nb (half-life $2.0 \cdot 10^4$ years) from then to 100 years.

3.3.5. Radial profile across the blanket for decay heat and nuclear heating responses

The aim of this section is to provide a radial decay heat profile across the blanket in order to see if there is a significant difference when compared to the calculated homogenized value. In other words, results of activation calculations using radial fluxes are compared to activation results when using the volume averaged flux.

This radial assessment was performed for different components, namely: top and bottom walls, lateral walls and breeder. For this purpose, components are radially split into ten equally spaced slices. Figure 6.33 shows this division and the assigned number for each of the slices, in the breeder case. For the other components (top and bottom walls, and lateral walls), the division is made using the same planes (in fact, Figure 6.33 shows, aside from the breeder division, the top and bottom one), resulting the same numbering for the slices: slice #1 is that closest to the plasma and slice #10 the farthest.

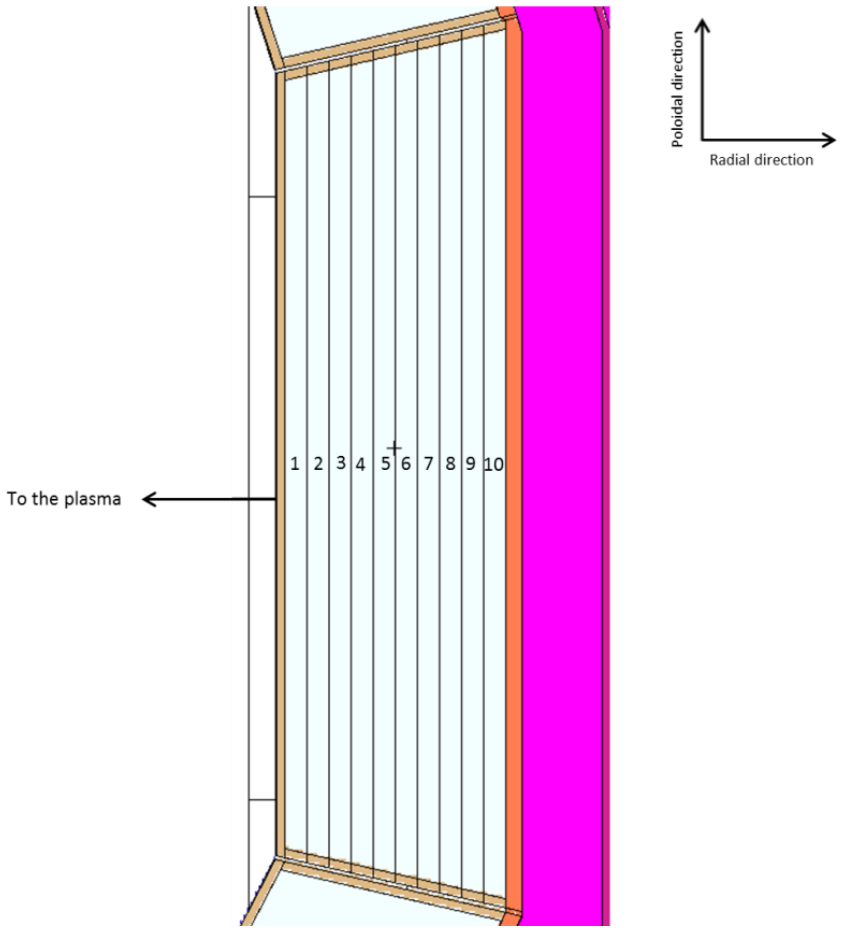

Figure 6.33. Breeder division into 10 slices.

2.3.2.3. Decay heat radial profile

The following figures show the decay heat evolution across the slices for the breeder (Figure 6.34), top and bottom walls (Figure 6.35), and lateral walls (Figure 6.36) from the module #13. These figures reveal that the importance of considering different slices, instead of an only one, is more important at short times. In addition, the difference between the shutdown decay heat value and the value at 1000 years is different for each of the slices, being precisely conditioned by the difference of these values at short times.

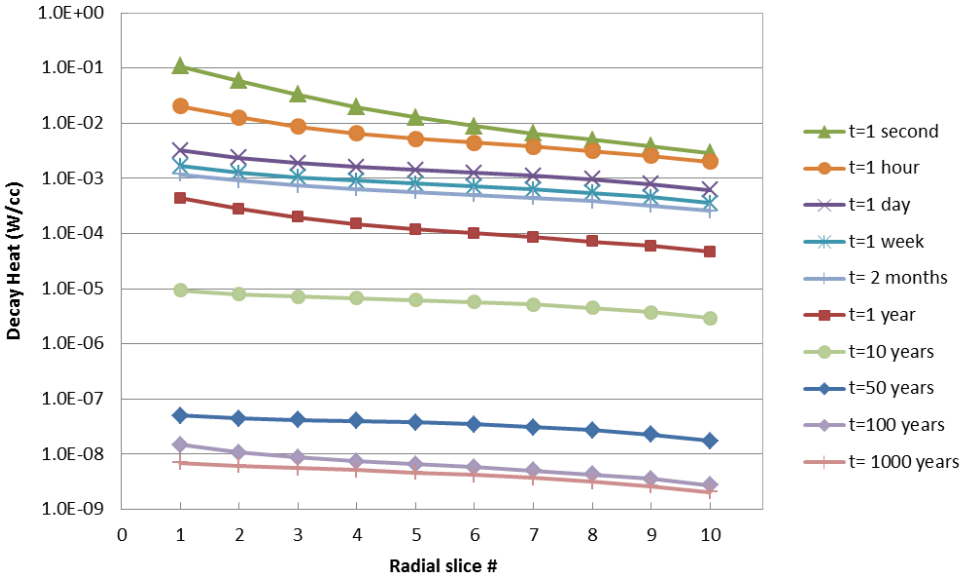

Figure 6.34. Decay heat radial for the different slices of the breeder from equatorial outboard module (#13).

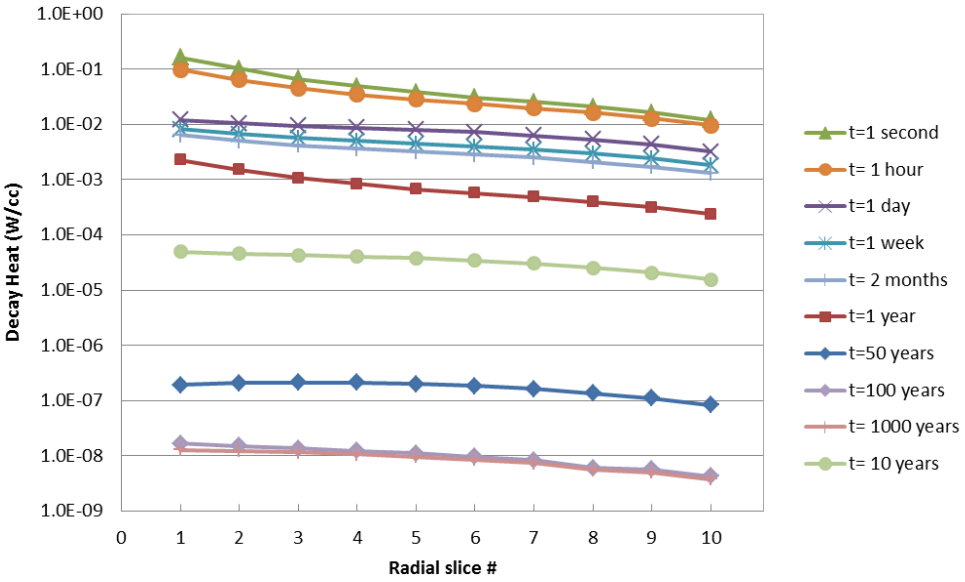

Figure 6.35. Decay heat radial for the different slices of the top and bottom walls from equatorial outboard module (#13).

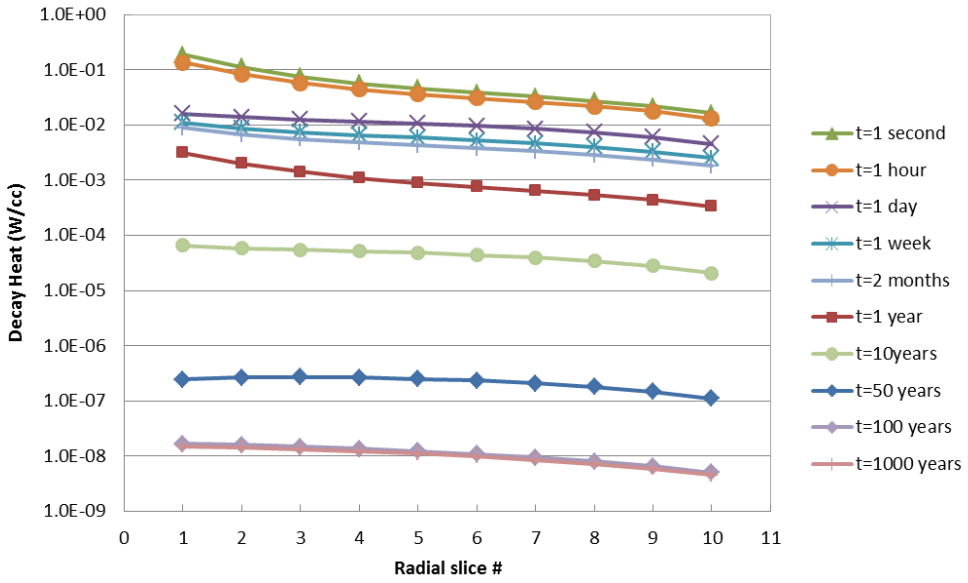

Figure 6.36. Decay heat radial for the different slices of the lateral walls from equatorial outboard module (#13).

Regarding to the comparison with the decay heat obtained with a homogenized flux for the whole volume (H) of the component, one can see that, for the breeder case, the H value is located in the first half of the slices (between #1-#5, depending on the considered cooling time), i.e. closer to the plasma than the average. For the top and bottom walls, the H value is located, except at the shutdown, between the values corresponding to slices #7 and #8. Finally, for the lateral walls, the H value is similar to those obtained for the #4 and #5 slices.

To be more specific, the differences between considering specific slices (where the decay heat was calculated using the corresponding flux) or H, using the following formula:

$$\mathrm{Diff}(\%) = \frac{\#-\mathrm{H}}{\mathrm{H}} \cdot 100 \tag{6.1}$$

Where # is referred to a specific slice number. The following tables (Table 6.22 - Table 6.24) summarize these differences considering three values for #, namely: the closest to the plasma (#1), an intermediate one (#5), and the farthest (#10).

Table 6.22. Differences between considering slices or a whole volume, for the breeder module from equatorial outboard module (#13).

Cooling time (years)	% diff with # 1	% diff with # 5	% diff with # 10
$0.00 \cdot 10^{0}$	377.2%	-54.9%	-92.8%
$3.17 \cdot 10^{-8}$	343.1%	-48.1%	-88.2%
$9.51 \cdot 10^{-6}$	214.8%	-22.7%	-71.1%
$5.71 \cdot 10^{-5}$	211.0%	-22.0%	-70.5%
$1.14 \cdot 10^{-4}$	206.9%	-21.2%	-70.0%
$3.42 \cdot 10^{-4}$	189.4%	-17.9%	-67.9%
$5.71 \cdot 10^{-4}$	171.8%	-14.5%	-65.7%
$1.14 \cdot 10^{-3}$	136.7%	-7.7%	-61.2%
$2.74 \cdot 10^{-3}$	116.5%	-4.0%	-58.4%
$8.21 \cdot 10^{-3}$	118.4%	-4.8%	-58.4%
$1.92 \cdot 10^{-2}$	104.0%	-2.3%	-56.4%
$3.84 \cdot 10^{-2}$	95.8%	-0.9%	-55.2%
$7.67 \cdot 10^{-2}$	97.5%	-1.3%	-55.4%
$1.53 \cdot 10^{-1}$	104.3%	-2.7%	-56.4%
$5.01 \cdot 10^{-1}$	140.1%	-9.6%	-61.4%
$9.99 \cdot 10^{-1}$	192.0%	-19.5%	-68.9%
$9.99 \cdot 10^{0}$	61.1%	7.4%	-50.0%
$5.00 \cdot 10^{1}$	47.5%	11.1%	-48.0%
$9.99 \cdot 10^{1}$	121.5%	-1.9%	-58.7%
$3.00 \cdot 10^{2}$	81.5%	3.2%	-55.5%
$9.99 \cdot 10^{2}$	61.2%	7.3%	-53.0%

Table 6.23. Differences between considering slices or a whole volume, for the top and bottom walls from equatorial outboard module (#13).

Cooling time (years)	% diff with # 1	% diff with # 5	% diff with # 10
$0.00 \cdot 10^{0}$	238.0%	-31.1%	-79.3%
$3.17 \cdot 10^{-8}$	216.8%	-26.5%	-76.6%
$9.51 \cdot 10^{-6}$	193.9%	-21.5%	-73.7%
$5.71 \cdot 10^{-5}$	188.8%	-20.4%	-73.1%
$1.14 \cdot 10^{-4}$	183.7%	-19.4%	-72.5%
$3.42 \cdot 10^{-4}$	161.6%	-14.6%	-69.9%
$5.71 \cdot 10^{-4}$	137.7%	-9.5%	-67.0%
$1.14 \cdot 10^{-3}$	87.9%	1.1%	-61.0%
$2.74 \cdot 10^{-3}$	59.0%	6.9%	-57.2%
$8.21 \cdot 10^{-3}$	75.7%	2.8%	-58.6%
$1.92 \cdot 10^{-2}$	84.0%	0.7%	-59.3%
$3.84 \cdot 10^{-2}$	85.4%	0.3%	-59.3%
$7.67 \cdot 10^{-2}$	88.2%	-0.5%	-59.6%
$1.53 \cdot 10^{-1}$	94.4%	-1.7%	-60.4%
$5.01 \cdot 10^{-1}$	126.2%	-8.5%	-64.7%
$9.99 \cdot 10^{-1}$	173.3%	-18.3%	-71.2%
$9.99 \cdot 10^{0}$	44.7%	11.0%	-54.7%
$5.00 \cdot 10^{1}$	14.1%	17.6%	-51.0%
$9.99 \cdot 10^{1}$	62.3%	7.4%	-58.1%
$3.00 \cdot 10^{2}$	51.4%	9.0%	-57.1%
$9.99 \cdot 10^{2}$	46.1%	10.2%	-56.5%

Table 6.24. Differences between considering slices or a whole volume, for the lateral walls from equatorial outboard module (#13).

Cooling time (years)	% diff with # 1	% diff with # 5	% diff with # 10
$0.00 \cdot 10^{0}$	212.8%	-23.4%	-72.7%
$3.17 \cdot 10^{-8}$	212.9%	-23.5%	-72.8%
$9.51 \cdot 10^{-6}$	210.6%	-23.0%	-72.4%
$5.71 \cdot 10^{-5}$	204.6%	-21.8%	-71.7%
$1.14 \cdot 10^{-4}$	199.1%	-20.7%	-71.1%
$3.42 \cdot 10^{-4}$	174.2%	-15.7%	-68.2%
$5.71 \cdot 10^{-4}$	147.4%	-10.3%	-65.1%
$1.14 \cdot 10^{-3}$	91.7%	0.8%	-58.6%
$2.74 \cdot 10^{-3}$	59.7%	6.9%	-54.6%
$8.21 \cdot 10^{-3}$	79.1%	2.2%	-56.3%
$1.92 \cdot 10^{-2}$	90.0%	-0.3%	-57.4%
$3.84 \cdot 10^{-2}$	92.2%	-0.9%	-57.5%
$7.67 \cdot 10^{-2}$	95.3%	-1.6%	-57.9%
$1.53 \cdot 10^{-1}$	101.8%	-2.9%	-58.7%
$5.01 \cdot 10^{-1}$	135.7%	-9.6%	-63.2%
$9.99 \cdot 10^{-1}$	185.6%	-19.4%	-69.9%
$9.99 \cdot 10^{0}$	48.3%	8.8%	-53.0%
$5.00 \cdot 10^{1}$	13.4%	15.7%	-49.0%
$9.99 \cdot 10^{1}$	50.1%	9.1%	-55.6%
$3.00 \cdot 10^{2}$	48.1%	9.6%	-55.2%
$9.99 \cdot 10^{2}$	47.1%	9.7%	-55.0%

From these tables it can be deduced that, when comparing the values for H with the values obtained for slice #1, in all cases and times the H values are lower, whereas when compared with slice #10, the opposite happens: values obtained for H overestimate those for slice #10. When compared with slice #5, depending on the considered cooling time the values for the H case are higher or lower than those of this slice. So, generally speaking, when calculating H, we are underestimating the real value in those areas closer to the plasma, whereas, zones located farther will be overvalued.

However, if the total decay is considered (instead of volumetric decay heat) there is no difference between taken into account the whole breeder (with its corresponding average flux) or several slices of this volume (each one with each own average flux). Therefore, it can be affirmed that, when the component will be treated as a whole (for example in the lateral walls

case), homogenization calculations will lead to enough accurate results, without no difference compared to radial-dependence estimations. On the contrary, if the whole volume will be treated as several parts (for example, separating in the breeder module the stiffenings from the LiPb), results will be overvalued in those areas farthest from the plasma, and underestimated in zones close to the plasma.

This can be verified by comparing, on the one hand, the results of the decay heat data obtained for the lateral walls in block (i.e. with a volume averaged neutron flux) in the equatorial outboard module #13, with those obtained from the sum of the 10 slices (in W) and, on the other hand, those corresponding to the FCI in the equatorial outboard module #13, with the average flux for the homogenized breeder and those if the FCI decay heat is calculated as the sum of the result of its different parts (see Figure 6.37) in which the activation of each of these parts is performed with its own characteristic flux.

As can be seen in Figure 6.38, for FCI differences are in the range of 75-95%, while for the lateral walls these differences are minimum, being the maximum found under 0.5%.

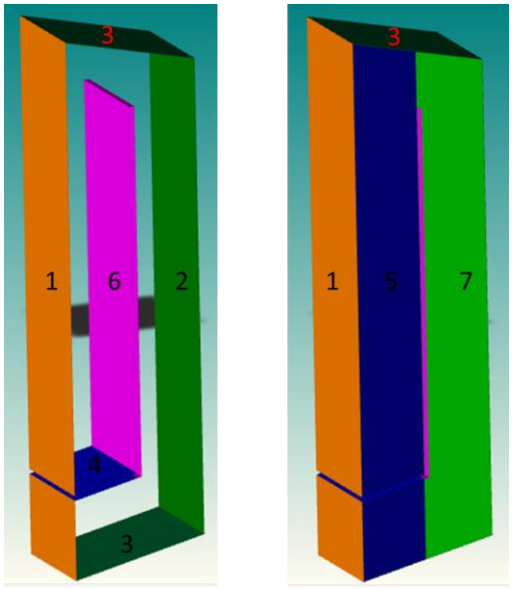

Figure 6.37. Division for the FCI component in the equatorial outboard module (#13).

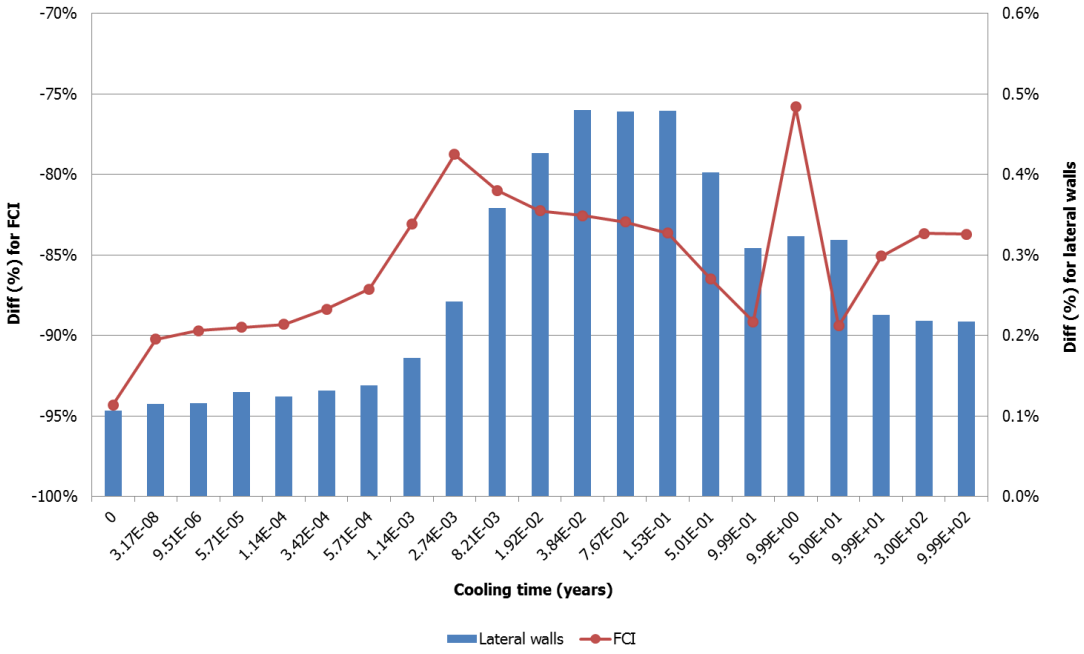

Figure 6.38. Differences between homogenized calculations and radial ones for the lateral walls and FCI components.

2.3.2.4. Nuclear heating radial profile

With regard to the nuclear heating, Figure 6.39-Figure 6.40 represent the total value due to both neutrons and photons, as well as the total for the different slices (see Figure 6.33) of the breeder (Figure 6.39), top and bottom walls (Figure 6.41), and lateral walls (Figure 6.40) from the equatorial outboard module #13, and 360º.

These figures show that the maximum difference (applying the same equation #1) between the slice #1 and #10 is found to be 239%. This increment is slightly higher for the breeder module compared to the top and bottom walls (233%) which, at the same time, have a slightly higher increase than the corresponding to the lateral walls (224%).

These increases are caused specially for the difference (in absolutely values) in the nuclear heating due to photons. The difference between slice #1 and #10 due to photons is especially relevant in the case of the breeder, where is found to be about 298.4%. However, the increases for the other two cases are less significant (222% for the top and bottom walls and 213% for the lateral walls).In the case of the nuclear heating due to neutrons the differences between the slice #1 and #10 are: 96% for the breeder, 276% for the lateral walls and 274% for the top and bottom walls.

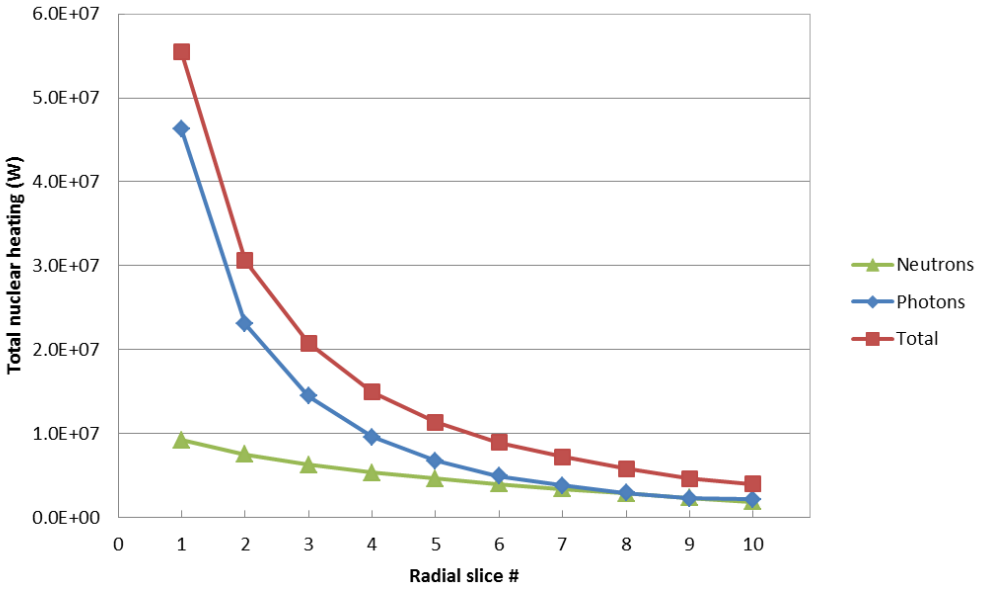

Figure 6.39. Total nuclear heating for the different slices of the breeder from module #13.

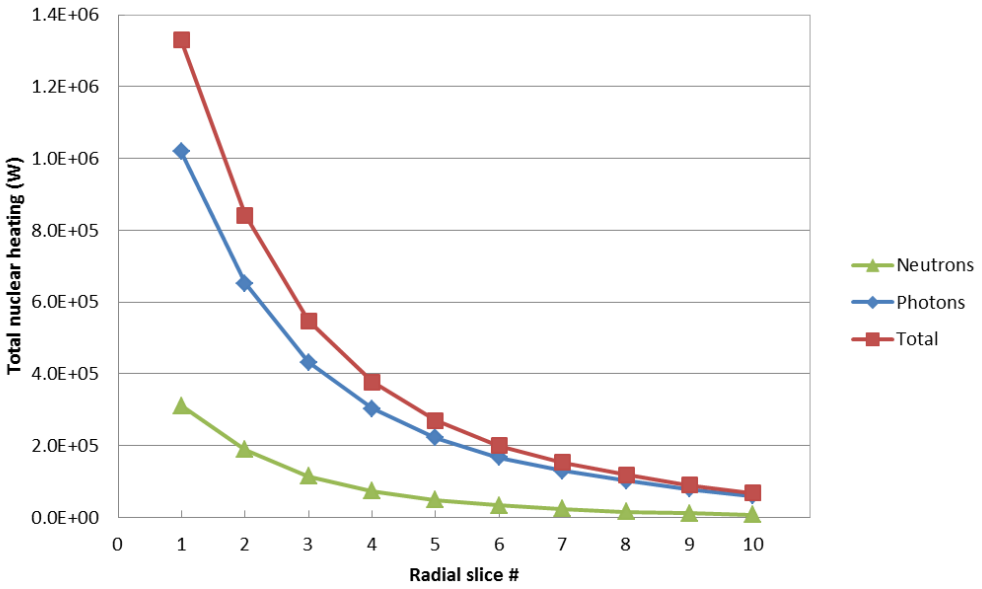

Figure 6.40. Total nuclear heating for the different slices of the top and bottom walls from module #13.

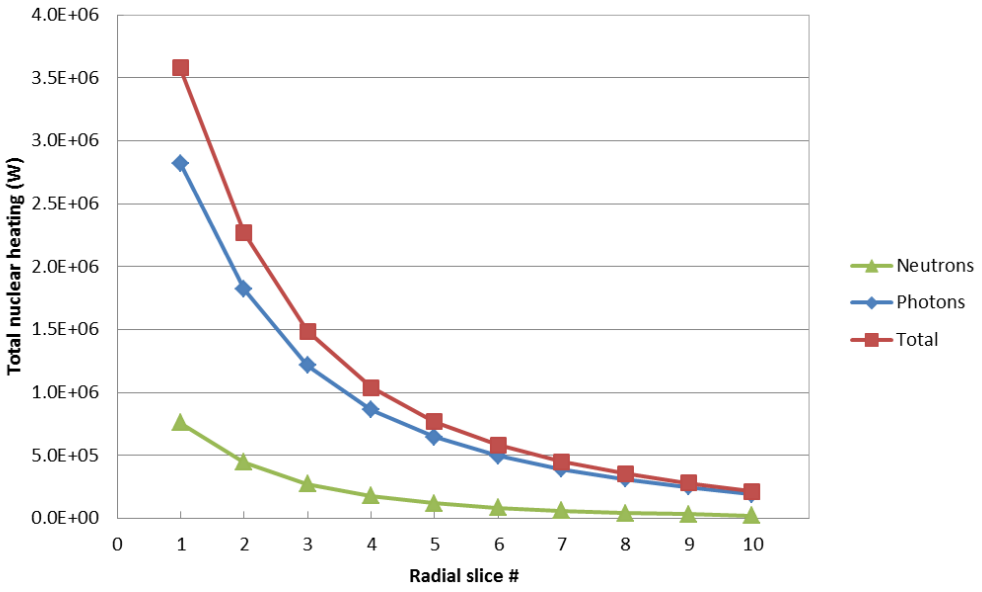

Figure 6.41. Total nuclear heating for the different slices of the lateral walls from module #13.

3.3.6. Decay heat, activity and nuclear heating in the manifold

Table 6.25 shows volumes for the two regions in which the manifold has been divided (inboard and outboard), for the entire reactor (360º). The corresponding calculated fluxes are also presented in the same Table 6.25.

Table 6.26 and Table 6.27 display the evolution of the decay heat and activity responses for the two regions, separated into materials, as well as for the whole manifold. Note that the T contribution to the LiPb has been excluded in both tables. For decay heat, total values are between $1.2 \cdot 10^{3}$ and $1.3 \cdot 10^{2}$ kW up to 2 months; just over 1 kW up to 10 years and finally, it drops to $4.8 \cdot 10^{-4}$ kW at 1000 years. In the case of activity, total value is $6.3 \cdot 10^{12}$-$1.4 \cdot 10^{12}$ MBq up to 2 months; around $4.5 \cdot 10^{10}$ MBq at 10 years and then it drops to $7.3 \cdot 10^{6}$ MBq at 1000 years of cooling. As it can be seen the outboard area shows, at all the considered times, higher values than the inboard region.

Table 6.25. Volume (cm^3) and total neutron flux for the manifold (10^{13} $n/cm^2/s$).

Manifold	Volume	Total neutron flux
Inboard	$1.53 \cdot 10^{8}$	12.12
Outboard	$6.52 \cdot 10^{8}$	3.64
Total	$8.05 \cdot 10^{8}$	

Table 6.26. Total decay heat from the manifold for the entire reactor (T excluded).

Time (years)	Inboard (W)				Outboard (W)				Total (W)	Total (kW)
	Eurofer	LiPb	He	Total	Eurofer	LiPb	He	Total		
$0.00 \cdot 10^{0}$	$5.06 \cdot 10^{5}$	$3.51 \cdot 10^{4}$	$4.10 \cdot 10^{-5}$	$5.41 \cdot 10^{5}$	$6.01 \cdot 10^{5}$	$3.47 \cdot 10^{4}$	$2.51 \cdot 10^{-5}$	$6.36 \cdot 10^{5}$	$1.18 \cdot 10^{6}$	$1.18 \cdot 10^{3}$
$3.17 \cdot 10^{-8}$	$5.05 \cdot 10^{5}$	$2.02 \cdot 10^{4}$	$4.10 \cdot 10^{-5}$	$5.25 \cdot 10^{5}$	$6.00 \cdot 10^{5}$	$2.11 \cdot 10^{4}$	$2.51 \cdot 10^{-5}$	$6.21 \cdot 10^{5}$	$1.15 \cdot 10^{6}$	$1.15 \cdot 10^{3}$
$9.51 \cdot 10^{-6}$	$4.74 \cdot 10^{5}$	$6.94 \cdot 10^{3}$	$4.10 \cdot 10^{-5}$	$4.81 \cdot 10^{5}$	$5.59 \cdot 10^{5}$	$8.23 \cdot 10^{3}$	$2.51 \cdot 10^{-5}$	$5.67 \cdot 10^{5}$	$1.05 \cdot 10^{6}$	$1.05 \cdot 10^{3}$
$5.71 \cdot 10^{-5}$	$4.32 \cdot 10^{5}$	$5.93 \cdot 10^{3}$	$4.10 \cdot 10^{-5}$	$4.38 \cdot 10^{5}$	$5.08 \cdot 10^{5}$	$6.98 \cdot 10^{3}$	$2.51 \cdot 10^{-5}$	$5.15 \cdot 10^{5}$	$9.53 \cdot 10^{5}$	$9.53 \cdot 10^{2}$
$1.14 \cdot 10^{-4}$	$4.00 \cdot 10^{5}$	$5.45 \cdot 10^{3}$	$4.10 \cdot 10^{-5}$	$4.06 \cdot 10^{5}$	$4.73 \cdot 10^{5}$	$6.42 \cdot 10^{3}$	$2.51 \cdot 10^{-5}$	$4.79 \cdot 10^{5}$	$8.85 \cdot 10^{5}$	$8.85 \cdot 10^{2}$
$3.42 \cdot 10^{-4}$	$3.09 \cdot 10^{5}$	$4.17 \cdot 10^{3}$	$4.10 \cdot 10^{-5}$	$3.13 \cdot 10^{5}$	$3.68 \cdot 10^{5}$	$4.93 \cdot 10^{3}$	$2.51 \cdot 10^{-5}$	$3.73 \cdot 10^{5}$	$6.86 \cdot 10^{5}$	$6.86 \cdot 10^{2}$
$5.71 \cdot 10^{-4}$	$2.53 \cdot 10^{5}$	$3.37 \cdot 10^{3}$	$4.10 \cdot 10^{-5}$	$2.56 \cdot 10^{5}$	$3.04 \cdot 10^{5}$	$3.99 \cdot 10^{3}$	$2.51 \cdot 10^{-5}$	$3.08 \cdot 10^{5}$	$5.64 \cdot 10^{5}$	$5.64 \cdot 10^{2}$
$1.14 \cdot 10^{-3}$	$1.88 \cdot 10^{5}$	$2.36 \cdot 10^{3}$	$4.10 \cdot 10^{-5}$	$1.90 \cdot 10^{5}$	$2.29 \cdot 10^{5}$	$2.79 \cdot 10^{3}$	$2.51 \cdot 10^{-5}$	$2.31 \cdot 10^{5}$	$4.21 \cdot 10^{5}$	$4.21 \cdot 10^{2}$
$2.74 \cdot 10^{-3}$	$1.41 \cdot 10^{5}$	$1.47 \cdot 10^{3}$	$4.10 \cdot 10^{-5}$	$1.43 \cdot 10^{5}$	$1.73 \cdot 10^{5}$	$1.73 \cdot 10^{3}$	$2.51 \cdot 10^{-5}$	$1.75 \cdot 10^{5}$	$3.18 \cdot 10^{5}$	$3.18 \cdot 10^{2}$
$8.21 \cdot 10^{-3}$	$9.80 \cdot 10^{4}$	$5.75 \cdot 10^{2}$	$4.09 \cdot 10^{-5}$	$9.85 \cdot 10^{4}$	$1.20 \cdot 10^{5}$	$6.69 \cdot 10^{2}$	$2.51 \cdot 10^{-5}$	$1.21 \cdot 10^{5}$	$2.19 \cdot 10^{5}$	$2.19 \cdot 10^{2}$
$1.92 \cdot 10^{-2}$	$8.28 \cdot 10^{4}$	$2.55 \cdot 10^{2}$	$4.09 \cdot 10^{-5}$	$8.31 \cdot 10^{4}$	$1.01 \cdot 10^{5}$	$2.97 \cdot 10^{2}$	$2.51 \cdot 10^{-5}$	$1.01 \cdot 10^{5}$	$1.85 \cdot 10^{5}$	$1.85 \cdot 10^{2}$
$3.84 \cdot 10^{-2}$	$7.82 \cdot 10^{4}$	$1.98 \cdot 10^{2}$	$4.09 \cdot 10^{-5}$	$7.84 \cdot 10^{4}$	$9.55 \cdot 10^{4}$	$2.35 \cdot 10^{2}$	$2.51 \cdot 10^{-5}$	$9.58 \cdot 10^{4}$	$1.74 \cdot 10^{5}$	$1.74 \cdot 10^{2}$
$7.67 \cdot 10^{-2}$	$7.13 \cdot 10^{4}$	$1.76 \cdot 10^{2}$	$4.08 \cdot 10^{-5}$	$7.15 \cdot 10^{4}$	$8.72 \cdot 10^{4}$	$2.10 \cdot 10^{2}$	$2.50 \cdot 10^{-5}$	$8.74 \cdot 10^{4}$	$1.59 \cdot 10^{5}$	$1.59 \cdot 10^{2}$
$1.53 \cdot 10^{-1}$	$5.96 \cdot 10^{4}$	$1.50 \cdot 10^{2}$	$4.06 \cdot 10^{-5}$	$5.98 \cdot 10^{4}$	$7.28 \cdot 10^{4}$	$1.79 \cdot 10^{2}$	$2.49 \cdot 10^{-5}$	$7.30 \cdot 10^{4}$	$1.33 \cdot 10^{5}$	$1.33 \cdot 10^{2}$
$5.01 \cdot 10^{-1}$	$2.79 \cdot 10^{4}$	$8.07 \cdot 10^{1}$	$3.98 \cdot 10^{-5}$	$2.80 \cdot 10^{4}$	$3.39 \cdot 10^{4}$	$9.69 \cdot 10^{1}$	$2.44 \cdot 10^{-5}$	$3.40 \cdot 10^{4}$	$6.20 \cdot 10^{4}$	$6.20 \cdot 10^{1}$
$9.99 \cdot 10^{-1}$	$1.05 \cdot 10^{4}$	$3.85 \cdot 10^{1}$	$3.87 \cdot 10^{-5}$	$1.05 \cdot 10^{4}$	$1.25 \cdot 10^{4}$	$4.63 \cdot 10^{1}$	$2.38 \cdot 10^{-5}$	$1.26 \cdot 10^{4}$	$2.31 \cdot 10^{4}$	$2.31 \cdot 10^{1}$
$9.99 \cdot 10^{0}$	$5.32 \cdot 10^{2}$	$7.17 \cdot 10^{-1}$	$2.34 \cdot 10^{-5}$	$5.33 \cdot 10^{2}$	$5.88 \cdot 10^{2}$	$8.26 \cdot 10^{-1}$	$1.43 \cdot 10^{-5}$	$5.89 \cdot 10^{2}$	$1.12 \cdot 10^{3}$	$1.12 \cdot 10^{0}$
$5.00 \cdot 10^{1}$	$2.87 \cdot 10^{0}$	$6.48 \cdot 10^{-2}$	$2.46 \cdot 10^{-6}$	$2.94 \cdot 10^{0}$	$3.19 \cdot 10^{0}$	$8.13 \cdot 10^{-2}$	$1.51 \cdot 10^{-6}$	$3.27 \cdot 10^{0}$	$6.20 \cdot 10^{0}$	$6.20 \cdot 10^{-3}$
$9.99 \cdot 10^{1}$	$1.90 \cdot 10^{-1}$	$5.88 \cdot 10^{-2}$	$1.49 \cdot 10^{-7}$	$2.48 \cdot 10^{-1}$	$2.42 \cdot 10^{-1}$	$7.40 \cdot 10^{-2}$	$9.13 \cdot 10^{-8}$	$3.16 \cdot 10^{-1}$	$5.65 \cdot 10^{-1}$	$5.65 \cdot 10^{-4}$
$3.00 \cdot 10^{2}$	$1.81 \cdot 10^{-1}$	$4.98 \cdot 10^{-2}$	$1.94 \cdot 10^{-12}$	$2.31 \cdot 10^{-1}$	$2.32 \cdot 10^{-1}$	$6.28 \cdot 10^{-2}$	$1.19 \cdot 10^{-12}$	$2.95 \cdot 10^{-1}$	$5.26 \cdot 10^{-1}$	$5.26 \cdot 10^{-4}$
$9.99 \cdot 10^{2}$	$1.75 \cdot 10^{-1}$	$3.83 \cdot 10^{-2}$	$1.64 \cdot 10^{-29}$	$2.13 \cdot 10^{-1}$	$2.24 \cdot 10^{-1}$	$4.81 \cdot 10^{-2}$	$1.01 \cdot 10^{-29}$	$2.73 \cdot 10^{-1}$	$4.86 \cdot 10^{-1}$	$4.86 \cdot 10^{-4}$

Table 6.27. Total activity from the manifold for the entire reactor (T excluded).

Time (years)	Inboard (Bq)				Outboard (Bq)				Total (Bq)	Total (Mbq)
	Eurofer	LiPb	He	Total	Eurofer	LiPb	He	Total		
$0.00 \cdot 10^{0}$	$2.66 \cdot 10^{18}$	$1.92 \cdot 10^{17}$	$4.48 \cdot 10^{10}$	$2.85 \cdot 10^{18}$	$3.25 \cdot 10^{18}$	$2.04 \cdot 10^{17}$	$2.75 \cdot 10^{10}$	$3.45 \cdot 10^{18}$	$6.31 \cdot 10^{18}$	$6.31 \cdot 10^{12}$
$3.17 \cdot 10^{-8}$	$2.64 \cdot 10^{18}$	$1.35 \cdot 10^{17}$	$4.48 \cdot 10^{10}$	$2.78 \cdot 10^{18}$	$3.23 \cdot 10^{18}$	$1.52 \cdot 10^{17}$	$2.75 \cdot 10^{10}$	$3.38 \cdot 10^{18}$	$6.16 \cdot 10^{18}$	$6.16 \cdot 10^{12}$
$9.51 \cdot 10^{-6}$	$2.45 \cdot 10^{18}$	$7.91 \cdot 10^{16}$	$4.48 \cdot 10^{10}$	$2.53 \cdot 10^{18}$	$2.99 \cdot 10^{18}$	$9.69 \cdot 10^{16}$	$2.75 \cdot 10^{10}$	$3.08 \cdot 10^{18}$	$5.61 \cdot 10^{18}$	$5.61 \cdot 10^{12}$
$5.71 \cdot 10^{-5}$	$2.32 \cdot 10^{18}$	$7.11 \cdot 10^{16}$	$4.48 \cdot 10^{10}$	$2.39 \cdot 10^{18}$	$2.83 \cdot 10^{18}$	$8.69 \cdot 10^{16}$	$2.75 \cdot 10^{10}$	$2.92 \cdot 10^{18}$	$5.31 \cdot 10^{18}$	$5.31 \cdot 10^{12}$
$1.14 \cdot 10^{-4}$	$2.23 \cdot 10^{18}$	$6.60 \cdot 10^{16}$	$4.48 \cdot 10^{10}$	$2.30 \cdot 10^{18}$	$2.73 \cdot 10^{18}$	$8.06 \cdot 10^{16}$	$2.75 \cdot 10^{10}$	$2.81 \cdot 10^{18}$	$5.11 \cdot 10^{18}$	$5.11 \cdot 10^{12}$
$3.42 \cdot 10^{-4}$	$1.97 \cdot 10^{18}$	$5.13 \cdot 10^{16}$	$4.48 \cdot 10^{10}$	$2.^{2} \cdot 10^{18}$	$2.42 \cdot 10^{18}$	$6.22 \cdot 10^{16}$	$2.75 \cdot 10^{10}$	$2.49 \cdot 10^{18}$	$4.51 \cdot 10^{18}$	$4.51 \cdot 10^{12}$
$5.71 \cdot 10^{-4}$	$1.79 \cdot 10^{18}$	$4.15 \cdot 10^{16}$	$4.48 \cdot 10^{10}$	$1.84 \cdot 10^{18}$	$2.22 \cdot 10^{18}$	$5.00 \cdot 10^{16}$	$2.75 \cdot 10^{10}$	$2.27 \cdot 10^{18}$	$4.11 \cdot 10^{18}$	$4.11 \cdot 10^{12}$
$1.14 \cdot 10^{-3}$	$1.55 \cdot 10^{18}$	$2.85 \cdot 10^{16}$	$4.48 \cdot 10^{10}$	$1.58 \cdot 10^{18}$	$1.94 \cdot 10^{18}$	$3.38 \cdot 10^{16}$	$2.75 \cdot 10^{10}$	$1.97 \cdot 10^{18}$	$3.56 \cdot 10^{18}$	$3.56 \cdot 10^{12}$
$2.74 \cdot 10^{-3}$	$1.27 \cdot 10^{18}$	$1.75 \cdot 10^{16}$	$4.48 \cdot 10^{10}$	$1.29 \cdot 10^{18}$	$1.60 \cdot 10^{18}$	$2.04 \cdot 10^{16}$	$2.75 \cdot 10^{10}$	$1.62 \cdot 10^{18}$	$2.91 \cdot 10^{18}$	$2.91 \cdot 10^{12}$
$8.21 \cdot 10^{-3}$	$9.08 \cdot 10^{17}$	$8.05 \cdot 10^{15}$	$4.48 \cdot 10^{10}$	$9.16 \cdot 10^{17}$	$1.15 \cdot 10^{18}$	$9.23 \cdot 10^{15}$	$2.75 \cdot 10^{10}$	$1.16 \cdot 10^{18}$	$2.07 \cdot 10^{18}$	$2.07 \cdot 10^{12}$
$1.92 \cdot 10^{-2}$	$7.75 \cdot 10^{17}$	$4.33 \cdot 10^{15}$	$4.47 \cdot 10^{10}$	$7.80 \cdot 10^{17}$	$9.85 \cdot 10^{17}$	$5.01 \cdot 10^{15}$	$2.75 \cdot 10^{10}$	$9.90 \cdot 10^{17}$	$1.77 \cdot 10^{18}$	$1.77 \cdot 10^{12}$
$3.84 \cdot 10^{-2}$	$7.30 \cdot 10^{17}$	$3.37 \cdot 10^{15}$	$4.47 \cdot 10^{10}$	$7.33 \cdot 10^{17}$	$9.30 \cdot 10^{17}$	$3.97 \cdot 10^{15}$	$2.74 \cdot 10^{10}$	$9.34 \cdot 10^{17}$	$1.67 \cdot 10^{18}$	$1.67 \cdot 10^{12}$
$7.67 \cdot 10^{-2}$	$6.66 \cdot 10^{17}$	$2.88 \cdot 10^{15}$	$4.46 \cdot 10^{10}$	$6.69 \cdot 10^{17}$	$8.51 \cdot 10^{17}$	$3.40 \cdot 10^{15}$	$2.74 \cdot 10^{10}$	$8.54 \cdot 10^{17}$	$1.52 \cdot 10^{18}$	$1.52 \cdot 10^{12}$
$1.53 \cdot 10^{-1}$	$5.68 \cdot 10^{17}$	$2.27 \cdot 10^{15}$	$4.44 \cdot 10^{10}$	$5.70 \cdot 10^{17}$	$7.27 \cdot 10^{17}$	$2.69 \cdot 10^{15}$	$2.73 \cdot 10^{10}$	$7.30 \cdot 10^{17}$	$1.30 \cdot 10^{18}$	$1.30 \cdot 10^{12}$
$5.01 \cdot 10^{-1}$	$3.38 \cdot 10^{17}$	$8.92 \cdot 10^{14}$	$4.36 \cdot 10^{10}$	$3.39 \cdot 10^{17}$	$4.42 \cdot 10^{17}$	$1.06 \cdot 10^{15}$	$2.67 \cdot 10^{10}$	$4.43 \cdot 10^{17}$	$7.82 \cdot 10^{17}$	$7.82 \cdot 10^{11}$
$9.99 \cdot 10^{-1}$	$2.19 \cdot 10^{17}$	$3.17 \cdot 10^{14}$	$4.23 \cdot 10^{10}$	$2.19 \cdot 10^{17}$	$2.93 \cdot 10^{17}$	$3.75 \cdot 10^{14}$	$2.60 \cdot 10^{10}$	$2.94 \cdot 10^{17}$	$5.13 \cdot 10^{17}$	$5.13 \cdot 10^{11}$
$9.99 \cdot 10^{0}$	$1.89 \cdot 10^{16}$	$1.41 \cdot 10^{13}$	$2.55 \cdot 10^{10}$	$1.89 \cdot 10^{16}$	$2.57 \cdot 10^{16}$	$1.65 \cdot 10^{13}$	$1.57 \cdot 10^{10}$	$2.58 \cdot 10^{16}$	$4.47 \cdot 10^{16}$	$4.47 \cdot 10^{10}$
$5.00 \cdot 10^{1}$	$1.38 \cdot 10^{13}$	$2.01 \cdot 10^{12}$	$2.69 \cdot 10^{9}$	$1.59 \cdot 10^{13}$	$1.64 \cdot 10^{13}$	$2.53 \cdot 10^{12}$	$1.65 \cdot 10^{9}$	$1.89 \cdot 10^{13}$	$3.48 \cdot 10^{13}$	$3.48 \cdot 10^{7}$
$9.99 \cdot 10^{1}$	$4.14 \cdot 10^{12}$	$1.30 \cdot 10^{12}$	$1.63 \cdot 10^{8}$	$5.44 \cdot 10^{12}$	$5.25 \cdot 10^{12}$	$1.66 \cdot 10^{12}$	$9.99 \cdot 10^{7}$	$6.91 \cdot 10^{12}$	$1.24 \cdot 10^{13}$	$1.24 \cdot 10^{7}$
$3.00 \cdot 10^{2}$	$3.13 \cdot 10^{12}$	$7.37 \cdot 10^{11}$	$2.12 \cdot 10^{3}$	$3.86 \cdot 10^{12}$	$3.96 \cdot 10^{12}$	$9.59 \cdot 10^{11}$	$1.30 \cdot 10^{3}$	$4.92 \cdot 10^{12}$	$8.78 \cdot 10^{12}$	$8.78 \cdot 10^{6}$
$9.99 \cdot 10^{2}$	$2.70 \cdot 10^{12}$	$5.25 \cdot 10^{11}$	$1.79 \cdot 10^{-14}$	$3.22 \cdot 10^{12}$	$3.41 \cdot 10^{12}$	$6.89 \cdot 10^{11}$	$1.10 \cdot 10^{-14}$	$4.10 \cdot 10^{12}$	$7.32 \cdot 10^{12}$	$7.32 \cdot 10^{6}$

Table 6.28. Nuclear heating (kW) for the manifold.

Manifold	Due to neutrons	Due to photons	Total
Inboard	$7.12 \cdot 10^{3}$	$3.67 \cdot 10^{4}$	$4.38 \cdot 10^{4}$
Outboard	$8.88 \cdot 10^{3}$	$3.83 \cdot 10^{4}$	$4.71 \cdot 10^{4}$
Total	$1.60 \cdot 10^{4}$	$7.50 \cdot 10^{4}$	$9.10 \cdot 10^{4}$

On another note, major radionuclides contributing to decay heat are: ^{56}Mn up to 3 hours (half-life 2.6 hours), followed by ^{187}W (half-life 24 h), which develops into the first contributor at 5 hours; then, ^{182}Ta becomes the main contributor up to one year (half-life 114.7 days), ^{60}Co is dominant up to 50 years (half-life 1925.3 days) and ^{94}Nb for larger cooling times (half-life $2.0 \cdot 10^{4}$ years).

Table 6.28 summarizes the nuclear heating results. As it can be seen, the total nuclear heating due to photons is higher than the one due to neutrons. Also, nuclear heating in the inboard region is slightly lower than in the outboard area.

4. Comparison between DCLL and other BB concepts

The focus of this section is to compare the activation results obtained for the DCLL (summarized in [3]) and those collected for the other three blanket module concepts [25]-[27]. As it has been previously commented, since the different BB concepts differ in layout, construction and materials, their associated nuclear responses under neutron irradiation will differ. This causes differences in the amounts of activation, damage and decay heat which could be crucial when performing radioactive waste management or safety analysis.

This assessment was performed based on the results of the calculations performed on 2015, using the 2014 DEMO model[23] and was presented at the 29th edition of the Symposium on Fusion Technology (SOFT 2016) hold in Prague (Czech Republic), from 5th to 9th September 2016, and there is a submitted paper for considering its publication in Fusion Engineering and Design [4].

For what concerns to codes and libraries, in the calculations carried out by each of the groups for the other three BB, MCNP was used to calculate the neutron flux and energy spectra across each of the blanket components, and cross section libraries were the agreed in the corresponding guidelines, i.e. JEFF-3.2 and FENDL-2.1. However, FISPACT was chosen to

[23] For 2015, a similar comparison is expected. However, at the time of presentation of this thesis the results corresponding to the other models were not yet widespread.

perform inventory calculations in the HCPB, HCLL and WCLL cases. Regarding activation cross sections, EAF-2007 and EAF-2010 were used.

As anticipated, the neutron spectra differ considerably among the BB concepts, due to the differing material compositions. For all blanket module concepts (see Figure 6.42), as would be expected, the 14.1 MeV peak is higher in the first wall when compared to the breeder material. As the neutrons pass through the FW and interact with the material some lose some of their energy and some are absorbed. As a result, the 14.1 MeV peak is lower 14.1 MeV in the areas deeper within the blanket.

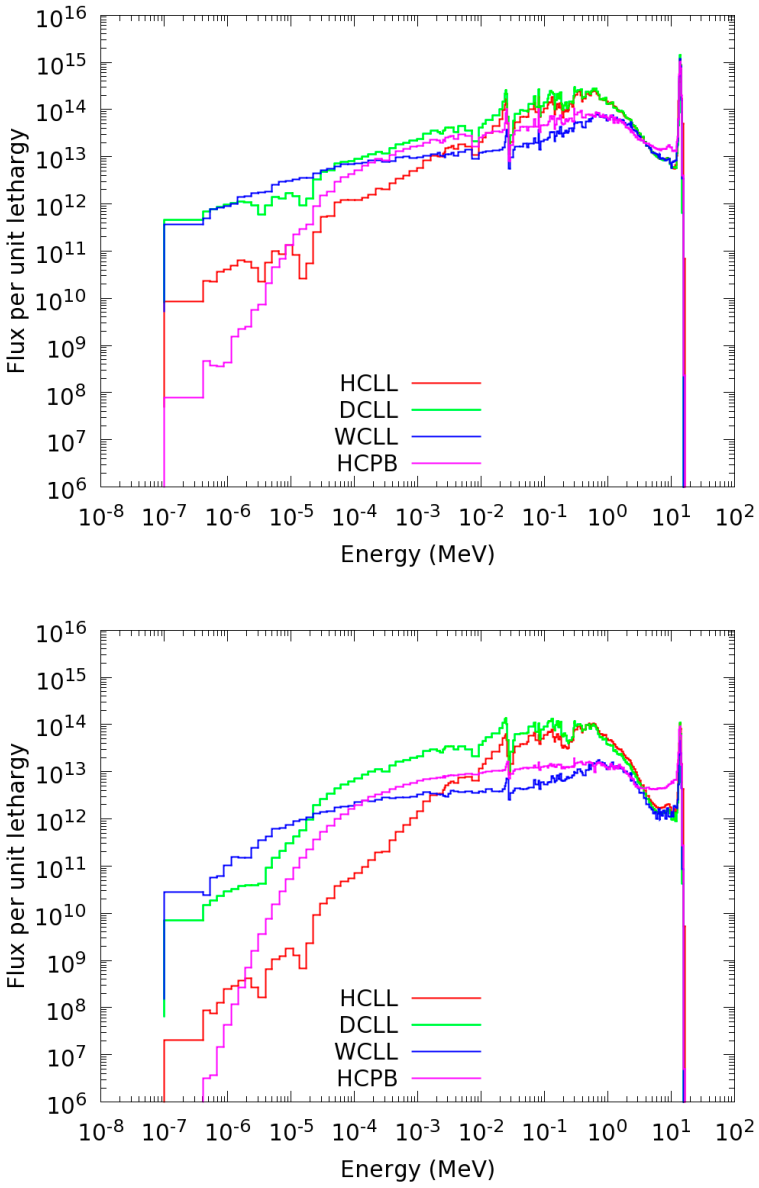

Figure 6.42. Neutron spectra for the FW (up) and breeder (down) each of the four blanket concepts [4].

The HCLL and DCLL concepts have similar high energy spectra in both the FW and breeder material. However the HCLL blanket has significantly lower low energy tails to the spectra for both the FW and breeder material. This is maybe due to the fact that the DCLL concept contains a larger fraction of Eurofer and He coolant compared to the HCLL and these are likely to be better moderator than the LiPb, leading to greater numbers of lower energy neutrons. The WCLL blanket concept has the most thermalized spectrum in both the FW and breeder material, mainly due to the presence of water as coolant. The HCPB has fewer very low energy neutrons and a greater number of neutrons in the range 1-10 MeV, compared to the other three concepts. Despite it is not clear why this might be, one possibility may be the reactions and scattering cross sections for beryllium when compared to lead (which is used in the other three concepts).

The decay heat against decay time for each of the reactor concepts can be seen in Figure 6.43. It is important to note that the given decay heat values do not contain the corresponding values for the T generated by the activation of the breeding material, since, as happens with the DCLL, for all blanket concepts T will be constantly extracted and therefore, it will not contribute to the blankets decay heat[24].

All of the blanket module concepts have decay heats in the tens of MW in the seconds after shutdown. The HCLL blanket has the lowest decay heat for short decay times (below 10^5 s) with 17.5 MW predicted 1 second after shutdown. This is approximately 17-22% lower than predicted for the other blanket concepts of 21.5-22.7 MW, 1 second after shutdown. For all concepts this is a significant amount of decay heat which will require dissipating in order to not over heat or melt components. At longer decay times (i.e. higher than 10^5 s) the HCPB concept generates the least decay heat of all concepts. This is followed by the HCLL. The DCLL and WCLL have decay heats which are 2-3 orders of magnitude higher for times longer than 10^5 s. This may mean that cooling for the DCLL and WCLL can be required for longer after shutdown. The DCLL has the highest decay heat up to decay times of $\sim 10^8$ s and the WCLL has the highest for cooling times higher than 10^8 s. For all concepts the greatest amount of decay heat is generated in the breeder material region of the blanket modules. Although this area does not have the greatest decay heat density, it does have significantly more mass than any other region. The areas towards the back of the blanket modules such as the BP and manifold tend to have the lowest contribution to the decay heat as they are in regions of relatively low neutron flux leading to lower activation and have relatively little mass.

[24] In reality there will be a steady state level of T in the blanket module which will contribute to the decay heat however this will only be a minor contribution.

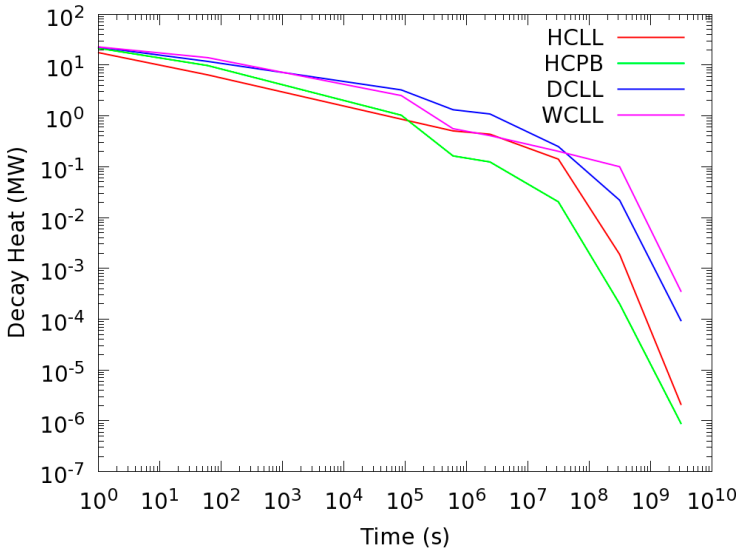

Figure 6.43. Decay heat for all blanket modules in the DEMO reactor for each concept [4].

In order to ensure adequate cooling is supplied to all blanket components a study into which components generate the highest decay heat density has been performed. The decay heat density (averaged over all blanket modules) for the different elements of each of the blanket concepts can be seen in Figure 6.44. Although there is some poloidal variation in the decay heat density the general trends are the same as the average.

As it would be expected, due to the high neutron flux, the highest decay heat density (for decay times lower than 10^8 s for the HCLL, HCBP and DCLL, and 10^5 s for the WCLL) occurs for the W armour for all blanket concepts. The dominant nuclides in the W armour at shorter decay times are W isotopes; mainly ^{187}W with a 23.9 hour half-life. At decay times longer than 10 years the products of the minor impurities in the W such as ^{60}Co and ^{39}Ar dominate the decay heat. It is therefore important to ensure they are minimized, where possible. The decay heat density at short decay times for the W armour is slightly higher for the WCLL and DCLL than for the HCLL and HCPB. The production of the dominant ^{187}W via (n,g) reaction with ^{186}W has the highest cross section at low neutron energies. As can be seen from Figure 6.44 the WCLL and DCLL have greater neutron moderation in the first wall area which leads to higher production of ^{187}W and, therefore, a higher decay heat density.

The other blanket areas have similar decay heat densities between concepts, apart from the manifold for the HCLL. For the HCPB, WCLL and DCLL the manifold has the lowest decay heat density. However, for the HCLL the decay heat density for the manifold is above that of the BP and breeder mixture for most decay times. This is likely due to the limited shielding that is offered by the HCLL blanket module design, which leads to higher neutron flux in the region of the manifold. As a result, more activation and subsequent decay heat is found for the HCLL.

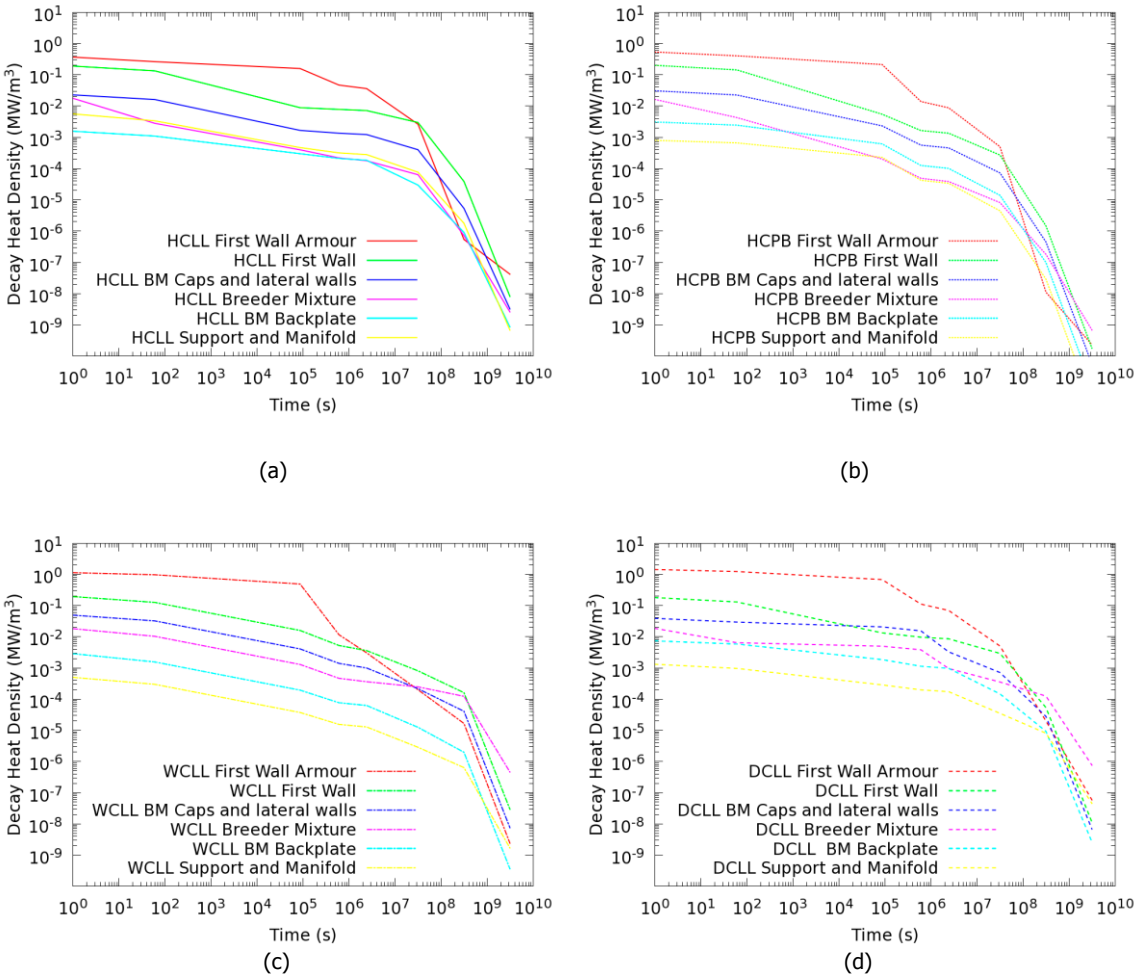

Figure 6.44. Decay heat density for each of the four blanket concepts: (a), HCLL; (b), HCPB; (c), WCLL; (d), DCLL [4].

5. Radioactive waste assessment for 2014 DEMO DCLL model

In large fusion machines, as the foreseen DEMO, the high energy neutrons produced will cause the transmutation of the interacting materials which become a source of radioactive waste. Beside the main constituents that could transmute but which presence is essential, the impurities either naturally occurring or accidentally, or inevitably added during the production process, often give rise to significant additional activation compared to the base material.

The goal of this section is to determine the composition limits for the considered DCLL materials in order to minimize the radiological impact of waste. Furthermore, the viability from the manufacturing and industrial point of view for reducing the suggested impurities was also assessed. The analyzed materials are those considered to be the main sources of radioactive

waste: the W coating, the Eurofer structure, and the LiPb breeder[25]. This assessment was performed based on 2014 DEMO DCLL model and was also presented at the SOFT 2016. Moreover, there is a submitted paper for considering its publication in Fusion Engineering and Design [5].

Searching for conservative results neutron fluences were calculated at different radial and poloidal positions (Figure 6.45) within the structures of the two most exposed equatorial inboard (#3) and outboard (#12) blanket modules for the different materials. The highest neutron fluences founded in the positions closest to the plasma, and assumed for the activation calculation of the three materials, are: $7.7004 \cdot 10^{14}$ n/cm^2 at the FW of blanket #12, $7.5898 \cdot 10^{14}$ n/cm^2 in the W coating of blanket #3, and $5.3248 \cdot 10^{14}$ n/cm^2 for the radial zone 1 of LiPb (see figure Figure 6.45) of blanket module #12.

To date, some internationally accepted criteria exist for the characterization of the radiological impact that the disposal of radioactive wastes has (e.g. dose limits for the most exposed individual of the public). However, the derived limits expressed in CDR, specific activities or total activities, show considerable discrepancies because of different country-specific waste management and disposal strategies. Nevertheless, there is a tendency to divide nuclear waste into three categories, namely High Level Waste (HLW), MLW/ILW (Medium/Intermediate Level Waste), and LLW. However, significant differences in the classification are appreciated from country to country.

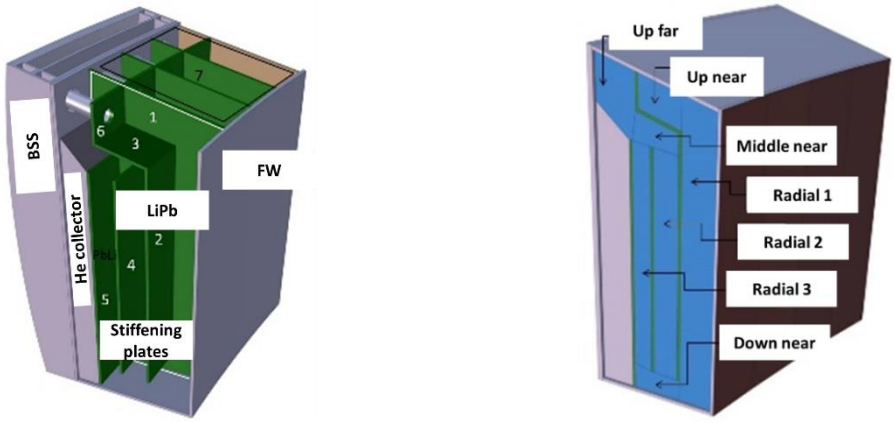

(a) (b)

Figure 6.45. DEMO DCLL detailed outboard equatorial module scheme for neutron fluences calculations. (a), global scheme; (b), LiPb zones.

[25] LiPb could be also reused, after purification, in other reactors. Nevertheless, its management as radioactive waste is also here studied.

In Europe, the waste classification and management policies are coordinated at a national level. Nevertheless, in general, most of the countries are following the IAEA categorization [28] into low and intermediate level waste, LILW-SL and LILW-LL (SL and LL refer to short lived and long lived respectively, being the limit between both at 30 years half-life), and HLW. Some countries like Spain, France, Finland, and Sweden are also introducing the concept of VLLW (Very Low Level Waste) for materials above the clearance level, but not requiring as much protection and engineering as the LILW.

There is no a currently operational disposal facility for HLW in Europe. Most spent fuel and fuel-reprocessing waste are stored either on the power plant site (dry or wet storage) or in centralized national storage. On the other hand, there are LILW repositories currently functioning in France (CSA), Spain (El Cabril), Sweden (SFR), United Kingdom (Drigg), and Finland (at each nuclear power plant site).

5.1. Waste classification and management criteria

In this section, the proposed criteria from the IAEA are followed [28]. That means a decay heat limit value of 2 kW/m^3 between LILW and HLW, and an alpha activity of 4000 Bq/g to separate between LILW-SL and LILW-LL (Table 6.29). Activated material from the PPCS fusion reactor models were categorized according to the SEAFP-2 classification system [29] (see Table 6.30). These are in line with the recommendations of ICRP 90 [30] and the older IAEA 96 [31]. Being more restrictive than the IAEA decay heat limits, and also considering CDR limits, the SEAFP-2 criterion is applied in the following assessments. According to [29], CRM corresponds to MLW while SRM does to LLW. Hence, hereinafter the acronym LLW is used instead of SRM.

Table 6.29. IAEA radioactive waste classification system [28].

Waste classes	Typical characteristics and disposal options	Disposal options
Exempted Waste (EW)	Activity levels < clearance levels → Annual dose to public < 0.01 mSv	No radiological restrictions
Low and Intermediate Level Waste (LILW)	Activity levels > clearance levels & termal power < 2 kW/m^3	
Short Lived Waste (LIWL-SL)	Restricted long lived radionuclide concentrations (limitation of long lived alpha emitting radionuclides to 4000 Bq/g in individual packages)	Near surface or deep underground disposal facility
Long Lived Waste (LILW-LL)	Long lived radionuclide concentrations > LILW-SL	Deep underground disposal facility
High Level Waste (HLW)	Thermal power > 2 kW/m^3 and long lived radionuclide concentrations > LILW-SL	Deep underground disposal facility

Table 6.30. Radiological complexity of operation based on handling.

Activated material classification	CDR @50y (mSv/h)	Decay heat @50y (W/m^3)
PWD (Permanent Disposal Waste), not recyclable	>20	>10
CRM (Complex Recycle Material), recyclable with complex RH procedures	2-20	1-10
SRM (Simple Recycle Material), Recyclable with simple RH procedures Hand on recycling for D < 10 μSv/h	<2	<1
NAW (Non Active Waste), to be cleared	<0.001	<1

Furthermore, the possibility of disposal in El Cabril (Córdoba, Spain) has been evaluated. El Cabril near-surface facility for the disposal of VLLW and LILLW is in operation since 1992. There, the primary waste package is normally package in 200 L drums. Before disposal the primary waste is stabilized with concrete or by super compaction. El Cabril is divided into two areas: one for VLLW and other one for LILW. This second zone, at the same time, has two levels. Waste with activity values for: i) total alpha, ii) total beta-gamma and iii) specific limits for certain nuclides is defined as El Cabril Level 1. Acceptance criteria for El Cabril Level 2 are also specific activity limits (above Level 1) for certain nuclides and total alpha activity [32].

5.2. Results for original compositions

Considering the previous explained conditions the decay heat, CDR, total alpha, total beta-gamma and specific activity for different nuclides have been analyzed with reference to the SEAFP-2 standards and to the specific regulations of El Cabril.

The total values of decay heat, CDR and beta-gamma activity at 50, 100 and 300 years are shown in Table 6.31 for W, Eurofer, and LiPb and displayed in Figure 6.46 along all the cooling time, as well as the corresponding limits. The alpha activity (not displayed) is several orders of magnitude below the limit for El Cabril in the three cases.

It is plain to see that activity is one of the most crucial parameters. In fact, while the limit of SRM is already fulfilled at 50 years for W, Eurofer, and LiPb, and the limit of LLW is respected since 100 years for W and Eurofer, and already at 50 years for LiPb, the limit on the total activity for Level 1 of El Cabril is not achieved even after 300 years for W and Eurofer, and only since 300 years for LiPb.

Table 6.31. Global activation responses for each material [5].

Material	Response	50 years	100 years	300 years	Limit
Tungsten	Decay heat (W/cm^3)	$1.83 \cdot 10^{-7}$	$8.42 \cdot 10^{-8}$	$3.49 \cdot 10^{-8}$	*SRM < $1 \cdot 10^{-6}$*
	CDR (Sv/h)	**$3.95 \cdot 10^{-3}$**	$1.49 \cdot 10^{-3}$	$8.60 \cdot 10^{-4}$	*LLW < $2 \cdot 10^{-3}$*
	Activity (Bq/g)	**$1.59 \cdot 10^{5}$**	**$7.96 \cdot 10^{4}$**	**$4.55 \cdot 10^{4}$**	*Level 1 < $3.7 \cdot 10^{4}$*
Eurofer	Decay heat (W/cm^3)	$4.55 \cdot 10^{-8}$	$6.73 \cdot 10^{-9}$	$5.64 \cdot 10^{-9}$	*SRM < $1 \cdot 10^{-6}$*
	CDR (Sv/h)	**$7.54 \cdot 10^{-3}$**	$5.11 \cdot 10^{-4}$	$4.92 \cdot 10^{-4}$	*LLW < $2 \cdot 10^{-3}$*
	Activity (Bq/g)	**$1.19 \cdot 10^{6}$**	**$1.38 \cdot 10^{5}$**	**$6.65 \cdot 10^{4}$**	*Level 1 < $3.7 \cdot 10^{4}$*
LiPb	Decay heat (W/cm^3)	$7.32 \cdot 10^{-7}$	$4.92 \cdot 10^{-8}$	$3.09 \cdot 10^{-9}$	*SRM < $1 \cdot 10^{-6}$*
	CDR (Sv/h)	$6.94 \cdot 10^{-4}$	$4.37 \cdot 10^{-4}$	$2.84 \cdot 10^{-4}$	*LLW < $2 \cdot 10^{-3}$*
	Activity (Bq/g)	**$8.28 \cdot 10^{7}$**	**$5.02 \cdot 10^{6}$**	$6.75 \cdot 10^{3}$	*Level 1 < $3.7 \cdot 10^{4}$*

Values above the limits are highlighted in bold.

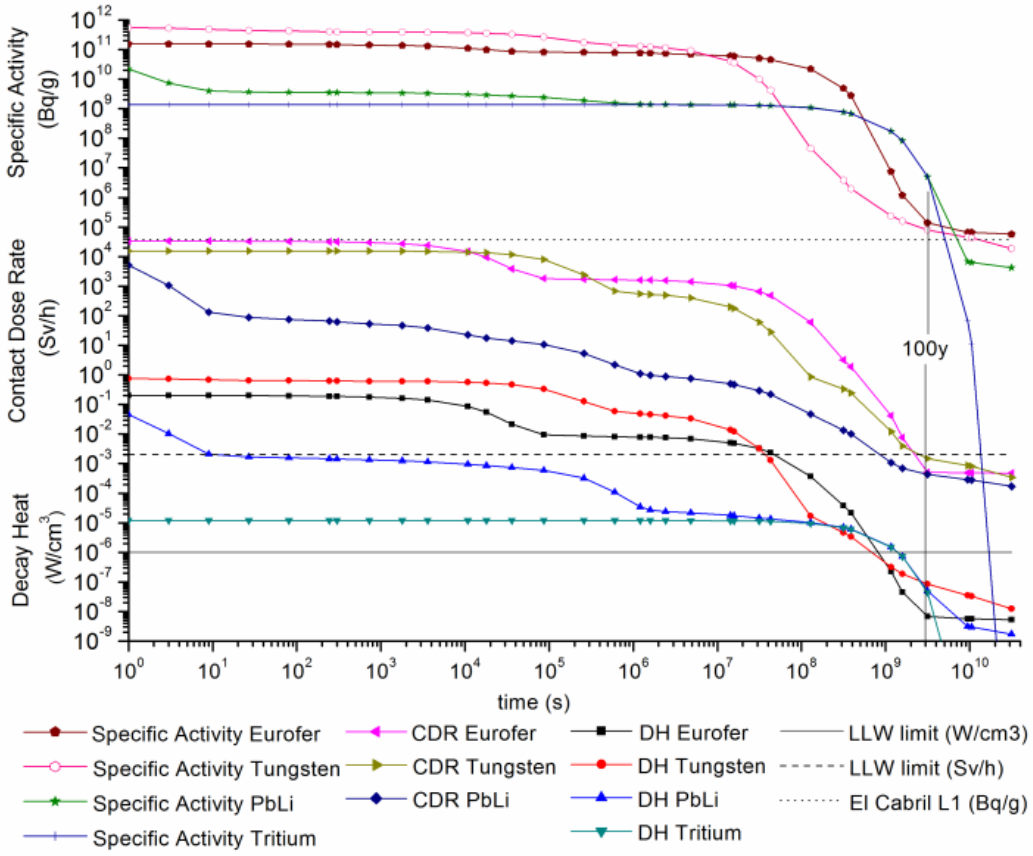

Figure 6.46. Global activation responses along the cooling time for W, Eurofer and LiPb [5].

The results of the contribution of each daughter nuclide to each of the responses are also shown in Table 6.32-Table 6.38 for W, Eurofer, and LiPb respectively, at 50 and 100 years since shutdown and separating the contributions in more than 0.1%, more than 1%, and more than 10%. As it can be seen, for the decay heat, contributors and percentages are similar to those given in Section 2.3.4 but with slight differences. Also, it is important to highlight that, unless there are many contributors for each response, most of them come from the main constituent nuclide. This is the case of $^{178m/s}$Hf come from W itself or ^{55}Fe which is intrinsic to Eurofer. Hence, these constituents can not be reduced. At other times, these contributors are not considered harmful because the limit for the global response is not overpassed.

Table 6.32. Contribution of activation products of W to the decay heat [5].

50 years			100 years		
>10%	^{178s}Hf	29.8%	>10%	^{39}Ar	28.0%
	^{178m}Hf	26.3%		^{108m}Ag	23.6%
	^{39}Ar	14.6%		^{178s}Hf	21.2%
	^{108m}Ag	11.8%		^{178m}Hf	18.7%
	^{60}Co	11.1%	>1%	^{186}Re	2.4%
>1%	^{93m}Nb	1.2%		^{94}Nb	2.2%
	^{186}Re	1.1%	>0.1%	^{91}Nb	1.0%
	^{113m}Cd	1.0%		^{186m}Re	0.9%
	^{94}Nb	1.0%		^{108}Ag	0.8%
>0.1%	^{91}Nb	0.5%		^{93m}Nb	0.5%
	^{186m}Re	0.4%		^{63}Ni	0.2%
	^{108}Ag	0.4%		^{113m}Cd	0.2%
	^{3}H	0.3%		^{14}C	0.1%
	^{133}Ba	0.2%		^{93}Mo	0.1%
	^{63}Ni	0.1%			

Table 6.33. Contribution of activation products of W to the CDR [5].

50 years			100 years		
>10%	^{60}Co	42.1%	>10%	^{108m}Ag	69.3%
	^{108m}Ag	28.5%		^{178m}Hf	22.8%
	^{178m}Hf	26.3%	>1%	^{94}Nb	7.2%
>1%	^{94}Nb	2.7%	>0.1%	^{91}Nb	0.2%
>0.1%	^{133}Ba	0.2%		^{60}Co	0.2%
				^{108}Ag	0.1%

Table 6.34. Contribution of activation products of W to the activity [5].

50 years			100 years		
>10%	^{39}Ar	25.0%	>10%	^{39}Ar	43.9%
	^{3}H	19.5%		^{91}Nb	18.1%
	^{93m}Nb	14.5%	>1%	^{178m}Hf	5.6%
>1%	^{91}Nb	9.5%		^{178s}Hf	5.6%
	^{178m}Hf	8.6%		^{93m}Nb	5.5%
	^{178s}Hf	8.6%		^{108m}Ag	4.9%
	^{63}Ni	3.0%		^{63}Ni	4.2%
	^{108m}Ag	2.7%		^{93}Mo	2.8%
	^{113m}Cd	2.1%		^{3}H	2.3%
	^{60}Co	1.6%		^{186}Re	2.3%
	^{93}Mo	1.4%		^{186m}Re	2.3%
	^{186}Re	1.2%		^{14}C	1.0%
	^{186m}Re	1.2%	>0.1%	^{108}Ag	0.4%
>0.1%	^{14}C	0.5%		^{94}Nb	0.4%
	^{108}Ag	0.2%		^{113m}Cd	0.4%
	^{94}Nb	0.2%			
	^{133}Ba	0.2%			

Table 6.35. Contribution of activation products of Eurofer to the decay heat [5].

50 years			100 years		
>10%	^{60}Co	65.4%	>10%	^{14}C	44.6%
	^{3}H	10.9%		^{94}Nb	37.9%
>1%	^{93m}Nb	7.1%	>1%	^{93m}Nb	5.8%
	^{14}C	6.6%		^{3}H	4.5%
	^{94}Nb	5.6%		^{63}Ni	3.5%
	^{55}Fe	2.6%	>0.1%	^{91}Nb	1.0%
>0.1%	^{63}Ni	0.7%		^{178s}Hf	0.7%
	^{178s}Hf	0.3%		^{178m}Hf	0.7%
	^{178m}Hf	0.3%		^{60}Co	0.6%
	^{91}Nb	0.2%		^{53}Mn	0.3%
				^{93}Mo	0.1%
				^{26}Al	0.1%

Table 6.36. Contribution of activation products of Eurofer to the CDR [5].

50 years			100 years		
>10%	^{60}Co	92.4%	>10%	^{94}Nb	96.1%
>1%	^{94}Nb	6.5%	>1%	^{60}Co	1.9%
>0.1%	^{55}Fe	0.7%		^{178m}Hf	1.0%
	^{178m}Hf	0.2%	>0.1%	^{91}Nb	0.4%
				^{26}Al	0.3%
				^{53}Mn	0.1%
				^{93m}Nb	0.1%

Table 6.37. Contribution of activation products of Eurofer to the activity [5].

50 years			100 years		
>10%	^{3}H	67.6%	>10%	^{14}C	40.7%
	^{55}Fe	16.4%		^{3}H	35.3%
>1%	^{93m}Nb	8.1%	>1%	^{63}Ni	9.2%
	^{14}C	4.7%		^{93m}Nb	8.5%
	^{63}Ni	1.5%		^{91}Nb	2.3%
>0.1%	^{60}Co	0.9%		^{52m}Mn	2.3%
	^{91}Nb	0.3%	>0.1%	^{94}Nb	1.0%
	^{52m}Mn	0.3%		^{93}Mo	0.4%
	^{94}Nb	0.1%		^{59}Ni	0.2%

Table 6.38. Contribution of activation products of LiPb to the decay heat [5].

50 years			100 years		
>10%	^{3}H	98.7%	>10%	^{3}H	88.6%
>0.1%	^{108m}Ag	0.4%	>1%	^{108m}Ag	4.9%
	^{207}Bi	0.3%		^{207}Bi	1.6%
	^{121}Sn	0.2%		^{121}Sn	1.4%
	^{93m}Nb	0.1%		^{94}Nb	1.1%
			>0.1%	^{208}Bi	0.7%
				^{121m}Sn	0.6%
				^{205}Pb	0.5%
				^{93m}Nb	0.2%
				^{108}Ag	0.2%
				^{63}Ni	0.1%

Table 6.39. Contribution of activation products of LiPb to the CDR [5].

50 years			100 years		
>10%	^{207}Bi	38.2%	>10%	^{108m}Ag	51.6%
	^{108m}Ag	35.3%		^{207}Bi	20.4%
>1%	^{60}Co	8.9%		^{208}Bi	14.0%
	^{208}Bi	8.8%		^{94}Nb	13.7%
	^{94}Nb	8.6%	>0.1%	^{26}Al	0.2%
>0.1%	^{26}Al	0.1%			

Table 6.40. Contribution of activation products of LiPb to the activity [5].

50 years			100 years		
>10%	^{3}H	100%	>10%	^{3}H	99.6%

5.3. Impurities assessment: maximum concentrations allowed for LLW classification and El Cabril near surface disposal

Table 6.41 details the pathways for the production of some critical radionuclides broken down into responses, specifying the main impurity parent which content must be reduced to fulfillthe limits, as explained in the following discussion.

Table 6.41. Relevant cross section pathways and contributions for radioactive waste [5].

Material	Response function	Pathway and contribution (%)
W	CDR	^{59}Co(n,g)^{60}Co (96.0)
		^{60}Ni(n,p)^{60}Co (1.6)
	Activity	^{39}K(n,p)^{39}Ar (96.3)
		^{93}Nb(n,g)^{94}Nb (93.7)
		^{92}Mo(n,np)^{91}Nb (76.0)
		^{92}Mo(n,g)^{93}Mo (64.1)
		^{94}Mo(n,2n)^{93}Mo (35.9)
Eurofer	CDR	^{59}Co(n,g)^{60}Co (96.9)
		^{60}Ni(n,p)^{60}Co (2.5)
	Activity	^{93}Nb(n,g)^{94}Nb (99.5)
LiPb	Activity	^{93}Nb(n,g)^{94}Nb (98.9)

Table 6.42. Specific activity for certain nuclides considered in the recommendations for storage unit in Level 2 of El Cabril [5].

Nuclide	Activity (Bq/g) @100y			
	W	**Eurofer**	**LiPb**	**El Cabril Level 2**
^{3}H	$1.87 \cdot 10^{3}$	$4.87 \cdot 10^{4}$	**$5.00 \cdot 10^{6}$**	*$< 1.0 \cdot 10^{6}$*
^{94}Nb	**$3.40 \cdot 10^{2}$**	**$1.36 \cdot 10^{3}$**	**$2.06 \cdot 10^{2}$**	*$< 1.2 \cdot 10^{2}$*

Values above the limits are highlighted in bold.

As it has been seen in the previous section, both W and Eurofer can not be classified as LLW until 100 years of cooling time. In order to achieve LLW since 50 years, a reduction of the produced ^{60}Co is required. Since ^{59}Co is the main precursor of ^{60}Co (Table 6.41), a reduction from the initial 10 ppm of Co content to 5.1 ppm should be implemented on the W composition and from 50 ppm to 6.8 ppm on the Eurofer composition. Moreover, if the Eurofer composition had less than 20 ppm of Co, the Eurofer from the FW would change from HLW to ILW in only 36 years.

Regarding the possible disposal of W waste in El Cabril facility, for being stored in Level 1 after 100 years, the ^{93}Mo specific activity should be diminished from $2.22 \cdot 10^{3}$ to its specific limit for the mentioned Level 1 ($3.7 \cdot 10^{2}$ Bq/g). This value can be achieved by reducing the Mo content from 100 to a maximum of 16.6 ppm. Most important, the total activity should be lowered almost to the half (from $7.96 \cdot 10^{4}$ to $3.7 \cdot 10^{4}$ limit,Table 6.31) implying that the activity coming from ^{39}Ar and ^{91}Nb (which sum about 60% of the total value) should be almost zeroed. This could be done by eliminating completely ^{39}K and ^{92}Mo which, according to the pathways analysis (Table 6.41), are the precursors of the two daughter nuclides. Since it is a very strict option the alternative of disposal in Level 2 is affordable only if the Nb content is set from 10 to 3.5 ppm, so the specific activity of ^{94}Nb is reduced from $3.4 \cdot 10^{2}$ Bq/g (contribution ~0.4%) to the limit required limit for this level ($1.2 \cdot 10^{2}$ Bq/g, Table 6.42).

With regard to the Eurofer, it seems very difficult to dispose the waste in the Level 1 of El Cabril (see Table 6.31). Nonetheless, after a 100-year cooling period it can be storage in Level 2 if a reduction of the Nb impurity content from the initial 50 ppm to 4.4 ppm is carried out and therefore, the specific activity on ^{94}Nb is lowered from $1.36 \cdot 10^{3}$ to the limit of $1.2 \cdot 10^{2}$ Bq/g for this radionuclide (see Table 6.42).

For the LiPb case, being difficult to reach the limit for storage in El Cabril Level 1, the option of Level 2 would be possible but only with a Nb reduction from 10 to 5.82 ppm in order to lower the ^{94}Nb specific activity from $2.06 \cdot 10^{2}$ to $1.2 \cdot 10^{2}$ Bq/g (see Table 6.42). Furthermore,

having taken into account in the responses all the T produced inside the breeder, a minimum T extraction requirement can be given in view of a feasible disposal in Level 2. According to the specific activity of T (see Table 6.42), a factor 5 of reduction should be applied, meaning that at least 80% of T extraction should be achieved by the T extraction system (TES).

5.3.1. Total amount of waste management

The total amount of waste produced by the activation of the W, Eurofer and LiPb materials inside the DEMO DCLL reactor is calculated applying conservatively the results to the rest of zones inside the modules, and to the rest of modules inside the reactor (Table 6.43). Thus, with the previous assumptions on impurities, 39 tons of W, 3513 tons of Eurofer, and 7242 tons of LiPb could be disposed (at least) in El Cabril LILW Level 2. Nevertheless, a dedicated assessment for the manifold could lead to lower waste level (Level 1).

Table 6.43. Volume and mass of W, Eurofer, and LiPb in the reactor.

Component	W (m^3)	Eurofer (m^3)	LiPb (m^3)
FW	2.02	16.65	
BP + Caps		61.73	
BB		136.86	559.71
BSS		231.09	199.87
total (m^3)	2.02	446.33	759.58
mass (tons)	38.97	3512.66	7241.65
% of the reactor weight (41600 tons)	0.093%	8.4%	17.4%

5.3.2. Industrial and manufacturing viability in the reduction of impurities

One of the main challenges is to determine if the suggested reduction of impurities for the materials is viable from the manufacturing and industrial point of view. There is no much information about this issue but, considering some inputs received from the WPMAT group, interesting information regarding new possibilities of treatment on Eurofer[26] (on how to reduce the amount of radiologically undesirable impurities) is found. The information was based on EFDA contracts 05/1244 and 06/1910 [33]. Unfortunately, results are not referred here too much in detail because of the confidentiality agreement with industry. This study showed that 4.7 ppm of Nb were achieved for Eurofer (specifically, Eurofer-97-3) but, however, the price

[26] Not for W and LiPb.

could be increased by a factor 2-4. As a conclusion, Eurofer from the DCLL is very near from being considered as LILW to be disposed in Level 2 of El Cabril (4.4 ppm vs. 4.7 ppm).

5.3.3. Preliminary assessment on cross section quality

With regard to the reliability of the results, a preliminary assessment about the quality of the cross section reactions leading to the critical radionuclides coming from impurities was also performed. For this purpose, the procedure for validating and testing the successive EAF versions described in [34] was followed, as previously applied Chapter 4 for ITER reactor.

As a result, Table 6.44 collects, besides the pathways, the QS for the total cross section and the split ones, for EAF-2007 and EAF-2010 cross section activation libraries, taken from [34] - [36]. One can see that there are not differences, in terms of QS, between the QS given in the EAF-2007 and that corresponding to EAF-2010.

Table 6.44. QS of relevant cross section pathways for radioactive waste.

Material	Response function	Pathway and contribution (%)	Nuclide	Half-life	QS		
					EAF-2007	Total cross section	EAF-2010
Eurofer	CDR	^{59}Co(n,g) (96.9)	^{60g}Co	1925.3 d	0	(6)	0
			^{60m}Co	10.5 min	5		5
		^{60}Ni(n,p) (2.5)	^{60g}Co	1925.3 d	4	(6)	4
			^{60m}Co	10.5 min	6		6
	Activity	^{93}Nb(n,g) (99.5)	^{94g}Nb	$2.1\cdot10^{4}$ y	4	-	4
			^{94m}Nb	6.3 min	6		6
W	CDR	^{59}Co(n,g) (96.0)	^{60g}Co	1925.3 d	0	(6)	0
			^{60m}Co	10.5 min	5		5
		^{60}Ni(n,p) (1.6)	^{60g}Co	1925.3 d	4	(6)	4
			^{60m}Co	10.5 min	6		6
	Activity	^{39}K(n,p) (96.3)	^{39}Ar	269 y	2	-	2
		^{93}Nb(n,g) (93.7)	^{94g}Nb	$2.1\cdot10^{4}$ y	4	-	4
			^{94m}Nb	6.3 min	6		6
		Mo92(n,np) (76.1)	^{91g}Nb	$6.8\cdot10^{2}$ y	1	-	1
			^{91m}Nb	60.9 d	6		6
		Mo92(n,g) (64.1)	^{93g}Mo	$4.0\cdot10^{3}$ y	1	-	0
			^{93m}Mo	6.9 h	3		3
		Mo94(n,2n) (35.9)	^{93g}Mo	$4.0\cdot10^{3}$ y	2	-	2
			^{93m}Mo	6.9 h	4		4
LiPb	Activity	Nb93(n,g) (98.9)	^{94g}Nb	2.1E+4 y	4	-	4
			^{94m}Nb	6.3 min	6		6

Considering that all the metastable isotopes decay by isomeric transition to the ground state (99.6% at least), and that the half-lives of the metastable states are negligible compared to the cooling times of interest (i.e. times higher than 50 years), it is only needed to take into account the total cross section.

As shown, only two total cross section reactions are validated: $^{59}Co(n,g)^{60}Co$ and $^{60}Ni(n,p)^{60}Co$. For the remaining, no QS is provided for the total reaction, but a comparison between the EAF-2007 and differential experimental data from EXFOR [38] shows that in most of the cases there are enough differential experiments, and they agree with the EAF-2007 data. This is especially important for the $^{93}Nb(n,g)^{94}Nb$ cross section which, as has been said, is the reaction that gives rise to the isotope that compromises the wastes disposal in El Cabril, Level 2: ^{94}Nb. The only case in which limited differential experiments (with weak agreement) were found is for the $^{39}K(n,g)^{39}Ar$ cross section. For ensuring validation, additional differential experiments for the last cross section reaction, and integral experiments for the un-validated cross section would be useful.

6. Summary and conclusions

This chapter deals with the characterization of the DCLL breeder blanket for safety and environment purposes, on the basis of using the 3D neutronic model developed for the DEMO DCLL reactor.

For this objective, DEMO DCLL models corresponding to 2014 and 2015 were used. Differences between both models are found in terms of fusion power (1572 MW and 2037 MW for the 2014 and 2015 models, respectively), plasma major and minus radius and elongation. Furthermore, in the 2014 model the torus was divided into 16 sectors of 22.5º, each having 3 outboard and 2 inboard blanket segments, and 15 blanket modules; whereas in the 2015 model configuration the torus was divided into 18 sectors of 20º, each having 3 outboard and 2 inboard blanket segments, and 16 blanket modules.

Using each of these models, the decay heat and activity from the blanket for the entire reactor, as well as for the individual blanket modules arranged around the plasma chamber, were calculated at a large number of cooling times after the reactor shutdown. In addition, activation calculations were also performed for the entire manifold. Thus, these results can be helpful for further safety and waste management assessments since the calculated magnitudes are a necessary input for the mentioned assessments.

It is worth mentioning that these calculations were obtained without considering the LiPb flow and that T coming from the activation of the LiPb (regardless of which component is

located in) was removed from the obtained results, since it will be extracted throughout the blankets life time. Hence, in the following summaries, as well as in the rest of the chapter, this contribution is avoided.

6.1. Summary for the blanket results

Results shown that the decay heat from the blanket modules for the entire reactor (excluding T from the activated LiPb) falls, as the decay time increases. More specifically, for the 2014 model values are the following: 22.5 – 11.7 MW up to 1 hour; just below 1 MW at 2 months, about 0.3 MW at 1 year; 4.5 W at 100 years and, finally, around 3 W after 1000 years of cooling time. For the 2015 model, there is not much difference, being 47.9 – 14.7 MW up to 1 hour; around 1 MW at 2 months and around 0.3 MW up to ~ 1 year; 7 W at 100 years and, finally, 4.6 W after 1000 years of cooling time.

With regard to activity values, for the 2014 model, total activity is between $1.3 \cdot 10^{14}$ and $1.1 \cdot 10^{12}$ MBq up to 10 years; $1.6 \cdot 10^{8}$ MBq at 100 years and then it drops to $\sim 10^{7}$ for longer cooling times. Results for the 2015 model are: $2.4 \cdot 10^{14}$ and $1.7 \cdot 10^{13}$ MBq up to 1 year; $5.1 \cdot 10^{8}$ MBq at 50 years and then it drops until 10^{7} at 1000 years.

The equatorial outboard blanket module is the one with the highest total values both in activity and decay heat in the two analyzed models. In this equatorial outboard module, precisely, is focused the following analyses. On the one hand, the contribution of the activation of each of its components to the decay heat and activity was assessed. On the other hand, major radionuclides contributing to the decay heat in each of the components were identified. For this analysis in the equatorial outboard module, materials of the breeder module (i.e. Eurofer, LiPb and He in the 2014 model and Eurofer, LiPb, Al_2O_3 and He in the 2015 one) were taken into account separately.

With regard to the contribution of the different components to the decay heat, LiPb is the main contributor both at shutdown and after a 100-year cooling period. In the remaining times Eurofer from the breeder module shows the highest values of decay heat while the Al_2O_3 (in the 2015 model) and BP (in the 2014 model) are those with the lowest contribution.

In the case of activity, LiPb is the main contributor both at shutdown and from 50-100 years of cooling time. At the remaining times, Eurofer from the breeder module (as well as from the FW in the case of results coming from the activation of the 2015 model) is the component with the highest values. Finally, as happened with the decay heat, (Al_2O_3 in the 2015 model) and BP (in the 2014 model) are the components with the lowest contribution, although with the 2014 model W armour is also the one contributing less at times ranging from 1-100 years.

Regarding major radionuclides contributing to the decay heat, it is importante to remark that compositions for the different components vary from one model to the other. Nonetheless, a brief summary is given in the following lines.

- For the W armour (in both models) ^{187}W, ^{185}W, ^{60}Co, ^{39}Ar and ^{94}Nb are the main contributors in at least one of the considered cooling times.
- For the FW, ^{56}Mn, ^{54}Mn, ^{60}Co and ^{94}Nb are dominant (in both models, although for the 2015 ^{55}Fe also appears). For the LiPb breeder (in both models) ^{207}Pb, ^{203}Pb, ^{210}Po, ^{204}Tl and ^{94}Nb are the major radionuclides.
- In the case of the Eurofer in the breeder module (in both models) ^{56}Mn, ^{187}W, ^{182}Ta, ^{60}Co and ^{94}Nb appear as relevant. Calculations performed with the 2015 model reveals that these are also the major radionuclides for decay heat in the top and bottom walls, as well as the lateral walls and the BP. However, in the 2014 model, dominant radionuclides contributing most to the caps and the BP are ^{56}Mn, ^{187}W, ^{182}Ta, ^{54}Mn, ^{60}Co and ^{94}Nb.
- Finally, for the Al_2O_3 from the FCI in the 2015 model, ^{28}Al, ^{24}Na, ^{3}H and ^{26}Al are the main contributors to the total decay heat.

It is worth underlining that the differences in the evolution of Eurofer placed in different components are due to the different major radionuclides appearing, which is due to the effect of the neutron spectrum.

To sum up, all the obtained results are similar between 2014 and 2015 models, being the differences due to the changes in both the generic DEMO design and the DCLL DEMO model.

Beyond these results, additional calculations were carried out based on the 2015 model but not on the 2014 one. This includes the nuclear heating calculation in the whole blanket, which reaches $1.6 \cdot 10^3$ MW, with a major contribution due to photons and being the breeder module the component contributing most, and the BP the lowest.

Furthermore, a radial assessment for the decay heat and nuclear heating was carried out based on the 2015 model. For the decay heat, it was found that calculations using a volume averaged flux lead to similar results than if performing several activation calculations with several radial fluxes. However, as would be expected, the decay heat spatial distribution will differ. Worth mentioning, this spatial distribution is different depending on the studied component. Therefore, given the current design stage for DEMO, it seems that the volume averaged fux approach is good enough, considering that the aim is to characterize the model, in

total terms. Decisions about which components worth the calculation considering radial fluxes, may be taken later when the design is in a more advanced state.

6.2. Summary for the manifold results

In regard to the manifold, for the 2014 model, the total decay heat is between $5.9 \cdot 10^{2}$ and $1.2 \cdot 10^{2}$ kW up to 1 day; about 10 kW at 1 year and finally, it drops to $2.8 \cdot 10^{-4}$ kW at 1000 years. For the 2015 model, the total decay heat is between $1.2 \cdot 10^{3}$ and $1.3 \cdot 10^{2}$ kW up to 2 months; just over 1 kW up to 10 years and finally, it drops to $4.8 \cdot 10^{-4}$ kW at 1000 years. On the other hand, the dominant radionuclides identified for the decay heat of this component are almost the same in both models, namely: ^{56}Mn, ^{182}Ta, ^{60}Co, ^{94}Nb and, for the 2015 model, ^{187}W, too.

For what concerns to the activity, results based on 2014 model are $2.8 \cdot 10^{12}$-$1.2 \cdot 10^{12}$ MBq up to 1 day; around $2.7 \cdot 10^{11}$ MBq at 1 year and then it drops to $3.8 \cdot 10^{6}$ MBq at 1000 years of cooling. Whereas for the 2015 model, total activity value is $6.3 \cdot 10^{12}$-$1.4 \cdot 10^{12}$ MBq up to 2 months; around $4.5 \cdot 10^{10}$ MBq at 10 years and then it drops to $7.3 \cdot 10^{6}$ MBq at 1000 years of cooling.

Based on the 2015 model, nuclear heating was calculated too, being the results for this component $9.1 \cdot 10^{4}$ kW.

As happened with the blanket, the calculated results are similar between 2014 and 2015 models, being the obtained differences due to the changes in both the generic DEMO design and the DCLL DEMO model.

6.3. Comparison among BB concepts

When comparing the DCLL results, based on the 2015 analysis (i.e. 2014 models), to those corresponding to the other three blanket concepts, it was found that the HCLL and DCLL concepts have similar high energy spectra in both the FW and breeder material. However the HCLL blanket has significantly lower low energy tails to the spectra for both the FW and breeder material.

With regard to the decay heat, the HCLL blanket modules provided the lowest total values for times below 10^{5} s (around 17-22% lower than the other three concepts) while, at longer times, HCPB did. The DCLL, whereas, has the highest decay heat up to decay times of $\sim 10^{8}$ s and the WCLL has the highest for cooling times higher than 10^{8} s.

This means that for HCLL and for the HCPB, the requirements for decay heat dissipation will be lower than for the other concepts. The implications that these differences would have in the decay heat shall be studied, to ascertain how important they are.

Finally, for most decay times, and all blanket concepts, the W armour has the highest decay heat density although the breeder material contributes the majority of the decay heat due to its large mass.

6.4. Radioactive waste assessment

Calculation and assessment of the waste production was performed. In addition, mitigation actions of the radiological impact of the waste coming from the structural and functional materials were identified, on the basis of 2014 DEMO DCLL model. According to the results, a reduction on Nb content from 10 to 3.53 ppm, from 50 to 4.4 ppm, and from 10 to 5.82 ppm is required respectively for the W, Eurofer, and LiPb impurity compositions in order to dispose respectively 3513, 7242 and 39 tons of such materials as LLW in El Cabril Level 2 after 100 years since shutdown. Ongoing work will determine if such impurity control is viable from the industrial and manufacturing point of view. To date, preliminary information has supported this possibility, although the industrial costs would be increased.

Last but not least, it is important to keep in mind that the quality of the cross section leading to the only critical radionuclide (^{94}Nb, via ^{93}Nb(n,g)) is not overall validated. In fact, the reaction leading to the metastable state is both differential and integral validated, but the one leading to the ground state is only validated against differential data, but not integral. In this sense, depending on the status of the total cross section for this reaction (which is the one to be focused on from the point of view of the radioactive waste), there might be differences from the calculated results.

7. References

[1] EFDA. *Fusion electricity. A roadmap to the realisation of fusion energy*. EUROFusion IDM location: https://idm.euro-fusion.org/?uid=2M8JBG (**2012**).

[2] D. Rapisarda, I. Fernandez, I. Palermo, M. Gonzalez, C. Moreno, A. Ibarra, E. Mas de les Valls. *Conceptual Design of the EU-DEMO Dual Coolant Lithium Lead Equatorial Module*. IEEE transactions on plasma science, Vol. 44, nº 9, pp. 1603 – 1612 (**2016**).

[3] J. Sanz, R. García, M. García, F. Ogando. *Decay heat and activity calculations for the DCLL DEMO neutronic model.* SAE-2.17.1-T01-D04. EUROFusion IDM location: https://idm.euro-fusion.org//?uid=2CZ6L5 (**2015**).

[4] T. Eade, M. Garcia, R. Garcia, F. Ogando, P. Pereslavtsev, J. Sanz, G. Stankunas, A. Travleev. *Activation and decay heat analysis of the European DEMO blanket concepts*. Fusion Engineering and Design (**submitted**).

[5] I. Palermo, R. García, M. García, J. Sanz. Radiological impact mitigation of waste coming from the European Fusion Reactor DCLL DEMO. Fusion Engineering and Design (**submitted**).

[6] P. Pereslavstev, P. Lu, U. Fischer, R. García, J.P Catalán, F. Ogando, J. Sanz, G. Stankunas. *WP13-SYS02-T08 Activation and radiation dose map calculations*. EUROFusion IDM location: https://idm.euro-fusion.org/?uid=2MDAS5 (**2014**).

[7] G. Stankunas, A. Tidikas, P. Pereslavstev, J. Catalán, R. García, F. Ogando, U. Fischer. *Activity inventories and decay heat calculations for a DEMO withHCPB and HCLL blanket modules*. Fusion Engineering and Design, Vol. 109 – 111, Part A, pp. 347 – 352 (**2016**). Doi: http://dx.doi.org/10.1016/j.fusengdes.2016.02.101

[8] R. García, J.P. Catalán. J. Sanz. *Assessment of radioactive wastes from a DCLL fusion reactor: Disposal in El Cabril facility*. Fusion Engineering and Design, Vol. 89, nº 9 – 10, pp. 2038-2042 (**2014**). Doi: http://dx.doi.org/10.1016/j.fusengdes.2014.04.024

[9] J.C. Jaboulay, F. Damian, G. Aiello, D. Taylor, S. Zheng, B. Bienkowska, K. Drozdowicz, G. Tracz, U. Fischer, C.Bachmann. Monte Carlo tools evaluation for nuclear analyses of the European DEMO. Fusion Engineering and Design, Vols. 98 – 99, p. 1800 – 1803 (**2015**). Doi: http://dx.doi.org/10.1016/j.fusengdes.2015.06.083

[10] C. Bachmann. *DEMO Generic MCNP model 11.25° degree*. EUROFusion IDM location: https://idm.euro-fusion.org//?uid=2MK5CV (**2013**).

[11] R. Kemp. *DEMO1_July_12*. EUROFusion IDM location: https://idm.euro-fusion.org//?uid=2LBVXZ (**2012**).

[12] L.V. Boccaccini, G. Aiello, C. Bachmann, T. Barrett, A. Del Nevo, D. Demange, L. Forest, F. Hernandez, P. Norajitra, G. Porempovic, D. Rapisarda, P. Sardain, M. Utili, L. Vala. *Objectives and status of EUROfusion DEMO blanket studies*. Fusion Engineering and Design, Vols. 109 – 111, Part B, pp. 1199 – 1206 (**2016**). Doi: http://dx.doi.org/10.1016/j.fusengdes.2015.12.054

[13] I. Palermo, D. Rapisarda, I. Fernández. *DEMO2014_DCLL_MCNP_model* 2KZTEM. EUROFusion IDM location: https://idm.euro-fusion.org/?uid=2AQ6EF (**2014**).

[14] U. Fischer. *Guidelines for Neutronic Analyses*. EUROFusion IDM location: https://idm.euro-fusion.org/?uid=2L8TR9 (**2016**).

[15] Plansee SE. *Tungsten. Material properties and applications*. Available: www.plansee.com, Reutte, Austria (**2007)**.

[16] Final Report on the EFDA Article 7 contract EFDA/06-1903 on *"Procurement of reduced activation ferritic-martensitic steel type 9CrWTaV (EUROFER) for the TBM fabrication technology trials and mock-ups"*, Saarschmiede GmbH (**2009)**.

[17] Technical specification for the EFDA Article 7 contract EFDA/05-998 on "*Procurement of the Pb-Li eutectic alloy for EBBTF facility and for dedicated neutronics experiment*" (**2009)**.

[18] X-5 Monte Carlo Team. *MCNP – A General Monte Carlo N-Particle Transport Code Version 5*. LA-CP-03-0245, Los Alamos National Laboratory (**2005**).

[19] J. Sanz, O. Cabellos, N. García-Herranz. *ACAB. Inventory code for nuclear applications. User's manual* (**2008**).

[20] P. Pereslavtsev. *2015 Generic DEMO Model for MCNP neutronic simulations*. EUROFusion IDM location: https://idm.euro-fusion.org/?uid=2AQ6EF (**2015**).

[21] I. Palermo, D. Rapisarda, I. Fernández. *DEMO2015_DCLL_MCNP_model*. EUROFusion IDM location: https://idm.euro-fusion.org/?uid=2AQ6EF (**2016**).

[22] R. Wenninger. *DEMO1 Reference Design - 2015 April ("EU DEMO1 2015") - PROCESS One Page Output*. EUROFusion IDM location: https://idm.euro-fusion.org/?uid=2LBJRY (**2015**).

[23] Meszaros Botond. *EU DEMO1 2015 Comparison to 2014*. EUROFusion IDM location: https://idm.euro-fusion.org//?uid=2LNLWE (**2015**).

[24] C. Soto, J.M. Martínez-Esnaola, C. García-Rosales. *Thermomechanical analysis of a Flow Channel Insert based on a SiC-sandwich material concept*. Nuclear Materials and Energy, Vol. 7, pp. 5 – 11 (**2016**). Doi: http://dx.doi.org/10.1016/j.nme.2016.04.005

[25] T. Eade. *Activation analysis and related studies on HCLL DEMO*. SAE-2.17-1-T01-D01. EUROFusion IDM location: https://idm.euro-fusion.org//?uid=2MXEGM (**2015**).

[26] P. Pereslavtsev, A. Travleev. *Decay heat and activity calculations for the HCPB DEMO neutronic model.* SAE-2.17.1-T01-D02. EUROFusion IDM location: https://idm.euro-fusion.org//?uid=2LMYAR (**2015**).

[27] G. Stankunas. *Decay heat and activity calculations for the WCLL DEMO neutronic model.* SAE-2.17.1-T01-D03. EUROFusion IDM location: https://idm.euro-fusion.org//?uid=2LDMUS (**2015**).

[28] IAEA. *Categorizing Operational Radioactive Wastes* (**2007**).

[29] P. Rocco, M. Zucchetti. *Recycling and clearance possibilities*. SEAFP-2/4.2/JRC/4 (**1998**).

[30] ICRP Recommendations, ICRP Publication 60, Annals of ICPR, Vol. 21, Nº 1-3 (**1990**).

[31] *Clearance Levels for Radionuclides in Solid Materials: Application of Exemption Principles*. Interim Report for Comment, IAEA TECDOC-855, Vienna (**1996**).

[32] Centro de Investigaciones Energéticas, Medioambientales y tecnológicas (Ciemat). *Curso sobre gestión de residuos radiactivos*. Series Ponencias. (**2009**).

[33] Private communication with Eberhard Diegele, EUROfusion PMU - Based on EFDA contracts 05/1244 and 06/1910.

[34] R.A. Forrest, J. Kopecky, M. Pillon, A. Klix, S.P. Simakov, J-Ch. Sublet, P. Bém, M. Honusek, E. Simeckova. *Validation of EASY-2007 using integral measurements*. (**2008**).

[35] R. Forrest. *The European Activation File: EAF-2007 neutron-induced cross section library* (**2007**).

[36] J-Ch. Sublet, L.W. Packer, J. kopecky, R.A. Forrest, A.J. Koning, D.A. Rochman. *The European Activation File: EAF-2010 neutron-induced cross section library* (**2010**).

[37] R. Garcia. M. Garcia, R. Pampin, J. Sanz. *Status of reliability in determining SDDR for manual maintenanceactivities in ITER: Quality assessment of relevant activation crosssections involved*. Fusion Engineering and Design, Vol. 112, pp. 177 – 191 (**2016**). Doi: http://dx.doi.org/10.1016/j.fusengdes.2016.08.016

[38] IAEA. *Experimental Nuclear Reaction Data, EXFOR* (**2016**).

Chapter 7
Summary and conclusions, future and ongoing work

The work presented in this thesis covers different aspects related to the development of MCF technology. This chapter presents a summary review about the most relevant achievements of the performed work as well as the acquired skills. The last part of the chapter is dedicated to introducing the future and ongoing work.

1. Summary and conclusions

This section includes a review about the different contributions and conclusions drawn for each of the three goals set out in this thesis, namely:

1. To check the status of the activation libraries for SDDR estimation in order to ascertain their trust (Section 1.1).
2. To evaluate the impact of four diagnostic systems on the radiation loads on both VV and TFCs (Section 1.2).
3. To characterize the DCLL model for further assessments on safety and/or waste management (Section 1.3).

1.1. Activation nuclear data for SDDR calculation in ITER

Large part of the present thesis has been dedicated to exploring the quality of available activation cross section data for accurate SDDR prediction in the ITER PC and PI areas, where different maintenance activities are foreseen and which feasibility requires that certain SDDR limits are met. In particular, the EAF (2007 and 2010) were checked as well as possible differences when compared to recent versions of TENDL (2013, 2014 and 2015). For this assessment, the considered materials were those being part of the components which activation will contribute significantly to the SDDR at both PC and PI areas, as well as some other concrete candidate materials for the bioshield.

Considering the current materials and fluxes in ITER, generally, the usually used libraries allow obtaining reliable SDDR values for maintenance purposes. This means that the safety

factors that should be taken into account may be minimum considering most of the cross sections involved in the SDDR calculation are validated (at least more than 90% of the cross sections involved in the CDR produced by each of the materials). However, it should be noted that the SDDR coming from the Cu activation is not overall trustworthy. Thus, validation work is recommended for those cross section involved in the SDDR coming from Cu.

Regarding the candidate materials studied, only the cross sections related to the barite concrete are found to be not validated. In this sense, if the barite concrete is finally used in ITER, validation work is suggested too. In addition, as it will be commented in Section 2, if any other material which use is not currently decided for ITER is finally considered, the reliability of the SDDR obtained from the activation of that material shall be also studied.

For the advancement of this work, it has been necessary to become familiar with the nuclear activation data libraries that are usually used for fusion applications. Furthermore, this work required a thorough study of the way in which these nuclear activation data are validated. This knowledge, acquired from this specific application (calculation of SDDR for ITER maintenance), can be extrapolated to any other fusion application and is much valuable, taking into account the influence of the nuclear data on any result.

1.2. Radiation loads on the ITER TFCs and VV

Another part of the work has been devoted to evaluate the impact of four in-vessel diagnostic systems on the radiation loads on the TFCs and the VV. The analyzed diagnostic systems were: reflectometry, NAS, FWS and bolometers. Regarding the six evaluated magnitudes, these were namely: nuclear heating on the VV surface, integral TFC nuclear heating, volumetric heating of the TFC casing, dose in TFC ground insulator and neutron fluence in TFC ground insulator.

Hence, two answers are sought: on the one hand, to know how these radiation loads change as a consequence of the inclusion of these diagnostic systems (compared to a case without diagnostics, called baseline) and, on the other hand, to assess if the limits for these radiation loads are met.

Results revealed that the NAS, FWS and bolometers systems present a negligible impact on all the radiation loads when compared to the baseline case. However, for the reflectometry system a maximum difference of 35% on the radiation loads on the TFC (segment #12 of the TFC inboard straight leg) is found comparing to the baseline case, corresponding with the region where the double antenna is located.

Regarding the compliance of the radiation load target limits, only two limits are exceeded for the four diagnostic systems cases, namely the nuclear heating on the TFC and the integral nuclear on the outboard VV surface. The contribution of the analyzed in-vessel systems to the integral nuclear heating on the TFC is around 2% of the target limit (which means about 2800 W more than the baseline case). For what concers to the nuclear heating on the outboard VV surface, as mentioned, all the studied systems have very low impact, obtaining almost the same values than the baseline case. The remaining calculated radiation loads for all the diagnostic cases are under the imposed limits. The excess on nuclear heating already appeared in the baseline case due to the current configuration of the blankets system of ITER, which is currently being modified.

Given the low contribution that the studied diagnostic systems have, this work has enabled ruled out that the diagnostics are an important cause in the fact that the radiation loads values on the TFCs and VV are close to (or even above) the required limits.

While working out in this issue, it was necessary to face the geometry process, one of the most critical stages for the nuclear analyst. Since this work started from the 3D engineering CAD models provided by the Diagnostics Division of ITER, the geometry process (described in Chapter 3, Section 2.1) was carried out completely, until obtaining fully C-lite integrated models. Thus, the geometry process was a key step in solving this problem as the ITER geometry models are among the most complex so far.

1.3. DEMO DCLL characterization for safety and environment purposes

On the way to moving towards a DEMO reactor, the last part of this thesis has been developed within the framework of the Eurofusion Consortium. This last part has been devoted to characterize the DCLL blanket concept in order to provide the essential input for further safety and/or radiological waste management assessments. In particular, decay heat and nuclide inventory were obtained using both 2014 and 2015 neutronic models. Additionally, nuclear heating was also determined for the 2015 model.

As a conclusion, all the calculated results are similar between 2014 and 2015 models, being the obtained differences due to the changes in both the generic DEMO design and the DEMO DCLL model. To give a figure of this characterization, the blanket decay heat at the shutdown is around 2% of the fusion power (~ 2 GW) while after 5 minutes it decreases to 0.9%.

In addition, decay heat and nuclear heating radial assessments were performed based on the 2015 model. It was found that, calculations for the total decay heat using an average flux for all the volume will lead to similar results than if performing several activation calculations

with several radial fluxes. However, as expected, the decay heat spatial distribution will differ. Worth mentioning, this spatial distribution is different depending on the studied component.

Given the design phase in which DEMO is, it seems that the average approach is good enough, taking into account that the aim is to characterize the model, in total terms. Decisions about which components worth the calculation considering radial fluxes, may be taken later when the design is in a more advanced state.

Aside from the use of a volume averaged neutron flux (which, as has been said, may affect the results when spatial distribution is relevant), these calculations are obtained without considering the LiPb flow, that is not a very realistic assumption. As it will be commented in Section 2, considering the effect of this movement is an open question.

For obtaining all these results, the use of the coupling scripts between transport and activation calculation has been essential, since they allow carrying out a large number of simulations at once. These scripts are especially useful when analyzing large reactor systems, such as the DEMO DCLL blanket study of this thesis in which about 100 different cases were run.

On another note, when comparing among the different blanket concepts, based on the 2015 analysis (i.e. 2014 models), results are in the same order of magnitude, with slight differences, namely: HCLL blanket modules gave the lowest values of decay heat for short and intermediate cooling times and HCPB does at long times, whereas the DCLL and WCLL have the highest decay heat at intermediate and long times, respectively. This implies that for the HCLL (at short times), and for the HCPB (at longer times), the requirements for decay heat dissipation will be lower than for the other two concepts. It would be necessary to evaluate the consequences that these differences in the decay heat would have, in order to determine how important they are.

Finally, considering that one of the presuppositions of fusion energy is that only low and medium radioactive waste are generated, a preliminary assessment of the radioactive waste coming from the 2014 DCLL model was carried out with reference to the IAEA/SEAFP-2 standards and to the specific regulations of El Cabril near-surface facility. In addition, considering the important role that impurities play in the activation of the different materials, the possible need of impurities mitigation, in wastes, was also assessed.

According to the results, it would only be necessary to reduce one impurity (Nb) content for the three considered materials (W, Eurofer, and LiPb), in order to dispose these wastes as LLW in Level 2 of El Cabril, after 100 years since shutdown. Specifically, a reduction, from 10 to

3.5 ppm, from 50 to 4.4 ppm and from 10 to 5.8 ppm is required for W, Eurofer, and LiPb respectively.

Ongoing work will determine if such impurity control is viable from the industrial and manufacturing point of view, although preliminary information have confirmed such possibility, but at high industrial costs. In addition, one should not lose sight of the fact that the reliability of these results depends on the quality of the total cross section leading to the critical radionuclide (^{94}Nb via ^{93}Nb(n,g)).

2. Future and ongoing work

In order to conclude the chapter, and thus the thesis, some comments about future and ongoing work related with this thesis are presented in this section.

Regarding the activation nuclear data, a continuation of the performed work might be needed focused on other possible equipment and coating materials in ITER leading to a significant SDDR, when more information about location, geometry or composition is available. Beyond ITER, this kind of analysis might be extended to other facilities. In this sense, preliminary work within the IFMIF (International Fusion Materials Irradiation Facility) device is an ongoing task, recently started some months ago. In addition, possible studies in the DEMO framework might be part of the future work.

With regard to the activation characterization of the DCLL, future work should be focused on searching ways for taking into account the flow of LiPb around the system for decay heat and nuclide inventory calculations. In this way, setting the influence that considering this LiPb static would have on the results, a better characterization of the DCLL model can be obtained. In fact, the assessment of the impact that the LiPb has on the activation calculations is a common need with other DEMO concepts.

For this analysis some information is needed. Specifically, the time that the LiPb is inside the blanket and the time outside or, in its absence, some other data that allow deducing these times (for example, pipe length and LiPb speed). To date, these data are not exactly known, given the degree of development in which the model is. However, some estimation has been done about the time within the blanket (close to 4 minutes), the number of daily cycles (~290) or the speed with which it circulates (~10 cm/s). Therefore, a sensitivity analysis could be carried out to evaluate the effect of the time inside or outside the blanket (more or less short), on activation response functions.

Reference summary

M. **Abdou**, N. B. Morley, S. Smolentsev, A. Ying, S. Malang, A. Rowcliffe, M. Ulrickson. *Blanket/first wall challenges and required R&D on the pathway to DEMO*. Fusion Engineering and Design, Vol. 100, pp. 2 – 43 (**2015**). Doi: http://dx.doi.org/10.1016/j.fusengdes.2015.07.021

The **Attila** Software Suite. Productive enhancing solutions for radiation transport simulations (**2014**).

C. **Bachmann**. *DEMO Generic MCNP model 11.25°* degree. EUROFusion IDM location: https://idm.euro-fusion.org//?uid=2MK5CV (**2013**).

V. **Barabash**. *Role and contribution of ITER in research of materials and reactor*. Journal of Nuclear Materials, Vols. 2329 – 333, Part A, pp. 156 – 160 (**2004**). Doi: http://dx.doi.org/10.1016/j.jnucmat.2004.04.015

V. **Barabash**. *Chemical compositions of materials representing the components included into basic model for nuclear analysis of ITER* (**2015**).

P. **Batistoni**, U. Fischer, K. Ochiai, L. Petrizzi, K. Seidel, M. Youssef. *Neutronics and nuclear data issues in ITER and their validation*. Fusion Engineering and Design, Vol. 83, nº 7 – 9, pp. 834 – 841 (**2008**). Doi: http://dx.doi.org/10.1016/j.fusengdes.2008.04.009

L. **Bertalot**, R. Barnsley, M.F. Direz, J.M. Drevon, A. Encheva, S. Jakhar, Y. Kashchuk, K.M. Patel, A.P. Arumugam, V. Udintsev, C. Walker and M. Walsh. *Fusion neutron diagnostics on ITER tokamak*. Journal of Instrumentation, Vol. 7, nº 4 (**2012**). Doi: http://dx.doi.org/10.1088/1748-0221/7/04/C04012

Biblioteca digital del Instituto Latinoamericano de la Comunicación Educativa (ILCE). *Qué es la fusión nuclear*. Available:

http://bibliotecadigital.ilce.edu.mx/sites/ciencia/volumen2/ciencia3/106/htm/sec_4.htm
[Accessed: 20 July 2016].

L.V. **Boccaccini**. *EU blanket design and R&D for DEMO*. University of California, Los Angeles (UCLA): Second EU–US DCLL Workshop (**2014**).

L.V. **Boccaccini**, G. Aiello, C. Bachmann, T. Barrett, A. Del Nevo, D. Demange, L. Forest, F. Hernandez, P. Norajitra, G. Porempovic, D. Rapisarda, P. Sardain, M. Utili, L. Vala. *Objectives*

and status of EUROfusion DEMO blanket studies. Fusion Engineering and Design, Vols. 109 – 111, Part B, pp. 1199 – 1206 (**2016**). Doi: http://dx.doi.org/10.1016/j.fusengdes.2015.12.054

A.M. **Bradshaw**, T. Hamacher, U. Fischer. *Is nuclear fusion a sustainable energy form?* Fusion Engineering and Design, Vol. 86, pp. 2770 – 2773 (**2011**). Doi: http://dx.doi.org/10.1016/j.fusengdes.2010.11.040

J.H. **Brown**, W.R. Burnside, A.D. Davidson, J.R. Delong, W.C. Dunn, M.J. Hamilton, N. Mercado-Silva, J.C. Nekola, J.G. Okie, W.H. Woodruff, W. Zuo. *Energetic limits to economic growth*. BioScience, Vol. 61, nº 1, pp. 19 – 26 (**2011**). Doi: http://www.jstor.org/stable/10.1525/bio.2011.61.1.7

E. **Brun**, F. Damian, C.M. Diop, E. Dumonteil, F.X. Hugot, C. Jouanne, Y.K. Lee, F. Malvagi, A. Mazzolo, O. Petit, J.C. Trama, T. Visonneau, A. Zoia. *TRIPOLI-4®, CEA, EDF and AREVA reference Monte Carlo code*. Annals of Nuclear Energy, Vol. 82, pp. 151 – 160 (**2015**). Doi: http://dx.doi.org/10.1016/j.anucene.2014.07.053

J.P. **Catalán**, R. García, A. Suárez. *Impact of Neutron Activation System (NAS) diagnostic on the radiation loads of the Vacuum Vessel and Toroidal Field Coils.* ITER Neutronics Report. ITER IDM location: https://user.iter.org/?uid=QEKTWA (**2014**).

J.P. **Catalán**, R. García, A. Suárez. *Nuclear heating in the antenna of the reflectometry diagnostic*. ITER Neutronics Report. ITER IDM location: https://user.iter.org/?uid=Q5MJSQ (**2014**).

J.P. **Catalán**, R. García, A. Suárez. *Impact of blanket cutouts for bolometers on the radiation loads of the Vacuum Vessel and Toroidal Coils*. ITER Neutronics Report. ITER IDM location: https://user.iter.org/?uid=QEYKCW (**2015**).

J.P. **Catalán**, R. García, A. Suárez*. Impact of reflectometry diagnostic on the radiation loads of the Vacuum Vessel and Toroidal Field Coils*. ITER Neutronics Report. ITER IDM location: https://user.iter.org/?uid=QEJYFF (**2015**).

J.P. **Catalán**, R. García, A. Suárez. *Neutronics for the First Wall Diagnostics and impact on toroidal field coils (TFC) and vacuum vessel (VV) heating*. ITER Neutronics Report. ITER IDM location: https://user.iter.org/?uid=QN66Q7 (**2015**).

J.P. **Catalán**, A. Suárez, L. Bertalot, T. Giacomin, J. Sanz, V. Udintsev, M. Walsh. *Neutronics in support of the bioshield plug design of equatorial port 12 for ITER*. Fusion Engineering and Design, Vols. 96 – 97, pp. 231 – 235 (**2015**). Doi: http://dx.doi.org/10.1016/j.fusengdes.2015.06.015

J.P. **Catalán**, R. García, A. Suarez, L. Bertalot, J. Sanz, G. Vayakis, V. Krasilnikov, P. Shigin, R. Reichle, V. Udintsev, M. Walsh. *Impact of ITER in-vessel diagnostics on the radiation loads of the Vacuum Vessel and Toroidal Field Coils* (**under ITER review**).

CATIA. *Shape the world we live in.* Available: http://www.3ds.com/products-services/catia/ [Accessed 8 November 2016].

Centro de Investigaciones Energéticas, Medioambientales y tecnológicas (Ciemat). *Curso sobre gestión de residuos radiactivos*. Series Ponencias. (**2009**).

M.A. **Cooper**, E.W. Larsen. *Automated Weight Windows for Global Monte Carlo Particle Transport Calculations*. Nuclear Science and Engineer, nº 137 (**2001**). Doi: http://dx.doi.org/10.13182/NSE00-34

E.T. **Cheng**, R.A. Forrest, A.B. Pashchenko. *Report on the second international activation calculation benchmark comparison study*. International Nuclear Data Committee-INDC (NDS)-300, TSIR-21 (**1994**).

M.S. **Cheon**, S. Pak, C.R. Seon, H.G. Lee, L. Bertalot, R. Barnsley. *Evaluation of the neutron flux effect on the ITER VUV diagnostic system in the upper port*. Journal of the Korean Physical Society, Vol. 59, nº 3, pp. 2228 – 2232 (**2011**). Doi: http://dx.doi.org/10.1016/j.fusengdes.2016.02.009

M.S. **Cheon**, C.R. Seon, S. Pak, H.G. Lee, L. Bertalot, R.A. Forrest. *Operational Radioactivity Evaluation of ITER Diagnostic Neutron Activation System*. IEEE Transactions on Plasma Science, Vol. 38, nº 3, pp. 274 – 277 (**2010**). Doi: http://dx.doi.org/10.1109/TPS.2009.2036917

Clearance *Levels for Radionuclides in Solid Materials: Application of Exemption Principles*. Interim Report for Comment, IAEA TECDOC-855, Vienna (**1996**).

A.G. **Croff**. *A User's Manual for the ORIGEN2 computer code.* ONRL /TM-7175 (**1980**).

A. **Davis**, A. Turner. *Applications of novel global variance reduction methods to fusion radiation transport problems*. International Conference on Mathematics and Computational Methods Applied to Nuclear Science and Engineering (M&C), Rio de Janeiro. ISBN 978-85-63688-00-2 (**2011**).

A. **Davis**, S. Zheng, L.W. Parker, A. Turner. *Neutronics and activation analysis for the european TBS with improved nuclear shielding*. F4E-2008-OPE-02-01-04 deliverables 4 & 5 (**2012**).

T. **Eade**. *Activation analysis and related studies on HCLL DEMO*. SAE-2.17-1-T01-D01. EUROFusion IDM location: https://idm.euro-fusion.org//?uid=2MXEGM (**2015**).

T. **Eade**, M. Garcia, R. Garcia, F. Ogando, P. Pereslavtsev, J. Sanz, G. Stankunas, A. Travleev. *Activation and decay heat analysis of the European DEMO blanket concepts*. Fusion Engineering and Design (**submitted**).

EFDA. *Fusion electricity. A roadmap to the realisation of fusion energy*. EUROFusion IDM location: https://idm.euro-fusion.org/?uid=2M8JBG (**2012**).

A. **Encheva**, L. Bertalot, B. Macklin, G. Vayakis, C. Walker. *Integration of ITER in-vessel diagnostic components in the vacuum vessel.* Fusion Engineering and Design, Vol. 84, pp. 736 – 742 (**2009**). Doi: http://dx.doi.org/10.1016/j.fusengdes.2008.12.101

The **European** Fusion Education Network (Fusenet). *What is Plasma?.* Available: http://www.fusenet.eu/node/35 [Accessed: 14 July 2016].

FDS team. MCAM. Frequently Asked Questions. Available: http://fds.org.cn/english/mcam/mcam_faq.html#4 [Accessed 21 April 2016].

Final Report on the EFDA Article 7 contract EFDA/06-1903 on *"Procurement of reduced activation ferritic-martensitic steel type 9CrWTaV (EUROFER) for the TBM fabrication technology trials and mock-ups"*, Saarschmiede GmbH, (**2009)**.

U. **Fischer**. *Guidelines for Neutronic Analyses*. EUROFusion IDM location: https://idm.euro-fusion.org/?uid=2L8TR9 (**2016**).

U. **Fischer**, P. Batistoni, A. Klix, I. Kodeli, R.L. Perel. *Neutronics R&D Efforts in Support of the European Breeder Blanket Development Programme*. Nuclear Fusion, Vol. 49, nº 6 (**2009**). Doi: http://dx.doi.org/10.1088/0029-5515/49/6/065009

U. **Fischer**, P. Batistoni, R. Forrest, C. Konno, R.L. Perel, K. Seidel, S.P. Simakov. *Development needs of nuclear data for fusion technology*. International Conference on Nuclear Data for Science and Technology (**2007**). Doi: http://dx.doi.org/10.1051/ndata:07494

R. **Forrest**. *Data requirements for neutron activation. Part I: Cross sections*. Fusion Engineering and Design, Vol. 81, pp. 2143 – 2156 (**2006**). Doi: http://dx.doi.org/10.1016/j.fusengdes.2006.01.001

R.A. **Forrest**. *EAF-2007 decay data library*. UKAEA FUS 537 report (**2007**).

R. A. **Forrest**. *FISPACT 2007 user manual*. UKAEA FUS 534 report (**2007**).

R. **Forrest**. *The European Activation File: EAF-2007 neutron-induced cross section library* (**2007**).

R. **Forrest**. *Nuclear science and data needs for advanced nuclear systems*. Energy Procedia, Vol. 7, pp. 540 – 552 (**2011**). Doi: http://dx.doi.org/10.1016/j.egypro.2011.06.075

R.A. **Forrest**, J. Kopecky, J.-Ch. Sublet. *The European Activation File: EAF-2007 neutron-induced cross section libraries*. UKAEA FUS 535 report (**2007**).

R.A. **Forrest**, J. Kopecky, M. Pillon, K. Seidel. *Validation of EASY-2005 using integral measurements*. UKAEA FUS 526 report (**2006**).

R.A. **Forrest**, M. Pillon, U. Von Möllendorff, K. Seidel. *Validation of EASY-2001 using integral measurements*. UKAEA FUS 467 report (**2001**).

R.A. **Forrest**, A. Tabasso, C. Danani, S. Jakhar, A.K. Shaw. *Handbook of activation data calculated using EASY-2007*. UKAEA FUS 552 report (**2009**).

R.A. **Forrest**, M. Pillon, U. Von Möllendorff, K. Seidel, J. Kopecky, J-Ch. Sublet. *Validation of EASY-2003 using integral measurements*. UKAEA FUS 500 report (**2003**).

R.A. **Forrest**, J. Kopecky, M. Pillon, A. Klix, S.P. Simakov, J-Ch. Sublet, P. Bém, M. Honusek, E. Simeckova. *Validation of EASY-2007 using integral measurements*. UKAEA FUS 547 report (**2008**).

Fusion for Energy. *Understanding fusion. The merits of fusion*. Available: http://fusionforenergy.europa.eu/understandingfusion/merits.aspx [Accessed: 11 July 2016].

R. **García**, J.P. Catalán. J. Sanz. *Assessment of radioactive wastes from a DCLL fusion reactor: Disposal in El Cabril facility*. Fusion Engineering and Design, Vol. 89, nº 9 – 10, pp. 2038-2042 (**2014**). Doi: http://dx.doi.org/10.1016/j.fusengdes.2014.04.024

R. **García**. M. García, R. Pampin, J. Sanz. *Status of reliability in determining SDDR for manual maintenance activities in ITER: Quality assessment of relevant activation cross sections involved*. Fusion Engineering and Design, Vol. 112, pp. 177 – 191 (**2016**). Doi: http://dx.doi.org/10.1016/j.fusengdes.2016.08.016

R. **García**, M. García, F. Ogando, R. Pampin, J. Sanz. *Reliability of activation cross sections for estimation of shutdown dose rate in the ITER port cell and port interspace*. Proceeding of ND 2016 International Conference on Nuclear Data for Science and Technology. EPJ Web of Conferences (**submitted**).

L.M. **Giancarli**, V. Barabash, D.J. Campbell, S. Chiocchio, J.J. Cordier, A. Dammann, G. Dell'Orco, J. Elbez-Uzan, J.M. Fourneron, J.P. Friconneau, M. Gasparotto, M. Iseli, C.Y. Jung, B.Y. Kim, D. Lazarov, B. Levesy, M. Loughlin, M. Merola, J.C. Nevière, R. Pascal, W. Ring, I.

Schneiderova, S. Willms, A. Siarras, W. Shu, J.A. Snipes, J.G. van der Laan. *Progress and challenges of the ITER TBM Program from the IO perspective*. Fusion Engineering and Design, Vol. 109 – 111, pp. 1491 – 1497 (**2016**). Doi: http://dx.doi.org/10.1016/j.fusengdes.2015.11.046S.

S. **Glasstone**, R. Lovberg. *Controlled Thermonuclear Reactions. An Introduction to Theory and Experiment*. Huntington, New York: Robert E. Publishing Company (**1960**).

D. **Haikney**. *CPD - Install Diagnostics, Instrumentation and Fuelling Installation - Lower Port Extensions*. ITER IDM location: https://user.iter.org/?uid=Q3ZES6 (**2014**).

J. **How**, R. Reichle. *Plant Description (PD)*. ITER IDM location: https://user.iter.org/?uid=2X6K67 (**2009**).

IAEA. *Categorizing Operational Radioactive Wastes* (**2007**).

IAEA. *Experimental Nuclear Reaction Data, EXFOR* (**2016**).

ICRP Recommendations, ICRP Publication 60, Annals of ICPR, Vol. 21, Nº 1-3 (**1990**).

H. **Iida**. *Fast Neutron Flux and Nuclear Heat in the TF Coil Inboard Legs vs. Gap Width among Blanket Modules (NAR)*. Design Integration Unit Analysis Report. ITER IDM location: https://user.iter.org/?uid=226DRK (**2003**).

H. **Iida**. *The Contributions of the Vertical and Horizontal Gaps among the Blanket Modules to the Inboard TF Coil Leg Nuclear Heating (NAR)*. Design Integration Unit Analysis Report. ITER IDM location https://user.iter.org/?uid=22A4H8 (**2003**).

H. **Iida**. *The Nuclear Heat Local Peaking at the first Turn of the Winding Pack of Inboard TF Coil Legs due to Gaps among Blanket Modules (NAR)*. Design Integration Unit Analysis Report. ITER IDM location: https://user.iter.org/?uid=2267AX (**2003**).

H. **Iida**, V. Khripunov, L. Petrizzi, G. Federici. *Nuclear Analysis Report*. ITER IDM location https://user.iter.org/?uid=22F2ST (**2004**).

Institute of Energy and Climate Research. Plasma Physics IEK-4. *Plasma-Wall Interaction - A Key Issue in Progress Towards Fusion Power Plants*. Available: http://www.fz-juelich.de/iek/iek-4/EN/Research/01_Plasma-Wall_Interaction/artikel_2014.html?nn=1500486 [Accessed: 11 July 2016].

ITER Organization. *ITER. 60 years of progress*. Available: https://www.iter.org/sci/BeyondITER [Accessed: 8 August 2016].

ITER Organization. *ITER. Advantages of fusion*. Available: https://www.iter.org/sci/Fusion [Accessed: 14 July 2016].

ITER Organization. *ITER. Diagnostics*. Available: https://www.iter.org/mach/diagnostics [Accessed 5 October 2016].

ITER Organization. News and Media. *First Plasma: 2025*. Available: http://www.iter.org/mag/9/65 [Accessed: 17 November 2016].

ITER Organization. *ITER. What is ITER?*. Available: https://www.iter.org/proj/inafewlines [Accessed: 8 August 2016].

J.C. **Jaboulay**, F. Damian, G. Aiello, D. Taylor, S. Zheng, B. Bienkowska, K. Drozdowicz, G. Tracz, U. Fischer, C.Bachmann. Monte Carlo tools evaluation for nuclear analyses of the European DEMO. Fusion Engineering and Design, Vols. 98 – 99, p. 1800 – 1803 (**2015**). Doi: http://dx.doi.org/10.1016/j.fusengdes.2015.06.083

R. **Juárez**, L. Pérez, F. Ogando, J. P. Catalán, R. García, A.J. López. *HCLL/HCPB nuclear analysis - Second run of calculations* (**2014**).

R. **Juárez**, P. Sauvan, J.P. Catalán, L. Pérez, R. García, A.J. López. *Shielding proposal to reduce the neutron cross talk between EP and LP of ITER*. ITER IDM location: https://user.iter.org/?uid=QPYYNV (**2015**).

R. **Juárez**, P. Sauvan, L. Pérez, D. Panayotov, J. Vallory, M. Zmitko, Y. Poitevin, J. Sanz. *Shudown dose rate analysis of european test blanket modules shields in ITER equatorial port #16*. Fusion Engineering and Design, Vols. 109 – 111, Part B, pp. 1554 – 1558 (**2016**). Doi: http://dx.doi.org/10.1016/j.fusengdes.2015.11.023

S.T. **Keller**. *Modeling the Oregon State University TRIGA Reactor Using the Attila Three-Dimensional Deterministic Transport Code*. Thesis. Oregon State University (**2007**).

R. **Kemp**. *DEMO1_July_12*. EUROFusion IDM location: https://idm.euro-fusion.org//?uid=2LBVXZ (**2012**).

B.Y. **Kim**. *Final report on neutronic analysis of the ITER TBM PP (CDR)*. ITER IDM location: https://user.iter.org/?uid=JR5EZH (**2013**).

J. **Kopecky**. *Validation of TENDL-2009 using integral measurements* (**2010**).

A. **Kyrieleis**. *Development of MCNP Models of In-vessel Components in Blanket Rows 1-6 and the Divertor*. F4E_D_24XRLK v1.1 (**2016**).

D. **Leichtle**. *Quality of Nuclear Analysis (QNA)*. Nuclear Integration Unit (NIU) Progress Report. ITER IDM location https://user.iter.org/?uid=T8JRTQ (**2016**).

J. **Li**, S. Liu, P. Zhao, Y. Li, Y. Peng. *Activation analysis and comparison of bio-shield under ITER and ASP neutron irradiation*. Journal of Fusion Energy, Vol. 34, pp. 727 – 732 (**2015**). Doi: http://dx.doi.org/10.1007/s10894-015-9850-6

H. **Liu**. *Final report on the ITER automated transfer cask biological and absorbed dose rate analysis*. ITER IDM location: https://user.iter.org/?uid=N6DH9T (**2014**).

D. **López** Aldama, A. Trkov. *FENDL-2.1 Update of an evaluated nuclear data library for fusion applications*, INDC(NDS)-467 Distr. FE. IAEA.

M. **Loughlin**. *Guidelines for Nuclear Analyses*. ITER IDM location: https://user.iter.org/?uid=R7XRXB (**2015**).

M. **Loughlin**. *C-model Terms of Use.* ITER Memorandum/Note. ITER IDM location: https://user.iter.org/?uid=TR7YME (**2016**).

M. **Loughlin**, E. Polunovskiy. *ITER neutronic model: A-lite*. ITER IDM location: https://user.iter.org/?uid=2NEZZS (**2009**).

M.J. **Loughlin**, N.P. Taylor. *Recommendation on plasma scenarios*. ITER IDM location: https://user.iter.org/?uid=2V3V8G (**2009**).

M. **Loughlin**, E. Polunovskiy, K. Ioki, M. Merola, G. Sannazzaro, M. Sawan. *Nuclear Shielding for the Toroidal Field Coils of ITER*. Fusion Science and Technology, Vol. 60, nº 1, pp. 81 – 86 (**2011**).

M. **Loughlin**, M. Angelone, P. Batistoni, L. Bertalot, J. Eskhult, C. Konno, R. Pampin, A. Polevoi, E. Polunovskiy. *Status and verification strategy for ITER neutronics*. Fusion Engineering and design, Vol. 89, pp. 1865 – 1869 (**2014**). Doi: http://dx.doi.org/10.1016/j.fusengdes.2014.03.070

L. **Lu**, U. Fischer, P. Pereslavtsev. *Improved algorithms and advanced features of the CAD to MC conversion tool McCad*. Fusion Engineering and Design, Vol. 89, pp- 1885 – 1888 (**2014**). Doi: http://dx.doi.org/10.1016/j.fusengdes.2014.05.015

D. **Maisonnier**, I. Cook, P. Sardain, R. Andreani, L. Di Pace, R. Forrest, L. Giancarli, S. Hermsmeyer, P. Norajitra, N. Taylor, D. Ward. *A conceptual study of commercial fusion power plants. Final report of the European Fusion Power Plant Conceptual Study (PPCS)*, EFDA-RP-RE-5.0 (**2005**).

G. **Martínez**, A. Martina, C. Watts, E. Veshcheva, R. Reichlea, P. Shigina, F. Sabourinc, S. Gicquela, R. Mitteaua, J. González. *Diagnostic integration solutions in the ITER first wall*. Fusion Engineering and Design, Vols. 98 – 99, pp. 1548 – 1551 (**2015**). Doi: http://dx.doi.org/10.1016/j.fusengdes.2015.06.046

Meszaros Botond. *EU DEMO1 2015 Comparison to 2014*. EUROFusion IDM location: https://idm.euro-fusion.org//?uid=2LNLWE (**2015**).

X-5 **Monte** Carlo Team. *MCNP – A General Monte Carlo N-Particle Transport Code Version 5*, LA-CP-03-0245, Los Alamos National Laboratory (**2005**).

S.W. **Mosher**, et al. *ADVANTG, An Automated Variance Reduction Parameter Generator*. ORNL/TM 2013/416 Rev. 1. Oak Ridge National Laboratory (**2015**).

T. **Murphy**. *Do the math. Nuclear fusion* (**2012)**. Available: http://physics.ucsd.edu/do-the-math/2012/01/nuclear-fusion/ [Accessed: 12 July 2016].

H. **Nasif**, F. Msuda, H. Morota. H. Iida, S. Sato, C. Konno. *Development of CAD-MCNP interface program GEOMIT and its applicability for ITER neutronics design calculations*. Nuclear Technology, Vol. 180, nº 1, pp. 89 – 102 (**2012**).

Next *Big Future* (**2016**). Available: http://www.nextbigfuture.com/2016/05/compact-spherical-tokamak-would-be-100.html [Accessed: 11 December 2016].

Objectives. *About F4E*. Available: http://fusionforenergy.europa.eu/aboutfusion/ [Accessed: 28 November 2016].

I. Palermo, D. Rapisarda, I. Fernández. *DEMO2014_DCLL_MCNP_model* 2KZTEM. EUROFusion IDM location: https://idm.euro-fusion.org/?uid=2AQ6EF (**2014**).

I. **Palermo**, D. Rapisarda, I. Fernández. *DEMO2015_DCLL_MCNP_model* 2LNT7C. EUROFusion IDM location: https://idm.euro-fusion.org/?uid=2AQ6EF (**2016**).

I. **Palermo**, R. García, M. García, J. Sanz. Radiological impact mitigation of waste coming from the European Fusion Reactor DCLL DEMO. Fusion Engineering and Design (**submitted**).

R. **Pampin**. *Quality document. Note on F4E provisions for nuclear analysis management*. F4E_D_26NR86 v2.1 (**2015**).

R. **Pampin**, A. Davis, S. Lilley. *European ITER TBS neutronics, activation and shutdown dose preliminary mapping.* F4E-2008-OPE-02-01 v1.0 (**2010**).

R. **Pampin**, A. Davis, J. Izquierdo, D. Leichtle, M.J. Loughlin, J. Sanz, A. Turner, R. Villari, P.P.H. Wilson. *Developments and needs in nuclear analysis of fusion technology*. Fusion Engineering and design, Vol. 88, pp. 454 – 460 (**2013**). Doi: http://dx.doi.org/10.1016/j.fusengdes.2013.03.049

Paraview. Available: http://www.paraview.org/

P. **Pereslavtsev**. *2015 Generic DEMO Model for MCNP neutronic simulations*. EUROFusion IDM location: https://idm.euro-fusion.org/?uid=2AQ6EF (**2015**).

P. **Pereslavtsev**, A. Travleev. *Decay heat and activity calculations for the HCPB DEMO neutronic model.* SAE-2.17.1-T01-D02. EUROFusion IDM location: https://idm.euro-fusion.org//?uid=2LMYAR (**2015**).

P. **Pereslavstev**, P. Lu, U. Fischer, R. García, J.P Catalán, F. Ogando, J. Sanz, G. Stankunas. *WP13-SYS02-T08 Activation and radiation dose map calculations*. EUROFusion IDM location: https://idm.euro-fusion.org/?uid=2MDAS5 (**2014**).

L. **Pérez**. *Optimization of stochastic global variance reduction techniques for Monte Carlo neutron transport with applications to the ITER geometry*. Thesis dissertation. Universidad Nacional de Educación a Distancia (UNED) (**2016**).

PHITS. *Particle and Heavy Ion Transport code System*. http://phits.jaea.go.jp/index.html [Accessed 10 August 2016].

R.A. **Pitts**. *ITER status and challengues*. ITER IDM location: https://user.iter.org/?uid=S3W8V7 (**2015**).

Plansee SE. *Tungsten. Material properties and applications*. Available: www.plansee.com, Reutte, Austria (**2007)**.

E. **Polunovskiy**. *ITER neutronic model: C-lite v.1, R.131031*. ITER IDM location: https://user.iter.org/?uid=M2TKBE (**2013**).

E. **Polunovskiy**. *Nuclear responses in TFC*. ITER IDM location: https://user.iter.org/?uid=BP6B8V (**2015**).

E. **Polunovskiy**, A. Serikov, A. Suarez*. ITER neutronic model: B-lite v.3 R121217.* ITER IDM location: https://user.iter.org/?uid=9KKVQR (**2012**).

Private communication with Eberhard Diegele, EUROfusion PMU - Based on EFDA contracts 05/1244 and 06/1910.

D. **Rapisarda**, I. Fernandez, I. Palermo, M. Gonzalez, C. Moreno, A. Ibarra, E. Mas de les Valls. *Conceptual Design of the EU-DEMO Dual Coolant Lithium Lead Equatorial Module*. IEEE transactions on plasma science, Vol. 44, nº 9, pp. 1603 – 1612 (**2016**).

P. **Rocco**, M. Zucchetti. *Recycling and clearance possibilities*. SEAFP-2/4.2/JRC/4 (**1998**).

F. **Sánchez**. *EU contribution to the Diagnostics of ITER*. Danish Big Science Network Meeting 2014: Fusion for Energy (**2014**). Available: https://industryportal.f4e.europa.eu/IP_EXT_REFERENCE_DOCUMENTS/F4E%20-%20Diagnostics%20-%20Counsell%20IBF-13.pdf [Accessed: 10 December 2015].

A. **Santamarina**, D. Bernard, Y. Rugama. *The JEFF-3.1.1 Nuclear Data Library.* JEFF Report 22, ISBN 978-92-64-99074-6 (**2009**).

J. **Sanz**, O. Cabellos, N. García-Herranz. *ACAB Inventory code for nuclear applications. User's manual* (**2008**).

J. **Sanz**, R. García, M. García, F. Ogando. *Decay heat and activity calculations for the DCLL DEMO neutronic model.* SAE-2.17.1-T01-D04. EUROFusion IDM location: https://idm.euro-fusion.org//?uid=2CZ6L5 (**2015**).

A. **Serikov**, U. Fischer, D. Leichtle, C.S. Pitcher. *Monte Carlo radiation shielding and activation analyses for the Diagnostic Equatorial Port Plug in ITER*. Fusion Engineering and Design, Vol. 87, pp. 690 – 694 (**2012**). Doi: http://dx.doi.org/10.1016/j.fusengdes.2012.02.003

A. **Serikov**, L. Bertalot, U. Fischer, C.S. Pitcher, A. Suárez, V.S. Udintsev, B. Weinhorst. *Shut-down dose rate analysis for ITER diagnostic equatorial and upper ports*. Fusion Engineering and Design, Vol. 89, pp. 1964 – 1968 (**2014**). Doi: http://dx.doi.org/10.1016/j.fusengdes.2014.01.025

***Serpent**. A Continuous-energy Monte Carlo reactor physics burnup calculation code*. http://montecarlo.vtt.fi/index.htm [Accessed 10 August 2016].

Y. **Shengpeng**, C. Mengyun, S. Jing, L. Pengcheng, H. Liqin. *Convex-based void filling method for CAD-based Monte Carlo geometry modeling*. Annals of Nuclear Energy, Vol. 85, pp. 380 – 385 (**2015**). Doi: http://dx.doi.org/10.1016/j.anucene.2015.04.029

N. **Soppera**, M. Bossant, E. Dupont. JANIS 4: An Improved Version of the NEA Java-based Nuclear Data Information System. Nuclear Data Sheets, Vol. 120, pp. 294 – 296 (**2014**). Doi: http://dx.doi.org/10.1016/j.nds.2014.07.071

C. **Soto**, J.M. Martínez-Esnaola, C. García-Rosales. *Thermomechanical analysis of a Flow Channel Insert based on a SiC-sandwich material concept*. Nuclear Materials and Energy, Vol. 7, pp. 5 – 11 (**2016**). Doi: http://dx.doi.org/10.1016/j.nme.2016.04.005

SpaceClaim. Available: http://www.spaceclaim.com/ [Accessed 8 November 2016].

G. **Stankunas**. *Decay heat and activity calculations for the WCLL DEMO neutronic model.* SAE-2.17.1-T01-D03. EUROFusion IDM location: https://idm.euro-fusion.org//?uid=2LDMUS (**2015**).

G. **Stankunas**, A. Tidikas, P. Pereslavstev, J. Catalán, R. García, F. Ogando, U. Fischer. *Activity inventories and decay heat calculations for a DEMO withHCPB and HCLL blanket modules*. Fusion Engineering and Design, Vol. 109 – 111, Part A, pp. 347 – 352 (**2016**). Doi: http://dx.doi.org/10.1016/j.fusengdes.2016.02.101

A. **Suárez**. *Impact of blanket cutouts for bolometers in VV and TFC neutronics.* ITER IDM location: https://user.iter.org/?uid=LADD8Q (**2014**).

J-Ch. **Sublet**, M.R. Gilber. *Decay heat validation, FISPACT-II & TENDL-2012,-2011 and EAF-2010 nuclear data libraries* (**2013**).

J-Ch. **Sublet**, L.W. Packer, J. kopecky, R.A. Forrest, A.J. Koning, D.A. Rochman. *The European Activation File: EAF-2010 neutron-induced cross section library* (**2010**).

K. **Tahiliani**, R. Jha. *Chapter 7: Bolometers for Fusion Plasma Diagnostics*. India, Institute for Plasma Reserach (**2012**). Doi: http://dx.doi.org/10.5772/33466

N. **Taylor**. *Safety and Environment Project*. Project Management Plan (PMP). EUROFusion IDM location: https://idm.euro-fusion.org/?uid=2L9WGS (**2016**).

Technical specification for the EFDA Article 7 contract EFDA/05-998 on "*Procurement of the Pb-Li eutectic alloy for EBBTF facility and for dedicated neutronics experiment*" (**2009)**.

Technical *specification for the engineering support in the area of Test Blanket Module (TBM) systems design and technological demonstration* (**2011**).

TRIPOLI-4 Project Team. *TRIPOLI-4 version 8.1, 3D general purpose continuous energy Monte Carlo Transport code*. Available: http://www.oecd-nea.org/tools/abstract/detail/nea-1716/ [Accessed 8 August 2016].

V. **Udintsev**, M. Walsh. *ITER Diagnostics. First Wall Samples* (**2014**). Available: http://www.bigscience.dk/media/46778/iter_diagnostics_udintsev_v1_0.pdf [Accessed: 10 December 2015].

G. **Vayakis**, C.I. Walker, F. Clairet, R. Sabot, V. Tribaldos, T. Estrada, E. Blanco, J. Sánchez, G.G. Denisov, V.I. Belousov, F. Da Silva, P. Varela, M.E. Manso, L. Cupido, J. Dias, N. Valverde, V.A. Vershkov, D.A. Shelukhin, S.V. Solda. *Status and prospects for mm-wave reflectometry in ITER*. Nuclear Fusion, Vol. 46, nº 9, pp. 836 – 845 (**2006**). Doi: http://dx.doi.org/10.1088/0029-5515/46/9/S20

J.C. **Wagner**, A. Haghighat. *Automated variance reduction of Monte Carlo shielding calculations using the discrete ordinates adjoint function*. Nuclear Science and Engineering, nº 128, pp. 186 – 208 (**1998**).

J.C. **Wagner**, E.D. Blakeman, D.E. Peplow. *Forward-Weighted CADIS method for global variance reduction*. Transactions of the American Nuclear Society, nº 97, pp. 630 – 633 (**2007**).

J.C. **Wagner**, D.E. Peplow, S.W. Mosher, T.M. Evans. *Review of Hybrid (Deterministic/Monte Carlo) Radiation Transport Methods, Codes, and Applications at Oak Ridge National Laboratory*. Progress in Nuclear Science and Technology, Vol. 2, pp. 808 – 814 (**2011**). Available:https://www.varian.com/sites/default/files/resource_attachments/AttilaBriefFinal_0.pdf [Accessed 23 September 2016].

F. **Wasastjerna**. *Using MCNP for fusion neutronics*. Thesis dissertation. Helsinki University of Technology (**2008**). ISBN 978-951-38-7129-1.

R. **Wenninger**. *DEMO1 Reference Design - 2015 April ("EU DEMO1 2015") - PROCESS One Page Output*. EUROFusion IDM location: https://idm.euro-fusion.org/?uid=2LBJRY (**2015**).

S. **Wold**. *Spline functions in data analysis*. Technometrics, Vol. 16, nº 1, pp. 1 – 11 (**1974**).

World Nuclear Association. *Nuclear Fusion Power* (**2016**). Available: http://www.world-nuclear.org/information-library/current-and-future-generation/nuclear-fusion-power.aspx [Accessed: 12 July 2016].

Y. **Wu**. *CAD-based interface programs for fusion neutron transport simulation FDS Team*. Fusion Engineering and Design, Vol. 84, pp. 1987 – 1992 (**2009**). Doi: http://dx.doi.org/10.1016/j.fusengdes.2008.12.041

H. **Zohm**. *From ITER to DEMO* (**2014**). Available: http://www.dpg-physik.de/dpg/pbh/aktuelles/pdf/Zohm6.pdf [Accessed: 8 August 2016].